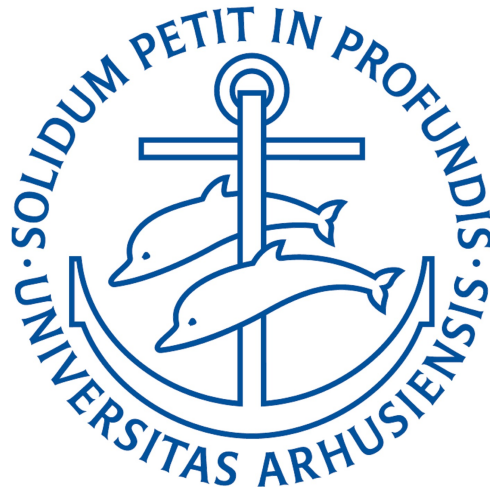


PhD THESIS

Materials and plasmon optimization
for efficient upconversion in
 Er^{3+} -doped TiO_2 and NaYF_4 : Towards
c-Si solar cell efficiency enhancement



AARHUS UNIVERSITY

Department of Physics and Astronomy

September 2018

Author:

Harish Lakhotiya

Supervisors:

Brian Julsgaard

Peter Balling

This thesis was submitted to the Faculty of Science and Technology at Aarhus University, Denmark, in order to fulfill the requirements for obtaining the PhD degree in physics. The work has been carried out under the supervision of Dr. Brian Julsgaard and co-supervision of Prof. Dr. Peter Balling at the Department of Physics and Astronomy from June 2015 to August 2018.

Contents

Contents	1
Abstract	5
Dansk resumé	7
List of Publications	9
Abbreviations	10
Acknowledgements	12
1 General Introduction	13
1.1 Introduction and motivation	13
1.2 Aim of the research	15
1.3 PhD dissertation outline	15
1.4 Contributions to the PhD work	16
References	18
2 Lanthanides and Theory of Upconversion	19
2.1 Introduction	19
2.2 Electronic structures of lanthanides	19
2.3 $4f$ Energy levels of lanthanides	19
2.4 Excitation and emission processes in lanthanides	20
2.4.1 Excitation processes in lanthanides	21
2.4.2 Emission processes in lanthanides	22
2.4.2.1 Radiative emission	23
2.4.2.2 Non-radiative decay	23
2.4.2.3 Energy transfers	24
2.5 The concept of upconversion	25
2.5.1 Main upconversion mechanisms	26
2.6 Details of the upconverter system of the present PhD work	26
2.6.1 Erbium (Er^{3+}) ions as an upconverter	27
2.6.2 TiO_2 as a host	28
2.6.3 NaYF_4 as a host	28
References	30
3 Theory of Plasmonics and Plasmon-Enhanced Upconversion	32
3.1 Introduction	32
3.2 Principle of plasmonics	32
3.3 Calculation of localized surface plasmon	34
3.3.1 Electrostatic approximation	34
3.3.2 Mie Theory or the optical properties of large spherical particles	36

3.3.3	The optical properties of non-spherical large particles (Numerical approaches)	37
3.4	Localized surface plasmon resonance (LSPR) dependence	37
3.4.1	Geometric dependence	37
3.4.2	Material dependence	39
3.5	Plasmon-enhanced upconversion	40
	References	42
4	Experimental: Fabrication Methods	44
4.1	Introduction	44
4.2	Upconversion materials fabrication	44
4.2.1	Radio frequency magnetron sputtering	44
4.2.1.1	Growth of the films	45
4.2.1.2	Controlling parameters	46
4.2.1.3	Experimental details of our experiment	46
4.2.2	Nanoparticle synthesis	47
4.2.3	Drop-cast assisted spin coating	47
4.3	Focused-ion beam technique	47
4.4	Electron beam lithography	48
	References	50
5	Experimental: Characterization Tools	51
5.1	Introduction	51
5.2	Structural characterizations	51
5.2.1	Scanning electron microscopy	51
5.2.2	Transmission electron microscopy	52
5.2.3	X-ray diffraction technique	53
5.2.4	Inductive-coupled plasma optical emission spectroscopy (ICP-OES)	53
5.2.5	Rutherford backscattering spectroscopy	53
5.2.6	Secondary ion mass spectroscopy	54
5.3	Optical characterizations	55
5.3.1	Spectroscopic ellipsometry	55
5.3.2	UV-Vis-NIR spectrophotometry	56
5.3.3	Upconversion luminescence (steady-state) measurements	58
5.3.4	Time-resolved photoluminescence measurements	60
	References	61
6	Results and Discussions	62
6.1	Introduction	62
6.2	Summary of Article 1	63
6.2.1	Introduction	63
6.2.2	Summary	63
6.3	Unpublished work	67
6.3.1	Motivation and numerical predictions	67

6.3.2	Fabrication and the fabrication challenges	69
6.3.3	Results and discussions	71
6.3.4	Conclusions	74
6.4	Summary of Article 2	75
6.4.1	Introduction	75
6.4.2	Summary	75
6.5	Summary of Article 3	79
6.5.1	Introduction	79
6.5.2	Summary	80
6.6	A correlation between the luminescence of Er^{3+} ions present in TiO_2 and NaYF_4 films	83
6.6.1	Calculation of normalized UCL yield for Er^{3+} -doped TiO_2 film	84
6.6.2	Calculation of normalized UCL yield for Er^{3+} -doped NaYF_4 monolayer	85
	References	86
7	Summary and Future Perspective	89
7.1	Summary	89
7.2	Future perspective	91
7.2.1	Fabrication of Au-discs embedded multilayered Er^{3+} -doped TiO_2 system	91
7.2.2	Chemically synthesized Au-nanorods for embedded Er^{3+} -doped NaYF_4 system	91
7.2.3	Photo-current measurements in upconversion based-c-Si solar cells	92
	References	93
8	Contributions to co-author articles	94
8.1	Introduction	94
8.2	Summary of Article 4	94
8.3	Summary of Article 5	94
8.4	Summary of Article 6	95
8.5	Summary of Article 7	95
	References	96

Abstract

The overuse of fossil fuels is a crisis for the existence of man-kind. Fossil fuels, such as coal and natural gases, are limited, and the rapid increasing demand of energy will exhaust them. Apart from their limited availability, they are harmful to the environment. One way to cut back the uses of natural resources is to rely on an unconventional, unlimited, and constant source of energy, such as solar energy. Currently, this alternative and renewable source of energy may not be as cost-effective as fossil fuels but the cutting-edge research in the fabrication of solar devices could match this discrepancy. Silicon (Si) is the most frequently employed material in the fabrication of solar cells. Therefore, there is a demand of the efficient and cost-effective Si-solar cells.

The present study focuses on the efficiency-improvement of Si-solar cells by reducing the spectral losses arising due to the spectral mismatching between the solar spectrum and the absorption spectrum of Si. Photons with energy lower than the bandgap of Si, called sub-bandgap photons, can not be absorbed, therefore, their conversion into photons with energy either equal or higher than the bandgap could improve Si-based device performance. The process of this conversion, where two- or more low energy sub-bandgap photons are converted into one higher-energy photon, is called upconversion. Upconversion is an inefficient process observed in Lanthanides but has the potential to be improved by optimizing the host material for the optically active Lanthanide dopant and/or enhancing by plasmonic coupling with the dopants. This is the main objective of this PhD study. In this work, I have optimized two hosts; TiO_2 and NaYF_4 in their film configurations for Er^{3+} ions and ensured the optimal coupling between the ions and the electron-beam-lithographic designed Au-nanodiscs for the efficient conversion of 1500 nm wavelength photons, considering their possible collective implementation in crystalline (c)-Si solar cells. The optimal coupling was ensured in two ways: (1) by determining the best possible arrangement of Au-discs close to the ions, and (2) by geometric optimization of Au-discs for the maximum e-field accumulation for nearby ions. The arrangements and geometry of the discs were numerically guided by a simple single-particle finite element method for both TiO_2 and NaYF_4 films.

The Er^{3+} -doped (5.1 at%) TiO_2 thin film fabricated at 350 °C substrate temperature was investigated as an efficient upconverter. The external quantum upconversion luminescence efficiency (EQLE), a ratio of the number of upconverting photons to the incoming 1500 nm photons, of the efficient 100 nm thin film was measured to be 1.5×10^{-6} at an irradiance of 0.3 kW/cm². The upconversion luminescence (UCL) yield of the film was enhanced by depositing numerically guided Au-nanodiscs on top of the films. Experimentally, a maximum 7 folds UCL-enhancement was observed for the discs, where the localized surface plasmon resonance (LSPR) wavelength matched with the excitation wavelength (1500 nm).

The next stage upconversion-improvement in this sputtered oxide was ensured by fabricating Au-discs-embedded multi-layered Er^{3+} -doped TiO_2 . However, the encountered fabrication challenges demanded a detailed study of the impact of temperatures (deposition and annealing) on a single layer TiO_2 film. It was observed that the annealing has adverse impact on the UCL of the thin films. However, it was proposed that the annealing in hydrogen atmosphere could resolve the encountered challenges of the multi-layered system fabrication.

The UCL yield of Er^{3+} -doped $\beta - \text{NaYF}_4$ upconversion nanocrystals (UCNCs) was investigated in their two-dimensional arrangements. The UCL yields of spin coat-assisted self-assembled monolayers were improved by optimizing the NaLuF_4 shell thickness around the Er^{3+} -doped core-nanocrystals. A maximum ~ 100 folds UCL-improvement was observed for a core-shell UCNC monolayer, where the shell thickness was 10.1 nm. The EQLE of the most efficient monolayer was measured to be 9.3×10^{-10} at an irradiance of 0.3 kW/cm^2 . The next stage UCL-improvement in the monolayers was performed by depositing resonant Au-discs either on top or buried in monolayers. The maximum Au-discs induced UCL-enhancement was ~ 5 folds in the core-UCNC monolayers, which dropped exponentially to 1.5 folds in the monolayer where the core was shelled by 10.1 nm NaLuF_4 .

The normalized UCL yield (UCL per Er^{3+} ion) was $\sim 5 \times$ larger for the optimized $\text{NaYF}_4 - \text{NaLuF}_4$ UCNC monolayer as compared to the optimized TiO_2 thin film at an irradiance of 0.3 kW/cm^2 , while the longest decay times were $\sim 54 \times$ higher. In addition, the ions in NaYF_4 host would be much more efficient for intensities below saturation, i.e. for lower-laser irradiance or one sun irradiance. Therefore, not only laboratorial but also in practice, NaYF_4 hosts are comparably better for solar cells.

Dansk resumé

Overforbruget af fossile brændstoffer udgør en krise for menneskeheden, som vi kender den i dag. Fossile brændstoffer, såsom kul og naturlige gasser er begrænsede, og derfor vil den øgede efterspørgsel på energi udtære de fossile brændstoffer. De fossile brændstoffer har desuden en begrænset tilgængelighed, og samtidig er de skadelige for miljøet. En måde at reducere forbruget af fossile brændstoffer på er, at udnytte den ukonventionelle, ubegrænsede og konstante energikilder, såsom solenergi. I øjeblikket er denne alternative og vedvarende energikilde måske ikke så omkostningseffektiv som fossile brændstoffer, men med den banebrydende forskning indenfor fremstillingen af solceller kan det, på sigt, være muligt imødegå dette problem. Silicium (Si) er det mest benyttede materiale til fremstilling af solceller. Derfor er der en stor efterspørgsel på effektive og billige Silicium-baserede solceller.

Den foreliggende undersøgelse fokuserer på effektivitetsforbedring af Si-solceller ved at reducere energitabet, der opstår på grund af den spektrale uoverensstemmelse mellem solspektret og absorptionsspektret af Si. Fotoner med energi lavere end båndgabet af Si, kaldet sub-båndgabsfotoner, kan derved ikke absorberes; deres omdannelse til fotoner med energi, lig med eller højere end båndgabet, kan derfor forbedre Si-baseret solcellers ydeevne. Processen for denne konvertering, hvor to eller flere lavenergi sub-båndgapfotoner omdannes til en foton med større energi, kaldes opkonvertering. Opkonvertering er en ineffektiv proces observeret i lanthanider, men kan potentielt forbedres ved at optimere værtsmaterialet for de optiskaktive doterede lanthanider, og / eller indføre en plasmonisk kobling til lanthaniderne. Dette er det vigtigste formål med dette ph.d.-studie. I dette arbejde har jeg optimeret to værter; TiO_2 og NaYF_4 i deres filmkonfigurationer for Er^{3+} -ioner. Her har jeg sikret den optimale kobling mellem ionerne og elektronstrålelitografisk degnere Au-nanodiske til effektiv omdannelse af 1500 nm bølgelængdefotoner under betragtning af deres mulige implementation i krystallinsk (c)-Si-baserede solceller. Den optimale kobling blev sikret på to måder: (1) ved at bestemme det bedst mulige arrangement af Au-diske tæt på ionerne, og (2) ved geometrisk optimering af Au-diske til maksimal elektriskfeltakkumulering for nærliggende ioner. Den eksperimentelle geometri og af fordeling af nanodiske blev guidet af enkeltpartikel finite-element beregninger for både TiO_2 - og NaYF_4 -film.

Er^{3+} -doterede (5,1 at%) TiO_2 tynde film, fremstillet ved 350°C , blev undersøgt som en effektiv opkonverterer. Den eksterne kvanteopkonverteringsluminescenseffektivitet (EQLE), dvs. forholdet mellem antallet af opkonverterende fotoner og antallet af indgående 1500 nm fotoner, blev målt til $1,5 \times 10^{-6}$ for 100 nm tyndfilm ved en intensitet på $0,3 \text{ kW} / \text{cm}^2$. Udbyttet af opkonverteringsluminescens (UCL) filmen blev forstærket ved at deponere Au-nanodiske, hvis størrelse blev vejledt af numeriske beregninger, oven på filmene. Et 7-gange forbedret UCL-udbytte blev observeret for nanodiske, optimeret således at den lokaliserede overfladeplasmonresonans (LSPR) var tilpassetmatchede med excitationbølgelængden (1500 nm).

Den næste fase af opkonverteringsforbedringen i TiO_2 blev sikret ved fremstilling Au-diskeindlejret i flerlagsstruktur bestående af Er^{3+} -doteret TiO_2 . Imidlertid viste fremstilling sig at være udfordrende, i det den krævede en detaljeret undersøgelse af virkningen af temperaturer (under deponering og udglødning) på enkeltlags- TiO_2 film. Det blev observeret, at

udglødningen havde en negativ indvirkning på UCL i de tynde film. Det blev imidlertid foreslået, at udglødningen i hydrogenatmosfære kunne løse de udfordringer, der opstår under multilag-fabrikationen.

UCL-udbyttet af Er^{3+} -doterede NaYF_4 opkonverterende nanokrystaller (UCNC'er) blev undersøgt i todimensionelle arrangementer. UCL-udbyttet af monolag, fremstillet ved spin-coating, blev forbedret, ved at optimere NaLuF_4 -skaltykkelsen omkring den Er^{3+} -doterede kerne i nanokrystallerne. En maksimal UCL-forbedring på en faktor 100 blev observeret for en UCNC monolag, med en skaltykkelse på 10,1 nm. EQLE af den mest effektive monolag blev målt til $9,3 \times 10^{-10}$ under bestråling ved $0,3 \text{ kW} / \text{cm}^2$. Den næste fase UCL-forbedring i monolagene blev udført ved deponering af resonante Au-diske enten ovenpå eller indeni i monolagene. Den maksimale Au-nanodisk-assisterede forbedring af UCL-udbyttet var 5 gange i for UCNC-monolagene uden skal, som faldt eksponentielt til 1,5 gange i monolag, hvor kernen var dækket med 10,1 nm tryk skal af NaLuF_4 .

Den normerede UCL yield (UCL yield pr. Er^{3+} -ion) for den optimerede Er^{3+} : $\text{NaYF}_4 - \text{NaLuF}_4$ monolag var 5 gange højere end den tilsvarende værdi for den optimerede Er^{3+} : TiO_2 tyndfilm under samme bestråling ved $0,3 \text{ kW}/\text{cm}^2$, mens den længste levetid var 54 gange højere. Grundet den lavere mætningsintensitet, vil ionerne i NaYF_4 -væerten fungere bedre under lavere intensiteter, fx under én sol. Derfor kan NaYF_4 -væerten være bedre til anvendelse i solceller.

List of Publications

This thesis is based on the following publications and manuscripts. The articles and manuscripts are ordered based on the my authorship position.

1. *Plasmonically enhanced upconversion of 1500 nm light via trivalent Er in a TiO₂ matrix.*
H. Lakhotiya, A. Nazir, S. P. Madsen, J. Christiansen, E. Eriksen, J. Vester-Petersen, S. R. Johannsen, B. Rolighed Jeppesen, P. Balling, A. Nylandsted Larsen, and B. Julsgaard, **Appl. Phys. Lett.** 109, 263102 (2016).
2. *Upconversion luminescence from magnetron-sputtered Er³⁺-doped TiO₂ films: Influence of deposition- and annealing temperatures and correlation to decay times.*
H. Lakhotiya, J. Christiansen, J. Lundsgaard Hansen, P. Balling, and B. Julsgaard
Revised version is submitted to **J. Appl. Phys.** (2018).
3. *Resonant Plasmon-Enhanced Upconversion in Monolayers of Core-Shell Nanocrystals: Role of Shell Thickness.*
H. Lakhotiya, A. Nazir, S. Roesgaard, E. Eriksen, J. Christiansen, M. Bondesgaard, F. C. J. M. van Veggel, B. B. Iversen, P. Balling, and B. Julsgaard
Submitted to **Nano Lett.** (August 2018).
4. *A model for 1500- to 980 nm photon upconversion in trivalent erbium.*
J. Christiansen, **H. Lakhotiya**, E. H. Eriksen, S. P. Madsen, P. Balling, and B. Julsgaard
Under preparation for **Phys. Rev. B** (expected submission September 2018).
5. *Plasmon-induced upconversion enhancement in TiO₂ : Er³⁺ films: the influence of scattering*
A. Nazir, **H. Lakhotiya**, E. Eriksen, S. Møller, J. Christiansen, S. P. Madsen, B. Julsgaard, P. Balling
Under preparation for **ACS photonics** (expected submission 2018).
6. *Particle-particle interactions in large, sparse arrays of randomly distributed plasmonic metal nanoparticles: a two-particle model.*
E. H. Eriksen, B. Julsgaard, S. P. Madsen, **H. Lakhotiya**, A. Nazir, and P. Balling, **Opt. Exp.** 25(16), 19354 (2017).
7. *Improving the efficiency of solar cells by upconverting sunlight using field enhancement from optimized nano structures.*
P. Balling, J. Christiansen, R. E. Christiansen, E. Eriksen, **H. Lakhotiya**, M. Mirsafaei, S. H. Møller, A. Nazir, J. Vester-Petersen, B. R. Jeppesen, P. B. Jensen, J. L. Hansen, S. K. Ram, O.Sigmund, M.Madsen, S.P.Madsen, and B.Julsgaard, **Opt. Mat.** 83, 279 (2018).

List of other Publications

My contributions in the articles are mentioned explicitly.

8. *Sputter Deposited TiO_x Thin-Films as Electron Transport Layers in Organic Solar Cells*

M. Mirsafaei, P. B. Jensen, **H. Lakhotiya**, J. L. Hansen, S. K. Ram, B. Julsgaard, P. Balling, H.-G. Rubahn, M. Madsen.

Under preparation for **ACS Appl. Mater. & Inter.** (expected submission September 2018).

[I have fabricated TiO_x thin films on various patterned ITO-coated quartz via sputtering technique.]

9. *Comparison of light-trapping potential of nanowrinkle textures for silicon thin-film solar cells*

R. Rizzoli, B. P. Falcao, E. H. Eriksen, **H. Lakhotiya**, D. Desta, M. Bellettato, B. R. Jeppesen, P. B. Jensen, C. Summonte, R. N. Pereira, A. Nylandsted Larsen, P. Balling, and S. K. Ram

Under preparation for **Nano Energy** (expected submission 2018).

[I have performed the extinction measurements of textured and non-textured cells and also participated in depositing various films via sputtering technique during the cell fabrication.]

10. *Application of nanowrinkle surfaces for efficient photon harvesting in ultra-thin amorphous silicon solar cells*

B. P. Falcao, R. Rizzoli, E. H. Eriksen, **H. Lakhotiya**, D. Desta, M. Bellettato, B. R. Jeppesen, C. Summonte, A. Nylandsted Larsen, R. N. Pereira, P. Balling, and S. K. Ram

Under preparation for **Nano Research (Springer)** (expected submission 2018).

[I have performed the extinction measurements of textured and non-textured cells and also participated in depositing various films via sputtering technique during the cell fabrication.]

Abbreviations

NIR	near-infrared
c-Si	crystalline-silicon
GaAs	gallium arsenide
GaN	gallium nitride
AlGaAs	aluminum gallium arsenide
RF-MS	radio frequency-magnetron sputtering
UCL	upconversion luminescence
PV	photovoltaic
Er^{3+}	trivalent erbium ions
AM	air mass coefficient
LSPRs	localized surface plasmon resonances
TiO ₂	titanium dioxide
NaYF ₄	sodium yttrium fluoride
UV	ultraviolet
Ln	lanthanide
SPPs	surface plasmon polaritons
E-field	electric-field
FEM	finite element method
FDTD	finite difference time domain
FIB	focused ion beam
UCNCs	upconverting nanocrystals
EBL	electron beam lithography
NCs	nanocrystals
RF	radio frequency
PMMA	polymethylmethacrylate
SEM	scanning electron microscope
TEM	transmission electron microscope
STEM	scanning transmission electron microscope
EDS	energy dispersive X-ray spectroscopy
HR-TEM	high resolution-transmission electron microscope
XRD	X-ray diffraction
ICP-OES	inductive coupled plasma optical emission spectroscopy
PMT	photomultiplier tube
CCD	charged-coupled device
AFM	atomic force microscopy
RBS	Rutherford backscattering spectroscopy
SIMS	secondary ion mass spectroscopy
SE	spectroscopic ellipsometry
EQLE	external quantum luminescence efficiency
TRPL	times-resolved photoluminescence
APD	avalanche photodiode
RECA	relative extinction cross-section

Acknowledgements

First and foremost, I would like to express my sincere gratitude to my supervisor Brian Julsgaard and co-supervisor Peter Balling for their guidance and extreme support over the last more than three years. Their significant contribution in upconverting materials brought me to Denmark. After coming here I realized that both are not just great researchers but also great human beings. Their trust and concerns on me allowed to keep my own scientific freedom. My several discussions with them have always been fruitful, inspired me to remain motivated, and helped me to learn various aspects of scientific career. I feel privileged to have worked under their supervisions.

I also want to express my gratitude to Arne Nylandsted Larsen for the extensive guidance in my early PhD period which led to fruitful results undoubtedly. I also want to thank Soren P. Madsen and Sanjay K. Ram for the scientific discussions. Sanjay has guided and motivated me during his tenure in the group. Apart, from the scientific discussions, he was more like a big brother who guided the right path whenever I was in dilemma. During this PhD duration, I also had the opportunities to work with fellow researchers, Postdocs, PhDs and masters of the Semiconductor group. I am grateful for their inputs in the SUNTUNE project on which my PhD thesis is based on. I am heartily thankful to all the Semiconductor group's technical staffs Pia Bomholt, Bjarke R. Jeppesen, John L. Hansen, and Jacques Chevallier for their unconditional support from the beginning of my tenure. Pia Bomholt were also an emotional support throughout my PhD. She always reminded me to take breaks from my scientific work for being more refreshed. I would also like to thank former PhD of this group Sabrina Johannsen for providing early stage training on most of the useful instruments.

I am also deeply thankful to Frank C.J.M. van Veggel for welcoming me in his group at University of Victoria as a 3 month visiting researcher. In addition, my thanks to Bo Brummerstedt Iversen for allowing me to build my nanocrystal synthesis setup in his lab. I also thank to Aref H. Mamakhel and Peter Hald for being always supportive during my chemistry experiments. I would like to sincerely thank to my coffee partners; Adnan Nazir, Raghavendra Rao, and Ievgen Boturchuk. We had tons of discussions on scientific, political, cultural, and social challenges across the globe, though we couldn't reached on one conclusion. I would like to take the opportunity to thank my partner in almost every publication, Adnan Nazir, for his support in sample preparation via lithographic technique on top-priority and for scientific discussions. My sincerest gratitude to Therese Andersen for being emotional support in the last period of my PhD duration.

Lastly, I would like to thank Søren Møller, Søren R. Nielsen, Samera Siddiqui, and Asif Equbal for proof-reading a large part of this thesis. Your corrections and inputs were really valuable. Last but not least, I would like to thank my family, especially my parents, B.L. Lakhotia and Kanta Lakhotia, and my siblings for always believing in me, for their continuous love and support in all my decisions. Without them I could not have made it till here.

I take this opportunity to sincerely acknowledge the Innovation foundation, Denmark for providing financial assistance under project SUNTUNE.

Harish Lakhotiya, Aarhus, August 2018

Chapter 1

General Introduction

1.1 Introduction and motivation

It has been reported that sunlight, which arrives on the surface of the earth, delivers energy 10,000 times the world energy demand [1, 2]. As a result, the use of solar energy has the potential to meet a large portion of future energy requirements. The high abundance and non-toxic nature of silicon (Si) makes it an attractive material over other materials (i.e. GaAs, GaN, AlGaAs/GaAs, etc) for the solar cell industries. Today, around 93 % of the total photovoltaic (PV) industries are based on Si-technology. Despite a significant development of the solar cell industry, an efficient and a cost-effective solar energy conversion is still a challenging task [3–5]. One of the main reasons for the poor conversion efficiency is the spectral mismatch between the very wide spectrum of photon energies of the solar radiation and the bandgap of the solar cell material [6]. When photons with energy lower than the bandgap of the absorbing materials, strike the surface of a solar cell, it simply passes through without being able to generate electron-hole pairs in the material. These losses of photons are called sub-bandgap or transmission losses. On the other side, photons with energy higher than the bandgap, are able to generate electron-hole pairs but lose the excess energy in the form of heat, and such losses are called thermalization losses. The contribution of the sub-band gap losses in a single junction crystalline-Si (c-Si) solar cells is around ~ 20 % whereas thermalization losses cover ~ 30 % of the total losses [7]. This limits the theoretical efficiency of an undoped crystalline-Si solar cell (110 μm thick) to 29.4 % for non-concentrating PV [8], also called Shockley-Queisser (S-Q) limit. However, control of these losses could further increase the efficiency limits in such devices.

One of the ways to reduce the sub-band gap or transmission losses of solar cells is to upgrade the low-energy photons into high-energy photons as depicted in Figure 1.1(a). The process of conversion of two or more low-energy photons into one high-energy photon is called upconversion. Upconversion is also known as anti-Stokes emissions as it violates the Stoke emission law where the emission energy must be lower than the absorption energy. Back in 1959, N. Bloembergen[9] has made breakthrough on photon upconversion based on lanthanide ion-doped material. The conventionally spaced $4f$ energy levels of lanthanides make them suitable for the upconversion process. Upconversion of photons from a non-coherent radiation source like the sun is mostly a multi-step process. Firstly, the meta-stable state gets populated by the absorption of low-energy photons. Afterwards, the energy transfer between neighboring ions or molecules leads to the population of higher excited state. The detailed upconversion processes are discussed in the Chapter 2 of the thesis. A ladder-like $4f$ energy levels of Er^{3+} ions [10], one of the lanthanides, allow the conversion of ~ 1500 nm wavelength photons into near-infrared (NIR) (< 1000 nm wavelength) and visible photons, which can be absorbed by c-Si solar cells. Therefore, Er^{3+} ions are one of the promising candidates for the efficiency enhancement in c-Si solar cells. However, Er^{3+} ions are needed to be incorporated into a host material for the upconversion process to occur. The upconversion luminescence (UCL) efficiency of incorporated Er^{3+} ions is the figure of merit for optimizing the fabrication of such upconversion materials. For the practicability in PV, the upconversion materials should be studied and optimized in the state of thin films.

This PhD work addresses some of unresolved questions in pursuit of understanding the physics of the UCL optimization and to develop flexible and highly efficient upconversion materials for c-Si solar cell applications. The first unresolved question is: (i) What are the underlying mechanisms that affect the upconversion in Er^{3+} -embedded thin films and how can the material be optimized for an efficient upconversion? Since the last decade, Er^{3+} -doped semiconductor nanocrystals are typically fabricated by chemical synthesis due to scalability and flexibility in the process. Previously, an extensive research in the luminescence-efficiency enhancement in such colloidal nanocrystals has been performed by several means [11, 12]. Application-wise, it is important to fabricate thin films from such nanocrystals. This leads to the second question (ii) how does the upconversion luminescence of colloidal nanocrystals vary with a transformation from the solutions to the films? Despite all the optimizations at material's level, the UCL efficiency stays limited due to the small absorption cross-section of Er^{3+} ions [13] and the non-concentrated light from the sun. Therefore, there is a need to increase the intensity of light around the luminescent centers so they can absorb more incident light and consequently, emit more upconverted light. This will improve the relevance of the materials for PV applications.

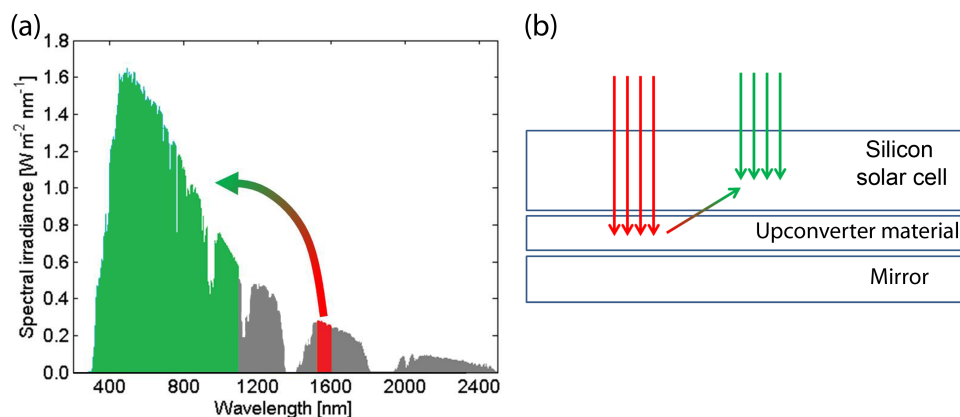


Figure 1.1: A demonstration of the concept of upconversion via a solar-spectrum and a plausible implementation of a upconverter material in a solar cell platform (a) A variation in irradiance of solar radiation with wavelength in AM-1.5 solar spectrum. The green section of the spectrum shows the absorbable light whereas gray and red sections represent the light considered as the transmission losses for c-Si solar cells. The red section of the spectrum overlaps with the absorption band of Er^{3+} . The curved arrow shows the conversion of the photons of the red section to the green section of the spectrum. (b) A sketch of a Silicon solar cell assembly with a upconversion layer at the back and a plausible mechanism of a conversion, via an angled arrow, of ~ 1500 nm wavelength photons (straight red arrows) to NIR and visible (straight green arrows) photons.

The conventional lenses could concentrate the solar radiation for Er^{3+} ions but the large size and the expensive installation make them impractical to implement. However, a manipulation of light-matter interactions at nanoscale with metallic nanostructures has been considered to be a very prominent way to concentrate light for the luminescent centers [14–18]. The free electrons of metal nanostructures interact strongly with light at the localized surface plasmon resonances (LSPRs) of the nanostructures. The LSPRs, collective oscillations of the free electrons in the metal nanostructures, localize the electric field (E-field) around the nanostructures [19]. The luminescent centers those are in close vicinity of the metal nanostructures feel such enhanced E-field that increase the absorption [20] of the ions and consequently enhance the UCL of materials. It is noteworthy to mention that the enhancement only works due to the non-linearity of the upconversion process. The LSPR frequency of metal-nanostructures can be tuned by the

geometry[21], and the refractive indices of the material[22, 23] and surroundings[24]. Considering the implementation of metal nanostructures with Er^{3+} ions, a tuning in plasmon frequency from visible to near-infrared to match the absorption in Er^{3+} ($\lambda \approx 1500$ nm) can be achieved by altering these parameters. This opens the discussions about (iii) what is the nature of interaction between metal nanostructures and the luminescence centers? and how does altering the interactions tune enhancement factors of the upconversion luminescence of the films? In principle, the implementation of such plasmon-enhanced upconversion thin films behind the commercially available solar cells, as shown in Figure 1.1(b), could make solar cells more efficient in photocurrent generation than the conventional cells.¹

1.2 Aim of the research

This PhD work is a part of a project entitled 'High-efficiency solar cells by spectral transformation using nano-optical enhancement', commonly abbreviated SUNTUNE. The SUNTUNE project is commenced with an aim to enhance solar cells efficiency by the spectral tuning of the solar radiation. The spectral tuning is achieved by an implementation of an efficient up-converting and a downshifting materials. An upconversion material should convert two or more low low-energy photons to one high-energy photon whereas a downshifting material should be in engagement of the conversion of one high-energy photon to one low-energy photon. The maximum efficiency in the upconversion material is ensured by the optimal arrangements of the topologically optimized metal nanostructures in a close vicinity of the luminescent centers. Ultimately, with use of both materials, a range of solar spectrum from $\lambda \approx 1100$ nm to $\lambda \approx 1550$ nm is converted to visible and lower-NIR photons, which can be absorbed by c-Si solar cells. This is a collaborative project among several universities and industries to find the practicability of the laboratorial deigned materials on the industrial prepared bi-facial c-Si solar cells and on the home-grown organic solar cells. The overall aim of SUNTUNE project is subdivided among several PhD studies including the present one.

In this PhD study, we optimize the upconversion luminescence of materials while ensuring their applicability in c-Si solar cells. Er^{3+} -doped TiO_2 and NaYF_4 are the studied materials of the present work. The optimum efficiencies of the upconversion materials are ensured by the use of Au-nanodiscs. The aim of this work is to answer all the above-asked questions in order to achieve the material optimization for the upconversion of 1500 nm wavelength photons.

1.3 PhD dissertation outline

The thesis is divided in 8 chapters. Chapter 2 and 3 collectively provide the theoretical background and literature overview of the fields related to this PhD work. Specifically, Chapter 2 presents the introduction about the trivalent lanthanides and discusses mainly about the $4f$ energy levels and possible transitions in lanthanides. The discussions further shift to the introduction of upconversion, mechanisms behind the upconversion process, and time-evolution of UCL emissions. In addition, an overview about the focused upconverter system, Er^{3+} ions doped in TiO_2 and NaYF_4 matrices, of this PhD work is presented. Chapter 3 provides the following overview: theoretical background behinds plasmonics, discussions on plasmonic materials (i.e.

¹As per rule of GSST (AU), it is allowed to reuse the text of part A report of the PhD study without any references. I would like to mention that some part of the Section 1.1 (Introduction and Motivation) are taken from my part A report.

Au-nanodiscs), and a link between plasmonics and upconversion. In this way, both the chapters cover the theoretical understanding of the work presented afterwards.

Chapter 4 and 5 collectively provide the theoretical and technical backgrounds behind the fabrication tools and the instruments used for the structural and the optical characterizations in this work. Chapter 4 discusses the different tools and methods used in fabrication of thin films and in chemical synthesis of the fluorides upconversion nanocrystals (UCNCs). The process for developing Au nanostructures is briefly discussed. Chapter 5 describes all techniques used for the structural and optical characterizations of the materials.

Chapter 6 exhibits all results and discussions of the PhD work. It summarizes all published and unpublished works. The summary of each article is presented as following: specific contributions to the work, introduction and motivation behind the work, summary, and conclusions of the work. The chapter summarizes three submitted or published works and a detailed descriptions of an unpublished work. Article 1, Article 2, and the unpublished work are based on the optimization of TiO_2 host for an efficient luminescence from Er^{3+} ions and Article 3 is mainly focused on the optimization of colloidal NaYF_4 UCNCs and their films for the same.

Chapter 7 summarizes the PhD project based on three articles and provides outlook of the presented work.

Chapter 8 briefly describes all other articles relevant to the thesis. It also defines my contribution in the articles.

1.4 Contributions to the PhD work

The PhD work involved both experimental and numerical tasks. I have been engaged in about all the experimental work, unless stated explicitly. All numerical computation for the PhD work were performed by Søren P. Madsen, Associate Professor at Department of Engineering, (data are presented in Article 1) and by Emil Eriksen, PhD student at Department of Physics and Astronomy (data are presented in Article 3). The experiments planning, fabrications of sputtered thin films, chemical synthesis of nanocrystals, monolayers and multilayers formation of nanocrystals, and nearly all structural and optical measurements were performed by the author. Other contributions to the experimental work are explicitly mentioned in Chapter 6. However, the major contributions to the experimental work are as following: all metal nanostructures used in this PhD work were fabricated by Adnan Nazir, Postdoc at IFA (data are presented in Article 1 and 3) and all time-resolved photoluminescence experiments and data analysis were performed by Jeppe D. Christiansen, PhD student, and Søren Roesgaard, Postdoc at IFA (data are presented in Article 1 and 3). A schematic is presented in Figure 1.2 for a simplified overview of the contributors of this PhD work.

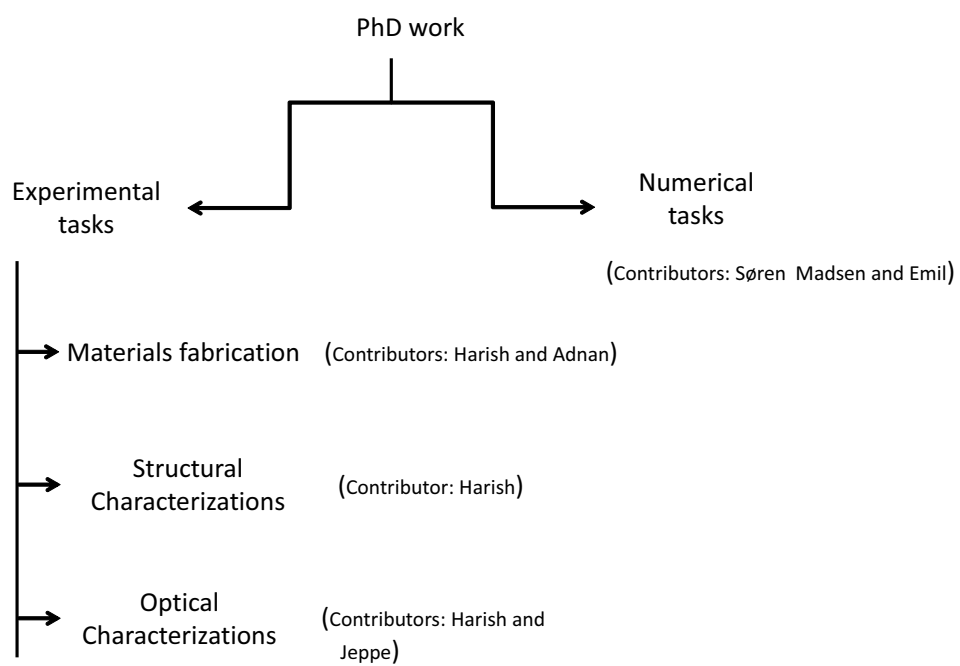


Figure 1.2: PhD work distributions and major contributors to the specific tasks.

Bibliography

- [1] Solar Generation: Solar Photovoltaic Electricity Empowering the World, European Photovoltaic Industry Association—EPIA, 2011.
- [2] World Energy Assessment Report: Energy and the Challenge of Sustainability, United Nations Development Program, United Nations, New York (USA), 2000, 162.
- [3] H. A. Atwater and A. Polman, Plasmonics for improved photovoltaic devices, *Nat. Mater.* 2010, 9, 205.
- [4] A. J. Nozik and J. Miller, Introduction to solar photon conversion, *Chem. Rev.* 2010, 110, 6443.
- [5] P. K. Nayak, G. Garcia-Belmonte, A. Kahn, J. Bisquert, and D. Cahen, Photovoltaic efficiency limits and material disorder, *Energy Environ. Sci.* 2012, 5, 6022.
- [6] X. Huang, S. Han, W. Huang, and X. Liu, Enhancing solar cell efficiency: the search for luminescent materials as spectral converters, *Chem. Soc. Rev.* 2013, 43, 173.
- [7] S. Fischer, J. C. Goldschmidt, P. Loper, G. H. Bauer, R. Brüggeman, K. Kramer, D. Biner, M. Hermle, and S. W. Glunz, Enhancement of silicon solar cell efficiency by upconversion: Optical and electrical characterization, *J. Appl. Phys.* 2010, 108, 044912.
- [8] A. Richter, M. Hermle, and S. W. Glunz, Reassessment of the Limiting Efficiency for Crystalline Silicon Solar Cells, *IEEE J. Photovoltaics* 2013, 3(4), 1184.
- [9] N. Bloembergen, Solid State Infrared Quantum Counters, *Phys. Rev. Lett.* 1959, 2, 84.
- [10] F. Auzel, Upconversion and Anti-Stokes Processes with f and d ions in Solids, *Chem. Rev.* 2004, 104, 139.
- [11] S. Fischer, N. D. Bronstein, Joseph K. Swabeck, Emory M. Chan, and A. Paul Alivisatos, Upconversion quantum yield of Er^{3+} -doped $\beta\text{-NaYF}_4$ and Gd_2O_3 : The effects of host lattice, Er^{3+} doping, and excitation spectrum bandwidth, *Nano Lett.* 2016, 16, 7241.
- [12] S. Fischer, R. Martin-Rodriguez, B. Frohlich, K. W. Kramer, A. Meijerink and J. C. Goldschmidt, Precise Tuning of Surface Quenching for Luminescence Enhancement in Core Shell Lanthanide-Doped Nanocrystals, *J. of Luminescence* 2014, 153, 281.
- [13] F. Auzel, Upconversion Processes in Coupled Ion Systems, *J. of Luminescence* 1990, 45, 341.
- [14] D. M. Wu, A. Garcia-Etxarri, A. Salleo, and J. A. Dionne, Plasmon-Enhanced Upconversion, *J. Phys. Chem. Lett.* 2014, 5, 4020.
- [15] S. R. Johannsen, S. P. Madsen, B.R. Jeppesen, J. V. Nygaard, B. Julsgaard, P. Balling, and A. Nylandsted Larsen, Upconversion enhancement in Er^{3+} doped TiO_2 through plasmonic coupling: Experiments and finite-element modeling, *Appl. Phys. Lett.* 2015, 106, 053101.
- [16] A. E. Christensen, C. Uhrenfeldt, B. Julsgaard, P. Balling, and A. Nylandsted Larsen, Interaction between Au nanoparticles and Er^{3+} ions in a TiO_2 matrix: Up-conversion of infrared light, *J. Eglypro.* 2011, 10, 111.
- [17] H. Mertens, and A. Polman, Plasmon-enhanced erbium luminescence, *Appl. Phys. Lett.* 2006, 89, 211107.
- [18] H.P. Paudel, D. Dachhepati, K. Bayat, S.S. Mot-taghian, P.S. May, C. Lin, S. Smith, and M.F. Baroughi, Design, fabrication, and characterization of a plasmonic upconversion enhancer and its prospects for photovoltaics, *J. Photon. Energy.*, 2013, 23, 035598.
- [19] S. Møller, J. Vester-Petersen, A. Nazir, E.H. Eriksen, B. Julsgaard, S. Madsen, and P. Balling, Near-field marking of gold nanostars by ultrashort pulsed laser irradiation: experiment and simulations, *Appl. Phys. A* 124(2), 210.
- [20] S. Fischer, F. Hallermann, T. Eichelkraut, G. v. Plessen, K. W. Krämer, D. Biner, H. Steinkemper, M. Hermle and J. C. Goldschmidt, Plasmon enhanced upconversion luminescence near gold nanoparticles-simulation and analysis of the interactions: Errata, *Opt. Express* 21(9), 2013.
- [21] C. Noguez, Surface Plasmons on Metal Nanoparticles: The Influence of Shape and Physical Environment, *J. Phys. Chem. C* 2007, 111, 3806.
- [22] A. Agrawal, I. Kriegel, and D. J. Milliron, Shape-Dependent Field Enhancement and Plasmon Resonance of Oxide Nanocrystals, *J. Phys. Chem. C*, 2015, 119 (11), 6227.
- [23] I. Zoric, M. Zach, B. Kasemo, and C. Langhammer, Gold, Platinum, and Aluminum Nanodisk Plasmons: Material Independence, Subradiance, and Damping Mechanisms, *ACS Nano*, 2011, 5, 2535.
- [24] Mahmoud A. Mahmoud, Maysamreza Chamanzar, Ali Adibi, and Mostafa A. El-Sayed, Effect of the Dielectric Constant of the Surrounding Medium and the Substrate on the Surface Plasmon Resonance Spectrum and Sensitivity Factors of Highly Symmetric Systems: Silver Nanocubes, *J. Am. Chem. Soc.* 2012, 134, 6434.

Chapter 2

Lanthanides and Theory of Upconversion

2.1 Introduction

The chapter begins with a literature review of the optical properties of lanthanide ions. The electronic structures, $4f$ energy-levels in particular, and the mechanisms involved in excitations and de-excitations of lanthanide ions are discussed in the very first section. The next section describes the physics of upconversion and provides a literature review on the lanthanide-based upconversion. This section consists of the definition of upconversion and the mechanisms involved in upconversion. Finally we describe in detail the specific lanthanide and the host lattices involved in the present work.

2.2 Electronic structures of lanthanides

Lanthanides have unique luminescent properties in conversion of photons and are considered to be non-toxic. Their ability to emit ultraviolet (UV), visible, and near-infrared (NIR) lights of the spectrum make them suitable for applications in optical (e.g. lasing and optical fibers), electronic (e.g. photovoltaic), medical (e.g. tissue sensing and cancer diagnosis), and life science (e.g. biological assay sensitivity) fields. The lanthanides (Ln) comprise fifteen metallic elements from lanthanum (atomic number = 57) through lutetium (atomic number = 71) in the periodic table. Ln along with the chemically similar elements scandium and yttrium, are collectively called the rare-earth elements. The electronic configuration of neutral Ln is a xenon core ($1s^2 2s^2 2p^6 3s^2 3p^6 3d^{10} 4s^2 4p^6 4d^{10} 5s^2 5p^6$) with two or three out shells ($6s^2 4f^{0-14}$ or $6s^2 5d^1 4f^{0-14}$). Neutral lanthanides are optically inactive and for optical activation they needed to be mixed in a solid. In a solid, Ln become in trivalent state, represented as Ln^{3+} , by losing electrons from $6s$ and $5d$ shells. The electrons of the $4f$ shell are non-interacting with the external environment due to shielding from the outermost shells ($5s$ and $5p$) even in their 3^+ configurations. Therefore, in Ln^{3+} , $4f$ energy levels are essentially uninfluenced by various hosts. Transitions involved in the upconversion processes mentioned in the thesis are $4f-4f$ transitions, which is considered in the next section.

2.3 $4f$ Energy levels of lanthanides

In this section, L , S , and J are the total orbital angular momentum, the total spin, and the total angular momentum, respectively, of the lanthanide element. The total angular momentum is given by $\vec{J} = \vec{L} + \vec{S}$ where J is restricted to $|L-S| \leq J \leq |L+S|$. The perturbation of Ln $4f$ levels are caused by the Coulomb interaction between the electrons and spin-orbit coupling of the electron's spin with its motion. The Coulomb repulsion between the electrons within the $4f$ shell has the largest contribution to the energy splitting followed by the spin-orbit coupling as mentioned in Figure 2.1. The Coulomb interaction splits the $4f$ energy levels into ^{2S+1}L energy levels with a multiplicity of $(2S+1)(2L+1)$ micro states and spin-orbit interactions further split

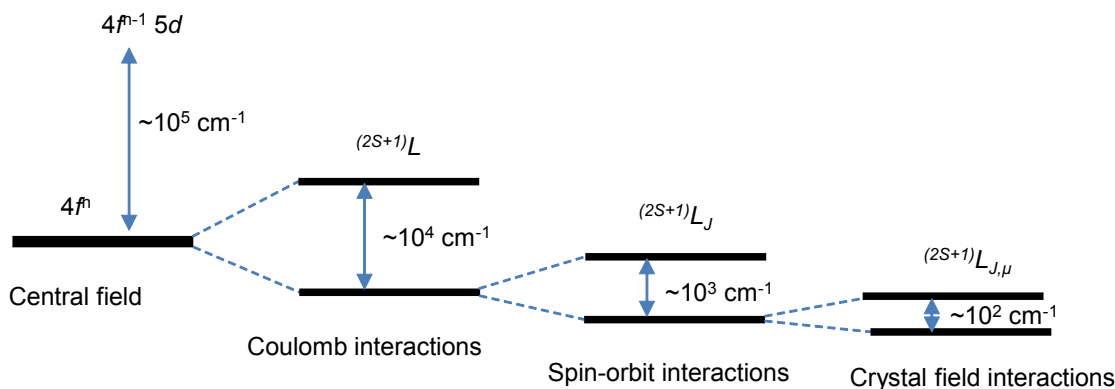


Figure 2.1: Interactions responsible for the perturbation in the $4f$ levels of lanthanides

this into $^{2S+1}L_J$, each with multiplicity of $(2J+1)$. On the insertion of Ln into solids, $4f$ energy-levels interact with the crystal field of host lattice. This results in a further splitting called Stark splitting or crystal field splitting as depicted in Figure 2.1. The interaction with the crystal field is weaker than the other two discussed interactions thus its influence on the energy-level splitting is minor. It is worth to mention that the number of Stark sub-levels depend upon the point group symmetry of the crystal-host, in which they are inserted.

Figure 2.2 shows the arrangements of the sub-levels of $4f$ energy levels in energy scale in different lanthanide ions doped in LaCl_3 host. This arrangements was first measured by Dieke [1] therefore it is also called Dieke diagram, which became a reference used to approximate the energy levels of the $^{2S+1}L_J$ multiplets of trivalent lanthanides doped in any host afterwards. The diagram represents the above mentioned splittings in the $4f$ energy levels. The width of each sub-levels in Figure 2.2 represents the magnitude of the Stark splitting, and the center of each multiplets approximates the position of the free ion $^{2S+1}L_J$ level.

In the next section we discuss more about the excitation of the lanthanides by electromagnetic radiations and the number of the ways of their de-excitations.

2.4 Excitation and emission processes in lanthanides

The excitations in lanthanide ions involve three possible transitions: $4f-4f$, $4f-5d$, and charge-transfer transitions.

$4f-4f$ transitions

These transitions are important in the spectroscopy and are also the focus of this PhD work. They involve the transitions of electrons upon electromagnetic excitation among various $4f$ energy levels in the same ion. Such transitions are forbidden in the electric dipole approximation because the states have the same parity. However, insertion of ions in inorganic solids could lift the forbidden transition: the intermixing of $4f$ orbitals of ions with the crystal field of the host relax the selection rule due to the insertion of the electronic states of opposite parity of the host and allow the electric dipole transitions to occur.

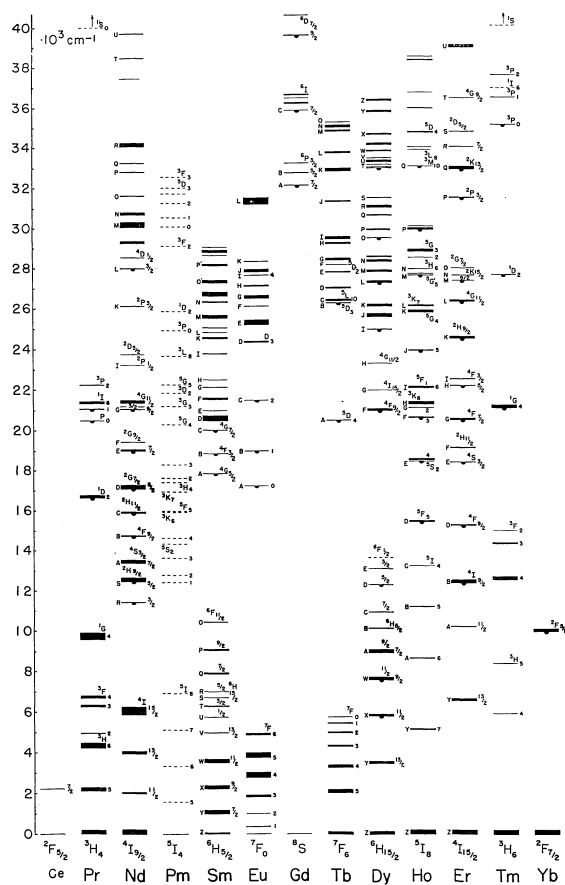


Figure 2.2: Dieke diagram: $4f$ energy levels of $2S+1L_J$ multiplets of trivalent lanthanides embedded in LaCl_3 host [2].

4f-5d transitions

An excitation of $5d$ orbitals to higher energy from the electrons of $4f$ orbitals constitute the $4f$ - $5d$ transitions. Such transitions, also called $4f^n \rightarrow 4f^{n-1}5d$, occur in the ions where the $4f$ shell has excess electrons to loose to achieve most stable configuration (i.e. empty, half filled or full filled $4f$ shell) afterwards, i.e. Ce^{3+} , Sm^{3+} , Eu^{3+} , and Pr^{3+} ions. The observed spectra of this transitions are called fd spectra. Unlike $4f$ - $4f$ transitions, such transitions are dipole-allowed therefore, the absorption and emission are broad and intense.

Charge-transfer state transitions

This transition involves a transfer of $2p$ electrons from the host anions (e.g. O^{2-} in oxides and F^- in fluorides) to the $4f$ orbitals. These kind of transitions are observed in the lanthanides which requires one or two electrons to achieve stable configuration. The transitions are allowed and result in larger absorption.

2.4.1 Excitation processes in lanthanides

Consider a simplified two-level quantum system. Upon absorption of a photon with an energy of $h\nu$, an electron is excited from the ground state $|1\rangle$ of energy E_1 to an excited state $|2\rangle$ of energy E_2 , where the energy of the incident photon is equal to the energy gap between both

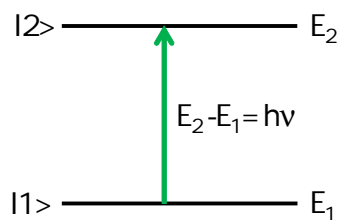


Figure 2.3: Two-level excitation processes in trivalent lanthanides

states ($E_2 - E_1 = h\nu$). If the light interaction is treated as a perturbation, the probability of transferring an electron from $|1\rangle$ to $|2\rangle$ is proportional to $|\langle 2|H|1\rangle|^2$, where H is a Hamiltonian operator that describes the interaction between the incoming light and the atomic structure of the system. This transferring probability is called transition rate. In the electric dipole nature of the transition, the Hamiltonian can be described as $H = \vec{p} \cdot \vec{E}$, where \vec{p} is a dipole operator and \vec{E} is an electric field component of the incoming light. The electric dipole operator is basically a product of the charge of the electron and the position of the electron from the nucleus (r). If the wavelength of the electromagnetic wave is much larger than the size of the atom, the field (E_s) of the incoming light is considered constant. This is the dipole approximation. Therefore, the transition probability (Γ) is

$$\Gamma \propto (eE_s)^2 \cdot |\langle 2|r|1\rangle|^2 \quad (2.1)$$

Such transitions are called electric dipole (ED) transitions and from (2.1) it depends upon the electric dipole moment only. Therefore, this transition is allowed on the condition of $\langle 2|r|1\rangle \neq 0$. The odd parity of r operator allows the possibility of $\langle 2|r|1\rangle = 0$ with the same parity of $|1\rangle$ and $|2\rangle$. As per Laporte's parity selection, the states with the same parity cannot be connected by ED transitions. However, the interaction with a non-centrosymmetric crystal field causes mixing between $4f$ orbitals and orbitals of opposite parity, thus relaxing the selection rules. Consequently, the transitions are partly allowed and are called forced ED transitions. The magnetic dipole (MD) processes (the interactions of atoms with the magnetic field of the incoming light) are, in contrast, weak but allowed transitions. The interaction Hamiltonian is $\vec{\mu}_m \cdot \vec{B}$, where \vec{B} is the magnetic field and $\vec{\mu}_m$ is the magnetic dipole moment. The magnetic dipole moment (μ_m) has even parity, therefore transitions between states of the same parity are allowed. Apart from the MD transitions, the electric quadrupole (EQ), and vibronic and forced ED are some other possibilities of transitions. The EQ transitions, on the one hand, are usually not visible due to much weaker strength than MD transitions but they are partly allowed. The magnetic and forced electric dipole transitions, on the other hand, are the one which have been observed [3].

2.4.2 Emission processes in lanthanides

The transitions of electrons from the excited state $|2\rangle$ to the lower-lying state $|1\rangle$ can be either radiative or non-radiative. In this section we study both of these decay processes associated with lanthanides.

2.4.2.1 Radiative emission

In the de-excitation of an electron from the high-excited energy level $|2\rangle$ to the low-excited level $|1\rangle$, a photon with energy, $E_2 - E_1 = h\nu$, is emitted. The rate equation provides the time-evolution of the population in a given energy level. It also describe the decays from the higher excited energy levels. The time evolution of the population of the state $|2\rangle$ is given by

$$dN_2/dt = -A_t N_2(t) = -(A_r + A_{nr})N_2(t) \quad (2.2)$$

where A_t is the total decay rate from the level $|2\rangle$ to the level $|1\rangle$, which is a combination of a radiative part of the decay rate, A_r and non-radiative part of the decay rate, A_{nr} . The solution of Equation 2.2 provides the following expression for the population of the level $|2\rangle$

$$N_2(dt) = N_2(0).e^{-(A_r+A_{nr})t} \quad (2.3)$$

where $N_2(0)$ is the population before any decay. Therefore, we can conclude that the population decays exponentially with time. The decay time or lifetime of level $|2\rangle$ is as follows

$$\tau = (A_r + A_{nr})^{-1} \quad (2.4)$$

where τ is the lifetime of an electron remains in the excited state. We can also determine the radiative quantum efficiency of the level by

$$\eta_r = A_r/(A_r + A_{nr}) \quad (2.5)$$

For a high upconversion yield, the radiative quantum efficiency must be high. In other words, the radiative decay should be higher than the non-radiative decay.

2.4.2.2 Non-radiative decay

In this de-excitation, an electron from the high-excited energy level $|2\rangle$ to the low-excited level $|1\rangle$ decays without emitting a photon. Some of the most relevant non-radiative processes are discussed below.

Concentration quenching

This is observed in the system when the average distance between lanthanide-dopants is small while assuming their homogeneous distribution in a host. High dopant concentrations vigorously increase the energy transfer between the dopants. Sometimes the excited-ions transfer their energy for a long distance involving multiples ions before relaxing. In this long distance excited energy transfer, the possibility of trapping the energy in the host lattice, defects, or impurities is very high, therefore increasing the probability of non-radiative decay.

Multiphonon relaxation

The emission of a photon in the de-excitation of an electron also depends upon the spacing between the excited energy level and the level below. In the large energy-spacing between the participant energy levels, the probability of the emission of a photon is higher compared to the

case were the energy-spacing is very low. The multiphonon relaxation rate (A_{mp}) decreases exponentially with the energy-spacing (ΔE) between the involved energy-levels and it also depends upon temperature. As shown below

$$A_{mp}(T) = A_{mp}(0)e^{-\alpha\Delta E} \quad (2.6)$$

where $A_{mp}(0)$ is the multiphonon rate at $T = 0 K$ and α is a positive constant depends upon the host lattice. The phonon energy of host materials is important in deciding the non-radiative decays. The high-phonon energy materials are more likely to bridge the gap between the energy levels and that eventually increase the multiphonon relaxation rate and consequently, more non-radiative decays. The needed number of phonons (p) needed for bridging a energy-spacing is

$$p = \Delta E/h\nu_{max} \quad (2.7)$$

where $h\nu_{max}$ is the maximum energy of a phonon. The rule of thumb is that if $\Delta E \leq 5p$ (i.e. if the spacing can be bridged by less than or equal to 5 phonons), then multiphonon relaxation is likely to occur[4]. Therefore, the selection of low-phonon energy hosts is important for an efficient upconversion luminescence from the optically active lanthanide dopants.

2.4.2.3 Energy transfers

The de-excitation of an electron is also possible if the electron transfers its energy to a nearby Ln ion. In this process, the ion, which absorb the photon is called the sensitizer and the ion, which receives the energy from the sensitizers is called the activator. The relaxation of the sensitizer ion to the ground state involves the transfer of excited energy, either radiative or non-radiative, to the activator ion. Note that the activator ion can be either in its ground state or an excited state before the energy transfer occurs. Based on this the energy transfer are two types:

Radiative energy transfers consist of the emission of a photon during the energy transfer. The emitted photon then gets absorbed by the activator ion. The excited activator then emit a photon with the same as energy or a different energy depending upon the energy-level arrangements. It is important to mention that this process is only possible within a photon travel distance.

Non-radiative energy transfers, in contrast, do not emit any photons during the transfer process. Depending upon the distance between the neighboring ions the process is governed by two interactions. For short distance (high dopant concentrations), exchange interactions happens between the involved activator and sensitizer ions. In this interaction, the energy transfers occur via exchanging the electrons between both ions however, the overlapping between the energy-levels is important. The transfer probability decreases exponentially with increasing the distance [4]. In case of comparably long-distances between neighboring ions, the electromagnetic interaction dominates. The electric dipole nature of the activator and sensitizer ions make this a dipole-dipole interaction. The transfer consists of oscillations in the activator induced by the excited sensitizer. The transfer probability in the dipole-dipole interactions depends upon several factors: (1) The distance between the activator and sensitizer ($\propto 1/R^6$ where R is the distance), (2) The spectral overlap between the emission spectrum of the sensitizer and the absorption spectrum of the activator, and (3) The associated oscillator strength.

Therefore, an efficient energy transfer demands a sensitizer with a large and a broad absorption cross section as well as with a longer decay rate than the transfer rate.

2.5 The concept of upconversion

The conversion of low-energy incident light to high-energy emitted light is well-known and several processes may be involved. The most relevant processes are summarized in Figure 2.4, all the processes are non-linear, where two low-energy photons are converted into a photon with higher energy. The emitted intensity of upconverted light (I_{em}) varies typically quadratically with the incident intensity (I_{in}): $I_{em} = \mu I_{in}^2$, where μ is proportionality coefficient. There are several ways to define an energy conversion efficiency. The way adopted for this PhD work is mentioned in Chapter 4. For a fair comparison among all the shown processes (Figure 2.4), one can compare the values of μ .

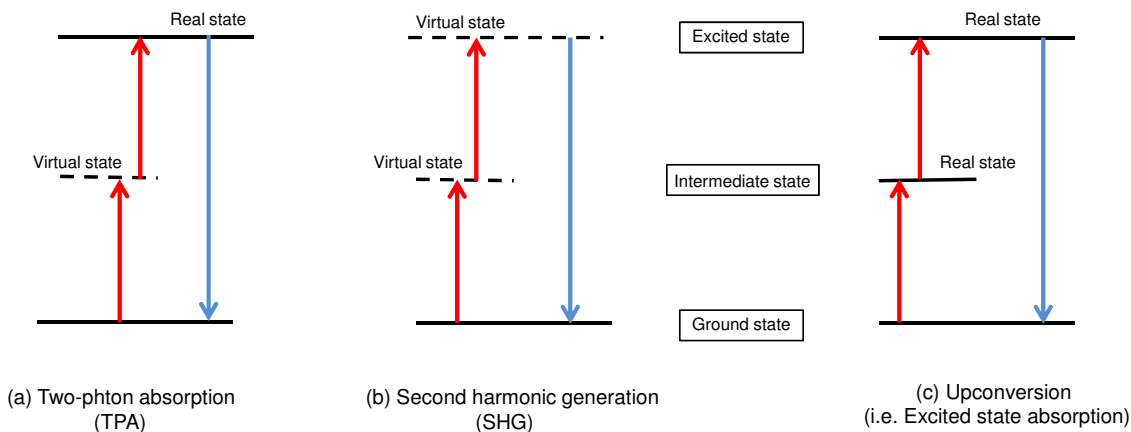


Figure 2.4: A conversion of two low-energy photons (represented by red arrows) to one high-energy photon (represented by blue arrows) by three different processes (a), (b), and (c). The dashed and solid lines indicate virtual and real nature of the energy-states.

Figure 2.4 shows the two-photon absorption and single photon emission processes via three different processes. From left to right, the first two processes are the less efficient compared to the process depicted in Figure 2.4(c). TPA and SHG involve virtual intermediate states which implies a must coincide of two-excited photons whereas SHG also has a virtual excited state that resembles the requirement of a coherency in excited photons for the process to be occurred. These qualities make the TPA and SHG very unlikely to happen and consequently, very inefficient. Therefore, they require very high excitation power. Upconversion, on the other hand, is a process, which depends upon a real intermediate state. The intermediate state must have a sufficiently long lifetime for storing the excitation so that a second photon or even a third photon can participate in excitation of an electron to the state-lying above or beyond. Therefore, upconversion processes do not need high-excitation power compared to the SHG and TPA to occur. It is also important to mention that a coherent excitation source is also not required for upconversion. The high conversion efficiency and the low threshold power make the upconversion process applicable for the several fields of study ranging from medical to photovoltaic. Lanthanides are popular for UCL applications because the $4f - 4f$ transition lies in the Vis and NIR spectrum, where upconversion is most relevant. Therefore, as like other non-linear processes the dependency of the upconversion light on the incoming light is also non-linear and it can be generalize as follows:

$$I_{UC} \propto I_{in}^n, \quad (2.8)$$

In a weak pumping power regime, n shows the number of photons requires to populate the excited state [5]. It is worth to mention that the non-linearity as we see in SHG where the value

of n stays 2 even at infinite excitation power does not hold here in upconversion. In the low excitation power, on one hand, the process is non-linear and the value of n is two or three as in two-photon or three-photon upconversion processes. On the other hand, the excited states get saturates with electrons once pumping power raises to high limits and consequently, n decreases and approaches 1 at extreme pump power and ultimately, upconversion loses its non-linearity.

2.5.1 Main upconversion mechanisms

The most relevant upconversion processes are now described. Figure 2.5 shows three different processes namely: Ground state absorption-excited state absorption (GSA-ESA), and energy transfer processes either resonantly (ETU) or with assist of phonons (Ph-ETU). In GSA-ESA process, a photon with energy either equal to or higher than the band-gap (a gap between two consecutive states) excites the ions from the ground state to an intermediate state, and a further absorption by the same ion excites it to the emitting state. This process is likely to occur in the materials with a long lifetime of the intermediate state. Energy transfer processes, in contrast, involves the transfer of excited energy between two ions as explained in Section 2.4.2.3. The resonant ETU involves the overlapping between the intermediate states of the involved ions. As discussed earlier, firstly, a ground state absorption (GSA) of two photons in two different but nearby ions happens which excite them to the intermediate state. Then the first excited ion transfers its gained energy to the second excited ion. Now the second ion gets further excited to the emitting state while the first one goes to the ground state. Generally, this resonant ETU is the most efficient process observed in materials[6, 7]. Phonon-assisted ETU, in contrasts, happens in the materials where dopants intermediate levels do not share spectral overlapping instead they posses energy-gaps. It is a pre-requisite that the energy-gap should be in a covering range of 1-3 phonons energy ($\sim 100 \text{ cm}^{-1}$).

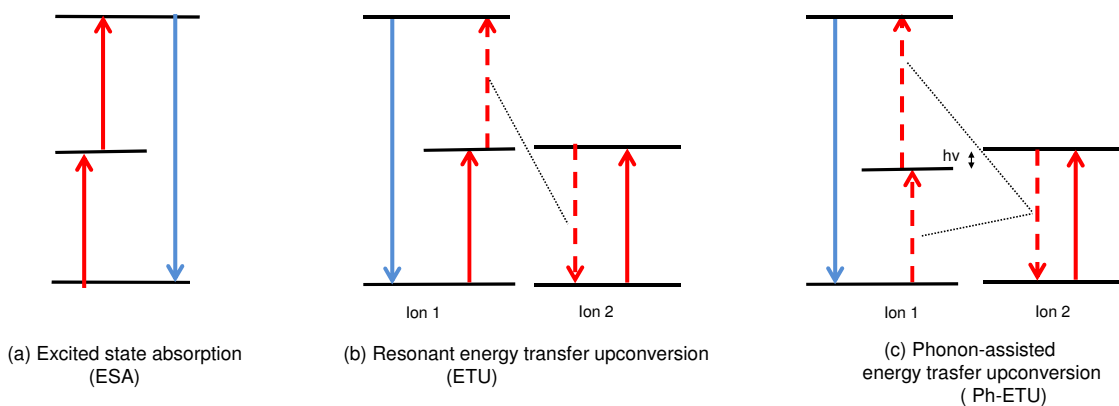


Figure 2.5: Upconversion mechanisms present in lanthanides: (a) a combination of two-step processes (ground-state absorption and excited-state absorption), (b) energy transfer between states of same energy, and (c) energy transfer with assistance of a phonon with energy $h\nu$. The red and blue arrows show the excitation with low-energy photons and de-excitation with the emission of high-energy photons. The dashed arrows represent the non-physical appearance of the excitation and de-excitation of energy-states.

2.6 Details of the upconverter system of the present PhD work

In this PhD study, we used Er^{3+} ions as an upconverter and focused on two host materials: TiO_2 , and NaYF_4 .

2.6.1 Erbium (Er^{3+}) ions as an upconverter

Erbium is a lanthanide that comprises a xenon core with two electron in its $6s$ shell and twelve electron in its $4f$ shell. The element becomes interesting only when it is in stable ionic state. The eleven $4f$ electrons of Er^{3+} ions are responsible of its unique luminescence properties. A complete $4f$ energy-level diagram of this element along with other lanthanides is shown in Dieke-diagram, Figure 2.2. In this section, we will discuss about the excitation of Er^{3+} ions via 1500 nm wavelength photons. The ladder-like energy levels of Er^{3+} allow the possibility of multiple excitations with photons of different energy. However, only the excitation by 1500 nm wavelength photons is considered in this PhD work. Figure 2.6 shows the involved energy levels of Er^{3+} ions in the upconversion of 1500 nm wavelength photons. Upon excitation, an electron is lifted from the ground state ($^4I_{15/2}$) to the first excited state via the transition $^4I_{15/2} \rightarrow ^4I_{13/2}$. Depending on the lifetime of the energy level, which also depends on the host matrices, the second photon is absorbed by the excited electron via the ESA process. This pumps the excited electron to $^4I_{9/2}$ energy state. Now the excited-electron either can absorb another 1500 nm wavelength photon and jump to above-lying state or de-excite to ground state via two possible ways. Either the excited-electron decay from the $^4I_{9/2}$ to the $^4I_{15/2}$ with an emission of a photon with 810 nm wavelength or the excited electron first decay non-radiatively to the $^4I_{11/2}$ and then radiatively via $^4I_{11/2} \rightarrow ^4I_{15/2}$, thus emitting a 980 nm photon. In contrast, if the excited-electron absorb another photon while at $^4I_{9/2}$, it is elevated to $^2H_{11/2}$. In consideration further possible non-radiative decays (see gray-dashed arrows in Figure 2.6), the excited electron may decay radiatively via: $^2H_{11/2} \rightarrow ^4I_{15/2}$ with an emission of 525 nm wavelength photon, $^4S_{3/2} \rightarrow ^4I_{15/2}$ with an emission of 550 nm wavelength photon, and $^4F_{9/2} \rightarrow ^4I_{15/2}$ with an emission of 660 nm wavelength photon.

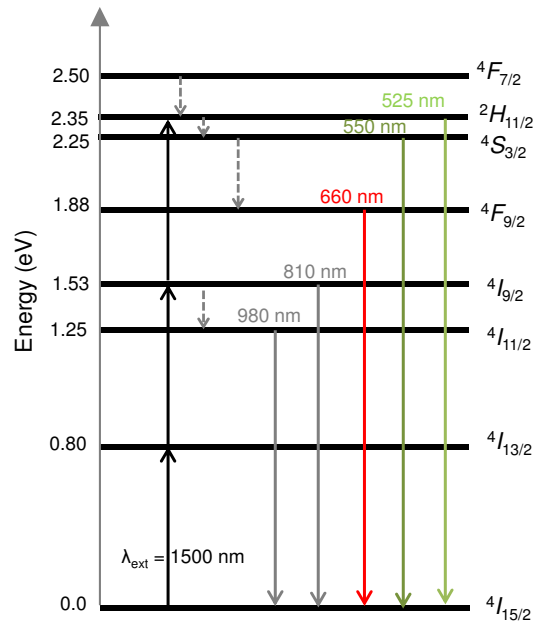


Figure 2.6: The involved $4f$ energy levels in the upconversion of 1500 nm wavelength photons in Er^{3+} . The black upward arrows represent the excitation whereas the downward solid and dashed arrows show the radiative and non-radiative decays, respectively. The color in arrows are linked to the wavelength of the emitted photons.

The photons with wavelength >1100 nm or energy <1.1 eV do not participate in the photocurrent generation in crystalline-Si solar cell, therefore, their conversion to higher-energy photons

would allow their participation. The energy-levels of Er^{3+} ion give the environment for such conversion by converting 1500 nm photons to the photons with wavelength 980 nm, 810 nm, 660 nm, and 550 nm.

2.6.2 TiO_2 as a host

Titanium dioxide (TiO_2) is considered to be a possible host for the optically active lanthanides. Previously, it has been observed that all three crystal phases of the material: anatase, brookite, and rutile, and amorphous phase are suitable in lanthanide-based upconversion [8–10]. There are mainly few reasons regarding the choice of the material for upconversion. Firstly, the low-phonon energy of the host lattice reduces the vibration and consequently, reduces multiphonon relaxation, mentioned in Section 2.4.2.2. It has been found that the phonon energy of TiO_2 stays nearly same in all crystal structures as expected. The phonon energy in anatase and rutile crystal phases are 639 cm^{-1} and 612 cm^{-1} , respectively [8, 11]. The 1500 nm excitation involves the transition between the $^4S_{3/2}$ and the $^4I_{15/2}$ energy levels and the bridging between these levels requires 10 phonons. Therefore, the multiphonon relaxation can not be possible at room temperature between these levels. Secondly, TiO_2 is a widely acceptable material for solar cell industry and it is a cheap material. Thirdly, the large bandgap of this material doesn't allow any absorption in the emission spectrum of the luminescence dopant (i.e. Er^{3+}). Thus the material will not absorb any upconverted light generated by Er^{3+} ions. Lastly, the fabrication of the material is easier in both thin films as well as nanostructures forms.

The insertion of Er^{3+} into TiO_2 lattice either substitutes the cations (Ti^{4+} ions) or settle on interstitial sites[12]. Independent of the site-occupancy, distortion in the lattice is likely present due to the difference in the ionic radii of both cations. In case of Er^{3+} doped TiO_2 system, the ionic radii of Er^{3+} and Ti^{4+} are 0.89\AA and 0.69\AA . Recently, it has also been seen that the high dopant concentration can also affects the crystallinity of the materials due to the possible lattice distortion [9, 11]. Despite the distortions in the host symmetry, TiO_2 is still an obvious choice for the lanthanide-dopants.

2.6.3 NaYF_4 as a host

NaLnF_4 (Ln= lanthanide and yttrium) is one of the well-known fluoride used for upconversion. Cations such as Na^+ , Ca^{2+} , Gd^{3+} , and Y^{3+} are chosen in the host lattices to match the ionic radii of the lanthanide dopant ions. The radii-matching prevents the formation of crystal defects and lattice stress, and thus generally Na^+ and Ca^{2+} fluorides are superior host materials for upconversion [13, 14]. Likewise, Gadolinium (Gd) and Yttrium (Y) are the most studied due to their optically inert nature. In the composite form (NaYF_4 or NaGdF_4) both elements are in their 3+ ionic state which make their electronic configuration either half-filled or filled stable. NaYF_4 is extensively studied in its microstructures and nanostructures forms. Its microstructure form is limited in applicabilities due to their comparably large size therefore, nanostructures form of the material is the current interest. However, the luminescence efficiency of the nanostructures is much lower than the microstructures and thus present research is mostly focused on enhancing the upconversion efficiency by chemical modifications of NaYF_4 nanostructures. The chemical modifications involves the dopant concentration variation, formation of optically active [15] or inactive [16] shells around the optically active core, size and shape variations [17], and the crystal phase variation [18]. NaYF_4 nanostructures are one of the best hosts available for lanthanide doping since it comprises (1) very high upconversion quantum efficiency [19] (2) very

low hygroscopic property, and multi-solvent dispersibility make them chemically stable [20, 21] (3) optical transparent over wide wavelength [22, 23] and (4) low phonon energies (350 cm^{-1}) [24].

Structurally, the material exist in two common phases: cubic (α) and hexagonal (β). The crystal structure of hexagonal phase possesses an ordered array of F^- ions and two types of low-symmetry lanthanide and Na^+ ions sites [25]. At the cation sites, distorted electron cloud forms strong coupling with lattice [25]. As a result, many non-harmonic phonons deprecating the energy transfer between absorption and emission centers. In the cubic phase, Na^+ and lanthanide cations randomly substitute with each other in the lattice [25], naturally complicating the bonding situation. This leads to even more non-harmonic phonon modes serving as the source of non-radiative decay pathways, in comparison with the highly ordered cation distribution in the hexagonal phase counterpart. For this reason, lanthanide-doped cubic NaYF_4 materials always exhibit an order-of-magnitude lower upconversion efficiency than their hexagonal counter-parts [25, 26]. Therefore, the present PhD work is focused on upconversion enhancement in hexagonal NaYF_4 material only.

Bibliography

- [1] G. H. Dieke and H. M. Crosswhite, The spectra of the doubly and triply ionized rare earths, *Appl. Opt.* 1963, 2(7), 675.
- [2] J.-C.G. Bünzli, and S.V. Eliseeva, *Basics of Lanthanide Photophysics*, Springer-Verlag: Berlin 2010.
- [3] L. J. F. Broer, C. J. Gorter and J. Hoogschagen, On the intensities and the multipole character in the spectra of the rare earth ions, *Physica B* 1945, 11(4), 231.
- [4] J. G. Solé, L.E. Bausá, and D. Jaque, *An Introduction to the Optical Spectroscopy of Inorganic Solids*, John Wiley and Sons Ltd: England 2005.
- [5] M. Pollnau, D. R. Gamelin, S. R. Lüthi, H. U. Güdel, and M. P. Hehlen, Power dependence of upconversion luminescence in lanthanide and transition-metal-ion systems, *Phys. Rev. B* 2000, 61, 3337.
- [6] F. Auzel, Upconversion and Anti-Stokes Processes with f and d ions in Solids, *Chem.Rev.* 2004, 104, 139.
- [7] Bo Zhou, Bingyang Shi, Dayong Jin, and Xiaogang Liu, Controlling upconversion nanocrystals for emerging applications, *Nat. Nano.* 2015, 10, 924.
- [8] A. Bahtat, M. Bouazaoui, M. Bahtat, C. Garapon, B. Jacquier, and J. Mugnier, Up-conversion fluorescence spectroscopy in Er^{3+} : TiO_2 planar waveguides prepared by a sol-gel process, *J. Non-Cryst. Solids* 1996, 202, 16.
- [9] S. R. Johannsen, S. Roesgaard, B. Julsgaard, R. A. S. Ferreira, J. Chevallier, P. Balling, S. K. Ram, and A. Nylandsted Larsen, Influence of TiO_2 host crystallinity on Er^{3+} light emission, *Opt. Mat. Exp.* 2016, 6(5), 1664.
- [10] S. R. Johannsen, L. R. Lauridsen, B. Julsgaard, P. T. Neuvonen, S. K. Ram, and A. Nylandsted Larsen, Optimization of Er^{3+} -doped TiO_2 -thin films for infrared light up-conversion, *Thin Solid Films* 2014, 550, 499.
- [11] S.-Y. Chen, C.-C. Ting, and W.-F. Hsieh, Comparison of visible fluorescence properties between sol-gel derived Er^{3+} - Yb^{3+} and Er^{3+} - Y^{3+} co-doped TiO_2 films. *Thin Solid Films*, 2003, 434(1-2), 171.
- [12] A. Patra, C. S. Friend, R. Kapoor, and P. N. Prasad, Fluorescence Upconversion Properties of Er^{3+} -Doped TiO_2 and BaTiO_3 Nanocrystallites, *Chem. Mater.* 2003, 15, 3650.
- [13] R. Yan and Y. Li, Down/Up Conversion in Ln^{3+} -Doped YF_3 Nanocrystals, *Adv. Funct. Mater.* 2005, 15(5), 763.
- [14] F. Wang and X. Liu, Upconversion Multicolor Fine-Tuning: Visible to Near-Infrared Emission from Lanthanide-Doped NaYF_4 Nanoparticles, *J. Am. Chem. Soc.* 2008, 130, 5642.
- [15] X. Li, D. Shen, J. Yang, C. Yao, R. Che, F. Zhang, and D. Zhao, Successive Layer-by-Layer Strategy for Multi-Shell Epitaxial Growth: Shell Thickness and Doping Position Dependence in Upconverting Optical Properties, *Chem. Mater.* 2013, 25, 106.
- [16] T. Rinkel, A. N. Raj, S. Dühren, and M. Haase, Synthesis of 10 nm NaYF_4 : Yb, Er/ NaYF_4 Core/Shell Upconversion Nanocrystals with 5 nm Particle Cores, *Angew. Chem.* 2015, 55, 1164.
- [17] F. Wang, Y. Han, C. Seong Lim, Y. Lu, J. Wang, J. Xu, H. Chen, C. Zhang, M. Hong, and X. Liu, Simultaneous phase and size control of upconversion nanocrystals through lanthanide doping, *Nature*, 2010, 463, 1061.
- [18] D. Li, Q. Shao, Y. Dong, J. Jiang, Phase-, shape- and size-controlled synthesis of NaYF_4 : Yb^{3+} , Er^{3+} nanoparticles using rare-earth acetate precursors, *J. rare earths*, 2014, 32(11), 1032.
- [19] J.-C. Boyer and F. C. J. M. van Veggel, Absolute quantum yield measurements of colloidal NaYF_4 : Er^{3+} , Yb^{3+} upconverting nanoparticles, *Nanoscale* 2010, 2, 1417.
- [20] S. Wilhelm, M. Kaiser, C. Würth, J. Heiland, C. Carrillo-Carrion, V. Muhr, O. S. Wolfbeis, W. J. Parak, U. Resch-Genger, and T. Hirsch, Water dispersible upconverting nanoparticles: effects of surface modification on their luminescence and colloidal stability, *Nanoscale* 2015, 7, 1403.
- [21] S. Heer, K. Kömpe, H. U. Güdel, and M. Haase, Highly Efficient Multicolour Upconversion Emission in Transparent Colloids of Lanthanide-Doped NaYF_4 Nanocrystals, *Adv. Mater.* 2004, 16, 2102.
- [22] E. M. Chan, G. Han, J. D. Goldberg, D. J. Gargas, A. D. Ostrowski, P. J. Schuck, B. E. Cohen, and D. J. Milliron, Combinatorial discovery of lanthanide-doped nanocrystals with spectrally pure upconverted emission, *Nano Lett.* 2012, 12, 3839.
- [23] J. M. Meruga, A. Baride, W. Cross, J. J. Kellar, and P. S. May, Red-green-blue printing using luminescence-upconversion inks. *J. Mater. Chem. C* 2014, 2, 2221.
- [24] K. W. Kramer, D. Biner, G. Frei, H. U. Güdel, M. P. Hehlen, and S. R. Lathi, Hexagonal sodium yttrium fluoride based green and blue emitting upconversion phosphors, *Chem. Mater.* 2004, 16, 1244.

-
- [25] G. S. Yi and G. M. Chow, Synthesis of Hexagonal-Phase NaYF_4 : Yb, Er and NaYF_4 : Yb, Tm Nanocrystals with Efficient Up-Conversion Fluorescence, *Adv. Funct. Mater.* 2006, 16, 2324.
- [26] K. W. Krümer, D. Biner, G. Frei, H. U. Güdel, M. P. Hehlen, and S. R. Lüthi, Hexagonal Sodium Yttrium Fluoride Based Green and Blue Emitting Upconversion Phosphors, *Chem. Mater.* 2004, 16, 1244.

Chapter 3

Theory of Plasmonics and Plasmon-Enhanced Upconversion

3.1 Introduction

The use of colloidal solutions of metal nanoparticles were in trend from 500 B.C. in making stained glass panels or giving different colors to glass [1]. It was 1908 when Gustav Mie proposed a mathematical explanation to different colors given by colloidal gold (Au) nanoparticles [2]. Mie calculated analytically the scattering and absorption in Au nanoparticles and also defined their variation with the size of the nanoparticles [2]. Despite his significant discoveries, the experimental and theoretical advancement in the field has only recently come into light. In the recent decades, the advancements in the field of fabrication tools, optical investigation tools and numerical tools have greatly progressed the research in metal nanostructures. Lithographies and chemical synthesis techniques are some of the fabrication tools those have contributed in the advancements. Electron microscopes and their modification with the associations of several other characterization techniques make them top-notch techniques in investigation of the material even at single-atom levels. The advancement in computational analysis tools increased the speed of calculations to find the physical phenomenon behind the experimental outcomes. Therefore, the applications of metal nanoparticles (i.e. plasmonic structures) have become broader and wider. Today they are applicable in biomedical as well as in energy fields.

In this chapter, we discuss plasmonics and plasmon-enhanced upconversion. The field of plasmonics has been attracting wide interest due to providing routes to guide [3–5] and concentrate [6] light at a scale smaller than the free space wavelength. Unlike the conventional optics, the major building block of plasmonics is metal. Plasmonics is a broad field but we mainly focus on defining localized surface plasmon resonance (LSPR) in this chapter. We explain the possible parameters tune the LSPR wavelength in detail. After achieving a understanding about LSPR and its possible controls, we shift our focus in finding the interaction between the lanthanide-based upconversion, explained in Chapter 2, and LSPR of metal nanoparticles. Furthermore, the possible ways to increase the plasmon-enhanced upconversion in optical emitters (lanthanides) is also proposed.

3.2 Principle of plasmonics

Metals contain a significant fraction of free electrons that may respond to external electromagnetic fields. Metals consist of a large number of unbound (free) electrons moving around randomly and colliding with each other in a background of bounded positive charged ions as per Drude, called Drude model. The numbers of positive and negative ions are constant in a defined volume at equilibrium. At non-equilibrium, the non-uniformity in charge distribution induces electric field to restore the charge neutrality. The induced electric field provides momentum to the electrons to overshoot the equilibrium and creates oscillations. Such collective oscillations

of electrons are termed as plasma oscillations and plasmons are the quanta of these oscillations. The resonance frequency of the plasmon is given by [7]

$$\omega_p = \sqrt{\frac{4\pi e^2 n_e}{m \epsilon_0}} \quad (3.1)$$

Where n_e is the free electron density, e is the charge of the electron, m is the mass of the electron and ϵ_0 is the dielectric constant of free space. There are mainly three kind of plasmon studied: bulk plasmons, surface plasmon polaritons (SPPs), and localized surface plasmons (LSPs). Bulk plasmons, shown in Figure 3.1(a), are longitudinal waves directing in the direction of resorting electric field due to charge separations and they cannot be excited by the light which are transverse wave (i.e. the electric field is perpendicular to the direction of propagation) [8]. On the surface termination of a bulk metal (at interface), new plasmons develop that are strongly localized to the surface. These surface plasmons are the SPPs (the name highlights the hybrid nature of the excitation) propagate parallel to the surface around few micrometers [8]. The SPPs propagate along the metal-dielectric interface (at the metal surface) as presented in Figure 3.1(b), until they decay either to absorption in the metal or scattering into random directions. SPPs have both transverse and longitudinal electric field components of the wave where the transverse component allows the interaction with light. However, the SPP can not be excited by freely propagating light due to it having a wave-vector whose magnitude greater than the incident light [7, 8]. A scattering of light via prism before its interaction with the metal or the dielectric could excite the SPPs.

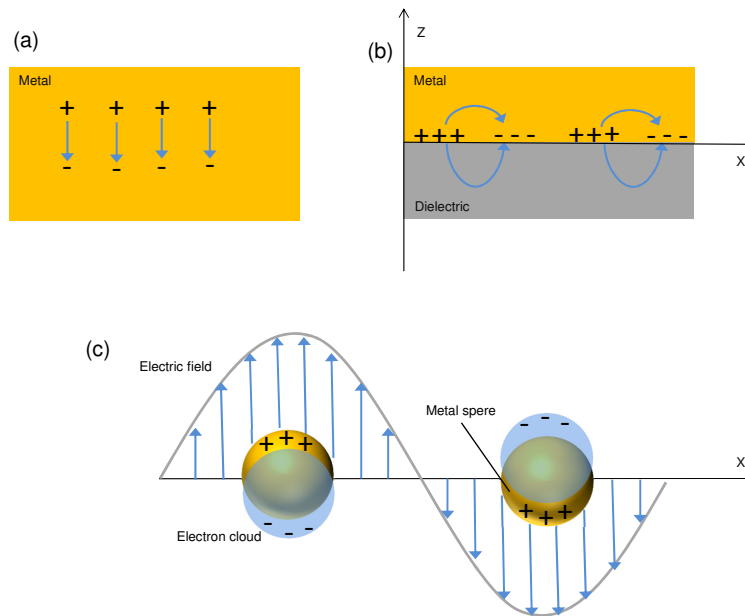


Figure 3.1: Schematic representations of (a) plasmon in bulk metal, (b) propagating plasmon at interface (i.e. SPPs), and (c) plasma oscillation at metal sphere coupled with electromagnetic wave, i.e. a localized surface plasmon.

In comparison to SPPs, LSPs are non-propagating plasma oscillations that are present in structures with sizes comparably smaller to the wavelength of light. The excitations of LSPs in nanostructures through direct electromagnetic illumination do not require any prisms or gratings configurations as we see in SPPs modes. At illumination, the conduction electrons inside the nanostructures experience the force from the induced electric field which displaces them with respect to the lattice as shown in Figure 3.1(c). However, the attraction to the ions provide the

restoring force of the oscillation. The matching between the incident light frequency and the frequency on which the electron oscillates inside the nanostructures creates resonance, called LSPR. The position and strength of the LSPR depends on the density of the electrons inside the nanostructures and the physical dimension of the nanostructures [9]. The LSPR are the responsible for strong absorption and efficient scattering of incident light therefore, it can be advantage to shift the LSPR frequency to that of the exciting light wave.

3.3 Calculation of localized surface plasmon

The LSP calculations are described based on the size and shape of metal particle. Electrostatic approaches are valid for very small nanoparticles ($a \ll \lambda$), Mie theory provides analytic solutions of spherical NPs embedded in homogeneous media. The response of more complicated system generally requires numerical approaches.

3.3.1 Electrostatic approximation

The particular section gives the analytical expressions of the interaction of a very small nanosphere with electromagnetic wave in the electrostatic approximation, i.e. $a \ll \lambda$. Therefore, the induced electric field is taken to uniform over the nanosphere which allows the electron to react simultaneously and be in phase with each other. In addition, the uniform field across the particle also allows the calculation of spatial field distribution with an assumption of one particle problem in an electrostatic field. Let us consider, a nanosphere with dielectric constant ϵ_{np} and radius a in a uniform E-field ($E=E_0\hat{z}$) (Figure 3.2). The surrounding medium is non-absorbing with the dielectric constant ϵ_m , and the field lines are parallel to the nanosphere surface. In the electrostatic approach, The potential outside and inside the sphere are obtained by solving the Laplace equation, $\nabla^2\phi = 0$, where ϕ is the potential. From this we can calculate the E-field, $E = -\nabla\phi$.

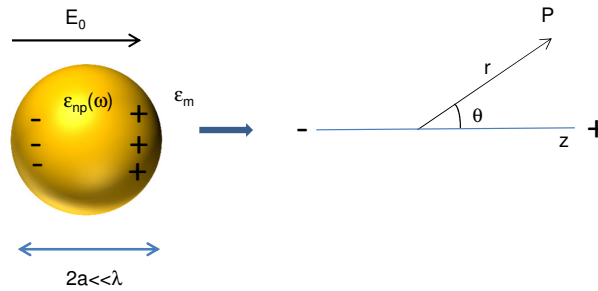


Figure 3.2: Electric field and a resultant charge distribution in a nanosphere in a quasi-static approximation.

The quasi-static solutions for the E-field inside and outside the nanosphere are given by

$$\vec{E}_{in} = E_0 \frac{3\epsilon_m}{\epsilon_m + \epsilon_{np}} \quad (3.2)$$

$$\vec{E}_{out} = E_0\hat{z} + E_0 \frac{\epsilon_{np} - \epsilon_m}{\epsilon_{np} + 2\epsilon_m} \frac{a^3}{r^3} (2\cos\theta.\hat{r} + \sin\theta.\hat{\theta}) \quad (3.3)$$

where θ is the angle between the position vector \mathbf{r} and z-axis. From (3.2) and (3.3), it is clear that at lowest value of $\epsilon_{np} + 2\epsilon_m$, the E-fields near the particle will be strongest. From the equations, we can conclude that the E-fields around the particle varies as $1/r^3$ and consequently, fields decay rapidly with the distance from the particle. This is achieved when

$$\text{Re}[\epsilon_{np}(\omega)] = -2\epsilon_m \quad (3.4)$$

where Re is the real part of the dielectric function. This relationship is known as Fröhlich condition or the associated mode (plasmon resonance) of the metal nanosphere. In metals, the dielectric function is described by

$$\text{Re}[\epsilon_{np}(\omega)] = 1 - \frac{\omega_p^2}{\omega^2 + \gamma^2} \quad (3.5)$$

where ω_p is the bulk plasmon frequency, presented in (3.1), γ is the collisions caused damping of the electron motion. If we neglect the damping term and insert (3.4) into the equation we achieve the resonance frequency of the metal nanosphere

$$\omega_{LSPR} = \sqrt{\frac{\omega_p^2}{1 + 2\epsilon_m}} \quad (3.6)$$

From the equation is it clear that the plasmon resonance of the metal nanosphere depends on its surrounding environment (ϵ_m). In the next section we will discuss this relationship in detail. In air ($\epsilon_m=1$), the LSPR for a spherical particle is defined by

$$\omega_{LSPR} = \frac{\omega_p}{\sqrt{3}} \quad (3.7)$$

Hence the LSPR of a metal nanosphere depends on the electron density and the effective electron mass via ω_p , referenced from (3.1).

Refreshing the memory of Figure 3.2, we see that the applied field induces dipole moment inside the sphere. The dipole moment can be calculated by

$$\mathbf{p} = \epsilon_m \alpha \mathbf{E}_0 \quad (3.8)$$

where α can be described by

$$\alpha = 4\pi^3 \frac{\epsilon_{np} - \epsilon_m}{\epsilon_{np} + 2\epsilon_m} \quad (3.9)$$

From an optical perspective, the resonantly enhanced polarization, α , is associated with enhanced absorption and scattering in the nanosphere. The associated absorption and scattering cross sections, C_{abs} and C_{scat} , can be calculated by [10]

$$C_{abs} = k \text{Im}(\alpha) = 4\pi a^3 \text{Im} \left[\frac{\epsilon_{np} - \epsilon_m}{\epsilon_{np} + 2\epsilon_m} \right] \quad (3.10)$$

$$C_{scat} = \frac{k^4}{6\pi} (|\alpha|^2) = \frac{8\pi}{3} k^4 a^6 \left| \frac{\epsilon_{np} - \epsilon_m}{\epsilon_{np} + 2\epsilon_m} \right|^2 \quad (3.11)$$

From (3.10) and (3.11), the absorption and scattering of light are hugely enhanced when the Fröhlich condition (3.4) is met [11]. For a small particle ($a \ll \lambda$), the absorption efficiency, scales according to a^3 , is dominant over the scattering efficiency, scaling at a^6 . Scattering is

therefore dominant for larger particles. The cross sections can be larger than the geometrical areas of the particle. Importantly, the difference in size become more observable where the incoming light frequency of the nanosphere is in the match with the excitation frequency (i.e. resonance), the cross sections get bigger than the geometric areas, presented in Figure 3.3(a). At resonance, the E-field lines get deflected to a large extent where some strongly converged at center of the nanosphere thus, the absorption as well as the scattering cross sections of the sphere are increased as shown in Figure 3.3(a). The dashed-line shows the diameter of extinction cross-section (sum of absorption- and scattering cross sections) and the bright area around the particle in the simulated image (inset image) also shows the near-field in Figure 3.3(a). Figure 3.3(b), in contrast, shows a small deflection of incoming E-field lines and most of them passes without being affected at out-of-resonance condition. The simulated image of Figure 3.3(b) show no E-field accumulation near the sphere. This points out the importance of hitting the LSPR.

The extinction cross-section is defined as $C_{abs} + C_{scat}$ for a sphere with volume V and complex dielectric constant, $\epsilon_{np} = \epsilon_1 + i\epsilon_2$, can be expressed as

$$C_{ext} = 9 \frac{\omega_p}{c} \epsilon_m^{3/2} V \frac{\epsilon_2}{[\epsilon_1 + 2\epsilon_m]^2 + \epsilon_2^2} \quad (3.12)$$

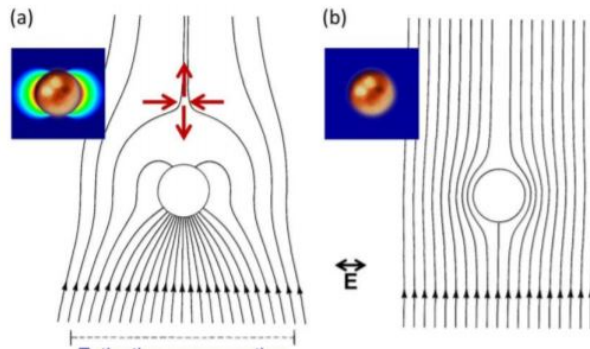


Figure 3.3: The E-field lines distribution around an aluminum nanosphere. (a) Plane wave incident from below of the frequency in resonance with dipole LSPR frequency and the E-field intensity distribution around a in-resonance nanosphere, and (b) the E-field intensity distribution around a off-resonance (LSPR frequency is not in match with the frequency of the incident light) nanosphere. The insets show the corresponding field distributions around the sphere. The dashed line shows the diameter of extinction cross section. The figure is taken from [12]

3.3.2 Mie Theory or the optical properties of large spherical particles

In the previous section, we have discussed how very small nanoparticle ($a \ll \lambda$) interacts with electromagnetic plane waves, considering uniform E-field across the particle. However, if the particle gets bigger and violets $a \ll \lambda$, the dipole approximation is not be applicable. In such cases, the full machinery of classical electrodynamics is required to determine the optical responses of larger spherical particles. Gustave Mie has proposed a theory called Mie theory which provides the analytical solution to Maxwell equations for a single sphere regardless the size of the particle and the wavelength of incoming light. It is worth to mention that the non-spherical particles can not be explained by Mie theory. Further details are accessible in book "Plasmonic fundamental and application" by Maier [7].

3.3.3 The optical properties of non-spherical large particles (Numerical approaches)

As per previous section, Mie theory only provides the complete solutions to Maxwell's equation for spherical particle in a non-absorbing homogeneous medium. Nevertheless, in practice, multiple examples are needed to be solved analytically. Recently, several numerical analysis tools have emerged in solving several complex shaped or sized structures. Finite element method (FEM) [13] and finite difference time domain (FDTD) [14] are the most used numerical approaches in solving Maxwell's equations for complex structures. FEM is one of the widely acceptable computational tool in determining the near-field in plasmonics. It is a technique to find the approximate solutions to the integral forms of partial differentiation equations under defined boundary conditions. The approach uses a computational domain where the integral are calculated based on the problem, required accuracy, and to include at least one wavelength of the electromagnetic field. The model computes the E-field distributions around a single particle of any geometry induced by a normal plane wave.

3.4 Localized surface plasmon resonance (LSPR) dependence

It has been discussed in section 3.2.1 that the LSPR depends on the particles geometry as well as the particle and surrounding materials. This allows an easy tunability of LSPR in metal nanostructures.

3.4.1 Geometric dependence

Geometric dependence has been studied on several chemically synthesized colloidal nanostructures as well as on lithographically designed nanostructures. Geometric alteration includes the variation in the size and the shape of nanostructures. In case of size alteration, a red-shift in the LSPR peak position is expected with increase in the size. The red-shift in LSPR can be translated as a decrease in the restoring force due to the increase in the distance between the opposite charges of the dipole [15, 16]. In addition, increase in size also leads to the higher-order modes of oscillations due to the non-homogeneously respond of spatial variation of the incident electric field across the particle [15, 16]. This non-homogeneous is due to a delay in the field across the structure [15]. The shift in LSPR wavelength becomes short or nearly invisible when the increase in size occurs in very small particles, considered under electrostatic approximation [17]. Here, we include an experimental example of Au-nanodiscs where the structures were fabricated by electron beam lithography [18] in Figure 3.4. From the figure, we can conclude that the increase in the size of nanodisc basically shifts the LSPR peak positing towards the higher wavelength. This is a very good example in demonstrating the shift in the LSPR from visible to NIR spectrum region with increasing the size roughly ten times the original one.

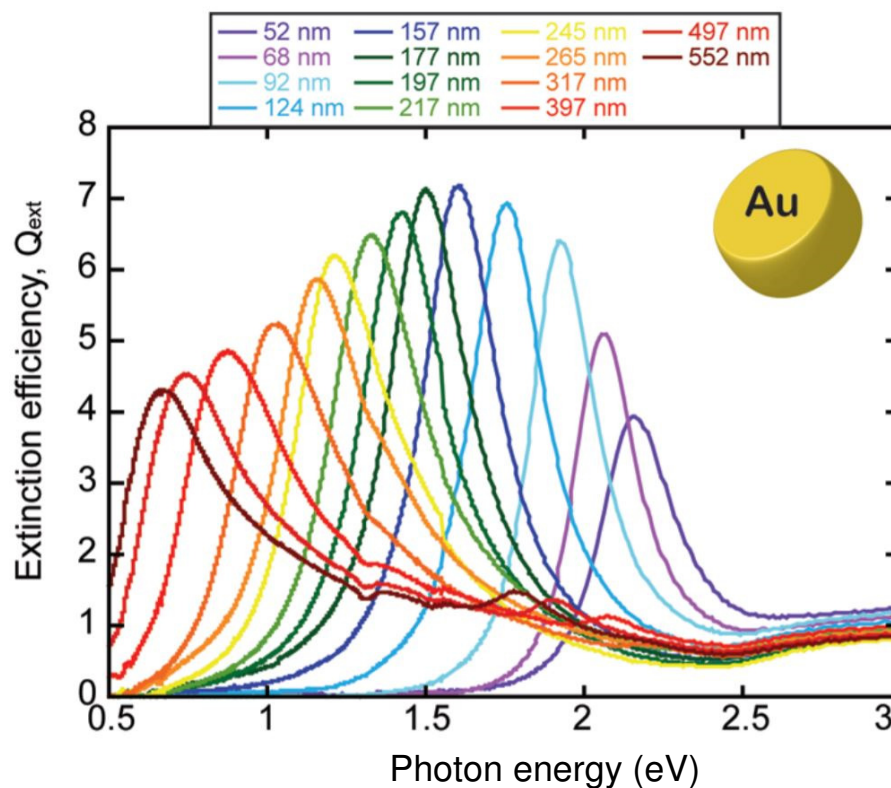


Figure 3.4: Extinction efficiency spectra of EBL-designed random arrays of Au nanodiscs. The variation in the LSPR peak positioning with the size of the nanodiscs is shown. The figure is adopted from [18].

The nanostructures shape dependence, on the other hand, is the other form of geometric alteration to vary the LSPR peak positioning. Apart from nanosphere which is a very common shape, plenty of other shapes can be designed experimentally and simulated numerically to enhance the strength of the localized field. The formation of many sharp edges around the structures is the main motivation in fabrication of multi-shaped particles. The increase in the sharpness in the edges shifts the LSPR peak positioning towards higher wavelength, as shown in Figure 3.5. In addition, the sharp edges are considered to be concentrating fields comparably more than the round shaped structures. They are therefore supposed to be more useful in upconversion enhancement by providing more incoming light to Er^{3+} emitters, discussed in details in section 3.5. The present advancement in both fabrication tools and computational domains allows the fabrication of several complex structures. In our research group, work in designing some hollow structures of different shapes to reduce the parasitic absorption in materials and simultaneously, concentrate more light by providing an extra boundary is in progress [19]. In addition, the advancement in both tools also makes it possible to topologically optimize the nanostructures for the desired application [20].

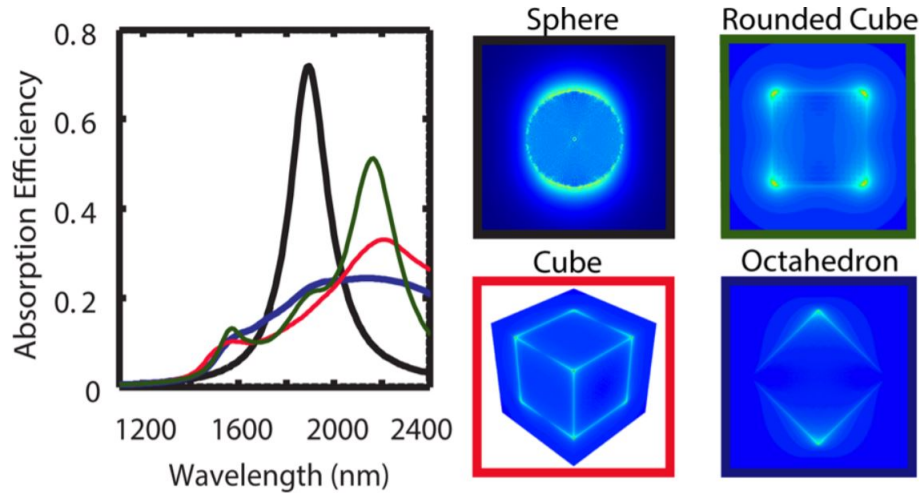


Figure 3.5: Absorption efficiency of differently shaped nanostructures with volume equivalent to the volume of a 10 nm nanosphere. Both cubes and octahedron have multiple peaks whereas the sphere is dominated by one peak in the spectra. The field enhancement in all simulated shapes are shown in the right panel of the figure. The figure is adopted from [21].

Here, we have included an example of relatively simple shape-dependent LSPR peak position in Indium-doped cadmium oxide nanostructures [21]. Figure 3.5, based on Agarwal *et al.* [21], shows the variation in the LSPR peak positioning in the absorption spectra with the different simulated shape of the nanostructures. It is clear that the increase in the number of sharp edges red-shifts the absorption peak (i.e. LSPR peak), however, the peaks also get broader. Furthermore, the increase in number of sharp edges around the structures also increase the number of oscillation modes and in results, multiple peaks observed going from sphere to octahedron.

3.4.2 Material dependence

The plasmonic material as well as the material surrounds the plasmonic structures affect the LSPR peak positioning. The dielectric properties of the nanostructures tune their LSPRs. The same geometric nanostructures in a same medium show different resonance positions if they are different materials. The dielectric function $[\epsilon_m(\omega)]$ of a material is a complex entity that defines the polarizability of the material under the electromagnetic wave illumination. The real part, $\text{Re}[\epsilon_m(\omega)]$, and imaginary part, $\text{Im}[\epsilon_m(\omega)]$, of the $\epsilon_m(\omega)$ describe the strength of the field induced polarization and the internal losses caused by polarization, respectively. $\text{Re}[\epsilon_m(\omega)]$ is a negative value entity in metals as well as in semiconductors with the high number of conduction electrons which is in agreement with Fröhlich condition, mentioned in (3.4). The wavelength-position of the internal absorptions or losses of plasmonic materials limit the applicability. In case of our Er^{3+} -based upconversion of 1500 nm wavelength photons system, the plasmonic structures should not be having internal losses or internal absorption at visible spectrum as the emitted upconverted photons will be in that range. Gold (Au), silver (Ag), copper (Cu), aluminum (Al), and tin (Sn) are some of the metals have negative real part of the dielectric function (i.e. permittivity (n)) and the abundance of conduction electron to support surface plasmon resonance. However their applicability depends upon their internal losses, reactive nature, and fabrication challenges. Al and Sn are well-suitable for far-UV range field-enhancement whereas Au and Ag are suitable for visible and NIR range field-enhancement. In our system, Au and Ag are appropriate, however, Ag has the tendency to get oxidize in air with time, and consequently, degrades

its plasmonic property. Thus, in the present thesis Au is chosen for its fairly low absorption at visible spectrum, effortless LSPR tunability, and chemically robust.

The effect of surrounding medium on the plasmonic resonance of the nanostructures is immense. It depends on the dielectric function of the media [22], the arrangements of the nanostructures on a solid support [23], distance between the supports and the nanostructures [23], and etc. It is for instance evident from (3.6) that the LSPR wavelength of the metal nanostructures is also influenced by the dielectric function of the surrounding media. Here, we show a shift in LSPR of a 10 nm Au nanoparticle in a different refractive media in Figure 3.6. It is clear that an increase in permittivity (n) shifts the LSPR towards higher wavelength.

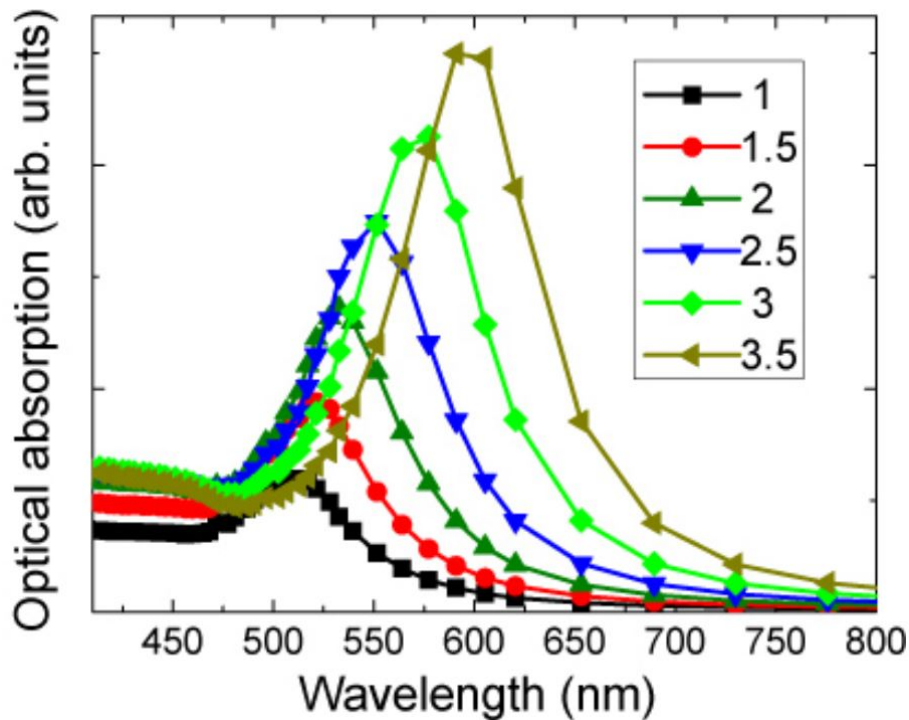


Figure 3.6: Calculated absorption spectra of 10 nm sized Au NPs embedded in different dielectric function media. The figure is adopted from [22]

3.5 Plasmon-enhanced upconversion

In this section we try to find the interaction between upconversion of lanthanides, that we studied in Chapter 2, and the E-field enhancement through metallic nanostructures. The partly forbidden transition in $4f - 4f$ states and low absorption cross section of lanthanides limit their upconversion efficiency. It has been extensively studied that the upconversion luminescence can be enhanced by the use of plasmonic structures in the close proximity of the emitters (optically active lanthanide dopants). The plasmonic structures alter the nearby environment by localizing the E-field near the emitters. The concentrated E-fields can enhance both absorption [24, 25] and emission [24] in the emitters. The strength of the enhancement in absorption and emission of emitters can be increased further by matching the LSPR of metal nanostructures with the optical transition of emitters. The resonance-matched plasmon enhanced upconversion is the one way to ensure the efficient upconversion. However, if the resonance-matched plasmonic structures

increase the non-radiative emission along with radiative then instead of overall enhancing it might result in quenching [26]. Previously, it has been reported [26] that at the smaller separation ($< 2 \text{ nm}$) between the emitters and metal nanoparticles the non-radiative decays were dominant whereas increasing the separation led to the more radiative decays until a maximum distance achieved. A further increase in spacing leads to a decrease in the upconversion enhancement due to the reduced localized-field for the emitters. Figure 3.7 shows the variation in upconversion enhancement, calculated by the ratio between the integrated area under the emission peaks of upconversion system with and without metal nanoparticles (Au and Ag), with a spacer thickness. The spacer was added by physical vapor deposition. It is very important how the spacer is maintained, and based on this, the present thesis shows the such variations in upconversion enhancement where the spacing is achieved by the shell of the upconversion nanoparticles instead. The obtained results are discussed in Chapter 6.

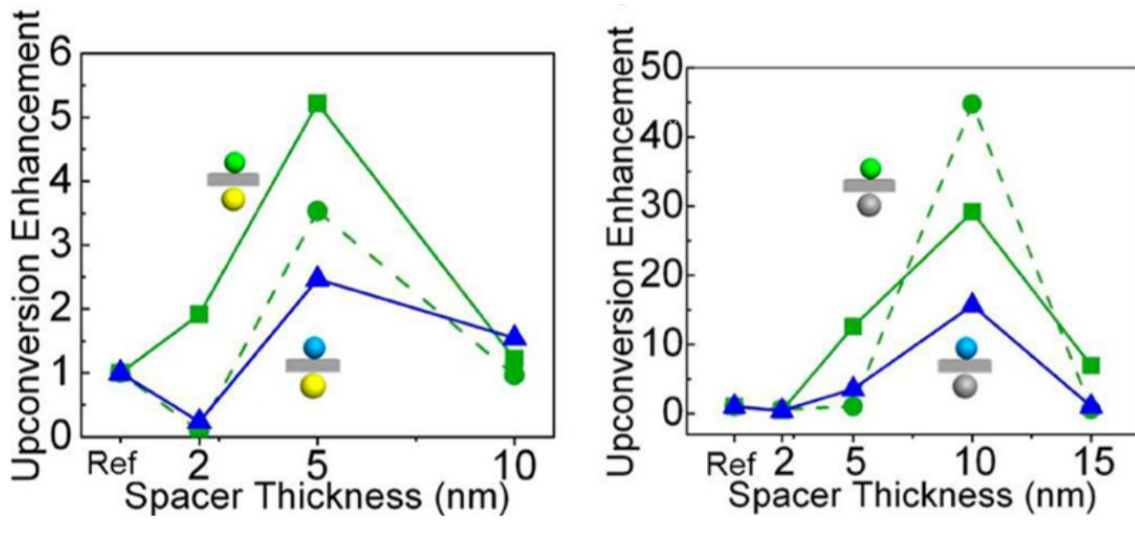


Figure 3.7: Upconversion enhancement (integrated area under the emission peak normalized to the pure upconversion films) as a function of Al_2O_3 spacer thickness. The left panel shows Au nanoparticles buried in two upconversion systems with a variable Al_2O_3 spacing: Yb, Er doped- NaYF_4 (green lines), and Yb, Tm doped- NaYF_4 nanoparticles (blue line). The right panel shows the Ag nanoparticles in both systems. The green solid lines correspond to the 540 nm emission band and the green dashed lines correspond to the 650 nm emission band of Yb, Er doped- NaYF_4 system. The blue solid lines correspond to the 475 nm emission band in Yb, Tm doped- NaYF_4 . The data point corresponding to pure upconversion films in the absence of metal nanoparticles as a reference (Ref) are added for comparison. The figure is taken from [26]

Therefore, by achieving an optimized distance between emitters and metal particles one can reduce non-radiative decay, and consequently increase the upconversion efficiency. The main focus in the present thesis is on the way to strengthen the plasmon-enhanced upconversion in Er^{3+} emitters incorporated into two host lattices, discussed in Chapter 2.

Bibliography

- [1] M. Faraday, The Bakerian Lecture: Experimental Relations of Gold (and Other Metals) to Light, Philosophical Transactions of the Royal Society of London 1857, 147, 145.
- [2] G. Mie, Beiträge zur Optik trüber Medien, speziell kolloidaler Metallösungen, Annalen der Physik 1908, 330(3), 377.
- [3] A. F. Koenderink, and A. Polman, Complex response and polariton-like dispersion splitting in periodic metal nanoparticle chains, Phys. Rev. 2006, B 74, 033402.
- [4] S. A. Maier, P. G. Kik, H. A. Atwater, S. Meltzer, E. Harel, B. E. Koel, and A. A. G. Requicha, Local detection of electromagnetic energy transport below the diffraction limit in metal nanoparticle plasmon waveguides, Nature Mater. 2003, 2, 229.
- [5] M. , A. Leitner, J. R. Krenn, and F. R. Aussenegg, Electromagnetic energy transport via linear chains of silver nanoparticles, Opt. Lett. 1998, 23, 1331.
- [6] D.-B. Li, X.-J. Sun, Y.-P. Jia, M. I Stockman, H. P Paudel, H. Song, H. Jiang, and Z.-M. Li, Direct observation of localized surface plasmon field enhancement by Kelvin probe force microscopy, Light-Sci. Appl. 2017, 6, e17038.
- [7] S.A. Maier, Plasmonics: Fundamentals and applications. 2007, USA: Springer.
- [8] W.A. Murray and W.L. Barnes, Plasmonic Materials, Adv. Mater.2007, 19(22), 3771.
- [9] K.L. Kelly, E. Coronado, L.L. Zhao, and G.C. Schatz, The Optical Properties of Metal Nanoparticles: The Influence of Size, Shape, and Dielectric Environment, J. Phys. Chem. B 2003, 107,668.
- [10] C.F. Bohren and D.R. Huffman, Absorption and scattering of light by small particles Weinheim, Germany: John Wiley and Sons, 1983.
- [11] U. Kreibig and M. Vollmer, Optical properties of metal cluster, Springer (Berlin), 1995.
- [12] S. V. Boriskina, Plasmonics with a twist: taming optical tornadoes on the nanoscale, Plasmonics: Theory and Applications 2014, 431.
- [13] C. Themistos, B. M. A. Rahman, and K. T. V. Gratin, Finite-element analysis of surface-plasmon modes for lossy optical waveguides by the use of perturbation techniques, Appl. Opt. 1995, 34(33), 7695.
- [14] S. Buil, J. Laverdant, B. Berini, P. Maso, J. Pierre Hermier, and X. Quélin, FDTD simulations of localization and enhancements on fractal plasmonics nanostructures, Opt. Exp. 2012, 20(11), 11968.
- [15] M. Meier and A. Wokaun, Enhanced fields on large metal particles: dynamic depolarization, Opt. Lett. 1983, 8(11), 581.
- [16] W. T. Doyle and A. Agarwal, Optical Extinction of Metal Spheres, J. Opt. Soc. Am. 1964, 55(3), 305.
- [17] S. Link and M.A. El-Sayed, Shape and size dependence of radiative, non-radiative and photothermal properties of gold nanocrystals, Int. Rev. Phys. Chem. 2000, 19(3), 409.
- [18] I. Zoric, M. Zach, B. Kasemo, and C. Langhammer, Gold, Platinum, and Aluminum Nanodisk Plasmons: Material Independence, Subradiance, and Damping Mechanisms, ACS Nano 2011, 5, 2535.
- [19] A. Nazir, H. Lakhotiya, E. H. Eriksen, S. P. Madsen, P. Balling. and B. Julsgaard, Plasmon-induced upconversion enhancement in TiO₂: Er³⁺ films: the influence of scattering, in preparation.
- [20] J. Vester-Petersen, S. P. Madsen, O. Sigmund, P. Balling, B. Julsgaard, and R. E. Christiansen, Field-enhancing photonic devices utilizing waveguide coupling and plasmonics - a selection rule for optimization-based design, Opt. Exp. 2018, 26(18), A788.
- [21] A. Agrawal, I. Kriegel, and D. J. Milliron, Shape-Dependent Field Enhancement and Plasmon Resonance of Oxide Nanocrystals, J. Phys. Chem. C 2015, 119, 6227.
- [22] M A Garcia, Surface plasmons in metallic nanoparticles: fundamentals and applications, J. Phys. D: Appl. Phys. 2011, 44(28), 283001.
- [23] C. Noguez, Surface Plasmons on Metal Nanoparticles: The Influence of Shape and Physical Environment, J. Phys. Chem. C 2007, 111, 3806.
- [24] D. M. Wu, A. García-Etxarri, A. Salleo, and J. A. Dionne, Plasmon-Enhanced Upconversion, J. Phys. Chem. Lett. 2014, 5, 4020.

-
- [25] S. Fischer, F. Hallermann, T. Eichelkraut, G. von Plessen, K. W. Krämer, D. Biner, H. Steinkemper, M. Hermle, and J. C. Goldschmidt, Plasmon enhanced upconversion luminescence near gold nanoparticles-simulation and analysis of the interactions: Errata, *Opt. Exp.* 2013, 21, 10606.
- [26] M. Saboktakin, X. Ye, S. J. Oh, S.-H. Hong, A. T. Fafarman, U. K. Chettiar, N. Engheta, C. B. Murray, and C. R. Kagan, Metal-Enhanced Upconversion Luminescence Tunable through Metal Nanoparticle-Nanophosphor Separation, *ACS Nano* 2012, 6, 8758.

Chapter 4

Experimental: Fabrication Methods

4.1 Introduction

This Chapter provides an overview of the experimental techniques employed to fabricate the materials used in this project. I begins with a description of the techniques incorporated in fabricating Er^{3+} -doped TiO_2 and NaYF_4 films, and in the deposition of Au-nanodiscs on top of quartz, TiO_2 , and NaYF_4 surfaces. This chapter will begin with an evaluation of the radio frequency magnetron sputtering (RF-MS) technique employed for the deposition of Er^{3+} -doped TiO_2 thin films. RF-MS parameters have carefully been considered, as this could affect the the deposition or make necessary changes to produce highly efficient upconversion films. Furthermore, the chemical synthesis of fluoride upconversion nanocrystals (UCNCs), Er^{3+} -doped NaYF_4 , is explained. The possible application of the nanocrystals in photovoltaic (PV) is in their film configuration, therefore, the spin-coating as a technique to produce such films of UCNCs will be introduced later in the chapter. Focused ion beam (FIB) tool which was employed for lamella preparation to measure the thickness of ultra-thin (~ 10 nm) Er^{3+} -doped TiO_2 films. Shifting from the upconversion materials to the plasmonic material, Au-nanodiscs were fabricated by the electron beam lithography (EBL). The chapter, thus, finishes with the discussions about the technique, the importance in this study, and the possible challenges and their solutions in the use of the technique for the desired outcomes.

4.2 Upconversion materials fabrication

Fabrication of Er^{3+} -doped TiO_2 , and NaYF_4 thin films were performed by the RF-MS and the chemical synthesis associated with the spin coating routes, respectively. The section begins with the full description about the RF-MS technique and its controlling parameters. The chemical synthesis route of the fluoride nanocrystals and their film realization via a drop cast-assisted spin coating technique is a follow-up discussion.

4.2.1 Radio frequency magnetron sputtering

Radio frequency magnetron sputtering (RF-MS) is a technique used to deposit thin films with the assistance of a plasma. The plasma is generated between the cathode (target side) and the anode (substrate side) by the application of a high radio frequency (RF) voltage in a vacuum chamber with a mtorr range gaseous pressure of Ar. The presence of permanent magnet under the target confines the plasma near the cathode (target), as illustrated in Figure 4.1. Under the RF voltage, the electrons are accelerated and collide with the neutral Ar atoms. The collision results in ionized Ar and a cascade effect breakdowns most of the neutral Ar atoms. The ionized atoms close to the cathode form a plasma. The applied RF voltage is an alternating voltage which periodically changes directions at 13.56 MHz frequency. The pulsating field hits the electrons in between the cathode and the anode, and under right circumstance the electrons may acquire additional force and ionize Ar effectively. Therefore, the generation and sustain of

the plasma is easier in RF-MS than its DC counterparts [1, 2]. During the plasma formation the chamber gets full of positive-ions and electrons. The lighter mass and the higher speed of electrons allow to make the cathode negatively charged. The negatively charged cathode attracts more Ar^+ ions and the bombardment of the ions knock-out the target atoms. The removal of target atoms is a consequences of the momentum transfer from Ar^+ ions. The removed target atoms travel towards the anode (substrate) when the alternating field reverses. The deposition of a single atom or the fragment of atoms on the substrate result in the formation of thin films, as illustrated in Figure 4.1 .

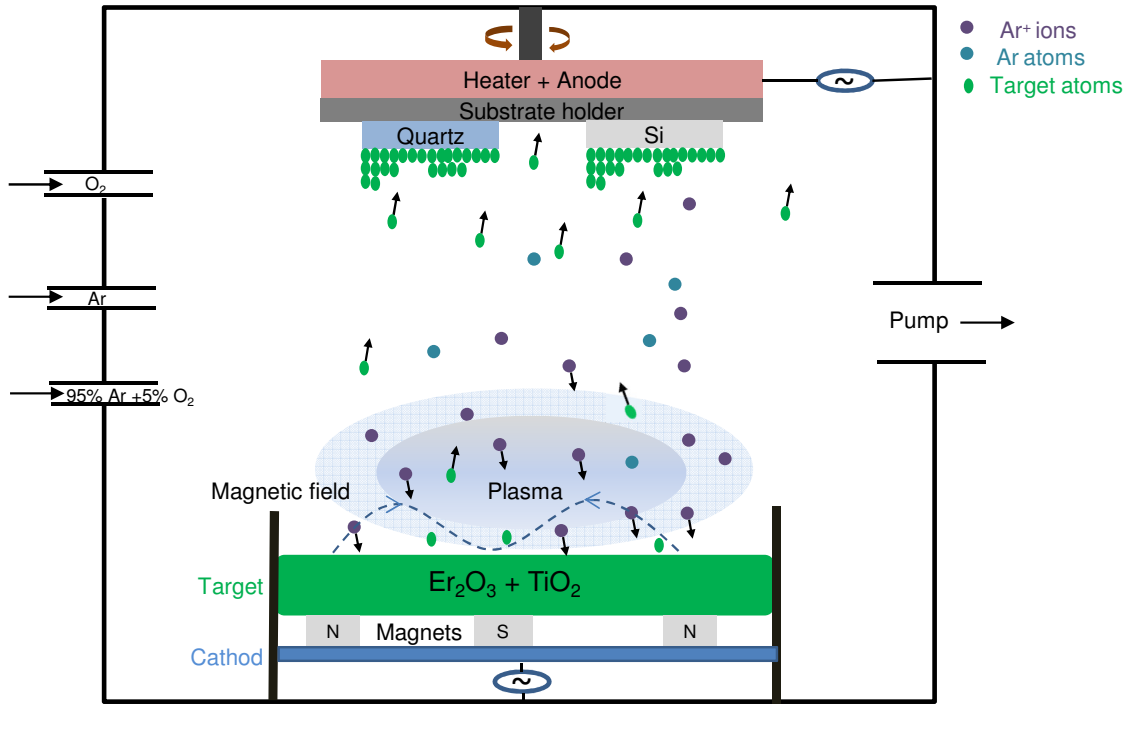


Figure 4.1: A schematic representation of RF-MS. The plasma creation and the film formation are illustrated.

4.2.1.1 Growth of the films

A continuous deposition of atoms on the substrate under Ar-plasma forms thin films, however, this is a complex process. In the process, the knocked-out atoms consist of different energies, which depend upon their generation by the ionized Ar and subsequently, deposit differently on the substrate based on the acquired energy. The probability of de-adsorption of atoms is higher for the initial few atoms, however, it gets lower with increasing number of pre-deposited atoms at the substrate. The continuous adsorption of atoms form clusters at different places of the substrate. The clusters continue to grow until it reaches to a critical size. The critical size provides stability for each cluster and therefore, no further de-adsorption of atoms takes place. These clusters are also termed nuclei, a unit of the process called nucleation. The growth of the nuclei is bi-directional; vertical (downwards or perpendicular to the substrate) and horizontal (lateral). The nuclei form islands of atoms with different crystallographic orientations. A continuous horizontal growth of the film eventually connects the islands. The resulting continuous film possesses grain boundaries to reduce the overall energy of the prepared film. Upon the continuity of the film at the surface, the lateral growth starts to thicken the film. The formed grain boundaries either, stay the same size and form columnar grains or increase in size within the resulting film.

4.2.1.2 Controlling parameters

The structural properties (i.e morphology, roughness, and thickness) of the grown films can be controlled by the deposition and post-deposition parameters. In addition, the optical properties of films, i.e. Er^{3+} -doped TiO_2 , can also be altered with these parameters, presented in Article 2. The temperatures and sputtering power are the two main parameters that control the structural and the optical properties of the Er^{3+} -doped sputtered oxides.

Deposition temperature

The rate of nucleation and deposition are directly associated with the temperature at which the films are grown. If the deposition of the film is performed at higher substrate temperatures, the atoms will have higher diffusion rates and as a result, form compact films [3]. However, a higher substrate temperature increases the critical size of the nuclei, which is the building block of film formation process, and consequently delay the continuous film formation in a defined period of sputtering. Therefore, an increase in the temperature decreases the possibility of the continuity in ultra-thin films [2, 3]. The probability in fabrication of a continuous ultra-thin (i.e. ~ 10 nm) film is low if the film is deposited at higher substrate temperatures compared to the low-temperature counterparts.

Annealing temperature

Annealing temperatures do not show any direct effect on the morphology of the deposited films. However, the annealing process plays an essential role in the creation and passivation of the defects present in sputtered films. A detailed study about the annealing effects on the optical properties of Er^{3+} -doped TiO_2 is presented in Article 2, Chapter 6. The variation in defects density associated with the annealing temperature strongly affects the optical properties of the films.

Sputtering power

The deposition rate is strongly influenced by the power of the RF-MS on which the films are deposited. The sputtering power alters the energy and number of target atoms and consequently, affects the growth rate and the thickness of films. An increase in the power pumps high energy to the deposited atoms which allows their diffusion efficiently to settle at the low-energy stable configuration.

4.2.1.3 Experimental details of our experiment

We employed a commercial ATC Orion RF-MS system from AJA International to deposit Er^{3+} -doped TiO_2 thin films. The target and the substrate were 10 cm apart from one another. During fabrication, the chamber was filled with Ar and O_2 gases. The flow rate of Ar was maintained to 13 sccm whereas O_2 was set to only 0.01 sccm. The gaseous (Ar and O_2) optimizations in the synthesis of TiO_2 thin films were acquired from the previous work performed on the same instrument by S. Johansen [4, 5]. The low amount of oxygen is unreliable if added separately, therefore it is supplied with oxygen with Ar (i.e. O_2 (5%) in 95% Ar) and monitored the flow with mass-flow controller. The pressure of the gas was set to 0.4 Pa. Er^{3+} -doped TiO_2 thin films were fabricated from a commercially available target consisted of a mixture of TiO_2 and Er_2O_3 powders. The targets were ordered with the desired concentration of dopant in the TiO_2 powder. The films were deposited at various substrate temperatures (25°C to the maximum possible temperature given in the RF-MS (420°C)) to optimize the optical properties of the films. The power of the RF-MS, in contrast, was set to 100W, optimized previously by Johansen et al. [5], for all depositions. The effect of the annealing temperature on the films were also examined, presented in Article 2. The employed target had a diameter of 5 cm and a thickness

of ~ 1 cm. The films were either deposited on Si substrate, for the thickness and the elemental composition analysis, or on quartz, for the optical investigations.

4.2.2 Nanoparticle synthesis

The fluoride host for Er^{3+} ions were fabricated as nanoparticles using the well-known chemical synthesis route [6, 7]. The present section gives an outline of the solvo-thermal method which was adopted for the synthesis of Er^{3+} -doped NaYF_4 nanocrystals.

In this method, Er^{3+} -doped NaYF_4 core nanocrystals were synthesized at 300°C reaction temperature. The shells of NaLuF_4 were developed around the core afterwards. In this study, I have varied the shell thickness by varying the amount of injected precursors. A complete description of the synthesis is reported in the Supporting Information of Article 3.

4.2.3 Drop-cast assisted spin coating

Once the nanoparticles were prepared, the next task was to cast them into films. The films were prepared by drop cast-assisted spin coating technique. The technique allowed the formation of thin films without assistance of external hosts (i.e. polymethylmethacrylate (PMMA)). In the film formation process I spread some drops of colloidal upconversion particles on quartz by the centrifugal spinning force. The thickness of the films were controlled by optimizing the spinning parameters of the spin-coater as well as by the colloidal solution properties (i.e. viscosity and volatility of solvent, and size distribution of synthesized nanoparticles). Furthermore, we were able to successfully lower the thickness down to one particle forming monolayers of nanocrystals. A complete description of the film formation is reported in the Supporting Information of Article 3.

4.3 Focused-ion beam technique

A focused ion beam (FIB) uses a beam of ions that can directly modify the sample surface, via a local sputtering process. The technique allows the milling with nanometer precision. This technique is useful in designing samples with nanometer sharpness or removing unwanted materials by the proper control over the energy and the intensity of the ion beam. It consists of positively charged Gallium ions (Ga^+) with the acceleration energy in range of 5 to 30 keV. The FIB is a self-sufficient technique, capturing pictures while milling or depositing materials. However, each scan of FIB damages the sample. Therefore, its integration with scanning electron microscope (SEM), explained in Chapter 5, is advantageous. The FIB and SEM are stand-alone instruments, however, their integration allows continuous monitoring while modifying sample by FIB column. The dual beam, the electron beam of SEM and the ion beam of FIB, intersect at an oblique angle at a coincident point close to the sample surface. This allows a high resolution imaging of FIB-milling via SEM. The non-conductive nature of a scanned sample possess the main challenge in the broad applicability of FIB-SEM instrument. The interaction of the dual beam with the electric insulator results in charge building on the sample surface that effects the analysis [8]. This potentially obstruct the applicability of the setup for a wide range of materials.

In this study, we used FEI-Versa 3D instrument (FIB-SEM) for the fabrication of lamella of Er^{3+} -doped TiO_2 sputtered thin films. The insulating nature of the films built-up the charge during FIB-milling and that affected in reaching the resolution for the cross-sectional analysis of the films in transmission electron microscope (TEM). The issue was dealt by evaporating

Au-thin films on top of the TiO_2 film before milling and conducting nature of Au removed the accumulation of charge as well as the Ga-contamination at the surface. The fabrication of lamella was important in the thickness determination of ultra-thin Er^{3+} -doped TiO_2 sputtered films, presented in unpublished work, Chapter 6.

4.4 Electron beam lithography

Unlike photo-lithography, electron beam lithography (EBL) is an advanced technique for the fabrication of patterned nanostructures with a resolution of a few nanometers. The technique directly writes at a nanoscale in a desired pattern using the electron beam on to an electron-sensitive layer. The process, with multiple steps is explained in Figure 4.2. Firstly, the electron-sensitive resist, i.e. polymethylmethacrylate (PMMA), is spin-coated on a clean quartz. Secondly, the resist is exposed to the e-beam for a patterned writing. Thirdly, the exposed part is dissolved in a developer which is a mixture of methyl isobutyl ketone (MIBK) and isopropanol (IPA). Fourthly, the desired metal (i.e. Au) is deposited via e-beam-gun source consisted physical-vapor deposition system. Finally, the desired metal structures are realized by dissolving in acetone for around 30 min with some mechanical vibration through ultra-sonication. Several challenges involved in the EBL-fabrication process are well reported [9, 10]. Low yield and proximity effects are the two main challenges with this technique. The proximity effect is a condition where surplus dose due to scattering of electrons limits the resolution of the tool. The yield is interpreted as the area of decorated nanostructures covered by the technique per unit time, which becomes more important when large area fabrication is needed.

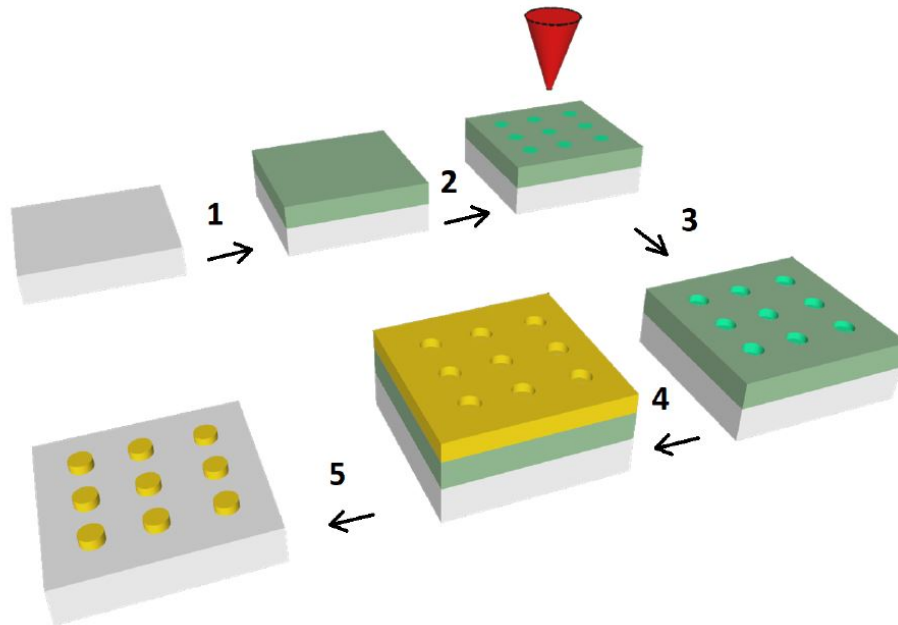


Figure 4.2: A systematic representation of the EBL processes. The figure is adopted from [11]

In this study, a FEI Magellan 30 kV scanning electron microscopy (SEM) system equipped with a Raith pattern generator was employed for the EBL process. The Au-nanostructures were fabricated in a random pattern on quartz substrate. The optical properties of metallic structures in a periodic arrangement are critically dependent on the angle of incidence due to

diffraction effects [12]. Therefore, to minimize this angle dependence we chose to randomize the nanostructure placement. The proximity effect (as discussed earlier in this section) in the random arrangements becomes more dominant in close-spacing nanostructures. However, we reduced this effect by assigning the electron dose close to the clearing-dose range. Furthermore, the structural diameter was increased by adding another step of plasma-etching after the development step in the EBL process. The simplest possible geometry that can be designed with a short EBL processing time is a truncated-cone. Therefore, we designed Au-nanostructures with this shape and abbreviated as nanodiscs. In addition, the shape also balances between the complexity of the structure and the cost of its production via EBL process. An increase in the complexity of the structures increase the time of production at EBL and as a result, increase the cost. The difference in the bottom and top diameters of a cone were dependent on the height and diameter of the structures. We chose two different heights (20 nm and 50 nm) for this work and the diameter were tuned between 150 nm to \sim 500 nm to achieve the LSPR peak position at 1500 nm wavelength (at the excitation of Er^{3+}), explained in Chapter 3. The variation in the size of the structures were controlled by the beam-current and the plasma-etching process. The nanodiscs were designed either on top or buried into Er^{3+} -doped TiO_2 and NaYF_4 films. The different surrounding medium changes the LSPR peak positioning to different wavelengths. Therefore, an optimization in the diameter was a necessity for each design to achieve resonant plasmon-enhanced upconversion, reported in Article 1 and 3.

Bibliography

- [1] K. Tsuchiya, T. Kitagawa, E. Nakamachi, Development of RF magnetron sputtering method to fabricate PZT thin film actuator, *Precision Eng.* 2003, 27, 258.
- [2] M. Ohring, *Materials Science of Thin Films: Deposition and Structure*, London, England: Elsevier 2002.
- [3] C.V. Thompson, Structure evolution during processing of polycrystalline films, *Ann. Rev. Mat. Sci.* 2000, 30, 159.
- [4] S. R. Johannsen, Upconversion of near-infrared light through Er doped TiO₂, and the effects of plasmonics and co-doping with Yb, Aarhus University, Denmark, 2015.
- [5] S. R. Johannsen, L. R. Lauridsen, B. Julsgaard, P. T. Neuvonen, S. K. Rama, and A. N. Larsen, Optimization of Er³⁺-doped TiO₂-thin films for infrared light up-conversion, *Thin Solid Films* 2014, 550, 499.
- [6] Z. Li and Y. Zhang, An Efficient and User-Friendly Method for the Synthesis of Hexagonal-Phase NaYF₄:Yb, Er/Tm Nanocrystals with Controllable Shape and Upconversion Fluorescence, *Nanotechnology* 2008, 19, 345606.
- [7] N. J. J. Johnson, A. Korinek, C. Dong, and F. C. J. M. Van Veggel, Self-Focusing by Ostwald Ripening: A Strategy for Layer-by-Layer Epitaxial Growth on Upconverting Nanocrystals, *J. Am. Chem. Soc.* 2012, 134, 11068.
- [8] F. Crococolo and C. Riccardi, Observation of the ion-mirror effect during microscopy of insulating materials, *J. Microsc.* 2008, 229, 39.
- [9] M. A. Mohammad, M. Muhammad, S. K. Dew, and M. Stepanova, *Fundamentals of Electron Beam Exposure and Development*, Springer Vienna, Vienna, 2012, 11.
- [10] M. Altissimo, E-beam lithography for micro-/nanofabrication, *Biomicrofluidics* 2010, 4 (2) 026503.
- [11] P. Balling, J. Christiansen, R. E. Christiansen, E. Eriksen, H. Lakhotiya, M. Mirsafaei, S. H. Moller, A. Nazir, J. Vester-Petersen, B. R. Jeppesen, P. B. Jensen, J. L. Hansen, S. Ram, O. Sigmund, M. Madsen, S. P. Madsen, B. Julsgaard, Improving the efficiency of solar cells by upconverting sunlight using field enhancement from optimized nano structures, *Optic. Mat.* 2018, 83, 279.
- [12] E. M. Hicks, S. L. Zou, G. C. Schatz, K. G. Spears, R. P. Van Duyne, L. Gunnarsson, T. Rindzevicius, B. Kasemo, and M. Käll, Controlling plasmon line shapes through diffractive coupling in linear arrays of cylindrical nanoparticles fabricated by electron beam lithography, *Nano Lett.* 2005, 5 (6), 1065.

Chapter 5

Experimental: Characterization Tools

5.1 Introduction

The understanding of the optical properties of the sputtered oxide films, the chemically synthesized fluoride nanocrystals, and the EBL-defined Au-nanodiscs can only be acquired if the structural properties of all are thoroughly investigated. The structural characterizations of the ultra-thin oxide films and fluoride nanocrystals poses several challenges. Electron microscopes (EM) is a well-established method for morphological and chemical determinations. In this chapter, a detailed description of EM techniques (i.e. scanning electron microscope (SEM) and transmission electron microscope (TEM)) will be given. In addition, a brief discussion of less-heavily-engaged EM tools (i.e. scanning transmission electron microscope (STEM) and energy dispersive X-ray spectroscopy (EDS)) are reported. It is desirable to quantify the chemical compositions of the prepared upconversion materials, therefore, I will discuss all the techniques employed for this. The optical properties of the sputtered oxide films and the fluoride nanocrystals in their colloidal solution and film configurations in presence and absence of Au-nanodiscs are determined by the absorption and emission measurements. The spectrophotometry of upconversion materials in both their configurations and the ellipsometry are performed to measure the absorption or absorption coefficient of the material, discussed in detail. The steady-state and the time-resolved measurements for the emission of Er^{3+} ions are described in detail at the end of this chapter.

5.2 Structural characterizations

5.2.1 Scanning electron microscopy

Unlike optical microscopy, where a white light (λ -380-700 nm) is used, a beam of electron ($\lambda \sim 0.0025$ nm at 200kV) is the imaging source in scanning electron microscope (SEM). The wavelength of the electron is dependent on the accelerating voltage, therefore, the SEM with a higher accelerating voltage provides better resolution, due to short wavelength. SEM uses a focused beam of electrons to image a sample and achieve information about the structure and the chemical composition using the secondary electrons emitted from the sample surface. There are four major regions in a SEM: (a) A stream of electrons is formed by the electron gun and a positive voltage accelerates it towards the sample surface. (b) The beam becomes monochromatic via further confining by the metal apertures and magnetic lenses. (c) The magnetic lens help in focusing the beam on the surface of the sample. (d) The bombardment of the scanning electron beam emits the secondary electrons from the sample and their detection are transformed into images.

For this study, the Megellan SEM from FEI was used to analyze the sputtered oxide films and the upconversion nanocrystals (UCNC) in the film configuration. The top- and cross-sectional views of the films were analyzed. Regarding the cross-sectional imaging, the samples were

bipartite from the center and the placed in a way to focus the beam on the broken edge with a tilting angle. The cross-sectional images of both types of films were hard to obtain due to the associated quartz substrate that accumulates charges and hinders the visualization, and due to the thin nature of the films that limits the resolution. Regarding the EBL process, explained in Chapter 4, this SEM instrument was extensively used to visualize the arrangements and the diameters of Au-structures.

5.2.2 Transmission electron microscopy

Transmission electron microscopy (TEM) is a technique where a beam of electrons interact with an ultra-thin sample whilst transmitting through it. The electrons are accelerated through a potential of 100-300 kV, depending upon the instrument, and passes through strong electromagnetic lenses. The achievable resolution from TEM is in range of 0.1-0.2 nm which is in range of the size of an atom. The electrons that pass through a samples either present bright-field contrast, diffraction contrast, or electron energy loss contrast. In bright field contrast, the image is formed by occlusion and absorption of electrons in the sample. Thicker samples or a sample with heavier atoms appear darker compared to the regions with lighter elements. The bright field contrast is the most common imaging method to determine the size of nano/microparticles, film thickness, and etc. In diffraction contrast, the contrast is formed by the elastically scattered electrons (i.e incident electrons those are elastically scattered by atoms). The scattered electrons form a pattern of spots, which represents a specific atomic spacing. From this pattern the information about the orientation, the atomic arrangements, and the phases of a sample can be achieved. In electron energy loss contrast the image is formed by inelastically scattered electrons. This provides a characteristics of the elements of a sample. Therefore, TEM provides morphological (size, shape and arrangements of particles), crystallographic (arrangements, order of atoms and atomic-scale defects), and compositional (chemical identity and elemental composition) information of the sample.

Scanning transmission electron microscopy (STEM) is similar to TEM apart from consisting a convergent beam. The beam raster-scans the surface of a sample and transmitted beam get detected by a range of detectors. Bright field detector, low angle- and high angle annular detectors collects the scattered electron.

Energy dispersive X-ray spectroscopy (EDS) uses the X-ray spectrum to investigate the chemical analysis obtained by the bombardment of a sample with a focused beam of electrons. The obtained spectra provide qualitative as well as quantitative analysis of the elements present in a sample. Raster-scanning the focused beam on a sample and showing the intensity of the selected X-ray line, provides the distribution of elements on a map, called elemental-map.

For this project, two different TEM instruments were used; FEI Talos F200X (operated at 300 kV) and Technai G2 Spirit Twins (workd at 120 kV). The former technique is a well equipped technique for multiple purposes. Talos TEM is able to produce high resolution-TEM (HR-TEM) images and equipped with scanning transmission electron microscope (STEM) and energy dispersive X-ray spectroscopy (EDS) configurations. Talos TEM was used to determine the atomic resolution of the chemically synthesized fluoride nanocrystals (UCNCs), the line-scan analysis of core-shell fluoride nanocrystals, and the cross-sectional imaging of ultra-thin sputtered oxides whereas STEM was employed for the confirmation of the shells around the core UCNCs by differentiating dark (core) to light (shell) contrast. The line-scan analysis provides the distributions

of the selected elements over the drawn line on the nanocrystals, analysis can be observed in the supporting information, Article 3. HR-TEM analysis of the fluoride nanocrystals were difficult due to the material degradation under the continuous electron illuminations, but were achieved by reducing the time of scan. The fabrication of lamella for the thickness determination in the ultra-thin sputtered films was prepared by the FIB-SEM instrument (detailed in Chapter 4). TEM sensitivity over the size of a lamella made it challenging. TEM is thus a very useful technique but requires a considerable care for sample preparation.

5.2.3 X-ray diffraction technique

X-ray diffraction (XRD) is a well-established technique to investigate the structure of materials, applied at almost every field of science. XRD technique measures the diffracted beam generated through a crystalline material after an incidence of X-rays. The direction and the intensity of the diffracted beams depend upon the orientation of the crystal lattice with X-rays. In case of amorphous material, the random arrangement of atoms cause the beam to randomly interfere and develop a non-distinctive pattern. In contrast, the developed diffraction pattern of crystalline material consists of the characteristics of the arrangement of atoms within the material. The pattern specifically provides details about the chemical content and the crystal phase of the material. In this study, we have employed two different XRD instruments for two different configuration of materials. The film configuration (TiO_2 thin films) were measured by a Bruker D8 Discover diffractometer equipped with a $\text{Cu K}\alpha$ source whereas the powder configuration of NaYF_4 upconversion nanocrystals (UCNC) were measured by Rigaku SmartLab diffractometers (Rigaku, Japan) with a $\text{Cu K}\alpha$ source using a curved Ge (111) Johnson monochromator.

5.2.4 Inductive-coupled plasma optical emission spectroscopy (ICP-OES)

ICP-OES is a trace-level technique to analyze the elemental composition of a sample via the obtained emission spectra. The technique uses the inductively coupled plasma to generate excited ions or atoms and records their emissions, the wavelength of which, is a characteristic for a specific element. The technique consists of the ICP and the optical spectrometer. The ICP chamber has three quartz tubes surrounded by a radio frequency coil. The chamber is filled with Ar gas which creates plasma after switching on the ICP torch which generates EM-field. The sample is dissolved into an organic or acidic environment to separate the atoms or elements, introduced into the plasma. An interaction of the sample with the plasma develops charged ions which emit radiation based on the involved elements at the characteristics wavelength. The wavelength separated spectrographs are measured in the optical chamber. The intensity of the peaks are recorded by either photomultiplier tube (PMT) or charged-coupled device (CCD) detectors. Here, this technique was used to determine the elemental composition of $\text{Er}^{3+}:\text{NaYF}_4\text{-NaLuF}_4$ core-shell nanocrystals. It was important to determine the concentration of the dopant (Er^{3+}) in the fluoride host for a comparison among nanocrystals with different shell thicknesses, as shown in the Supporting Information, Article 3.

5.2.5 Rutherford backscattering spectroscopy

Rutherford backscattering spectroscopy (RBS) is a technique ideally used to measure the thickness and depth-revolved chemical composition of thin films [1–3]. In the RBS experiment, a film is bombarded by a high-energy (MeV) ion beam (i.e. $^4\text{He}^+$ or $^4\text{He}^{2+}$). The high energy of the beam allow the ions to penetrate deep in the sample until they backscattered. The backscattered ions are detected for their yield and energy distributions and the recorded spectrum is the

base of the depth-profiling. The energy distribution is a function of the chemical composition and thickness of a film and the classical Rutherford model can be used to calculate the energy distribution of the backscattered ions. The calculated energy distribution can be written as

$$E_{out} = KE_{in} \quad (5.1)$$

$$K = \left(\frac{M_{ion}\cos\theta + \sqrt{M_t^2 - M_{ion}^2\sin^2\theta}}{M_{ion} + M_t} \right)^2 \quad (5.2)$$

where E_{in} and E_{out} are the energies of the incident and backscattered beams, respectively, M_t and M_{ion} are the masses of the target atoms and the ions of the incident beam (i.e. α -particles), respectively, and K is the kinematic factor. For a fixed direction, the kinematic factor depends upon the mass of the target atoms (M_t). Therefore, the α -particles scattered differently for the target atoms of different masses.

The yield of the backscattered ions can be represented by the calculation of scattering cross section. The scattering cross section is proportional to the incident flux and can be written as

$$\sigma(\theta, M_{ion}, M_t) = \left(\frac{Z_{ion}Z_t e^2}{4E_{ion}} \right)^2 \times \frac{4}{\sin^4\theta} \frac{\left(\cos\theta + \sqrt{1 - \left(\sin\theta \frac{M_{ion}}{M_t} \right)^2} \right)^2}{\sqrt{1 - \left(\sin\theta \frac{M_{ion}}{M_t} \right)^2}} \quad (5.3)$$

where Z_{ion} and Z_t are the atomic number of the ions (i.e. α -particles) and target atoms, respectively. If α -particles are the source of the incident beam then $M_{ion} = M_\alpha \ll M_t$ and therefore, (5.3) can be simplified as

$$\sigma(\theta, M_{ion}, M_t) = \left(\frac{Z_{ion}Z_t e^2}{4E_{ion}} \right)^2 \frac{4}{\sin^4(\frac{\theta}{2})} \quad (5.4)$$

Since the scattering cross section is proportional to Z_t^2 , RBS is more sensitive to heavier elements (elements with higher atomic mass). Therefore, it is a well-suited technique for the detection of heavier elements like Er atoms in TiO₂ matrix.

The experiment was performed with the use of 5 MeV Van de Graff accelerator at the Department of Physics and Astronomy, Aarhus University. A beam of 2 MeV α -particles were incident normally at the Er³⁺-doped TiO₂ thin films deposited on Si substrate. The detector was placed 70° in angle. The thickness of the films varied in a range of 20 nm to 100 nm for this measurements. The smaller the thickness of the films and the higher penetration depth of the beam made the depth-profiling an easily-achievable task. The achieved spectra were analyzed in RUMP software.

5.2.6 Secondary ion mass spectroscopy

Secondary ion mass spectroscopy (SIMS) is a technique to quantitatively determine the chemical composition of materials. In SIMS, a beam of ions (i.e. Cs⁺ or Bi⁺) is bombarded on the surface of a specimen and in results, neutral atoms and charged ions (secondary ions) are sputtered out. The secondary ions are guided to a mass spectrometer by electrostatic lenses. The spectrometer

then organizes the ions based on the mass-to-charge ratio.

In the present work, IonToF IV SIMS instrument was employed. It is a dynamic SIMS with a time of flight (TOF)-based mass spectrometer (MS) detector. The instrument is equipped with several gaseous source of bombarding ions. A depth profile of the elemental concentration of a material can be achieved. The concentration profile can be generated via a layer-by-layer removal of the sample. A lower-energy (6 keV) Cs⁺ ion beam for the sputtering of the top layer and a higher-energy (25 KeV) pulsed beam of Bi⁺ ions for the subsequent sputtering of the sample were used. The TOF-MS measures the time taken by the secondary ions to travel from the sample surface to the detector. It record the mass spectrum (mass/charge ratio) of the extracted elements or molecules. The higher the atomic or molecular mass of an element, the higher TOF due to the slower speed. Therefore, the elements or fragments can be separated on the spectrum based on their TOF which is correlated to their mass and charge.

In the present study, SIMS has played a big role in determining the variation in the atomic or molecular components with the depth of the sputtered oxide films. The technique was employed to determine the distribution of ErO⁻ and ErO²⁻ fragments in the films. In addition, a depth profiling of a multi-layered Er³⁺ doped-TiO₂ thin films (deposited at different substrate temperatures) has been performed to determine the variation in H₂ from one layer to another. The role of H₂ was associated with the point defects in the films, details are presented in Article 2.

5.3 Optical characterizations

5.3.1 Spectroscopic ellipsometry

Spectroscopic ellipsometry (SE) is an optical technique used to analyze the optical constants (n=refractive index and k=extinction coefficient) and the thickness of a specimen. SE measures the change in the polarization state of a linearly polarized light reflected at an oblique incidence from the surface of a specimen. Upon interaction with the surface, the linearity of the light changes to the elliptical due to the variation in the phase and amplitude components of p- and s- part of the electric field. Therefore, SE measures the amplitude-ratio

$$\psi = \tan^{-1} \frac{|R^P|}{|R^S|}, \quad (5.5)$$

where $|R^P|$ and $|R^S|$ are the total reflection coefficient of s- and p- polarized lights, and the phase-difference

$$\Delta = \delta_{in} - \delta_r, \quad (5.6)$$

where δ_{in} is the phase difference before, and δ_r the phase difference after the reflection, in both s- and p- parts of the incident and reflected lights. The change in the polarization is governed by the refractive index and the thickness of the specimen. SE provides the amplitude ratio and the phase difference as a function of the wavelength. SE is a theoretical model based technique. Therefore, the obtained experiential data is matched with a model that suits well with the materials characteristics. From the match or fit one receive theoretical constant and thickness of the specimen. The values of ψ and Δ are always correct whereas thickness and optical constants depends upon the model from they acquired.

In this study, Sentech SE850 ellipsometer was employed in the spectral range of 300 nm - 2500 nm wavelength with 40° to 70° (most common at 70°) angle of incidence. I measured the optical

constants and the thicknesses of several sputtered- Er^{3+} -doped- TiO_2 thin films and spin-coated Er^{3+} -doped- NaYF_4 UCNC mono- and multi-layers. Tauc-Lorentz dispersion model [4] was used in these studies. The films were defined from bottom to top: Si substrate of 0.5 mm thickness, 2 nm native SiO_2 , a film of desired material (TiO_2 or NaYF_4), and a roughness layer (made of desired layer and voids). For Er^{3+} -doped- NaYF_4 monolayers, the measurements were performed at three different angle of incidence and an averaged optical constant were collected whereas the Er^{3+} -doped- TiO_2 were measured at 70° angle of incidence. The technique was to obtain the optical constants ($n(\lambda)$ and $k(\lambda)$) and the thicknesses of the films to be utilized in the numerical modeling (finite element modeling).

5.3.2 UV-Vis-NIR spectrophotometry

This technique was used to measure the absorption of a material in solution and/or film configurations. The technique is important to verify either zero or a little absorption of upconverted light (infra red (980 nm and 810 nm) and visible light) in the host materials chosen for Er^{3+} dopants in this PhD study. In addition, it is employed to determine the position of localized surface plasmon resonance (LSPR) peak on the wavelength scale of Au-nanodiscs, explained in Chapter 3. Precisely, I determined the absorption and the extinction (absorption + scattering) of Er^{3+} doped- TiO_2 and - NaYF_4 thin films in the presence and absence of Au-nanodiscs as well as colloidal solutions of Er^{3+} doped- NaYF_4 nanocrystals. The spectrophotometer introduced in this study does not directly measure the absorption instead measures the reflectance and transmittance of the materials. A Lambda 1050 instrument from Perkin Elmer equipped with a 150 mm integrating sphere was used in this study. An integrating sphere is a sphere coated inside with a white spectralon to capture the diffused or scattered light from a material. The employed equipment is able to scan at 175-3300 nm wavelength scale, however, a high signal to noise ratio limits its application in range of 300-2500 nm wavelength, which is also appropriate for the present study. The sphere has multiple entries for the beam to enter and based on the experiment some entries were plugged-in with white reflector lids whereas others were open to allow the beam to enter or exit. Depending upon the placement of a sample, one can measure four different entities from this instrument. Total transmittance (T_T), total reflectance (R_T), direct transmittance (T_D), and diffused reflectance (R_{Diff}) are the four entities measured on this instrument. Before coming to the measurements of the transmittance and reflectance, it is important to understand the interaction between the light and the material. The schematic representation (Figure 5.1(A)) shows the direct interaction of the beam with the surface of films in the present experiment and the observed transmittance and reflectance phenomenons. Based on where and how the sample is placed, there are four possible ways: Firstly, a samples is placed next to the sphere and detector (placed at the base of the sphere) then the sphere captures both direct and diffuse (scatter) light transmitted through the sample after the normal incidence and the measured quantity is T_T (Figure 5.1(B-1)). Secondly, if the sample is placed far from the detector as shown in Figure 5.1(B-2) then the sphere can not collect the diffused or scattered light and only captures direct transmitted light and records T_D . For the reflectance measurements, the sample needed to be placed at the back opening of the sphere. Thirdly, the configuration presented in Figure 5.1 (B-3) allows the capturing of both direct and scattered reflected light therefore, provides R_T of the sample. It is noteworthy to explain that the samples in this configuration are 8° rotated to the normal to avoid the escape of R_T from the front opening. Finally, if the white standard plug, which is 8° from the front opening towards the opening for reference beam is removed then the direct reflected beam can be taken out of the sphere and the measured reflected beam is R_{Diff} , shown in Figure 5.1(B-4). The reference beam (a beam of light which does not interact with sample) has a separate entry to the sphere in all four possible configurations during the experiment. The reference beam calibrates the instrument by comparing with the samples beam (a beam that passes through samples) in the absence of a sample.

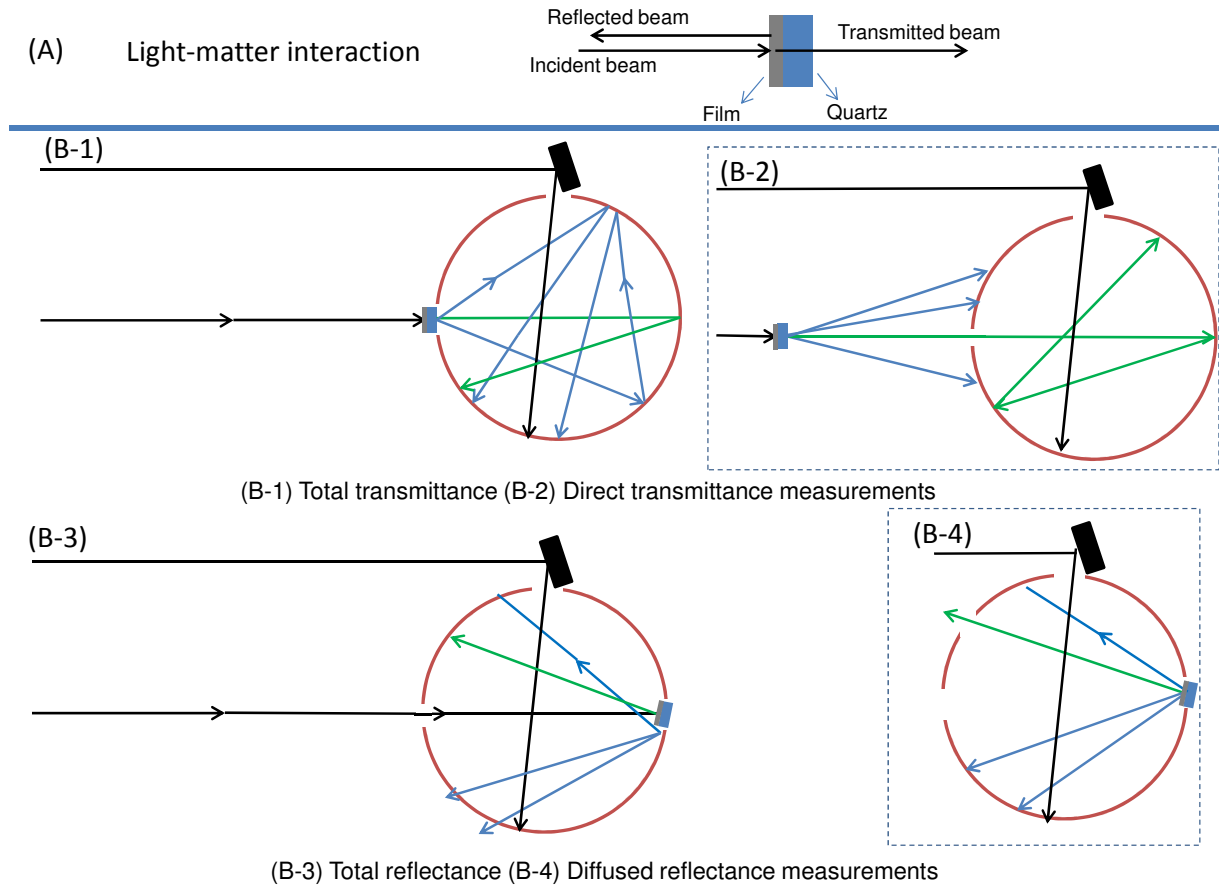


Figure 5.1: Panel (A) shows the interaction of the light with the surface of a film. The lower panel shows the transmittance and reflectance measurements of a thin film deposited on quartz. The red sphere is a representation for an integrated sphere coated inside white spectralon. The black rectangle is a mirror. The black arrows are the direct rays ($\lambda=300\text{nm}-2500\text{nm}$), the blue arrows are diffused transmitted and reflected rays, and the green arrows are the direct reflected and transmitted rays. The lower panel is divided among the four sub-panels: B-1 and B-2 show the different position of the sample in order to measure the total and direct transmittance, respectively. B3 and B4, on the other hand, show the same position of the sample at the back of the sphere for the reflectance measurements but based on the opening of the hole (between the main entrance hole and the reference hole) in the sphere one can measure the total and diffused reflectance.

After measuring the four entities, the rest two (diffused transmittance (T_{Diff}) and direct reflectance (R_D)) were calculated by

$$T_T = T_D + T_{Diff} \quad (5.7)$$

$$R_T = R_D + R_{Diff} \quad (5.8)$$

The absorption (A) and extinction (E) were calculated afterwards from the measured and the calculated transmittance and reflectance by

$$A(\%) = 100 - T_T(\%) - R_T(\%), \quad (5.9)$$

$$E(\%) = 100 - T_D(\%) - R_D(\%), \quad (5.10)$$

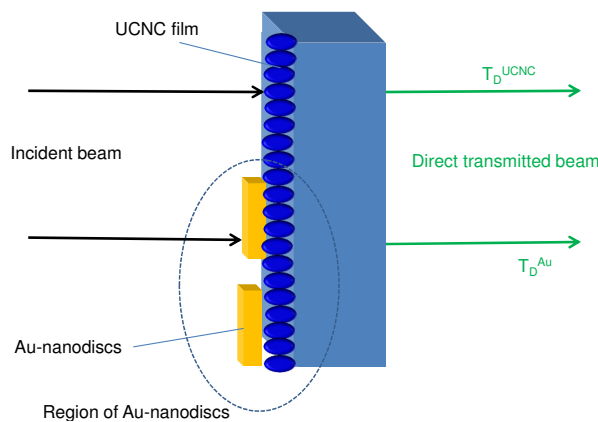


Figure 5.2: A schematic representation of the interaction of the white light with an Au-deposited UCNC monolayer (film). The sketch shows the two possible regions, Au-nanodiscs consisted UCNC monolayer and UCNC monolayer, for the incident beam interaction and defines the direct transmittance from both.

To reduce the EBL efforts for the nanodiscs formation, the present setup of measurements were modified, to focus the beam at a small area (i.e. $1 \times 1 \text{ mm}^2$) of Au-region deposited on NaYF_4 UCNC monolayers. The extinction measurements on this setup and with such samples were performed by measuring the direct transmittance in the presence and the absence of Au-discs. The sample was placed in front of the sphere as shown in Figure 5.1 (B-2). This direct transmittance measurements were performed on a single sample where both regions with and without Au-discs are present as shown in Figure 5.2. The diagram shows the Au-nanodiscs deposited on top a UCNC film. The incident beam either hit the region UCNCs consisting Au-nanodiscs and provides direct transmittance (T_D^{Au}) or the region of UCNCs then the observed direct transmittance is (T_D^{UCNC}). The extinction is calculated afterwards by [5]

$$E(\%) = T_D^{UCNC}(\%) - T_D^{Au}(\%), \quad (5.11)$$

The determined values of the extinction calculated as (5.10) and (5.11) is not appropriate to compare among samples where the diameter of deposited Au-discs is different (due to match the LSPR, explained in the Section 3.4.1 of Chapter 3). Therefore, the relative cross section is required to be calculated for a fair comparison. First, the extinction cross section (σ_E) is calculated by dividing the extinction with the particle density (PD) and then divided further by the area of the particle (A_{Au}) to get the relative cross section (σ_E/A).

$$\sigma_E/A = \frac{E(\%)}{100} \frac{N}{A_R} \frac{1}{A_{Au}}, \quad (5.12)$$

where N is the number of particle present in A_R area and the ratio of this gives PD. The obtained relative extinction cross section should be higher than 1 when the nanodiscs are in resonance with the excitation wavelength (i.e. 1500 nm), as explained in Figure 3.3 of Chapter 3.

5.3.3 Upconversion luminescence (steady-state) measurements

Upconversion luminescence (UCL) measurements are the essence of this PhD work. The fabricated thin films or colloidal solutions of nanocrystals (UCNCs) were excited by the laser with a wavelength of 1500 nm and the emitted upconverted light were captured by a spectrograph. The source of the laser has maximum power of 20 mW. The spectrograph is an instrument

to separate and record the light on wavelength scale using a camera. In these studies SP2358 spectrograph from a Princeton Instrument was used, which was coupled with a PIXIS 100BR CCD camera. The camera captured the spectrum on 500 nm to 1100 nm wavelength spectrum. The illumination process of a sample during the experiment is mentioned in the caption of Figure 5.3. The sample can either be placed in the beam path without the sphere on a holder or inside the sphere, presented in Figure 5.3. If the sample is on a holder without the sphere then the diffused reflection of light will not be efficiently captured by the collecting lens, placed next to this as shown in Figure 5.3. However, if the sample is inside the sphere then the several reflections will isotropically spread the light over the sphere and luminescence will no longer be spatially distributed. This will allow the collection of all upconverted light. Therefore, most of the luminescence were performed in this configurations otherwise stated explicitly.

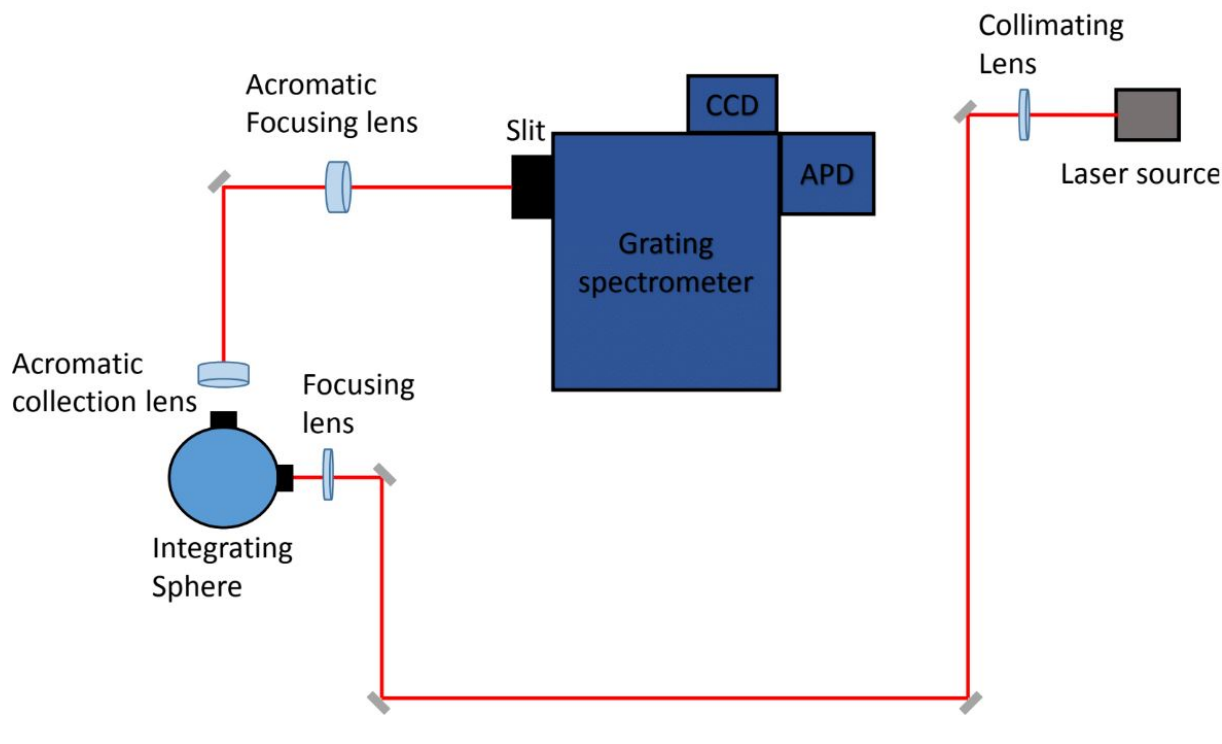


Figure 5.3: Schematic representation of the photoluminescence setup. A source of laser either a 1500 nm wavelength continuous-wave (CW) or a 35 fs pulsed Ti:sapphire laser with a peak wavelength of 800 nm is used for the laser generation. A cylindrical lens collimates the CW-laser whereas a reflection telescope collimates for the pulsed laser. Passing through silver mirrors the beam get focused on the sample by plano-convex lens. The sample is placed inside the integrating sphere, discussed in Section 5.3.2. The light further guides via a achromatic lens to the entrance slit of the spectrometer. The detection of the luminescence is either on CCD camera or on an avalanche photodiode (APD) detector based on the chosen experiment between the steady-state and time-resolved luminescence. The picture is adopted from [6]

Beam area measurement

The area of a laser beam was measured in the optical setup prepared for the UCL measurements. Assuming a Gaussian intensity profile with an elliptical shape, the area of the beam was calculated by measuring the beam-width using Knife-edge method. In the method, the total power of the beam was recorded with a translation of the knife-edge in horizontal and vertical directions. The obtained experimental data were fitted to the analytic expression found in literature [7] to get the width and consequently, the area of the beam ($0.20 \pm 0.02 \text{ mm}^2$).

External quantum luminescence efficiency (EQLE) calculation-

EQLE was calculated by dividing the incoming 1500 nm wavelength photons to the upconverted photons. The number of upconverted photons were calculated by multiplying the upconversion counts of the steady-state UCL spectrum to a conversion factor. An estimation of the conversion factor was performed based on the known power from a 980 nm diode laser. The number of incoming photons were calculated by Planck's energy equation. We measured the EQLE of Er³⁺-doped NaYF₄ UCNCs and reported in Article 3. The EQLE of 100 nm TiO₂ thin films were also measured and reported in Chapter 6.

5.3.4 Time-resolved photoluminescence measurements

Time -resolved photoluminescence (TRPL) measurements provide the insights the nature of the upconversion and the underline dynamics. Ultra-thin films of these studies were nearly non-detectable via steady-state luminescence measurements due to the multiple reflections of the emitted light inside the sphere reduces the intensity of the UCL. TRPL, in contrast, were measured outside sphere and it measured the decays of the excited states which is independent on the thickness of the material. The measured decays provide the lifetime of the energy levels of a dopant (i.e. Er³⁺). In this work, we performed TRPL via TOPAS instruments pumped by a Ti:Sapphire pulsed laser with peak wavelength at 800 nm. The 1 kHz repetition rate of the pulsed laser was enough to detect 1 ms interval and that was sufficient for the decay investigation. The detection of the emitted light was performed either via an avalanche photodiode (APD) or via a photo-multiplier tube (PMT) based on the detected spectral region. The illustration process is same as shown in Figure 5.3. The use of TRPL was in measuring several poor performing TiO₂ thin films, reported in Article 2, and the NaYF₄ UCNC monolayers, reported in Article 3.

Bibliography

- [1] M. Ohring, *Materials science of thin films: deposition and structure*, Elsevier, London, England, 2002, 2.
- [2] L. C. Feldman, J. W. Mayer, and S. T. A. Picraux, *Materials analysis by ion channeling*, Academic Press, New York, 1982.
- [3] W. K. Chu, J. W. Mayer, and M. A. Nicolet, *Backscattering spectroscopy*, Academic Press Inc., New York, 1978.
- [4] G. E. Jellison Jr., F. A. Modine, P. Doshi, and A. Rohatgi, Spectroscopic ellipsometry characterization of thin-film silicon nitride, *Thin Solid Films* 1998, 313-314, 193.
- [5] S. H. Møller, J. Vester-Petersen, A. Nazir, E. H. Eriksen, B. Julsgaard, S. P. Madsen, and P. Balling, Near-field marking of gold nanostars by ultrashort pulsed laser irradiation: experiment and simulations, *Appl. Phys. A* 2018, 124(210), 1.
- [6] J. D. Christiansen, *Optical Characterization of Photon Upconversion in Trivalent Lanthanide Ions*, PhD progress report, Department of Physics and Astronomy, Aarhus University, Denmark 2017.
- [7] M. González-Cardel, P. Arguijo, and R. Díaz-Urbe, Gaussian beam radius measurement with a knife-edge: a polynomial approximation to the inverse error function, *Appl. Opt.* 2013, 52(16), 3849.

Chapter 6

Results and Discussions

6.1 Introduction

The chapter consists of the results and discussions of the PhD work. It has summaries of three either published or submitted manuscripts (Article 1, 2, and 3) and a detailed description of an unpublished work. The chapter ends with a fair comparison between the luminescence of Er^{3+} ions present in both TiO_2 and NaYF_4 hosts. At the beginning of the summary of each article, the contributions of all authors are mentioned explicitly. At the end of each summary, I have also added the conclusions of each work.

6.2 Summary of Article 1

I performed thin films fabrication, structural characterizations via ellipsometry, X-ray diffraction (XRD), atomic force microscope (AFM), and optical characterization via UV-Vis-NIR spectrophotometry. Fabrication of Au-nanodiscs via electron beam lithography (EBL), luminescence measurements, and numerical analysis of all films were performed by three co-authors of this work; Dr. Adnan Nazir (Postdoc at IFA), Jeppe Christiansen (PhD student at IFA), and Dr. Søren P. Madsen (Associate Professor at Department of Engineering), respectively. I prepared the first draft of the article and all co-authors contributed in the construction of the final version of it.

Article 1: Plasmonically enhanced upconversion of 1500 nm light via trivalent Er in a TiO₂ matrix

Harish Lakhotiya, Adnan Nazir, Søren P. Madsen, Jeppe Christiansen, Emil Eriksen, Joakim Vester-Petersen, Sabrina R. Johannsen, Bjarke Rolighed Jeppesen, Peter Balling, Arne Nylandsted Larsen, and Brian Julsgaard

Appl. Phys. Lett. 109, 263102 (2016).

6.2.1 Introduction

The ladder-like energy levels of Er³⁺ ions allow the upconversion of 1500 nm, 980 nm, and 810 nm light as discussed previously in Chapter 2. In the conversion of 1500 nm wavelength photons dominantly into 980 nm involves an excitation via the $^4I_{15/2} \rightarrow ^4I_{13/2}$ transition and an emission via the $^4I_{11/2} \rightarrow ^4I_{15/2}$ transition, as shown in Figure 2.6. Potentially, this conversion is applicable in crystalline silicon (c-Si) photovoltaic (PV) devices due to the non-absorbing nature of c-Si for the photons with $\lambda > 1100$ nm. Therefore, the upconversion of 1500 nm photons via Er³⁺ ions will make it available light to the PV devices. However the small absorption cross section of Er³⁺ ions, as discussed earlier in Section-2.6.1, poses the limitation in the upconversion efficiency. The role of metal nanostructures in the upconversion luminescence (UCL) enhancement in Er³⁺ ions could resolve the issue of limited luminescence. As explained in Chapter 3, metal nanostructures accumulate the incoming 1500 nm light in the close vicinity of an upconversion material (Er³⁺ ions) which further enhances the absorption in the ions. Previously, some separate experimental [1] and numerical [2] studies were performed in this direction. Christiansen *et al.* showed the UCL-enhancement experimentally with the use of geometrically unoptimized Au-nanostructures and a separate numerical study of Goldschmidt *et al.* [2] predicted the UCL-enhancement with spherical nanostructures and mentioned the necessity of a complex model. Therefore, an in-depth study of a numerically guided plasmonically enhanced upconversion of 1500 nm wavelength photons is required. In the present work, we investigated a comparison between the numerical prediction and the experimental realization of plasmon-enhanced upconversion of 1500 nm wavelength photons in Er³⁺:TiO₂ thin films. The field accumulation around the films was performed by the EBL designed Au-nanodiscs. The Au-discs were optimized to match the localized surface plasmon resonance (LSPR) with the excitation wavelength (1500 nm) to maximize the absorption in the ions. A single-particle model was employed to validate the experimental results.

6.2.2 Summary

Er³⁺:TiO₂ thin films were sputtered at 355°C temperature on a 100 W radio frequency (RF) power in a Radio-frequency magnetron sputtering (RF-MS) technique for the present experiment.

The thickness of the films were kept at 100 nm with 5.1 at% Er^{3+} concentration. The Au-nanodiscs (truncated-cone shaped) were fabricated on top of the films in a $2 \times 2 \text{ mm}^2$ region to allow the UCL measurements in the presence and absence of Au-discs in a single sample. This reduced the sensitivity to variation in the sample fabrication. The particle density (PD) of the Au-nanodiscs in a $100 \times 100 \text{ mm}^2$ were restricted 4000, 6000, and 8000 and the diameter of the Au-nanodiscs were varied from 147 nm to 545 nm, while ensuring the LSPR at a wavelength of 1500 nm, for each particle density. The sample with PD 4000 was named S4k and similarly S6k and S8k for other two. The height of the discs were kept constant at 50 nm.

To interpret the actual multi-particle experiments, we developed a very simple finite element model (FEM) considering a single particle in a $2 \times 2 \mu\text{m}^2$ cross sectional computational domain. The electric field distribution around a single nanodisc was computed on the normal incidence of a plane wave to the surface of the sample (air/ $\text{Er}^{3+}:\text{TiO}_2$ /quartz layer). The relation between the upconverted light intensity (I_{UC}) and the incoming light (I_{in}), explained in eq.(2.8) of Chapter 2, allowed us to conveniently define the UCL-enhancement factors as

$$L^{(n)} = \frac{\int_{V_{UC}} E^{2n} dV}{\int_{V_{UC}} E_0^{2n} dV}, \quad (6.1)$$

where $n = 1.5$ is inherited from the experiment, V_{UC} shows the volume of the upconversion film, and E and E_0 are the electric field amplitudes inside the film in the presence and absence of the nanodiscs, respectively. In an initial simulation run, we scanned the $L^{(1.5)}$ over the diameter, ranging from 200 nm to 600 nm, and the height, ranging from 10 nm to 100 nm, of Au-discs. The inputs of the diameter and height of Au-discs for the experiments were adopted from the simulation. An initial comparison between the numerical prediction and the experimental outcomes was performed by evaluating the relative extinction cross-section (RECA) of the films. Numerically, we calculated the extinction by summing the absorption, ohmic heating within the Au-discs, and the scattering as integrated scattered power around the single disc. Experimentally, we measured the transmittance and reflectance of the Au-discs deposited on the $\text{Er}^{3+}:\text{TiO}_2$ thin films in an integrating sphere, as shown in Figure 5.1 and 5.2 of Chapter 5. Equations (5.10) and (5.12) of Chapter 5 were adopted for the calculations of RECA from the measured transmittance and reflectance of the films. The results showed that the predicted dimensions (diameter 315 nm and height 50 nm) of the optimized sample was in a good agreement with the LSPR peak position for similar dimensions samples of each set. This indicated that the single particle numerical model matches well in both the shape and amplitude of the RECA curves with the real multi-particle experiment. However, the optimized sample of S6k and S8k showed a double-peak instead the single peak predicted by the model. In order to understand this double-peak behavior, we plotted the RECA of five samples from a diameter 255 nm (abbreviated as D255) to the diameter of 380 nm (abbreviated as D380) of S6k with the wavelength. It was clear from the plot that there was a gradual shift of the dominance of one peak to another by passing double-peak system.

To understand this double-peak system in all sets and to validate the models for all samples, we plotted the inverse diameter (nm^{-1}) with the extinction energy resonance (eV) for all experimentally produced samples and simulations as shown in Figure 3(a) of Article 1, attached at the end of the thesis. The resonance peak positioning of all samples were in a good agreement with the simulations and showed a linearity between the inverse diameter and the resonance energy [3]. This depicted the validity of the model over the range of samples. The double-peak system were present in all sets and moved towards the higher emission wavelength for the smaller PD (S4k set) or large inter-particle distance. This implies the origin of two-peak system via an inter-particle interaction phenomenon. The phenomenon can be explained as a results of collective oscillations of neighboring dipoles. Previously, Zoric *et al.* [3] suggested that an inter-particle interactions can be minimized by maintaining the inter-particle spacing of at least 6 times the nanostructure diameter. In our work, the average spacing between the nanodiscs for all three

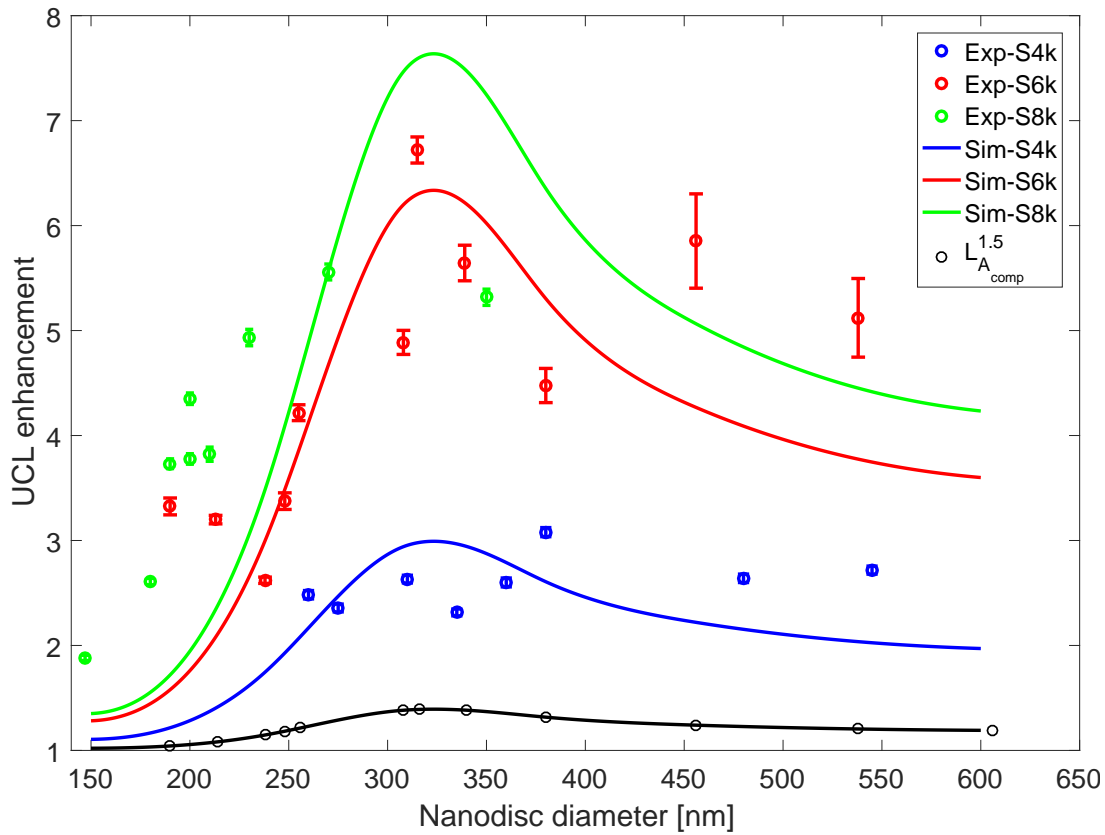


Figure 6.1: The variation in the UCL enhancement with the nanodisc diameter of experimentally produced samples are shown in colored circles. The error bars represents the standard deviation of repeated measurements on the same sample location. The black curve is a spline interpolation to the data points (represented as black circles) acquired from the $L^{(1.5)}$. The colored curves are also spline interpolation to the experimental data points (colored circles) acquired from $L_{scaled}^{(1.5)}$. The idea is adopted from Figure 5 of Article 1.

S4k, S6k, and S8k sets was around 4-5 times the diameter and thus, we observed the double-peak system.

The steady-state luminescence measurements of the samples were performed under illumination of a continuous wave laser with a peak wavelength of 1500 nm. The measurements were performed at a laser power of 22.9 mW. The experimental setup information can be seen in Section 5.3.3. In this luminescence experiment, the ${}^4I_{13/2}$ energy level has been excited and the emission of the transition ${}^4I_{11/2} \rightarrow {}^4I_{13/2}$ has been recored and plotted. The measurements were performed on samples with and without Au-discs regions. The observed UCL-spectrum measured in the presence of Au-discs showed more emitted light compared to the film measured in the absence of Au-discs. A laser-power dependence of the UCL was performed to determine the value of n used in Eq. (6.1). The n is the slope of the double-logarithmic plot between the UCL and the beam intensity (power density) and the obtained value was 1.5. This justified the value of n adopted in the numerical calculation. The UCL-enhancement was the ratio between the UCL yield measured in the presence of Au-discs and in the absence of the Au-discs on the films. In order to understand the impact of the nanodiscs diameter on the UCL-enhancement and its comparison with the simulation, we plotted the UCL-enhancement of all samples with their disc diameter in Figure 6.1. The figure depicts an increase in the UCL-enhancement with the disc diameter and a maxima (~ 7 times) at the disc diameter ~ 300 nm, a diameter where the LSPR of the discs reaches to 1500 nm wavelength in all three sets (S4k, S6k, and S8k), and a

decrease with further increase in the diameter. The larger PD provides larger UCL-enhancement probably due to a higher number of Au-discs in a constant area. The experimental data points cannot directly be compared with the calculated $L(1.5)$ from Eq. (6.1), shown as black curves in Figure 6.1, instead it needed to be scaled to provide a similar environment as experienced by the samples. Therefore, we scaled the $L(1.5)$ as shown in Eq. (6.2)

$$L_{scaled}^{(1.5)} = 1 + \alpha \times A_{comp} \times PD \times (L^{(1.5)} - 1), \quad (6.2)$$

A_{comp} is the area of the computational domain and α is a free scaling parameter. The product of A_{comp} with the PD gives the actual number of particle present in the computational area ($2 \times 2 \mu m^2$). The subtraction and addition of 1 ensure the scaling of only UCL-enhancement not the background UCL. If the single-particle model explains all the physics of the multi-particle experiment then α should be 1 and the prediction of Eq. (6.2) should directly describe the experimental data. However, this is not the case and we need a parameter which can scale the $L^{(1.5)}$. By a least-square method we obtained $L_{scaled}^{(1.5)}$ with α in range of 3-5 for three sets of samples. From Figure 6.1, we see a rough agreement of the scaled curves (colored) with the experimental data points. The higher value of α could be associated to the multi-particle scattering and trapping of light in the films. The single-particle model can be used in the future optimization steps in nanostructures geometry. Despite the limitations of the model it can provide fast calculations in a large parameter space.

All in all, plasmon-enhanced upconversion of 1500 nm wavelength was shown experimentally and modeled numerically via a single-particle model. We depicted the validity of the model in explaining the main features of the multi-particle experiment. The highest UCL-enhancement was ~ 7 times, achieved with the disc of diameter 315 nm of S6k set. We observed the inter-particle interaction (the double peak systems), beyond the explanation of the numerical model, and understood qualitatively. The work defined our first step towards the use of the metallic structures in the UCL efficiency improvement. The work also became a motivation for Emil Eriksen, PhD at IFA and a co-author of the publication of the present work, to extend the single-particle model to capture the double-peak system numerically. In that direction, we used same FEM numerical model and instead of considering a single particle, we considered two particles to determine the interaction and consequently, defines the double-peak system. The detail of the work is beyond this thesis but details can be found in Publication 6 in the List of Publication.

6.3 Unpublished work

I performed thin films fabrication, structural characterizations via ellipsometry and optical characterization via UV-Vis-NIR spectrophotometry and steady-state UCL measurements. Fabrication of Au-nanodiscs via electron beam lithography (EBL) and the numerical analysis of samples were performed by two contributors of this work; Dr. Adnan Nazir (Postdoc at IFA) and Emil Eriksen (PhD student at IFA), respectively. I have presented this work at SHIFT conference-2017, Tenerife.

Upconversion from Au-discs embedded multilayered Er^{3+} -doped TiO_2

Contributors: Harish Lakhotiya, Adnan Nazir, Emil Eriksen, Peter Balling, and Brian Julsgaard

6.3.1 Motivation and numerical predictions

In Article 1, we presented the role of Er^{3+} -doped TiO_2 sputtered film in the upconversion of 1500 nm wavelength photons. We investigated the importance of Au-discs in the improvement of upconversion luminescence (UCL) of the sputtered films. The truncated cone shape of Au-nanodiscs allows the localization of the incoming field more efficiently on the sharp edges of the geometry as shown in Figure 3.5 of Chapter 3. Therefore, a proper arrangement of the optically active dopant and Au-discs is important in achieving maximum benefit of the field-accumulation. Figure 6.2 (a) shows a schematic representation and the finite element numerical (FEM) calculated electric field distribution around sharp edges of an Au-nanodisc. The larger part of the accumulated field is not captured by Er^{3+} ions. Therefore, an appropriate arrangement of the ions is a pre-requisite for an efficient plasmon enhanced upconversion. Figure 6.2 (b) thus shows the schematic of the numerically optimized system for the maximum achievable UCL-enhancement. The thickness of the upconverting film and the height of Au-discs are optimized by FEM, discussed in Article 1. A $3\times$ UCL-enhancement via the near-field was predicted for the optimized Au structures. It is noteworthy to mention that the UCL-enhancement observed in Article 1 was around $7\times$, however, the predicted contribution of the near field was only $1.4\times$. Therefore, the present embedded system might produce more than $7\times$ UCL-enhancement with the contribution of scattering.

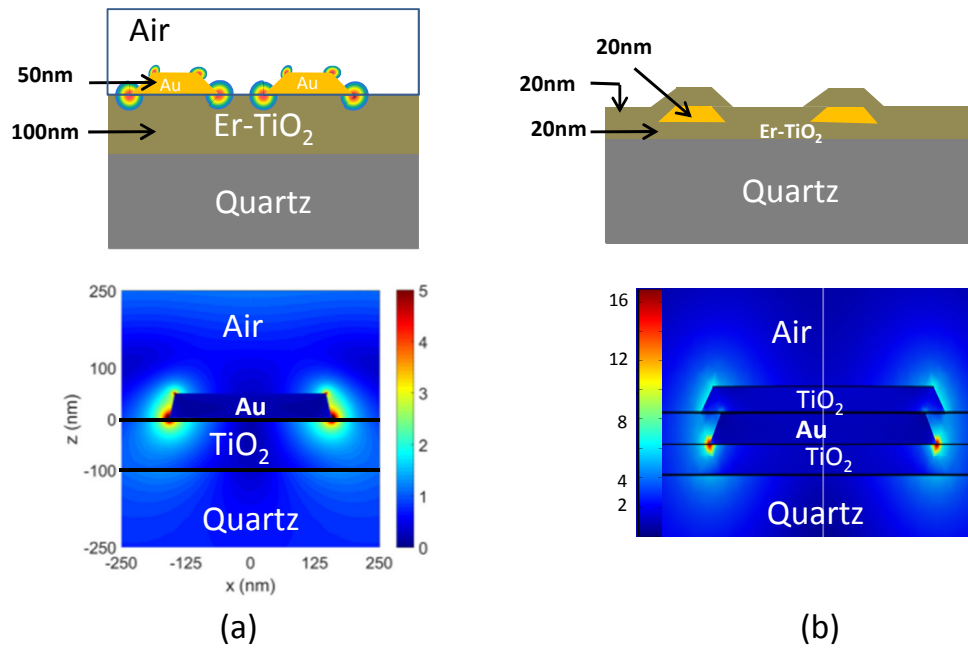


Figure 6.2: Schematic representations of Au-nanodiscs deposited on top of (a) and embedded in (b) Er^{3+} -doped TiO_2 thin films and the distribution of the electric field amplitude around an optimized Au nanodisc calculated in FEM numerical approach for each case.

The fabrication of optically active 20 nm Er^{3+} -doped TiO_2 films was possible via radio-frequency magnetron sputtering (RF-MS) but very unreliable. It was observed that the consistency in the optical activity of the films was poor, therefore, a new simulation was considered with the fabrication limitations, e.g. the films should have minimum thickness of 30 nm for the optical activity. It was observed that an increase in thickness of the Er^{3+} -doped TiO_2 films reduced the field enhancement and consequently, the UCL-enhancement. Figure 6.3 depicts new Au-embedded TiO_2 system with increase thickness of the films while ensuring their optical activity. It also depicts the distribution of the e-field around the optimized disc. It was observed that the UCL-enhancement factor was dropped to $1.9\times$ from $3\times$ (higher than the Au-discs on the top of TiO_2 configuration but lower than the optimized embedded Au-discs configuration). Therefore, while keeping the practical applicability of the system we aimed to design the Au-discs embedded Er^{3+} -doped TiO_2 films as shown in the schematic of Figure 6.3.

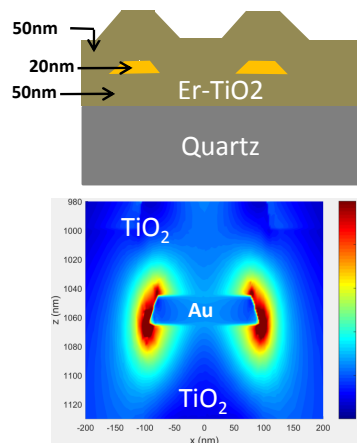


Figure 6.3: Schematic representations of Au-nanodiscs embedded in the 50 nm thin Er^{3+} doped TiO_2 films and the distribution of the electric field amplitude around an optimized Au-nanodisc calculated in the FEM numerical approach.

6.3.2 Fabrication and the fabrication challenges

The fabrication of 50 nm Er^{3+} -doped TiO_2 films on a quartz substrate was performed by RF-MS at the optimized parameters, mentioned in the summary of Article 1. The Au-nanodiscs were deposited on top of the fabricated films via EBL technique, details can be fetched from Section 4.4 of Chapter 4. The nanodiscs were designed with a height of 20 nm and the diameter were optimized by a finite element method (FEM) calculation to match the wavelength of the localized surface plasmon resonance (LSPR) with the excitation wavelength (1500 nm). The discs were fabricated on a $2 \times 2 \text{ mm}^2$ area of the film so the UCL measurements both with and without Au-discs could be performed. The top layer deposition for the fabrication of the embedded Au-discs system was performed at elevated substrate temperature. We deposited 50 nm Er^{3+} -doped TiO_2 film at 350 °C temperature. However, the high-temperature fabrication of the top layer developed two challenges in the fabrication of Au embedded TiO_2 system. The challenges were

1. The heating deformed the Au-discs and consequently, changed the LSPR wavelength.
2. The bottom Er^{3+} -doped TiO_2 layer gets reheated and that might change the UCL of the bottom layer.

One of the way to avoid the Au-discs deformation was to introduce a room temperature (RT) deposited undoped- TiO_2 film as a protector before the deposition of top upconverting layer. Previously, the optimization of the distance (maintained by optically inactive film) between the Au-discs and the upconverting films has been established in the improvement of UCL-enhancement [4, 5]. Therefore, the use of buffer layers not only protect the Au-discs from deforming but also maintain the spacing between the optically active ions and the discs. Therefore, in the present work, we have introduced top- and bottom-buffer layers for the experiments. The optimization of the thickness of buffer layer was taken into consideration first, where four sets of samples were fabricated by RF-MS. The thickness of the undoped- TiO_2 film was varied from 0 to 20 nm. The Au-discs were deposited on top of the films afterwards. The schematic representation of the samples are shown in Figure 6.4.

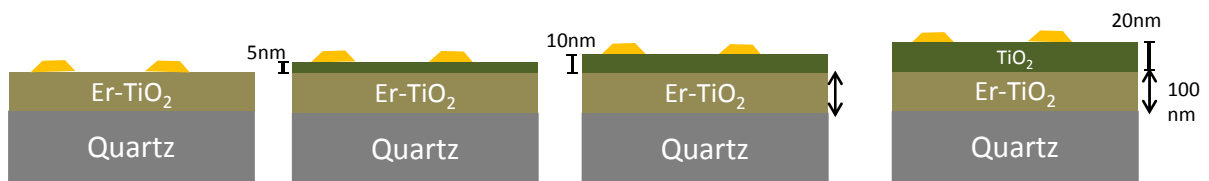


Figure 6.4: Schematic representations of Au-nanodiscs deposited on top of the Er^{3+} -doped TiO_2 and the undoped- TiO_2 (buffer) thin films. The buffer film maintains the spacing between the Au-nanodiscs and the Er^{3+} doped TiO_2 films. From left to right the thickness of the buffer layer is varied from 0 to 20 nm.

The diameter of the discs were varied from 290 nm to 315 nm after the numerical guidance to achieve the LSPR at 1500 nm for each set. The optical characterizations of the samples were performed by both observing the LSPR peak position at 1500 nm wavelength in the extinction plots (not presented) and measuring the UCL in the presence and absence of nanodiscs presented in Figure 6.5. Figure 6.5(a) shows the schematic representation of the UCL experiment, where a beam of 1500 nm wavelength either hits the Er^{3+} doped- TiO_2 surface or the surface with Au-discs on top and collects the emitted 980 nm wavelength light called the UCL spectrum. The

UCL spectra shown in Figure 6.5(b) were recorded under continuous-wave (CW) laser illumination at a wavelength of 1500 nm using a power of 18.9 mW and a beam area (full width at half maximum) of $6.5 \times 10^{-5} \text{ cm}^2$. The figure shows the UCL spectra of three different stages of the fabrication of structures shown in Figure 6.4. In the first stage, four 100 nm Er^{3+} doped- TiO_2 films are measured and the four spectra are plotted in section (i) of Figure 6.5(b). In the second stage, the undoped- TiO_2 films with the thicknesses of 5 nm, 10 nm, and 20 nm were deposited on top of three out of four samples. The three spectra are depicted in section (ii) of the figure. It is noteworthy to mention that the UCL yield of the samples drops with the deposition of a buffer layer, comparing section (ii) to section (i). In stage three, the Au-discs were deposited on top of all four samples (one without and three with undoped- TiO_2 films on top of upconverting layer) and the spectra are recorded by hitting the Au-regions with the 1500 nm laser and are presented in section (iii) of the figure. In general, the UCL of all films are increased. The enhancement in the UCL is determined by dividing the area under the 980 nm peak (called as the UCL-yield) of section (iii) to the UCL yields of samples without Au-discs (i.e. sections (i) and (ii)). The UCL and the calculated UCL-enhancement of all four films are plotted against the buffer (undoped- TiO_2 films) thickness in Figure 6.5(c). An insertion of the buffer layer, on the one hand, significantly drops the UCL of the film and there is a slight decrease with an increase in the buffer thickness. The UCL-enhancement, on the other hand, is not affected with the buffer thickness, that indicates no importance of the buffer layer in the improvement of the UCL-enhancement factors. The obtained results of the variation in the UCL-enhancement were not in agreement with the results previously observed in NaYF_4 matrix [4]. From the experiment we observed nearly no impact of the buffer layer thickness on the UCL improvement induced by the Au-discs. Therefore, the thickness of the buffer layer was fixed to 10 nm for the embedded Au-discs experiment for two reasons: (a) Thinnest buffer which can also maintain the geometry of discs during the top Er^{3+} doped- TiO_2 film deposition at 350 °C substrate temperature. (2) The minimum thickness of the RF-MS developed films.

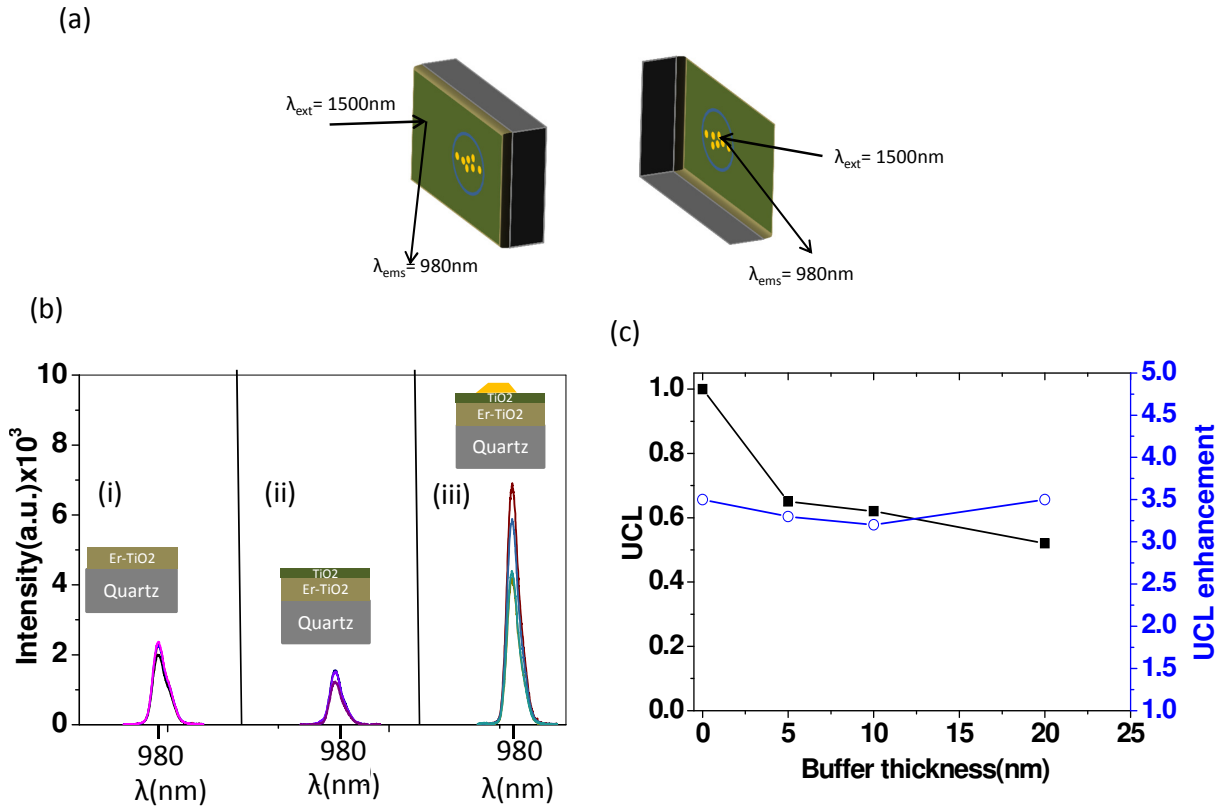


Figure 6.5: Schematic representations of the UCL experiment and the obtained UCL spectra of three types of samples. (a) shows the schematics of the excitation and emission from two different regions of a sample. (b) The UCL spectra in three types of samples: (i) The UCL spectra of four 100 nm thin Er^{3+} -doped TiO_2 films (the spectra are overlapped), (ii) The UCL spectra of three films from the previous four with different buffer (undoped- TiO_2) layer on top of the Er^{3+} -doped TiO_2 films, and (iii) The UCL spectra of all four samples, where one is without the buffer layer and the rest are with the buffer layers, with Au-discs on top. (c) A variation in the UCL of the films measured in the absence of Au-discs and the UCL enhancement (a ratio between the calculated area of 980 nm emission peak of the UCL spectra measured in the presence and absence of the Au-discs) with the buffer layer thickness.

6.3.3 Results and discussions

The 50 nm thin Er^{3+} doped- TiO_2 and the 10 nm buffer-assisted 50 nm thin Er^{3+} doped- TiO_2 films with Au-discs on top were used in the next stage experiment. In this experiment the Au-discs embedded Er^{3+} doped- TiO_2 thin films were designed by depositing 10 nm buffer-assisted Er^{3+} doped- TiO_2 thin films on top of the Au-discs. The fabrication of the top layers was performed by RF-MS. Firstly, the buffer layer (undoped- TiO_2) was deposited at RT on top of the Au-discs and subsequently, the deposition of 50 nm upconversion layer was performed at elevated temperature. Figure 6.6 represents the comparative optical studies of Au-discs on top and Au-discs embedded samples. (A-1 and B-1) of the figure show the cross-sectional schematic representation of the samples. The extinction curves of both samples are depicted in (A-2) and (B-2), where the LSPR peak positioning was shifted to higher wavelength due to the increased refractive index of the surrounding materials. It is important to note that the shift in the LSPR peak position was nominal compared to the numerical prediction at 1500 nm wavelength. The UCL experiment depicted in (A-3) and (B-3) is conducted by exciting Er^{3+} ions in the presence and absence of Au-discs as shown in the associated schematics. The UCL of the 50 nm films is nearly the half of the 100 nm films employed in the previous experiments,

mentioned in the section (i) of Figure 6.5(b). However, the UCL intensity measured in the presence of the Au-discs is not significantly higher than the UCL measured in the absence of the discs. However, if we calculate the UCL-enhancement it is merely $2\times$, which is lower than what was observed for the 100 nm films (nearly $3.5\times$) in Figure 6.5(c). The possible explanation could be that the LSPR wavelength of the Au-discs are not well matched with the excitation wavelength. Comparing (A-3) with (B-3), the UCL of the films drops around $5\times$ and the UCL measured with Au-discs is even lower than the bottom Er^{3+} doped- TiO_2 film alone (black curve of (A-3)). The possible explanation of the decrease in the UCL of the film could be the negative impact of the elevated temperature on the bottom upconverting layer and inefficient deposition of the top layer on the buffer layer.

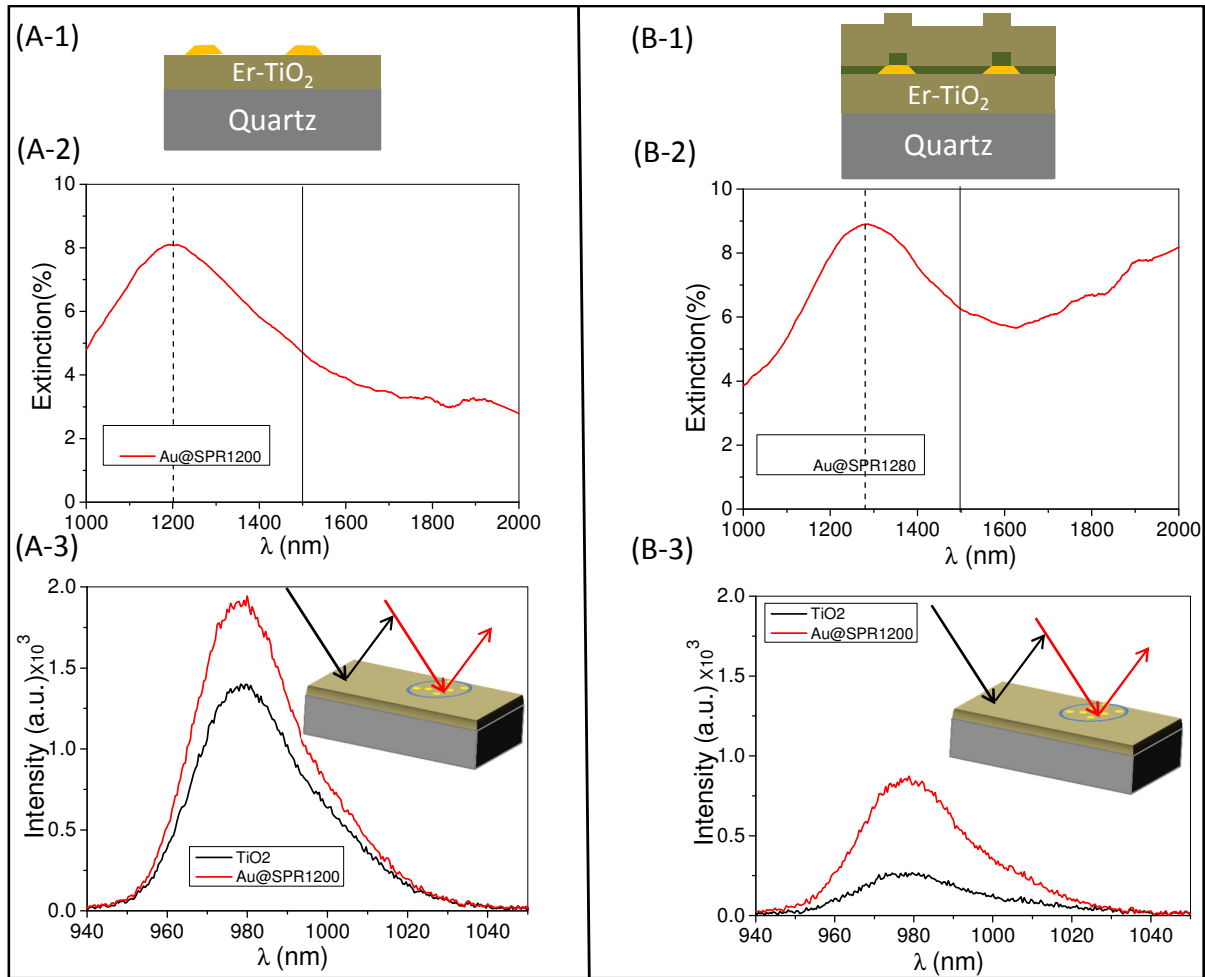


Figure 6.6: Schematic representations and optical measurements of Au-discs on top of and Au-discs embedded in Er^{3+} doped TiO_2 thin films. The left column (A-1 to A-3) depicts the cross-sectional representation of the sample where Au-discs are on top of the film, in (A-1). The LSPR-peak positioning of the deposited Au-discs in the extinction versus wavelength plot in (A-2), and the UCL spectra measured in two different sections of the sample in (A-3). The right column (B-1 and B-3), on the other hand, shows the cross-section representation of the buried Au-discs in the undoped- TiO_2 (buffer) and the Er^{3+} -doped TiO_2 thin films in (B-1), the extinction plot (B-2) shows the shift in the LSPR peak from (A-2) due to the deposition of the undoped and doped- TiO_2 thin films, and (B-3) shows the UCL spectra measured at two different regions.

A second Au-discs embedded sample set was prepared on the base with the 10 nm buffer underneath the Au-discs. The top layer deposition was performed by the RF-MS in the same way

explained for the first sample. Figure 6.7 shows the schematics of different stages of the samples fabrication and the optical results at each stage. The cross-sectional schematic of Au-discs on top of a buffer layer-assisted 50 nm Er^{3+} -doped TiO_2 film is represented in (A-1) and (A-2) shows the extinction plot of the samples. The two curves of the extinction are the results of two Au-regions with different diameter on the sample. The UCL-spectra measured at three different places of the sample are shown in (A-3). It is clear that the Au-discs with LSPR matched with the excitation wavelength gives the maximum intensity (the spectra in red). The enhancement in UCL is roughly in the range of 3-3.5 \times similar to what was achieved in 100 nm TiO_2 film Figure 6.5(c). After deposition of the first buffer layer on top of the Au-discs, the LSPR peak should shift towards higher wavelength, however, the extinction plot (B-2) is unaffected from (A-2). Unfortunately, this is beyond our explanation.

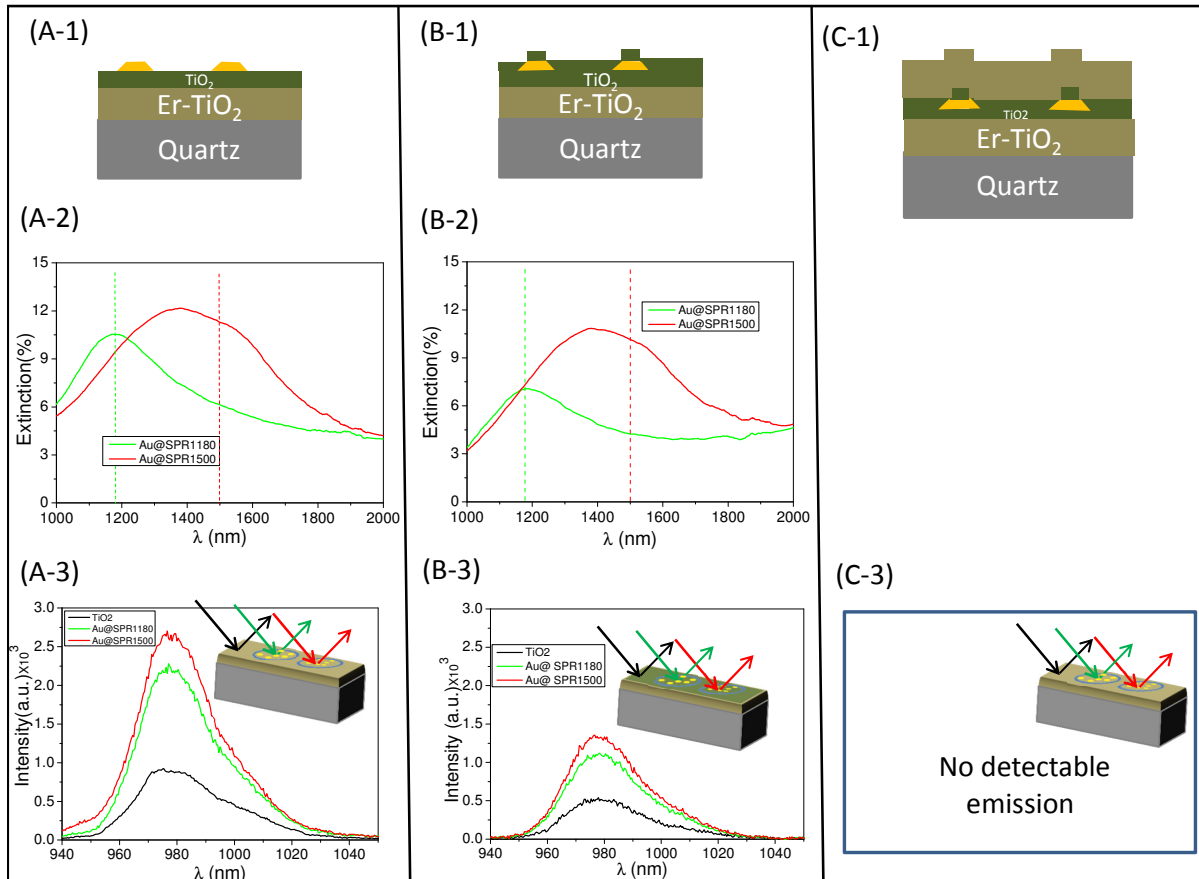


Figure 6.7: Schematic representations and optical measurements of three configurations: Au-discs on top, Au-discs buried in the buffer layer, and in the buffer and upconverting (Er^{3+} doped TiO_2) layers are shown in the left column (A-1 to A-3), in the middle column (B-1 to B-3), and in the right column (C-1 and C-3), respectively. A-1, B-1, and C-1 represent the cross-sectional sketch of all three configurations. Each sample has two Au-regions with different diameters. A-2 shows the extinction plot of Au-discs of the both regions on Au-discs on top configuration and B-2 shows the shift in the LSPR peak positioning of A-2 after depositing buffer on top of the Au-discs. A-3, B-3, and C-3 show the UCL results obtained in all three configurations measured on two different regions, mentioned in the attached top-view sketches.

However, the UCL-spectra measured without Au-discs, shown in (B-3), dropped to around 30% compared to the black curve of (A-3), is in an agreement with the black curve of Figure 6.5(c), observing the decrease in the UCL going from 10 nm to 20 nm buffer layer. In addition, (B-3) shows higher UCL yield for the measurements with the Au-discs (green curve of the plot) and the maximum for the discs in the resonance with the excitation wavelength (red curve of the plot).

After depositing the top upconverting layer, shown the schematic in (C-1), the Au-embedded sample is ready for the final optical measurements. The extinction plot of the sample is not measured due to no importance at this stage. Therefore, firstly I have measured the UCL of the sample and the observed optically inactive nature did not allow for measuring the extinction plot. The optical inactivity of the system could be explained by the annealing effect on the bottom layer whereas the Er^{3+} ions of the top layer might get some non-radiative channels due to their deposition on the buffer layer, which increases the non-radiative decays in the film.

6.3.4 Conclusions

In this experiment, we have tried to increase the UCL-enhancement by intermixing plasmonic structures (i.e. Au-nanodiscs) with the optically active dopants (i.e. Er^{3+} ions) in a best-possible way. We have fabricated the Au-discs embedded Er^{3+} -doped TiO_2 system for this purpose. The high temperature deposition of Er^{3+} -doped TiO_2 film introduced some fabrication challenges for the embedded sample. The buffer (undoped- TiO_2) film was considered as a solution for the shape deformation of the Au-discs induced by the top layer deposition at an elevated temperature. The thickness of the buffer layer was optimized to 10 nm. Two samples, where Au-discs either deposited directly on top of the upconverting layer or on the buffer layer first, were used for the fabrication of the embedded samples. The upconversion in the both embedded samples were found significantly lower than the upconversion of the bottom layer itself. It can be assumed that the heating either reduced or vanished the upconversion of the Er^{3+} doped TiO_2 thin films. From the present experiment, we couldn't not achieve the desired outcomes but we received the motivation of our next experiment, mentioned as Article 2 of the thesis.

6.4 Summary of Article 2

I was engaged in all experimental work related to the material fabrication, structural characterizations and some optical characterizations of this study, except stated explicitly. Specifically, I performed fabrications, structural characterizations via ellipsometry, X-ray diffraction (XRD) and atomic force microscope (AFM), and steady-state luminescence measurements of all films. Rutherford backscattering spectrometry and time-resolved photoluminescence (TRPL) measurements of all films were performed by two co-authors of this work John Lundsgaard Hansen (Senior researcher at IFA) and Jeppe Christiansen (PhD student at IFA), respectively. I prepared the first draft of the article and all co-authors contributed in the construction of the final version of it.

Article 2: **Upconversion luminescence from magnetron-sputtered Er³⁺-doped TiO₂ films: Influence of deposition- and annealing temperatures and correlation to decay times**

Harish Lakhotiya, Jeppe Christiansen, John Lundsgaard Hansen, Peter Balling, and Brian Julsgaard

Revised submission Journal of Applied Physics August, 2018

6.4.1 Introduction

Chemical [6] and thermal stabilities [7], relatively low phonon energy [7], and nearly zero absorption in visible, and near-infra red ($\lambda < 1100$ nm) light [8] makes TiO₂ a widely accepted material for upconversion process, a process where two or more low-energy photons are merged to produce one high-energy photon. Fabrication of TiO₂ thin films is well-established by physical vapor deposition (PVD) techniques [9, 10]. A radio-frequency-magnetron sputtering (RF-MS), a widely accepted PVD technique, is a cheap, fast, and simple technique to synthesize oxide thin films for solar cell applications [10, 11]. The technique can precisely control the oxide films thickness down to 10 nm. Fabrication of Er³⁺-doped TiO₂ thin films for the upconversion purpose is reported previously [12, 13]. It has been observed in the work of *Sabrina et al.* [12, 13] that upconversion luminescence (UCL) of radio-frequency magnetron sputtered Er³⁺:TiO₂ thin films can significantly be altered by the variation in deposition and material parameters during the fabrication process. They observed that an elevated temperature is a pre-requisite for a significant UCL from the films. However, a detailed study explaining the underlying mechanisms has never been carried out. This detailed study is not only important in understanding the fundamental science but also in optimizing the sputtered films for a further UCL improvements. A layer by layer growth of plasmonically enhanced Er³⁺-doped TiO₂ thin films could be a way to achieve such UCL improvements. However, the possibility of several fabrication steps at elevated temperatures in the layer by layer growth demands a thorough study of the impact of the deposition and annealing temperatures on the optical properties of the grown films, which is the focus of the present work.

6.4.2 Summary

In this work, several sets of 50 nm thin Er³⁺:TiO₂ films were sputtered at different deposition temperatures ranging from room temperature (RT) to 350 °C in an Ar with 2 % O₂ environment. The as-grown films were post annealed afterwards at several temperatures in the environment as same as the deposition environment (Ar/O₂ environment) with and without being exposed

to ambient air. The steady-state luminescence experiment was conducted by optical excitation of the as-grown and post-annealed films with a 1500 nm laser and collection of the emitted light at 980 nm wavelength (called as UCL signals), corresponding to the ${}^4I_{11/2} \rightarrow {}^4I_{15/2}$ (ground state) transition of Er^{3+} ions in $\text{Er}^{3+}:\text{TiO}_2$. It has been seen that samples deposited at RT and lower substrate temperatures are optically inert and the first observable UCL signal was achieved at a deposition temperature of 250 °C. The maximum UCL yield, the area under the 980 nm wavelength peak in the emission spectrum, was obtained for the film deposited at 350 °C temperature. Post annealing of such films, in general, has shown an adverse effect on the UCL yields of as-grown films. Figure 6.8, adopted from Article 2, shows the variation in UCL yields with the annealing temperatures on the films grown at different deposition temperatures. The films deposited at higher substrate temperatures are inclined towards becoming optically inert with an increase in annealing temperatures, whereas films deposited at lower substrate temperatures are unaffected by post annealing. However, the impact of post annealing on the UCL yields of as-grown films are comparably less adverse if the films are not exposed to ambient between the multiple temperature treatments, shown as dashed curves of Figure 6.8. Interestingly, air unexposed films deposited at lower substrate temperature are optically healed with an increase in post-annealing temperatures.

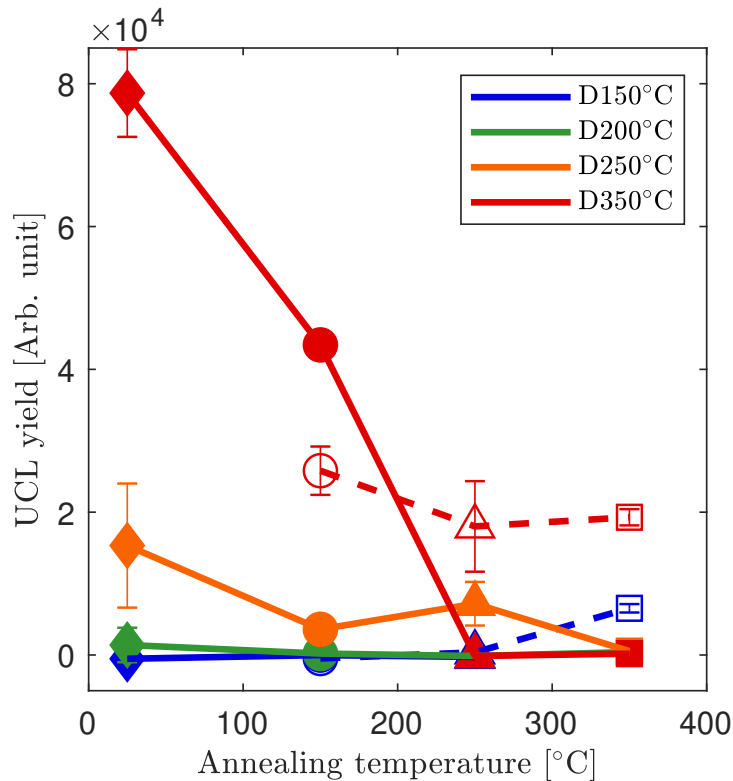


Figure 6.8: Upconversion luminescence yield (area under the 980 nm emission peak) as a function of annealing temperature for films deposited at different deposition temperatures (Dxxx°C). The diamonds represent the unannealed samples whereas circles, triangles, and squares correspond to the samples annealed at temperatures 150 °C, 250 °C, and 350 °C, respectively. The solid and open symbols correspond to samples being exposed and unexposed to ambient air, respectively, before annealing.

Along with steady-state luminescence measurements, all films were further analyzed by TRPL to determine the characteristic decay times of the involved energy levels of Er^{3+} in the films. In this experiment, we excited the samples with a 800 nm laser to populate the ${}^4I_{9/2}$ energy

level and recorded the emission at 980 nm and 1500 nm wavelengths, representing the two lowest excited energy levels ${}^4I_{11/2}$ and ${}^4I_{13/2}$ of the Er^{3+} ions. The characteristic decay times of the two energy levels were calculated by the fitting of raw data and are represented as $\tau_{11/2}$ and $\tau_{13/2}$, respectively. In the case of lowering the deposition temperatures from the temperature of maximized UCL (350 °C), lower decay times (faster decay) and smaller area under the decay curves were observed in the as-grown films. This clearly indicated of the presence of more non-radiative decay channels at the lower deposition temperatures. The adverse effect of post annealing on the UCL yield was also observed in the decay times ($\tau_{11/2}$ and $\tau_{13/2}$) of the same samples. The higher annealing temperatures, in general, decreased the decay times, however, unexposed films deposited at lower substrate temperatures have shown longer decay times which was in good agreements with the results obtained from the steady-state luminescence. As mentioned earlier in the text, if the non-radiative decay channels are the one which varied with the deposition and annealing temperatures then UCL yield should increase with respect to both $\tau_{11/2}$ and $\tau_{13/2}$. To establish this relation between these decay times and the observed UCL yields of all investigated samples, a plot was developed between the UCL yields and product of both $\tau_{11/2}$ and $\tau_{13/2}$ presented in Article 2. The figure provided an experimental fact that the data exhibited a reasonable approximation in a proportionality between the two. In fact, this relationship can be understood on the basis of a simple rate-equation model, which is presented by Christiansen *et al.* [14].

Despite the large variation in the optical properties, all films (unannealed and annealed) were structurally (amorphous and surface roughness) unchanged with the temperature treatments. Therefore, most likely the optical variation were the results of atomic scale variation in the films, i.e. point defects in the films. The presence of point defects and the variation in its density with the ambient air and temperatures in sputtered oxide films, e.g. TiO_2 and SnO_2 [15–18] were previously well studied. In the study of Pham *et al.* [19] the oxygen-vacancy defect states were observed at about 1.0-1.5 eV above the top of the valence band in amorphous- TiO_2 thin films deposited at 300 °C. We proposed that such oxygen-vacancies were present in our $\text{Er}^{3+}:\text{TiO}_2$ thin films. The transition energy (~ 1.27 eV) of the ${}^4I_{11/2} \rightarrow {}^4I_{15/2}$ and the transition energy (~ 0.82 eV) of the ${}^4I_{13/2} \rightarrow {}^4I_{15/2}$ were in good agreement with the energy difference between the defect states and the valence band of TiO_2 . Hence, the non-radiative decay paths from these two states of Er^{3+} ions could be associated with the excitation of valence-band electron to the defect states in TiO_2 . Previous works have reported on the role of hydrogen passivation of oxygen-vacancies in c- TiO_2 [20] as well as of dangling bonds in a- TiO_2 films [18, 21] through formation of O–H bonds [21]. We further proposed that the defects in as-grown films were possibly passivated by hydrogen (H) atoms (due to the presence of unintentional H-residuals in form of H-plasma during the sputtering process) and consequently, the films were optically active. Annealing of such films (in absence of H-plasma) removed the H-atoms from the passivated defects and the defects became optically active. Therefore, we assume that with an increase in annealing temperature, the number of non-radiative channels were increased for the excited electrons resulting in the drop in luminescence. In addition, the role of ambient air was understood by its possible assistance in an efficient H-removal from the defects compared to the H-removal in samples unexposed to air with rising annealing temperatures. Therefore, the effect of the annealing on the UCL was more adverse in air-exposed samples.

Additional experiment: So far, we discussed the possible role of H-atoms in the passivation or activation of the defects, arising during the fabrication process, in $\text{Er}^{3+}:\text{TiO}_2$ thin films. As per our understanding, the absence of H during the fabrication was nearly impossible to achieve, however, annealing could be performed in an intentional H_2 environment which will underline our current understanding of H-atoms in the defects passivation. Annealing of the films in molecular

hydrogen atmosphere can either reduce the dissociation of hydroxyl bonds at the surface of as-deposited TiO_2 films or can passivate the dangling bonds of Ar/O_2 annealed films. Thus, we performed another experiment where an annealing of two samples: the one deposited at $350\text{ }^\circ\text{C}$ with the maximum UCL yield, and other is deposited and annealed both at $350\text{ }^\circ\text{C}$ with zero UCL yield, was performed in H_2/N_2 environment in a tube furnace. Due to the absence of the H-plasma source in the sputtering chamber, molecular hydrogen was the obvious choice for the annealing environment in the experiment. Despite comparable high activation energy and weak interaction with TiO_2 surface, the reduction of the TiO_2 surface by molecular hydrogen during annealing under high vacuum is reported previously [22, 23]. After the treatment, we saw UCL signals in both films under the excitation of a 1500 nm laser. However the UCL yields were only 10 percent of the maximum in both samples. It is important to notice that the optically inactive sample now recovered and started to emit upconverted photons. This indicated the role of molecular hydrogen in the hydroxylation of the oxygen-vacancies in Er^{3+} -doped TiO_2 films. A possible explanation for the poor recovery of the UCL yield is the less-reactive nature of molecules compared to plasma [24].

All in all, the role of deposition- and annealing temperatures have been extensively studied in the present work. We observed the highest UCL yield at a deposition temperature of $350\text{ }^\circ\text{C}$ with a 5.1 at% concentration of Er^{3+} ions. In general, post-annealing of deposited films reduced the UCL. We determined that the air-exposure is detrimental to the UCL performance of the deposited films before the post-annealing. On the contrary, the post-annealing was beneficial if the films were deposited at lower substrate temperature and unexposed to air before the annealing process. The decay curves from the ${}^4I_{11/2}$ and ${}^4I_{13/2}$ of Er^{3+} ions showed the possible activation of non-radiative channels with annealing of the deposited films, and the $\tau_{11/2}$ and $\tau_{13/2}$ were in good agreement with the obtained UCL for all films. We proposed that the variation in the UCL of thin films was linked to an interplay between generation of O-vacancies and passivation by H-atoms. From the present understanding, we can define a suitable environment for annealing the films for the development of an Au-embedded multilayer system. From the additional experiment we learned the way to retain the UCL yield of the deposited films with annealing. In designing, thus, of a multi-layered structures, if the top layer is deposited at $350\text{ }^\circ\text{C}$ under H-plasma then possibly the bottom layer (that get heated) could retain its UCL and overall UCL will be doubled or more depending upon the number of deposited layer. This could further pave the way for the use of Au-embedded multi-layered $\text{Er}^{3+}:\text{TiO}_2$ in the upconversion-based solar cells.

6.5 Summary of Article 3

I was engaged in all experimental work related to the material fabrication, structural characterizations and some optical characterizations of this study, except stated explicitly. In the material fabrication, I performed the chemical synthesis of core-shell upconversion nanocrystals (UCNCs) and the UCNC monolayers formation via spin coating. In the structural characterizations, I conducted powder X-ray diffraction (PXRD) and transmission electron microscope (TEM) imaging for all colloidal UCNCs, and cross-section and top-view scanning electron microscope (SEM) imaging for all UCNC monolayers. In the optical characterizations of nanocrystals, I was involved in ellipsometry and steady-state luminescence (UCL) measurements. Inductive coupled plasma-optical emission spectroscopy (ICP-OES), scanning transmission electron microscope (STEM), and energy dispersive X-ray spectrometry (EDS)-line scan of colloidal UCNCs were performed by Martin Bondesgaard (PhD student at Chemistry). High-resolution TEM (HR-TEM) of colloidal UCNCs and time-resolved photoluminescence (TRPL) measurements of all samples in both films and solutions configurations were performed by Aref Mamakhel (Research associate at Chemistry) and Søren Roesgaard (Postdoc at IFA), respectively. Au-discs for the work were designed by Adnan Nazir (Postdoc at IFA) using electron beam lithography (EBL). I have prepared the first draft of the complete article (main letter and supporting information) and all co-authors contributed in the construction of the final version.

Article 3: **Resonant Plasmon-Enhanced Upconversion in Monolayers of Core-Shell Nanocrystals: Role of Shell Thickness**

Harish Lakhotiya, Adnan Nazir, Søren Roesgaard, Emil Eriksen, Jeppe D. Christiansen, Martin Bondesgaard, Frank C.J.M. van Veggel, Bo Brummerstedt Iversen, Peter Balling, and Brian Julsgaard

Submitted Nano Letters August, 2018

6.5.1 Introduction

The photon merging ability of trivalent lanthanide (Ln^{3+})-doped upconversion nanocrystals (UCNCs) make them suitable for biomedical imaging [25, 26], photovoltaic (PV) devices, [27, 28], display technologies [29], and many more applications [30]. Single-doped lanthanides (Er^{3+} or Tm^{3+}) [31, 32] have ability to convert near-infrared (NIR) photons ($\lambda > 1100$ nm) into visible photons whereas co-doped (i.e. Er^{3+} - Yb^{3+}) UCNCs are more efficient in the conversion of 980 nm NIR photons to visible photons. Therefore, the single lanthanide-doped UCNCs are more appropriate than the co-doped UCNCs for the photo-current efficiency enhancement in crystalline silicon (c-Si) solar cells by converting non-absorbable photon ($\lambda > 1100$ nm) to absorbable photons ($400 \text{ nm} > \lambda < 1100 \text{ nm}$). However, a small absorption cross-section [33, 34] and the faster non-radiative decays compared to the radiative emission of single lanthanide-dopants may introduce limitation to their upconversion luminescence (UCL) efficiency. The formation of optically inert shells around the optically active core-nanocrystals [35], on the one hand, is one of the way to deal the later limiting factor in UCL efficiency. The former limiting factor, on the other hand, can be dealt by concentrating the incoming light near the UCNCs by metal nanostructures [36], as explained in Chapter 3. For PV device applicability both optimizations need to be performed on the film configurations of the chemically synthesized colloidal UCNCs. Fabrication of UCNC monolayers demonstrate a well control film formation on atomic level. In addition, UCNC monolayers could show a single particle interaction with metal nanostructures, placed in close vicinity of UCNCs. An optimization of metal nanostructures for the UCL efficiency enhancement in UCNCs involves an enhanced absorption and emission within

the structures [37]. An enhanced absorption demands a resonant interaction with the optically active dopant of the UCNCs and an enhanced emission requires an optimized distance with the dopant of UCNCs, explained in Chapter 3. Therefore, an optimization of both absorption and emission could pave the way for an efficient upconversion layer for photo-current improvement in c-Si PV devices.

The present work investigated the variation in upconversion luminescence (UCL) of core-shell UCNCs with the shell thickness in their monolayer configuration. The work involved the decay times of the two lowest (most dominant) energy levels of Er^{3+} ions to study the possible activation of the non-radiative decay channels in the transformation of colloidal UCNCs to UCNC monolayers. The plasmon enhancement was ensured by depositing Au-nanodiscs via EBL either on top of or below the UCNC monolayers. The nanostructures were optimized by both matching their LSPR with the excitation wavelength (1500 nm) and determining their appropriate distance from the Er^{3+} ions.

6.5.2 Summary

The work involved the chemical synthesis of Er^{3+} -doped NaYF_4 nanocrystals by solvo-thermal method. Spherical core-nanocrystals, with a diameter of 19.7 ± 0.7 nm, were fabricated with 20 mol% Er^{3+} for the present experiment. A continuous growth of NaLuF_4 shells around the core was fabricated either by the sequential layer growth [38–40] or by the one-shot injection methods after retrieving one sample of core-nanocrystals. A set of samples were prepared with the shell thickness ranging from 0.8 nm to 10.1 nm around the core. The presence and the uniformity of the shell were verified by multiple techniques; HR-TEM of some UCNCs, STEM of core-shell UCNCs, EDS-line scan over a core-shell nanocrystal, and PXRD of all UCNCs. TEM images, on the other hand, confirmed the narrow size distributions ($< 5\%$) in all UCNCs. The introduced dopant concentration was analyzed by ICP-OES and the achieved value, 17 mol%, (close to the targeted 20 mol%) was very consistent among samples. All the structural characterizations of the colloidal UCNCs proved the appropriate structures formation for the optical studies.

Fabrication of UCNC monolayers was performed by drop-cast assisted spin coating technique. The technique involves the spinning of colloidal UCNCs drop on a quartz substrate. The UCNC monolayers were achieved by selecting an appropriate solvent for the UCNCs, achieving the right concentration of the UCNCs, and optimizing the spinning parameters of the technique. The monolayer verification was performed by intentional terminating the film with scotch-tape. The 2D-arrangements of UCNCs showed a close-packed ordering of nanocrystals with some minor defects. It has been observed that the ordering in the UCNCs arrangements gets worst with increasing nanocrystals size due to their dominance over the capillary forces during the solvent evaporation. Therefore, the UCNCs with the shell thickness of 10.1 nm showed a close-packed arrangements but without any specific orientation.

The optical investigations of the colloidal UCNCs and the UCNC monolayers were performed by the steady-state UCL and TRPL measurements. A continuous-wave (CW) laser with a wavelength of 1500 nm and a power density of 9.8 mW/cm^2 were used to excite the ${}^4I_{13/2}$ energy level of Er^{3+} ions in the UCL measurements. The measurements recorded the transitions of the ${}^4I_{11/2}$, ${}^4I_{9/2}$, ${}^4F_{9/2}$, ${}^4S_{3/2}$, and ${}^2H_{11/2}$, to the ground energy level (${}^4I_{15/2}$) with the emission-wavelengths of 980 nm, 810 nm, 660 nm, 550 nm, and 525 nm, respectively, as explained in

Section 2.6.1. The UCNC monolayers were performed inside an integrating sphere (explained in Section 5.3.3), however, the colloidal UCNCs were excluded from the UCL measurements in the preset study due to the similar published report by Fischer *et al.*[39]. An increase in the shell thickness reduces the number of nanocrystals and consequently, the number of Er^{3+} ions in the area illuminated by the laser. Therefore, the obtained UCL spectra were normalized with the number density of the Er^{3+} ions in the constant area. The total UCL yield (sum of area under the all emission peaks) was observed as a function of the shell thickness. The UCL yield of the core-nanocrystals was enhanced by $16.5\times$ and $94.4\times$ by the growth of ~ 3 nm and ~ 10 nm shell in their monolayer configuration. The external quantum luminescence (EQLE) were measured, explained in Chapter 5, Section 5.3.3, for all UCNC monolayers and EQLE showed an increasing function with the shell thickness. The increase has a low, steep, and a constant slopes until nearly 1 nm, 1 nm to 6 nm, and 6 nm to ~ 10 nm shell thickness, as shown in the Figure 6.9(a). The increasing EQLE could possibly be explained by two reasons. First, the presence of surface defects on the surface of core-nanocrystals provides a alternative paths to the Er^{3+} ions to decay non-radiatively. However, the surface passivation by a shell around the core reduces such pathways and consequently, increases the radiative emissions. Secondly, The nanocrystals posses ligands on the surface to be to stabilized in a colloidal solution. Therefore, an increase in the shell thickness increases the spacing between the Er^{3+} ions and the emission quenchers, -OH and -CH groups of ligands. This eventually, increases the radiative emissions from the Er^{3+} ions.

The TRPL measurements, in contrast, were performed by a pulsed laser with a peak wavelength of 800 nm. The experiment was performed outside the integrating sphere for both the colloidal solutions of UCNCs and the UCNC monoalyers. In this experiment, the ${}^4I_{9/2}$ energy level of Er^{3+} ions was populated and the decays from the ${}^4I_{11/2}$ and the ${}^4I_{13/2}$ to the ground level (${}^4I_{15/2}$) were recorded. The obtained decay curves were fitted by single- or double-exponential decay models (detailed in the submitted Article 3) and provided the lifetimes of both energy levels; the lifetime of ${}^4I_{11/2}$ represented by $\tau_{11/2}$ and the lifetime of ${}^4I_{13/2}$ represented by $\tau_{13/2}$. We observed longer lifetimes and the lager area of the decay curves interpreting increased amount of emitted light from the samples with thicker shells in their both solution and monolayer configurations. A plot between the decay curves and the shell thickness showed an increasing function with a low, a steep and a constant slops as observed in the variation in EQLE with the shell thickness as shown in Figure 2 of Article 3, attached at the end of the thesis. This indicates a good correlation between the UCL and the TRPL measurements.

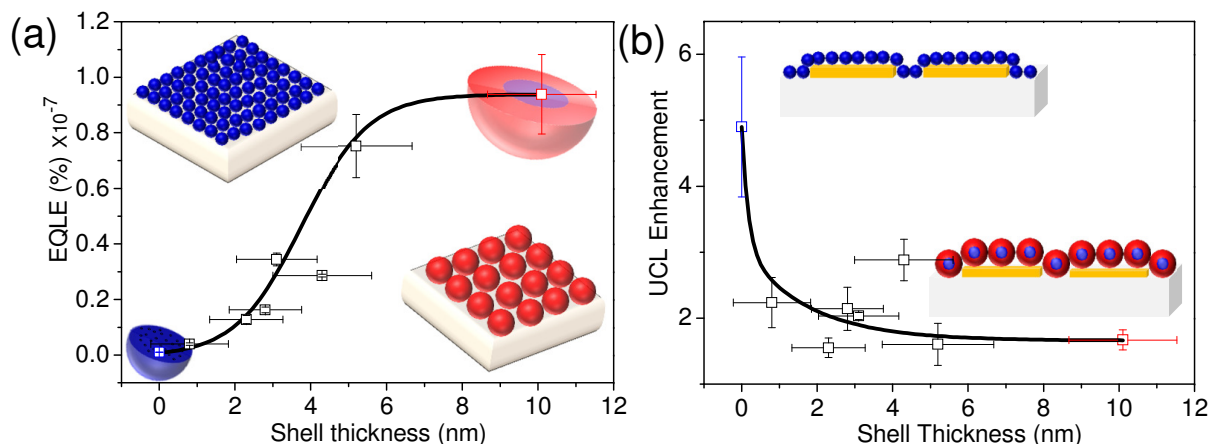


Figure 6.9: (a) A variation in the EQLE with the shell thickness in the UCNC monolayers. The blue spheres are the core-nanocrystals and the nanocrystals with the largest shell thickness (10.1 nm) around the core are represented by the red spheres. The schematics show their 2D-arrangement on quartz substrates. The colored data points are in agreement with the color of the schematic spheres whereas the black data points indicate the other core-shell UCNC monolayers. (b) shows a decreasing function of UCL-enhancement caused by the buried Au-nanodiscs with the shell thickness. The schematic representations depict the buried-Au-nanodiscs in the core and the core with thickest shell UCNC monolayers. The color code is in agreement with (a). The black curves in both panels (a) and (b) are guides to the eyes. The figure is a modified version of the schematic used in the graphical abstract of Article 3.

The role of metallic nanoparticles as an UCL-enhancer is determined by depositing Au-nanodiscs either on top of or buried in the UCNC monolayers after being deposited on quartz. EBL was employed for designing such truncated cone-shaped Au-nanodiscs in $1 \times 1 \text{ mm}^2$ area of the substrate (either the monolayers or quartz). The Au-discs were fabricated in a way that the UCL measurements both in the presence and absence of Au-discs can be performed on one sample. The Au-discs were geometrically optimized to match the localized surface plasmon resonance (LSPR) of the discs to the excitation wavelength (1500 nm). The shape and height of the discs were kept constant and the diameter was varied to shift the LSPR peak position. Experimentally, we tuned the LSPR by trial and error, and verified afterwards by finite element numerical approach with the experimentally optimized diameter. The numerical approach solved the Maxwell's equations to find the electric field distribution around a single nanodisc. The fabrication of Au-discs on top of the UCNC monolayers proved the concept of designing at atomic-scale as well as paved a path for the Au-embedded multi-layered UCNCs for an efficient upconversion. The UCNC monolayers were chemically and thermally stabilized for the next stage Au-discs deposition. Despite the fabrication success, the luminescence of the monolayers diminished after the electron beam exposure during the EBL process, possibly due to defect creation for the non-radiative decays in the UCNCs. However, a possible replacement of EBL could be a non e-beam technique like nanoimprinting, for the Au-structures deposition. In that way the observed drop in the UCL could be recovered.

Fabrication of Au-nanodiscs on quartz and buried in UCNC monolayers afterwards could be another solution to deal with the detrimental effect of e-beam on the UCNCs while achieving the plasmonic enhancement. In order to test this we prepared UCNC monolayers covering different sized Au-discs to match the LSPR to the excitation wavelength. The transmittance and reflectance of all samples were scanned over a wavelength-range (400 nm to 2000 nm) and the calculated relative extinction cross-section (explained in Section 5.3.2) showed the LSPR peak position at 1500 nm which was in a good agreement with the numerically calculated value. A

cross-sectional schematic representation of the present samples can be observed in Figure 6.9(b). The UCL measurements were performed on the samples either exciting the UCNCs with the Au-region (called in the presence of Au-discs measurements) or exciting the UCNCs without Au-region (called in the absence of Au-discs measurements). The enhancement in the UCL was calculated by dividing the UCL yields of the UCNCs in the presence of Au-discs to the UCL yield in the absence of Au-discs. The observed UCL-enhancement is plotted with the shell thickness in Figure 6.9(b). We observe that an increase in the spacing between the Er^{3+} (present in the core) and the Au-discs by the NaLuF_4 shells, decrease the UCL-enhancement factor. This could be interpreted as a continuous drop in the Au-discs generated concentrated E-fields with the shell thickness for Er^{3+} emitter. In contrast, previously it has been reported [4, 5] that an increase in spacing (maintained by physical vapor deposited layers) between the both showed an increase in UCL-enhancement for first few nanometer distances (5 nm - 10 nm) due to the drop in non-radiative quenching and subsequent, decrease due to the field reduction. The shell as a spacer in the present experiment not only maintain the distance but passivates the surface of nanocrystals simultaneously. Therefore, in the first few nanometers spacing, a competition between the improvement in UCL-enhancement caused by the Au-discs and the improvement in the UCL of UCNC monolayers caused by the shell formation happens. The resultant of both produces the trend seen in Figure 6.9(b). The surface passivation by the shells dominates in our study, therefore, we only observe the continuous drop in the UCL-enhancement caused by the Au-discs. Therefore, we do not observe the aforementioned parabolic improvement in UCL-enhancement in our study. The UCL improvement achieved by the Au-nanodiscs in the core UCNC monolayers, $5\times$, is very small compared to the enhancement observed by the thickest shelled UCNCs, $100\times$. However, a path of possible implementation of both in solar-cell devices could be opened more efficiently if the Au-discs are replaced by specially designed Au-structures. Such structures should produce more UCL-enhancement compared to the enhancement (2-3 folds) achieved by the Au-discs.

All in all, an investigation between the UCL yield and the shell thickness of the nanocrystals in the monolayer configuration has been performed. We observed that the $\tau_{13/2}$ and the $\tau_{11/2}$ of Er^{3+} ions do not change in the transition from solution to monolayer configuration which eliminates the possibility of activation of non-radiative decays. The maximum UCL improvement, $\sim 100\times$, was observed with the shell of 10.1 nm thickness. Further UCL enhancement was achieved by the nearby placement of in-resonance Au-nanodiscs. By placing Au-discs on top of the UCNC monolayers, on the one hand, opened a possible fabrication of Au-embedded multi-layered UCNCs for the photo-current improvement in the PV devices. On the other hand, the possible UCL-enhancement by burying Au-discs in the UCNC monolayers were determined. From the present work, we prove the UCL-enhancement by two separate routes; a structural modification in the nanocrystals by the inert shell formation and a modification in the nearby environment by placing Au-nanodiscs in the close proximity of the nanocrystals. These strategies can further be used in the fabrication of upconversion-based solar cells.

6.6 A correlation between the luminescence of Er^{3+} ions present in TiO_2 and NaYF_4 films

In this section, I make a correlation between the luminescence of Er^{3+} ions present in the optimized film of $\text{Er}^{3+} : \text{TiO}_2$ and the optimized monolayer of $\text{Er}^{3+} : \text{NaYF}_4 - \text{NaLuF}_4$ UCNCs. The TiO_2 film deposited at 350 °C with 5.1 at% dopant concentration and the monolayer of UCNCs with the shell thickness of 10.1 nm with 20 at% dopant concentration were found most efficient, used in this comparison. The luminescence from both samples were measured under

similar measurement conditions and at same laser irradiance of $0.3\text{kW}/\text{cm}^2$. The obtained UCL-spectra of both samples are presented in Figure 6.10. From the figure, one can easily conclude that the Er^{3+} present in NaYF_4 are comparably more luminescent. However, the different dopant concentrations and different effective thicknesses of the materials forbid a candid comparison between both. Therefore, I have calculated the normalized UCL yields, UCL yield per Er^{3+} ion, for both systems and a candid comparison was made at the end.

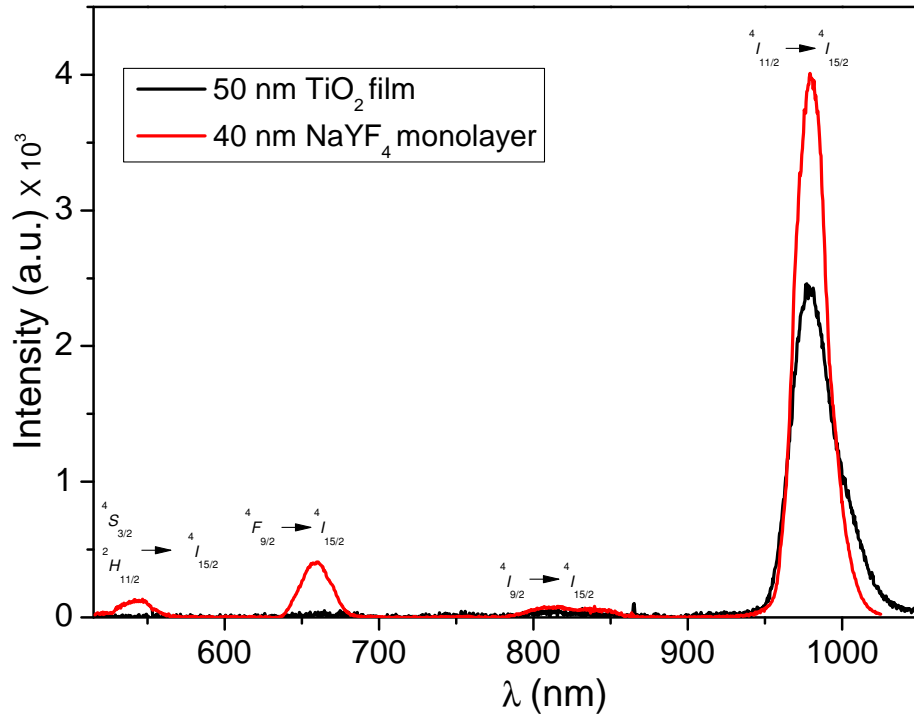


Figure 6.10: Upconversion luminescence of Er^{3+} -doped TiO_2 and NaLuF_4 films. The spectra show from five emission peaks originated from the transitions five excited energy levels to the ground-level (${}^4I_{15/2}$) of Er^{3+} ions, embedded in two different hosts.

6.6.1 Calculation of normalized UCL yield for Er^{3+} -doped TiO_2 film

The UCL yield (total area under the emission peaks) was calculated from the black curve of Figure 6.10. The obtained UCL yield value was 9.5×10^4 . The normalized UCL yield can be calculated as

$$\text{Norm.UCL} = \frac{UCL}{n \times A \times d} \quad (6.3)$$

where n is the ion density (cm^{-3}), A is the laser-beam area ($6.4 \times 10^{-5} \text{ cm}^2$), and d is the thickness of the film (50 nm). The n of (6.3) can be calculated as

$$n = \frac{N}{V(\text{cm}^3)} = \frac{\rho_{\text{TiO}_2}(\text{g}/\text{cm}^3)}{M_{\text{TiO}_2}} \quad (6.4)$$

where N is the number of Er^{3+} ions, V is the volume in cm^3 , ρ_{TiO_2} is the density of TiO_2 ($4.23 \text{ g}/\text{cm}^3$), and M_{TiO_2} is the mass of TiO_2 ($1.3 \times 10^{-22} \text{ g}$). After placing the value of n , A , and d

in (6.3), one can get the normalized UCL yield. The Norm. UCL yield of the optimized Er^{3+} (5.1 at%) : TiO_2 thin film was calculated to be 6.0×10^{-8} .

6.6.2 Calculation of normalized UCL yield for Er^{3+} -doped NaYF_4 monolayer

Similarly, the UCL yield of 40 nm Er^{3+} (20 at%) : NaYF_4 - NaLuF_4 core-shell UCNC monolayer was calculated from the red curve of Figure 6.10. The obtained UCL yield was 1.2×10^5 . The normalized UCL yield can be calculated as

$$\text{Norm.UCL} = \frac{UCL}{N_{tot}} \quad (6.5)$$

where N_{tot} is the total number of Er^{3+} ions present in the illuminated volume. That can be calculated as

$$N_{tot} = N_{UCNC} \times N_{ipn} \quad (6.6)$$

N_{UCNC} is the number of UCNCs and N_{ipn} is the number of ions present in one UCNC. N_{UCNC} can be calculated as

$$N_{UCNC} = \frac{A}{\pi r^2} \times PD \quad (6.7)$$

where r is the radius of the UCNC ($\sim 20 \times 10^{-7}$ cm), PD is the packing density of the UCNCs in 2-D array (~ 0.9), A is the area of the beam, and the area of the UCNC was calculated while considering as discs. N_{ipn} of (6.6) can be calculated as

$$N_{ipn} = n \times V_{UCNC} \quad (6.8)$$

n is the ionic density in the UCNC monolayer and V_{UCNC} is volume of the UCNC ($4/3\pi \times r^3$). n can be calculated as

$$n = \frac{N}{V(\text{cm}^3)} = \frac{\rho_{\text{NaYF}_4}(\text{g/cm}^3)}{M_{\text{NaYF}_4}} \quad (6.9)$$

where ρ_{NaYF_4} is the density of NaYF_4 (4.31 g/cm³ [41]), and M_{NaYF_4} is the mass of NaYF_4 material (3.38×10^{-22} g). Now introducing (6.6), (6.7), (6.8), and (6.9) into (6.5) will give us the desired Normalized UCL yield of the monolayer. The normalized UCL yield of Er^{3+} : $\text{NaYF}_4/\text{NaLuF}_4$ UCNC monolayer was calculated to be 3.2×10^{-7} .

It can be concluded that Er^{3+} ions present in NaYF_4 host are 5.3 times more luminescent than the ions present in TiO_2 host. It should be noted that the present comparison were made for the UCL yield obtained under highest-irradiance (i.e. 0.3kW/cm^2), which is a saturation regime for the Er^{3+} ions present in NaYF_4 , shown as red curve in Figure 2(a) of Article 3, compared to the ions of TiO_2 , shown as brown the curve in Figure 4(b) of Article 1. From Jeppe *et al.* [14], the UCL yield is a factor of ~ 2 (i.e. $100\times$) higher in the optimized Er^{3+} : NaYF_4 (i.e. UCNC with 10.1 nm shell) UCNC monolayer compared to the the Er^{3+} : TiO_2 film under lowest-irradiance (i.e. $1\text{-}2\text{W/cm}^2$). This implies that the Er^{3+} ions present in NaYF_4 system are much more efficient (i.e. $> (5\times)$). This indicates the possible applicability of $\text{Er}^{3+}:\text{NaYF}_4\text{-NaLuF}_4$ monolayers over the $\text{Er}^{3+}:\text{TiO}_2$ films in c-Si solar cells if the thick layers of the UCNCs can be developed efficiently.

Bibliography

- [1] A. E. Christensen, C. Uhrenfeldt, B. Julsgaard, P. Balling, and A. Nylandsted Larsen, Interaction between Au nanoparticles and Er^{3+} ions in a TiO_2 matrix: Upconversion of infrared light, *Energy Procedia* 2011, 10, 111.
- [2] S. Fischer, F. Hallermann, T. Eichelkraut, G. von Plessen, K. W. Kramer, D. Biner, H. Steinkemper, M. Hermle, and J. C. Goldschmidt, Plasmon enhanced upconversion luminescence near gold nanoparticles-simulation and analysis of the interactions: Errata, *Opt. Express* 2013, 21, 10606.
- [3] I. Zoric, M. Zach, B. Kasemo, and C. Langhammer, Gold, Platinum, and Aluminum Nanodisk Plasmons: Material Independence, Subradiance, and Damping Mechanisms, *ACS Nano* 2011, 5, 2535.
- [4] M. Saboktakin, X. Ye, S. J. Oh, S.-H. Hong, A. T. Fafarman, U. K. Chettiar, N. Engheta, C. B. Murray, and C. R. Kagan, Metal-Enhanced Upconversion Luminescence Tunable through Metal Nanoparticle-Nanophosphor Separation, *ACS Nano* 2012, 6(10), 8758.
- [5] A. L. Feng, M. Li You, L. Tian, S. Singamaneni, M. Liu, Z. Duan, T. J. Lu, F. Xu, and M. Lin, Distance-Dependent Plasmon-Enhanced Fluorescence of Upconversion Nanoparticles using Polyelectrolyte Multilayers as Tunable Spacers, *Sci. Rep.* 2015, 5, 7779.
- [6] A. Enesca, L. Andronic, A. Duta, and S. Manolache, Optical Properties and Chemical Stability of WO_3 and TiO_2 Thin Films Photocatalysts, *Romanian J. Info. Sci. and Tech.* 2007, 10(3), 269.
- [7] E. Shojaee, and M. R. Mohammadizadeh, First-principles elastic and thermal properties of TiO_2 : a phonon approach, *J. Phys.: Condens. Matter* 2010, 22, 015401.
- [8] L. Martinu and D. Poitras, Plasma deposition of optical films and coatings: A review, *J. Vac. Sci. Technol.* 2000, A(18), 2619.
- [9] D. Manova, L. F. Arias, A. Hofele, I. Alani, A. Kleiman, I. Asenova, U. Decker, A. Marquez, and S. Mändl, Nitrogen incorporation during PVD deposition of $\text{TiO}_2\text{:N}$ thin films, *Surf. and Coat.* 2017, 312, 61.
- [10] C. Chen, Y. Cheng, Q. Dai, and H. Song, Radio Frequency Magnetron Sputtering Deposition of TiO_2 Thin Films and Their Perovskite Solar Cell Applications, *Sci. Rep.* 2015, 5:17684, 1.
- [11] A. Gupta and A. D. Compaan, All-sputtered 14% CdS/CdTe thin-film solar cell with ZnO:Al transparent conducting oxide, *Appl. Phys. Lett.* 2004, 85(4), 684.
- [12] S. R. Johannsen, L. R. Lauridsen, B. Julsgaard, P. T. Neuvonen, S. K. Ram, and A. N. Larsen, Optimization of Er^{3+} -doped TiO_2 -thin films for infrared light up-conversion, *Thin Solid Films* 2014, 550, 499.
- [13] S. R. Johannsen, S. Roesgaard, B. Julsgaard, R. A. S. Ferreira, J. Chevallier, P. Balling, S. K. Ram, and A. N. Larsen, Influence of TiO_2 host crystallinity on Er^{3+} light emission, *Optic. Mat. Exp.* 2016, 6(5), 1664.
- [14] J. D. Christiansen, H. Lakhotiya, E. H. Eriksen, S. P. Madsen, P. Balling, and B. Julsgaard, in preparation.

- [15] S. Bansal, D. K. Pandya, and S. C. Kashyap, Electron transport and defect structure in highly conducting reactively sputtered ultrathin tin oxide films, *Appl. Phys. Lett.* 2014, 1045, 082108.
- [16] K Koski, J Hölsä, and P Juliet, Surface defects and arc generation in reactive magnetron sputtering of aluminium oxide thin films, *Surface and Coatings Tech.* 1999, 115, 163.
- [17] X. Pan, M.-Q. Yang, X. Fu, N. Zhang and Y.-J. Xu, Defective TiO₂ with oxygen vacancies; synthesis, properties and photocatalytic applications, *Nanoscale* 2013, 5, 3601.
- [18] M. Nakamura, S. Kato, T. Aoki, L. Sirghi, and Y. Hatanaka, Role of terminal OH groups on the electrical and hydrophilic properties of hydro-oxygenated amorphous TiO_x:OH thin films, *J. Appl. Phys.* 2001, 90(7), 3391.
- [19] H. H. Pham and L.-W. Wang, Oxygen vacancy and hole conduction in amorphous TiO₂, *Phys. Chem. Chem. Phys.* 2015, 17, 541.
- [20] W. Göpel, G. Rocker, and R. Feierabend, Intrinsic defects of TiO₂ (110): Interaction with chemisorbed O₂, H₂, CO, and CO₂, *Phys. Rev. B* 1983, 28, 3427.
- [21] U. Diebold, The surface science of titanium dioxide, *Surf. Sci. Rep* 2003, 48, 53.
- [22] M.S. Lazarus, and T. K. Sham, X-ray photoelectron spectroscopy (XPS) studies of hydrogen reduced rutile (TiO_{2-x}) surfaces, *Chem. Phys. Lett.* 1982, 92, 670.
- [23] Qian Zhong, John M. Vohs, and Dawn A. Bonnell, Local Structure of Defects on Hydrogen- and Vacuum-Reduced TiO₂ Surfaces, *J. Am. Ceram. Soc.* 1993, 76, 1137.
- [24] J.-M. Pan, B. L. Maschhoff, U. Diebold, and T. E. Madey, Interaction of water, oxygen, and hydrogen with TiO₂(110) surfaces having different defect densities, *J. Vac. Sci. Technol. A* 1992, 10(4), 2470.
- [25] F. Wang, D. Banerjee, Y. Liu, X. Chen, and X. Liu, Upconversion nanoparticles in biological labeling, imaging, and therapy, *Analyst* 2010, 135(8), 1839.
- [26] Y. Liu, D. Tu, H. Zhu, and X. Chen, Lanthanide-doped luminescent nanoprobe: controlled synthesis, optical spectroscopy, and bioapplications, *Chem. Soc. Rev.* 2013, 42(16), 6924.
- [27] X. Chen, W. Xu, H. Song, C. Chen, H. Xia, Y. Zhu, D. Zhou, S. Cui, Q. Dai, and J. Zhang, Highly Efficient LiYF₄:Yb³⁺,Er³⁺ Upconversion Single Crystal under Solar Cell Spectrum Excitation and Photovoltaic Application, *ACS Appl. Mat. & Inter.* 2016, 8(14), 9071.
- [28] J. Christoph Goldschmidt and S. Fischer, Upconversion for Photovoltaics -a Review of Materials, Devices and Concepts for Performance Enhancement, *Adv. Opt. Mater.* 2015, 3(4), 510.
- [29] H. Zhong, Z. Wang, W. Lu, J. Lui, and Y. wang, *Luminescent Materials for 3D Display Technology*, Springer Singapore 2016, 503.
- [30] J. Zhou, Q. Liu, W. Feng, Y. Sun, and F. Li, Upconversion Luminescent Materials: Advances and Applications, *Chem.Rev.* 2015, 115(1), 395.
- [31] E. Favilla, G. Cittadino, S. Veronesi, M. Tonelli, S. Fischer, J. Christoph Goldschmidt, A. Cassanho, and H. P. Jenssen, Comparative analysis of upconversion efficiencies in fluoride materials for photovoltaic application, *Sol. Energy Mater. Sol. Cells* 2016, 157, 415.

- [32] S. Fischer, E. Favilla, M. Tonelli, and J. Christoph Goldschmidt, Record efficient up-converter solar cell devices with optimized bifacial silicon solar cells and monocrystalline $\text{BaY}_2\text{F}_8:30\% \text{Er}^{3+}$ upconverter, *Sol. Energy Mater. Sol. Cells* 2015, 136, 127.
- [33] S. Dyøe Agger and J. Hedegaard Povlsen, Fiber optics and optical communications; Fiber characterization; Fiber optics amplifiers and oscillators; Lasers and laser optics; Lasers; Optical amplifiers, *Opt. Exp.* 2006, 14(1), 50.
- [34] D.-L. Zhang, W.-B. Sun, W.-H. Wong, and E. Yue-Bun Pun, Emission and absorption cross sections of $\text{Er}^{3+}:\text{LiNbO}_3$ crystal: composition effect, *Opt. Mater. Exp.* 2015, 5(9), 1920.
- [35] T. Rinkel, A. Naduviledathu Raj, S. Dühren, and M. Haase, Synthesis of 10 nm β - $\text{NaYF}_4:\text{Yb,Er}/\text{NaYF}_4$ Core/Shell Upconversion Nanocrystals with 5 nm Particle Cores, *Angew. Chem.* 2015, 55(3), 1164.
- [36] W. Park, D. Lu, and S. Ahn, Plasmon enhancement of luminescence upconversion, *Chem. Soc. Rev.* 2015, 44(10), 2940.
- [37] D. M. Wu, A. García-Etxarri, A. Salleo, and J. A. Dionne, Plasmon-Enhanced Upconversion, *J. Phys. Chem. Lett.* 2014, 5(22), 4020.
- [38] S. Fischer, J. K. Swabeck, and A. Paul Alivisatos, Controlled Isotropic and Anisotropic Shell Growth in β - NaLnF_4 Nanocrystals Induced by Precursor Injection Rate, *J. Am. Chem. Soc.* 2017, 139, 12325.
- [39] S. Fischer, N. D. Bronstein, J. K. Swabeck, E. M. Chan, and A. Paul Alivisatos, Precise Tuning of Surface Quenching for Luminescence Enhancement in Core-Shell Lanthanide-Doped Nanocrystals, *Nano Lett.* 2016, 16, 7241.
- [40] N. J. J. Johnson, A. Korinek, C. Dong, and F. C. J. M. van Veggel, Self-Focusing by Ostwald Ripening: A Strategy for Layer-by-Layer Epitaxial Growth on Upconverting Nanocrystals, *J. Am. Chem. Soc.* 2012, 134, 11068.
- [41] F. Zhang, R. Che, X. Li, C. Yao, J. Yang, D. Shen, P. Hu, W. Li, and D. Zhao, Direct Imaging the Upconversion Nanocrystal Core/Shell Structure at the Subnanometer Level: Shell Thickness Dependence in Upconverting Optical Properties, *Nano Lett.* 2012, 12(6), 2852.

Chapter 7

Summary and Future Perspective

7.1 Summary

The objective of this work was to optimize the materials and plasmonic structures for finding an efficient upconverter for the conversion of 1500 nm wavelength near infra-red (NIR) light to light which can be absorbed and contribute in photo-current enhancement in crystalline-silicon (c-Si) solar cells. The materials optimization involved the improvement in the fabrication parameters of the two hosts; TiO_2 and NaYF_4 , for the maximum upconversion in the optically active ions (Er^{3+}). The plasmonic structures optimization involves the geometric alteration and the appropriate arrangement within the upconverting films. In the work, Er^{3+} -doped TiO_2 and NaYF_4 films were fabricated by radio-frequency magnetron sputtering (RF-MS) and chemical synthesis-associated spin coating, respectively. The study on Er^{3+} -doped TiO_2 , on the one hand, was divided in three parts: the first study involved the geometric optimization of the Au-nanodiscs for an enhanced upconversion in the film where Au-discs were fabricated on the top of the film, the second study was focused on the enhancement caused by the Au-discs embedded in the upconversion layers, and the third study investigated the impact of the deposition- and annealing-temperatures on the luminescence of the upconverting films. On the other hand, the study on Er^{3+} -doped NaYF_4 consisted of the improvement in the UCL efficiency by changing the chemistry of the NaYF_4 nanocrystals and by altering their nearby environment via optimized Au-discs.

Er^{3+} -doped TiO_2 thin films were plasmonically enhanced by depositing the electron-beam lithographic designed Au-nanodiscs on top of the optimized films. The films were fabricated at 350 °C substrate temperature with 5.1 at% concentration of Er^{3+} ions. A finite element method (FEM), single-particle numerical approach were used to optimized the geometry of the Au-nanodiscs to enhanced the absorption via matching the localized surface plasmon resonance (LSPR) wavelength with the excitation wavelength (1500 nm). The report has revealed the feasibility of using single-particle simulations for explaining the main features of a multi-particle system. The experimental upconversion enhancement agreed qualitatively with the numerical model. A well explained reasoning is developed for the quantitative difference. The highest UCL enhancement of almost 7 times was found in the films with Au-discs of diameter 316 nm and a particle density 6000 per $100 \times 100 \mu\text{m}^2$. Using simple single-particle models, and understanding their limitations, is of importance in, e.g., future optimization steps for nanoparticle geometry or material composition, since fast computation is required for exploring large parameter spaces. Therefore, the present study opens an insight into numerically guided experimental investigations of the upconversion of 1500 nm light for its potential applicability in the photo-current enhancement of crystalline Si solar cells.

A further UCL-enhancement in the Er^{3+} -doped TiO_2 thin films were predicted by embedding the numerically guided Au-discs in the optimized upconverting layers. The FEM numerical approach predicted the near-field contribution in the UCL-enhancement, $\sim 1.9\times$, higher than the prediction made for the Au-discs on top of the films, $\sim 1.3\times$. Based on the motivation, numerically guided Au-discs for the LSPR at 1500 nm wavelength were embedded in between the optimized undoped- TiO_2 and Er^{3+} -doped TiO_2 thin films. However, the observed UCL of

the films (included top and bottom layers) were lower than the film of either one deposited on quartz. The deposition of the top Er^{3+} -doped TiO_2 thin film at elevated substrate temperature anneals the bottom Er^{3+} -doped TiO_2 thin film. There is a possibility of the adverse impact of the annealing temperatures on the optical activities of the films. The observed UCL-enhancement were found $\sim 3\times$ (possibly contributed from the near-field and scattering enhancements), lower than the $\sim 7\times$ for the system where the Au-discs were deposited on top of the films. Therefore, the experiment was unsuccessful in fabricating the Au-discs embedded in TiO_2 system, however, paved the path for the study of deposition and annealing temperatures on the sputtered oxides.

The effect of the deposition- and annealing-temperatures on the luminescence of the Er^{3+} -doped TiO_2 thin films were studied for the possible fabrication of Au-discs embedded TiO_2 system. We observed the highest-UCL yield for the film deposited at 350 °C substrate temperature before annealing. In general, post-annealing of deposited films reduced the UCL. The impact of the post-annealing was sensitive to the exposure of films to ambient air between the deposition and annealing processes. The annealing was found beneficial for the UCL-improvement in an only case, where films were deposited at lower-deposition temperature and unexposed to air between the processes. The multiplication of the measured decay times of the lowest excited states of Er^{3+} , ${}^4I_{13/2}$ and ${}^4I_{11/2}$, was in a good match with the UCL yields of the samples. In light of the structural similarities (i.e. atomic structure) among the samples, the UCL variation with the temperature was attributed to the activation and/or passivation of defects, originated during the sputtering. We experimentally proved the presence of the hydrogen in the deposited film and observed its variation with annealing temperatures. Presumably hydrogen affected the density of defects with annealing temperature. Therefore, the fabrication of Au-discs embedded TiO_2 system could be possible if the top Er^{3+} -doped TiO_2 thin film is deposited in hydrogen atmosphere.

An efficient UCL in Er^{3+} -doped NaYF_4 nanocrystals were ensured by passivating the defects present on the surface via optically inert shells of NaLuF_4 . The study involved a systematic variation in the UCL yield of the core-shell upconversion nanocrystals (UCNCs) with the shell thickness in their two-dimensional arrangements. The UCL yield of the UCNCs were observed as an increasing function of the shell thickness. Similar decay times ($\tau_{11/2}$ and $\tau_{13/2}$) of UCNCs in solution and monolayer configurations eliminated the possible activation of the non-radiative decay channels in the transition from colloidal solution to film configurations. The core-nanocrystals with a shell of 10.1 nm showed the maximum UCL yield, $\sim 100\times$ compared to the core-nanocrystals. A further enhancement in the UCL yield was ensured by the deposition of Au-discs either on top of or buried in the core-shell UCNC monolayers. The LSPR wavelength of the Au-discs were matched to the excitation wavelength for all samples to ensure efficient concentration of the light in Er^{3+} ions situated close to the discs. Similarly, the efficient radiative emission was ensured by finding the optimum distance between the discs and the Er^{3+} ions to eliminate the possibility of the non-radiative decays. The maximum UCL-enhancement factor, $5\times$, was observed for the core-UCNC monolayer and the factor decreased with the increase in the shell thickness in a buried-Au-discs configurations. By depositing Au-discs on top of the monolayers, we demonstrated good control of the fabrication process which can further be extended to Au-embedded multilayered systems. Overall, we proved the possible implementation of Au-discs-assisted UCNCs films in c-Si solar cells.

In a correlation of the optimized Er^{3+} -doped NaYF_4 UCNC (i.e. UCNC with the shell of 10.1 nm) monolayer to the optimized Er^{3+} -doped TiO_2 , the Er^{3+} ions present in NaYF_4 host are ~ 5 times more luminescent than the ions of TiO_2 under illumination of 0.3 kW/cm^2 . In addition, the decay times of two lowest-lying energy states (i.e. ${}^4I_{13/2}$ and ${}^4I_{11/2}$) of Er^{3+} ions present in the optimized NaYF_4 UCNC monolayer are 54 times and 45 times, respectively, higher than the decay times of the ions present in the optimized TiO_2 thin film.

7.2 Future perspective

After finishing my PhD, I am hired as a postdoc in the group to further work on solving all the remaining fabrication challenge of upconverting systems to achieve the final goal of fabricating upconversion-based solar cells. There are three task which I want to perform

7.2.1 Fabrication of Au-discs embedded multilayered Er^{3+} -doped TiO_2 system

The unpublished work of this thesis were unsuccessful due to the optical inactivation of the bottom Er^{3+} -doped TiO_2 film induced by the post-annealing occurred in the top-layer deposition process. From Article 2, we concluded that the deposition of the top-layer of the Au-embedded multilayered TiO_2 system in hydrogen-plasma could possibly retain the UCL yield of the bottom-layer. Therefore, in the near future, I will be working on the fabrication of the top-layer in hydrogen atmosphere. The work will include the optimization of H-plasma to successfully passivate the O-vacancies of the deposited films. The in-house unavailability of H-plasma in the RF-MS will be a challenge in this direction. The possible solution could be a collaboration with a group who has the particular facility.

7.2.2 Chemically synthesized Au-nanorods for embedded Er^{3+} -doped NaYF_4 system

We observed that the role of Au-nanodiscs in the UCL-improvement of the core-shell UCNCs were not significant. The EBL-defined Au-discs are enhancing nearly 2-3 folds for all the core-shell UCNCs. Therefore, a replacement of the lithographic Au-nanodiscs by chemically synthesized Au-nanorods could be beneficial for a higher-UCL-enhancement factor. The work will be performed in collaboration with a group at the chemistry department at Aarhus University. As we studied in Chapter 3 the LSPR peak position of metal nanostructures can be tuned by geometric alteration of the structures. Previously Xu *et al.* [1] have shown the shift in the LSPR of Au-nanorods to NIR spectrum with the geometric alteration, synthesized by the seedless method. The seedless method couples the nucleation and growth in a single step leading the anisotropic growth at the beginning of the synthesis. It has been observed in the previous study [1] that an aspect ratio (AR) of ~ 10 could tune the LSPR to the 1500 nm wavelength. The presence of either dipole or multi-pole LSPRs in the extinction of high AR Au-nanorods is well-reported. Therefore, their directional arrangement on a solid surface is important in order to increase the amplitude of NIR-LSPR instead of the one at visible wavelength. An alignment of nanorods has recently been shown by Band *et al.* [2]. Therefore, in this work, the shrinkage plastic sheet will be used for the directional arrangement of the optimized nanorods. The sheet along with the randomly spin coated nanorods will be clamped in one direction and a heating step will result in shrinkage and will direct the nanorods in the direction perpendicular to the shrinkage path. Once the rods will be arranged, the chemically synthesized core-shell UCNCs will be spin coated with an appropriate concentration. The UCL-enhancement will be measured by comparing the UCL of the system with the reference sample (the sample of nanocrystals without Au-rods on the same substrate). Some initial experimental trial have already been performed; an alignment of lower AR nanowires on the shrinkage sheet, fabrication of the reference samples and their UCL measurements, and the chemical synthesis of nanorods with AR 3. I assume that this Au-rods embedded Er^{3+} -doped NaYF_4 system will be a better system for the upconversion-based c-Si solar cell due to the maximum accumulated field availability for the Er^{3+} ions.

7.2.3 Photo-current measurements in upconversion based-c-Si solar cells

The majority of the work performed in this PhD study was focused on fundamental research and therefore, the aim of my postdoc work would be on the application of the fabricated upconverting films in c-Si solar cells. In this work, I will emphasis mainly on the fabrication of the thick (~ 500 nm) core-shell UCNCs films. Accounting the fabrication challenges and the degree of UCL-improvement, the shell of ~ 5 nm thickness will be preferred for the film formation. As mentioned in Chapter 1 about the involvement of the industrial collaborators of the SUNTUNE project, will provide the bi-facial c-Si solar cells with the dimension of 5×5 cm² for testing purpose. The first stage of device fabrication will involve gluing of the ~ 500 nm upconverting film deposited on quartz to the solar cell. The photo-current enhancement will be measured after comparing with the reference solar cell (the cell without the upconverting film). The second stage fabrication will include the plasmonic structures either lithographic/nano-imprinted Au-structures or chemically synthesized Au-rods with a defined directionality. We might have possibility of implementation of the specially designed Au-structures for the UCL-enhancement [3], mentioned in Publication 7 in the List of Publication.

Bibliography

- [1] X. Xu, Y. Zhao, X. Xue, S. Huo, F. Chen, G. Zou, and X.-J. Liang, Seedless synthesis of high aspect ratio gold nanorods with high yield, *J. Mater. Chem. A* 2014, 2, 3528.
- [2] J. Bang, J. Choi, F. Xia, S. S. Kwon, A. Ashraf, W. Park, and S. W. Nam, Assembly and Densification of Nanowire Arrays via Shrinkage, *Nano Lett.* 2014, 14, 3304.
- [3] P. Balling, J. Christiansen, R. E. Christiansen, E. Eriksen, H. Lakhotiya, M. Mirsafaei, S. H. Møller, A. Nazir, J. Vester Petersen, B. R. Jeppesen, P. B. Jensen, J. L. Hansen, S. K. Ram, O. Sigmund, M. Madsen, S. P. Madsen, and B. Julsgaard, Improving the efficiency of solar cells by upconverting sunlight using field enhancement from optimized nano structures, *Opt. Mater.* 2018, 83, 279.

Chapter 8

Contributions to co-author articles

8.1 Introduction

In this chapter I will briefly summarize the co-author articles related to this thesis. In addition, I will detail about my contributions in each and every articles.

8.2 Summary of Article 4

In this work, I prepared Er^{3+} -doped TiO_2 and NaYF_4 thin films. The TiO_2 films were prepared at two different substrate temperatures; 250 °C and 350 °C. Likewise, the core and core with the shell of 10.1 nm NaYF_4 nanocrystals were prepared for the present work. I have also contributed in the upconversion luminescence (UCL) measurements. I have participated in making the final version of the article.

The UCL efficiency of Er^{3+} -doped TiO_2 and NaYF_4 thin films can be increased if the dynamics in the upconversion process is well learned. In general, a complex interplay of radiative-, non-radiative transitions, energy transfer, and cross relaxation processes determines the upconversion efficiency. To investigate the dynamics in the upconversion processes we proposed a simple rate-equation model including the four lowest energy levels of Er^{3+} ions: ${}^4I_{15/2}$, ${}^4I_{13/2}$, ${}^4I_{11/2}$, and ${}^4I_{9/2}$. The model can be solved analytically to provide a measure of the UCL yield in terms of rate-equation parameters unlike previously reported models. The analytical result were compared to the measured UCL yield and decay times of the excited states (${}^4I_{13/2}$, ${}^4I_{11/2}$) for Er^{3+} -doped TiO_2 films of different UCL yields, presented in Article 2 of this thesis, and a good agreement was found over several orders of magnitude.

Moreover, we studied the saturation of the UCL by accounting for the experimental detection and hereby obtained saturation curve. It is well known that the upconversion scales non-linearly with intensity. In the extreme low excitation regime the UCL scales with the number of photons involved (two in this case) but this behavior will of course saturate as the intensity is increased. From the saturation curve we are able study rate-equation parameters among other the absorption cross section for the transition of ${}^4I_{15/2} \rightarrow {}^4I_{13/2}$ which so far has been in-accessible due to the extreme low value and the thin thickness of the investigated samples.

8.3 Summary of Article 5

I prepared Er^{3+} -doped TiO_2 thin films for the present work. In addition, I performed the extinction and steady-state upconversion luminescence measurements of the samples used in the article. I have participated in making the final version of the article

The plasmon enhanced upconversion in the optimized $\text{Er}^{3+}:\text{TiO}_2$ thin films was performed with the different geometries of Au-structures while considering the influence of scattering on the enhancement. The work is divided into two parts. In the first part of the work, different thickness of Er^{3+} -doped TiO_2 thin films were investigated for the efficient light-trapping. It was predicted that the thickness of the films sinusoidally varies the amount of light being trapped in the film. The maximum UCL per unit thickness was achieved for the ~ 300 nm thin films due to the significant contribution was from the scattering of the incoming light into the film. In the second part of the work, a coupling of the optically active ions with plasmonic structures was performed by depositing Au-structures on top of the 300 nm thin films. Few structures were designed to aim for efficient scattering and other were superior in near-field enhancement. The films with Au-discs and -squares deposited on top were more luminescent compared to the films with Au-circular rings, -square rings, and -cross-nanorods, designed for the near-field coupling. This concluded the dominance of the scattering over the near-field contributions of Au-structures in the UCL-enhancements.

8.4 Summary of Article 6

I prepared Er^{3+} -doped TiO_2 thin films for the present work. In addition, I performed the extinction measurements of the samples used in the article. I have participated in making the final version of the article

In Article 1, we have employed the single-particle model in explaining the multi-particle experiment. A qualitative agreement between the both were significant but failed to explain the peak splitting possibly due to the particle-particle interaction observed in the samples, shown in Figure 3 of Article 1. With this motivation, a two-particle model is developed to assess the experimentally observed inter-particle interaction in a randomly distributed Au-nanodiscs deposited on Er^{3+} -doped TiO_2 thin films. The proposed model was able to predict numerically the peak-splitting that was observed experimentally. It was found that the coupling is dominated by the far-field and strongly depend upon the dielectric medium.

8.5 Summary of Article 7

In this review article, I mainly contributed in the fabrication of $\text{Er}^{3+}:\text{NaYF}_4\text{-NaLuF}_4$ core-shell nanocrystals and in fabrication of their monolayers on quartz. In the article-writing process, I have written the Section 2.1 of the article including Figure 1 and 2. I have participated in making the final version of the article.

The review article gives a brief introduction about the ongoing activities aimed to enhance the upconversion processes by employing various geometries of plasmonic nanostructures of SUNTUNE project, on which my PhD thesis is based on. Numerically, we involved the finite element method numerical approach in optimizing plasmonic near-field via simple geometries of Au nanostructures as well as via the geometries optimized topologically [1]. Experimentally, the upconversion enhancement was achieved by depositing Au-nanostructures by electron beam lithography on top of the optimized Er^{3+} -doped TiO_2 and NaYF_4 thin films. In addition, the article discuss about the experimental measurements of predicted near-field enhancement using a technique of near-field-enhanced ablation by ultrashort laser pluses [2].

Bibliography

- [1] J. Vester-Petersen, S. P. Madsen, O. Sigmund, P. Balling, B. Julsgaard, and R. E. Christiansen, Field-enhancing photonic devices utilizing waveguide coupling and plasmonics - a selection rule for optimization-based design, *Opt. Exp.* 2018, 26(18), A788.
- [2] S. H. Møller J. Vester-Petersen A. Nazir E. H. Eriksen B. Julsgaard S. P. Madsen, P. Balling, Near-field marking of gold nanostars by ultrashort pulsed laser irradiation: experiment and simulations, *Appl. Phys. A*, 2018, 124:210, 1.

Article 1

Plasmonically enhanced upconversion of 1500 nm light via trivalent Er in a TiO₂ matrix

Harish Lakhotiya, Adnan Nazir, Søren P. Madsen, Jeppe Christiansen, Emil Eriksen, Joakim Vester-Petersen, Sabrina R. Johannsen, Bjarke Rolighed Jeppesen, Peter Balling, Arne Nylandsted Larsen, and Brian Julsgaard

Citation: *Appl. Phys. Lett.* **109**, 263102 (2016); doi: 10.1063/1.4972785

View online: <http://dx.doi.org/10.1063/1.4972785>

View Table of Contents: <http://aip.scitation.org/toc/apl/109/26>

Published by the [American Institute of Physics](#)

Plasmonically enhanced upconversion of 1500 nm light via trivalent Er in a TiO₂ matrix

Harish Lakhotiya,¹ Adnan Nazir,¹ Søren P. Madsen,² Jeppe Christiansen,¹ Emil Eriksen,¹ Joakim Vester-Petersen,² Sabrina R. Johannsen,³ Bjarke Rolighed Jeppesen,³ Peter Balling,^{1,3} Arne Nylandsted Larsen,^{1,3} and Brian Julsgaard^{1,3,a)}

¹Department of Physics and Astronomy, Aarhus University, Ny Munkegade 120, DK-8000 Aarhus C, Denmark

²Department of Engineering, Aarhus University, Inge Lehmanns Gade 10, DK-8000 Aarhus C, Denmark

³Interdisciplinary Nanoscience Center (iNANO), Aarhus University, Gustav Wieds Vej 14, DK-8000 Aarhus C, Denmark

(Received 31 October 2016; accepted 8 December 2016; published online 27 December 2016)

In this letter, we present a comparative experimental–simulation study of Au-nanodisc-enhanced upconversion of 1500 nm light in an Er³⁺ doped TiO₂ thin film. The geometry of the Au nanodiscs was guided by finite-element simulations based on a single nanodisc in a finite computational domain and controlled experimentally using electron-beam lithography. The surface-plasmon resonances (SPRs) exhibited a well-known spectral red shift with increasing diameter, well explained by the model. However, an experimentally observed double-peak SPR, which resulted from inter-particle interactions, was expectedly not captured by the single-particle model. At resonance, the model predicted a local-field enhancement of the upconversion yield, and experimentally, the luminescence measurements showed such enhancement up to nearly 7 fold from a nanodisc with 315 nm diameter and 50 nm height. The upconversion enhancement agreed qualitatively with the theoretical predictions, however with 3–5 times higher enhancement, which was attributed to scattered light from neighboring particles. *Published by AIP Publishing.* [<http://dx.doi.org/10.1063/1.4972785>]

Upconversion is a non-linear optical process where low-energy photons are converted into high-energy photons by sequential absorption in an appropriate host.^{1,2} Er³⁺ ions have conveniently spaced energy levels of partially filled 4f electronic shells that make them an ideal material for upconversion. Since a decade, the research in this field is commendable and significant upconversion of light at wavelengths of 1500 nm,^{3–8} 980 nm,^{9–13} and 808 nm^{14–17} was demonstrated. The absorption of two photons at ~1500 nm wavelength, corresponding to the ⁴I_{15/2} to ⁴I_{13/2} transition in the trivalent Er ion, leads to emission of a 980 nm photon at the ⁴I_{11/2} to ⁴I_{15/2} transition.¹⁸ From an application point of view, in crystalline silicon (c-Si) solar cells, an absorption of 1500 nm wavelength light is not possible because its corresponding energy is below the band gap of the c-Si. Therefore, the upconversion into 980 nm wavelength allows absorption in c-Si and potentially a higher photo-current. However, a small absorption cross section of Er³⁺ limits the efficiency of the upconversion process for solar radiation.

It was reported that upconversion can be enhanced by placing metal nanostructures close to Er³⁺ emitters.^{19–22} The metal nanostructures work as light concentrators which compensate the small absorption cross section of Er³⁺ ions. A careful design of metallic structures is a pre-requisite for an efficient upconversion enhancement at a desired wavelength. By tailoring dimensions,²³ shape,²⁴ and dielectric constant²⁵ of the metal nanostructures, the plasmon frequency can be tuned. At this frequency, the localized free electrons of the metal oscillate at resonance with the incident light, which among other things results in local-field enhancement.^{26,27}

Such local-field (plasmonic) enhancement was reported earlier in upconversion of 980 nm^{28,29} and 808 nm^{19,30} light. Plasmon enhanced upconversion of the important 1500-nm transition in Er³⁺ was explored experimentally by Christensen *et al.*²⁰ and numerically by Goldschmidt *et al.*^{31,32} The experiment showed a 27-fold enhanced upconversion of 1550 nm light using thin film-embedded self-assembled gold nanostructures without any numerically guided optimization.²⁰ The simulation studies used spherical gold nanoparticles of 200 nm diameter and showed the necessity of a complex model to evaluate the localized field intensity.^{31,32} High ohmic losses within the metallic nanostructures with such a large diameter lead to low enhancement factors and thus complicate the experimental observations. However, the importance of the 1500-nm region means that it is valuable to undertake an in-depth and well-controlled investigation of the possibilities of plasmonically enhanced upconversion, guided by numerical modeling.

This letter involves a comparison between a simple single-nanoparticle numerical model and results from multi-particle experiments of plasmon-enhanced upconversion of 1500 nm light in Er³⁺-doped TiO₂ thin films. The local electric-field enhancement was achieved experimentally by realizing electron-beam-lithography (EBL) defined random arrays of Au nanodiscs and by matching of their surface-plasmon resonance (SPR) with the ⁴I_{15/2} to ⁴I_{13/2} transition in Er³⁺. Random arrays were chosen in order to reduce interference effects from neighboring nanoparticles and hence to emphasize the pure SPR-related effects. The single-particle model was chosen for its simplicity and the experiments showed a good qualitative agreement between measured and simulated upconversion enhancements over a range of nanodisc diameters from 150 nm to 600 nm. The model predictions

^{a)}Electronic mail: brianj@phys.au.dk

were also used to design the geometric parameters of the Au nanodiscs used in the experiments.

100 nm thick Er^{3+} -doped TiO_2 films were fabricated by radio-frequency magnetron-sputtering on fused quartz substrates. During sputtering, the substrate temperature was 355°C with 100 W RF power and 0.4 Pa gaseous environment (2% O_2 in Ar atmosphere) inside the chamber. The sputtering target contained 5.1 at. % Er^{3+} in TiO_2 . The EBL-defined Au discs were fabricated in $2 \times 2 \text{ mm}^2$ regions on top of the TiO_2 film such that both measurements with and without Au structures could be performed on one sample in order to reduce the sensitivity to variation in sample fabrication. An overview of the sample geometries is shown in Fig. 1. Three sets of samples with different particle densities (PDs) have been fabricated as exemplified in Fig. 1. The random spatial distribution and the high degree of homogeneity in shape and size of the realized Au discs are evident from these images. The three sets are named S4k, S6k, and S8k, corresponding to, respectively, a particle density of 4000, 6000, and 8000 per unit $100 \times 100 \mu\text{m}^2$ area. Each set then consists of samples with varying disk diameter D , and each sample is named corresponding to the PD and D . For example, a sample with $D = 315 \text{ nm}$ diameter and $\text{PD} = 6000$ per unit $100 \times 100 \mu\text{m}^2$ area will be denoted as sample S6k-D315. All samples were fabricated with $H = 50 \text{ nm}$.

With the aim of interpreting the real multi-particle experiments by single-nanoparticle simulations, a simple model considering one particle in a computational box, with a $2 \times 2 \mu\text{m}^2$ cross section along the sample surface and a $4.1 \mu\text{m}$ long region perpendicular to the quartz/ TiO_2 : Er^{3+} /air layers, was employed. Using the finite element method, the model computed the electric field distribution around a single

particle induced by an incoming plane wave normal to the sample surface. The outer boundaries of the computational domain were passivated using perfectly matched layers,³³ and a range of wavelengths, diameters, and heights could be investigated. The domain size was chosen such as to include the electric near-field of the nanoparticle and also to include at least one wavelength of the electromagnetic field. In the numerical calculation, the tabulated refractive indices of Au³⁴ and quartz³⁵ were used whereas the refractive index of Er^{3+} -doped TiO_2 was measured by ellipsometry. The simulation used the truncated nano-cone as a shape for the Au structures with the bottom to top radius ratio of 1.1 in accordance with the experimentally realized shapes as exemplified by the transmission electron microscopy (TEM) image in Fig. 1.

As will be explained later in Fig. 4, the upconversion luminescence (UCL) intensity, I_{UC} , is related in a good approximation to the incoming pump intensity, I_{in} , by a simple scaling law, $I_{\text{UC}} \propto I_{\text{in}}^m$,¹⁴ over a wide range of intensities. For this reason, we conveniently define the simulated UCL enhancement factor as

$$L^{(m)} = \frac{\int_{V_{\text{UC}}} E^{2m} dV}{\int_{V_{\text{UC}}} E_0^{2m} dV}, \quad (1)$$

where V_{UC} represents the volume of the upconverting layer, E and E_0 are the electric field amplitudes inside the film with and without nanodiscs, respectively, and $m = 1.5$ is inherited from the experiment.

In an initial simulation run, the diameter and height of the nanodiscs were varied from 200 nm to 600 nm and 10 nm to 100 nm, respectively, while the wavelength was fixed at 1500 nm. The simulated values of $L^{(1.5)}$ are plotted in Fig. 2(a), and even though the largest UCL enhancement is expected for the smallest heights, our choice of 50 nm is convenient for minimizing the sensitivity to potential height variations in Au nanodiscs. The experimentally determined diameters of all samples range from 147 to 545 nm and thus allow for verifying the theoretical predictions across the relevant range. The field distribution around a nanodisc with $H = 50 \text{ nm}$ and $D = 315 \text{ nm}$, corresponding to a high value of $L^{(1.5)}$, is shown in Fig. 2(b).

In order to establish experimentally the dependence of the SPR on the nanodisc diameter, the extinction cross section, $\sigma_E = (1 - T_D - R_D)/\text{PD}$, was determined by measuring the wavelength-dependent direct transmittance, T_D , and direct reflectance, R_D , using a Perkin Elmer Lambda 1050 spectrophotometer. Figure 3(a) exemplifies the extinction cross sections, normalized to disc area (σ_E/A), as a function of the photon energy (E) and corresponding wavelength (hc/E). In each set, S4k, S6k, and, S8k, the sample with an achieved SPR closest to 1500 nm is presented. The data were smoothed by the Percentile and Savitzky Golay filters to reduce the noise. The experimental findings can be compared to numerical predictions, which are calculated by summing the simulated absorption and scattering cross sections. The absorption is calculated by ohmic heating within the metal nanodisc while the scattering is obtained by integrating the scattered power through a closed surface around the

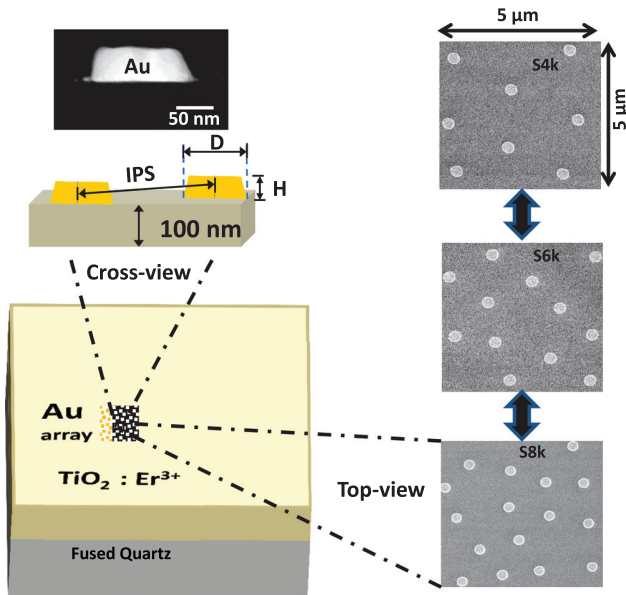


FIG. 1. A combination of schematic and experimental realization of the fabricated samples. The top-view SEM images exemplify the three sets of samples with different particle densities. The cross-view images depict the 100 nm thickness of the Er^{3+} -doped TiO_2 thin film and the variable parameters of the nanodiscs: diameter (D), height (H), and inter-particle spacing (IPS). On top, a transmission electron microscopy (TEM) image of a Au nanodisc with height 50 nm and diameter 147 nm exemplifies the realized structures.

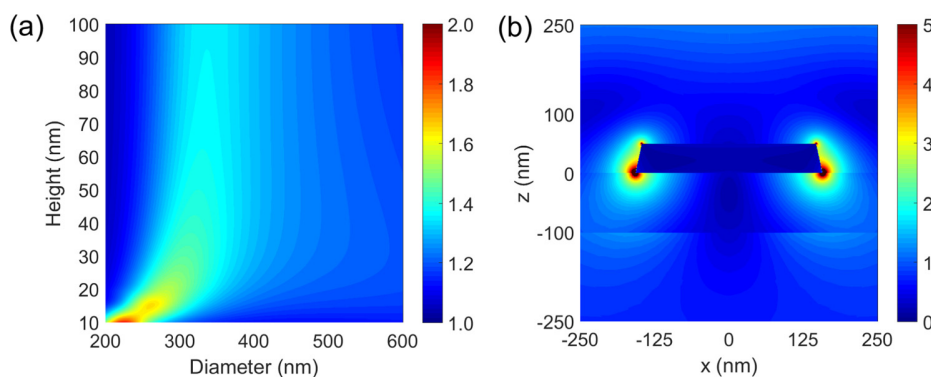


FIG. 2. (a) The UCL enhancement $L^{(1.5)}$ as a function of Au nanodisc diameter and height. (b) The distribution of the electric field amplitude around a Au nanodisc with $H = 50$ nm and $D = 315$ nm. The field amplitude is normalized to that of the incoming plane wave. In both panels, a wavelength of 1500 nm is used.

nanodisc. Both the experimental and simulation data show several orders of SPR peaks where the second order SPRs are in the visible range and the desired first order peaks are in the near infra-red (NIR) spectral range. The simulation shows the SPR peak position at 1500 nm wavelength for the sample with $D = 315$ nm, which is displayed in Fig. 3(a) for comparison. Most interestingly, the single-nanoparticle numerical prediction matches the experimental data of each set well in terms of both shape and amplitude. One important difference, however, materializes as the existence of a double-peak in the NIR region at $E = 0.72$ eV and 1.05 eV for the S6k-D315 sample and at $E = 0.82$ eV and 1.10 eV for the S8k-D270 sample. The appearance and disappearance of this double-peak system as a function of the nanodisc diameter are more evident in Fig. 3(b), which depicts a gradual

shift of the dominance from one peak to another by passing through the double-peak region.

Figure 3(c) shows the peak positions for all samples in comparison to the simulations, and we see a good agreement in the overall trend which exhibits the expected linearity between resonance energy and inverse radius.²³ This, together with the rough agreement shown in Fig. 3(a), validates largely the use of the single-particle model. The colored dashed circles in Fig. 3(c) indicate the regions of the double-peak system, which moves to larger emission wavelengths (smaller energies) for larger inter-particle spacings (IPSPs) (smaller PDs). This dependence indicates that the two-peak system originates from an inter-particle interaction phenomenon, which could be a result of collective oscillations of neighboring dipoles. Zoric *et al.*²³ have claimed the minimization of inter-particle

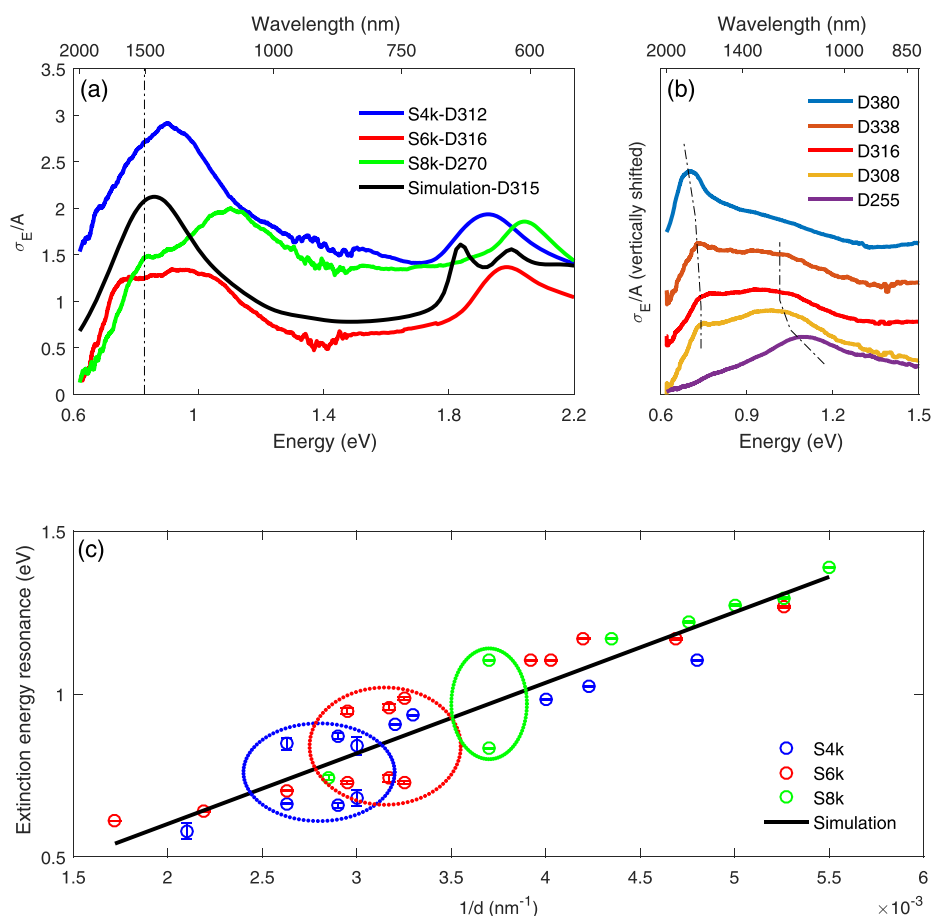


FIG. 3. (a) The experimental and simulated variation in extinction cross section per disc area with the emission energy and corresponding wavelength. The dashed line indicates the desired SPR peak position at 0.827 eV (1500 nm) resonant with the ${}^4I_{15/2} \rightarrow {}^4I_{13/2}$ transition in Er^{3+} . (b) The variation in SPR peak position with diameter for the set S6k is emphasized by the two dashed curves. (c) Scaling of the SPR energy with inverse nanodisc diameter. The discrete symbols correspond to experimental data points and the black solid line to the simulation. The dashed circles show the positions of the double-peak system in each set.

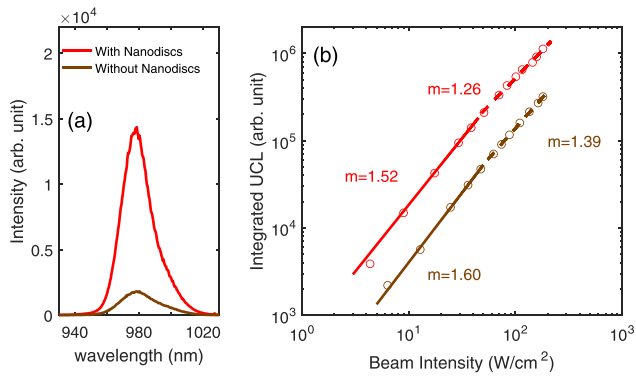


FIG. 4. (a) The spectrum of the UCL obtained from the sample Sk6-D315 with the spectral peak area enhanced by a factor of 6.7 ± 0.12 in the presence of nanodiscs. (b) Integrated UCL intensity as a function of pump intensity with and without nanodiscs for the same sample as in panel (a) [obtained outside the integrating sphere in order to increase the sensitivity]. The m -value is fitted in the high- and low-intensity regions in order to visualize its slight variation.

interactions in a random array of nanostructures by maintaining an IPS 6 times higher than the nanodisc diameter. In our samples, the characteristic IPS is equal to 1575, 1280, and 1112 nm for the sets S4k, S6k, and S8k, respectively, calculated as the mean IPS to the four nearest neighbors. For the samples with observed double peaks, the IPS/D ratio is found to be in the range ≈ 4 –5.

The upconversion luminescence (UCL) spectra were collected under illumination of a continuous 1503 nm wavelength (0.825 eV energy) single-mode laser delivering a power up to 22.9 mW. The setup consisted of a spectrometer coupled with a CCD array for capturing the emitted light. The samples were placed in an integrating sphere in order to prevent any impact from variations in the light-emission pattern. Figure 4(a) shows the spectrum of the upconverted light at 980 nm, and the UCL intensity is clearly enhanced in the presence of the Au nanodiscs, which do not introduce any significant changes to the UCL spectrum distribution. We define the UCL enhancement by the ratio of the two spectral peak areas as exemplified in Fig. 4(a). The power dependence of the UCL was measured to determine the value of m used in Eq. (1) and the result is shown in Fig. 4(b). In this double-logarithmic plot, the data follow essentially straight lines with minor curvature as indicated by the locally fitted slopes. Evidently, the choice of $m = 1.5$ represents reasonably the observed scaling as a whole. Turning toward the main scientific result of the present investigation—observing the impact of the metal nanodisc SPR on the enhancement and its comparison to simulations—we show in Fig. 5 the experimentally determined UCL enhancements for all samples under investigation. As main trends we observe: (i) an increasing UCL enhancement with nanodisc diameter until a peak or saturation point is reached around $D \approx 300$ nm and (ii) that larger PDs lead to larger UCL enhancement. In comparison, the calculated value of $L^{(1.5)}$ from Eq. (1) is also shown in Fig. 5, but we need to interpret it correctly for a fair comparison to the experimental data. For this reason, we define a scaled version of $L^{(1.5)}$ by

$$L_{\text{scaled}}^{(1.5)} = 1 + \alpha \cdot A_{\text{comp}} \cdot \text{PD} \cdot (L^{(1.5)} - 1), \quad (2)$$

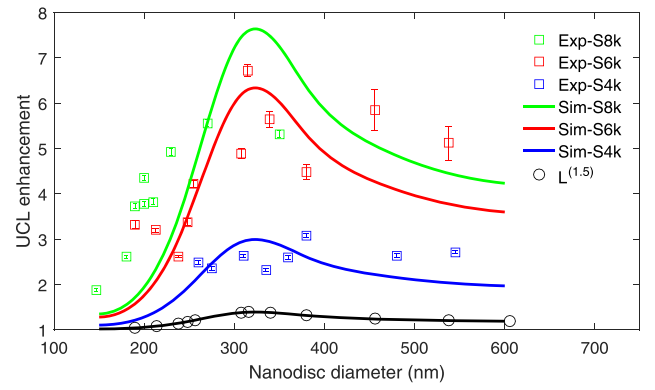


FIG. 5. The variation of the experimentally determined UCL enhancement with the nanodisc diameter is shown by the squares. The error bars correspond to the standard deviation of repeated measurements on the same sample location. The circles are numerical calculations of $L^{(1.5)}$, and the black curve is a spline interpolation to these. The blue, red, and green curves are scaled versions of the black curve according to Eq. (2), matched to the experimental data points.

where α is a free scaling parameter to be discussed below and $A_{\text{comp}} = 2 \times 2 \mu\text{m}^2$ is the cross sectional area of the upconverting film included in the computational box. The product $A_{\text{comp}} \cdot \text{PD}$ corresponds to the ratio of the sample area covered by the computation to the characteristic sample area per nanodisc and thus accounts for the pure particle-density effect indicated as observation (ii) above. The addition/subtraction of 1 ensures that only the effect of the nanodisc, and hence not the background UCL, is scaled. Now, if the single-particle model captured all the physics of the experiment, the prediction of Eq. (2) with $\alpha = 1$ should simply match the experimental data. However, this is not the case, which is the reason for including the α -parameter, and by a least-squares method we obtain the rough agreement shown in Fig. 5 with α in the range 3–5 for the three sets of samples. Note that the shape of $L_{\text{scaled}}^{(1.5)}$ captures in rough terms observation (i) above, and we attribute the fact that $\alpha > 1$ to multi-particle scattering and trapping of light within the upconverting film. Despite the fact that near-field enhancement and scattering originate from the same charge oscillations within the metal nanodiscs, these processes cannot be expected to scale in similar ways with nanodisc diameter, and hence the α -parameter must be considered as an ad-hoc extension to the single-particle prediction. With a view to the approximate agreement of experiment and simulation in Fig. 3, a better agreement than the one observed in Fig. 5 should not be expected. Using simple single-particle models, and understanding their limitations, is of importance in, e.g., future optimization steps for nanoparticle geometry or material composition, since fast computation is required for exploring large parameter spaces.

All in all, plasmonically enhanced UCL in Er^{3+} -doped TiO_2 thin films, targeted at the 1500 nm excitation wavelength, was demonstrated experimentally and verified in a reasonable approximation numerically. The report revealed the feasibility of using single-particle simulations for explaining the main features of a multi-particle system. The highest UCL enhancement of almost 7 times was found in the sample with diameter 316 nm and particle density 6000 per $100 \times 100 \mu\text{m}^2$. The role of inter-particle interactions

beyond the single-particle model was identified experimentally and understood qualitatively. Further model development is needed to obtain a better quantitative agreement with experimental findings.

The authors acknowledge the support from the Innovation Fund Denmark under the project “SunTune.”

- ¹F. Auzel, *Chem. Rev.* **104**, 139 (2004).
- ²G. H. Dieke and H. M. Crosswhite, *Appl. Opt.* **2**, 675 (1963).
- ³C. B. de Araújo, L. S. Menezes, G. S. Maciel, L. H. Acioli, A. S. L. Gomes, Y. Messaddeq, A. Florez, and M. A. Aegerter, *Appl. Phys. Lett.* **68**, 602 (1996).
- ⁴G. S. Maciel and C. B. de Araújo, *Phys. Rev. B* **55**, 6335 (1997).
- ⁵D. J. Simkin, J. A. Koningstein, P. Myslinski, S. A. Boothroyd, and J. Chrostowski, *J. Appl. Phys.* **73**, 8046 (1993).
- ⁶S. Fischer, J. C. Goldschmidt, P. Löper, G. H. Bauer, R. Brüggemann, K. Krämer, D. Biner, M. Hermle, and S. W. Glunz, *J. Appl. Phys.* **108**, 044912 (2010).
- ⁷R. Martín-Rodríguez, F. T. Rabouw, M. Trevisani, M. Bettinelli, and A. Meijerink, *Adv. Opt. Mater.* **3**, 558 (2015).
- ⁸D. Avram, B. Cojocaru, M. Florea, V. Teodorescu, and I. Tiseanu, *Opt. Mater. Express* **5**, 951 (2015).
- ⁹N. Menyuk, K. Dwight, and J. W. Pierce, *J. Appl. Phys.* **21**, 159 (1972).
- ¹⁰H. Guo, N. Dong, M. Yin, W. Zhang, L. Lou, and S. Xia, *J. Phys. Chem. B* **108**, 19205 (2004).
- ¹¹J. de Wild, J. K. Rath, A. Meijerink, W. G. J. H. M. van Sark, and R. E. I. Schropp, *Sol. Energy Mater. Sol. Cells* **94**, 2395 (2010).
- ¹²W. G. J. H. M. van Sark, J. de Wild, J. K. Rath, A. Meijerink, and R. E. I. Schropp, *Nanoscale Res. Lett.* **8**, 1 (2013).
- ¹³A. Prasad, C. S. Friend, R. Kapoor, and P. N. Prasad, *Chem. Mater.* **15**, 3650 (2003).
- ¹⁴M. Pollnau, D. R. Gamelin, S. R. Lüthi, and H. U. Güdel, *Phys. Rev. B* **61**, 3337 (2000).
- ¹⁵D. Wang, M. Yin, S. Xia, V. N. Makhov, N. M. Khaidukov, and J. C. Krupa, *J. Alloys Compd.* **368**, 337 (2004).
- ¹⁶L. Tian, Z. Xu, S. Zhao, Y. Cui, Z. Liang, J. Zhang, and X. Xu, *Materials* **7**, 7289 (2014).
- ¹⁷G. Yang, D. Yang, P. Yang, R. Lv, C. Li, C. Zhong, and F. He, *Chem. Mater.* **27**, 7957 (2015).
- ¹⁸P. Blixt, J. Nilsson, J. Carlnas, and B. Jaskorzynska, *IEEE Trans. Photonics Technol.* **3**, 996 (1991).
- ¹⁹S. R. Johannsen, S. P. Madsen, B. R. Jeppesen, J. V. Nygaard, B. Julsgaard, P. Balling, and A. Nylandsted Larsen, *Appl. Phys. Lett.* **106**, 053101 (2015).
- ²⁰A. E. Christensen, C. Uhrenfeldt, B. Julsgaard, P. Balling, and A. Nylandsted Larsen, *Energy Procedia* **10**, 111 (2011).
- ²¹H. Mertens and A. Polman, *Appl. Phys. Lett.* **89**, 211107 (2006).
- ²²H. P. Paudel, D. Dachhepati, K. Bayat, S. S. Mottaghian, P. S. May, C. Lin, S. Smith, and M. F. Baroughi, *J. Photonics Energy* **23**, 035598 (2013).
- ²³I. Zoric, M. Zach, B. Kasemo, and C. Langhammer, *ACS Nano* **5**, 2535 (2011).
- ²⁴A. Agrawal, I. Kriegel, and D. J. Milliron, *J. Phys. Chem. C* **119**, 6227 (2015).
- ²⁵C. Noguez, *J. Phys. Chem. C* **111**, 3806 (2007).
- ²⁶A. M. Michaels, M. Nirmal, and L. E. Brus, *J. Am. Chem. Soc.* **121**, 9932 (1999).
- ²⁷R. Esteban, M. Laroche, and J.-J. Greffet, *J. Appl. Phys.* **105**, 033107 (2009).
- ²⁸D. Lu, C. Mao, S. K. Cho, S. Ahn, and W. Park, *Sci. Rep.* **6**, 18894 (2016).
- ²⁹Y.-L. Wang, N. M. Estakhri, A. Johnson, H. Y. Li, L.-X. Xu, Z. Zhang, A. Alu, Q.-Q. Wang, and C.-K. Shih, *Sci. Rep.* **5**, 10196 (2015).
- ³⁰F. Ai, Q. Ju, X. Zhang, X. Chen, F. Wang, and G. Zhu, *Sci. Rep.* **5**, 10785 (2015).
- ³¹J. C. Goldschmidt, S. Fischer, H. Steinkemper, F. Hallermann, G. von Plessen, K. W. Krämer, D. Biner, and M. Hermle, *IEEE J. Photovoltaics* **2**, 134 (2012).
- ³²S. Fischer, F. Hallermann, T. Eichelkraut, G. von Plessen, K. W. Krämer, D. Biner, H. Steinkemper, M. Hermle, and J. C. Goldschmidt, *Opt. Express* **21**, 10606 (2013).
- ³³S. P. Madsen, S. R. Johannsen, B. R. Jeppesen, J. V. Nygaard, P. B. Jensen, J. Chevallier, B. Julsgaard, P. Balling, and A. Nylandsted Larsen, *Energy Procedia* **77**, 478 (2015).
- ³⁴P. B. Johnson and R. W. Christy, *Phys. Rev. B* **6**, 4370 (1972).
- ³⁵I. H. Malitson, *J. Opt. Soc. Am.* **55**, 1205 (1965).

Article 2

Upconversion luminescence from magnetron-sputtered Er^{3+} -doped TiO_2 films: Influence of deposition- and annealing temperatures and correlation to decay times

Harish Lakhotiya,¹ Jeppe Christiansen,¹ John Lundsgaard Hansen,^{1,2} Peter Balling,^{1,2} and Brian Julsgaard^{1,2, a)}

¹⁾*Department of Physics and Astronomy, Aarhus University, Ny Munkegade 120, DK-8000 Aarhus C, Denmark.*

²⁾*Interdisciplinary Nanoscience Center (iNANO), Aarhus University, Gustav Wieds Vej 14, DK-8000 Aarhus C, Denmark.*

(Dated: April 2018)

The optical properties of radio-frequency magnetron sputtered TiO_2 thin films doped with Er^{3+} are strongly influenced by the deposition and post-annealing temperatures. This has impact on applications of the material for upconversion, i.e. the merging of two low-energy photons to one photon of higher energy. Maximum upconversion luminescence (UCL) yield is obtained using a deposition temperature of 350 °C without post annealing. Motivated by the possibilities that become available by sequential depositions (several layers), the effect of post annealing is systematically investigated. In general, post-annealing treatments reduce the UCL; however, for the lowest deposition temperatures, post annealing has a positive impact on the UCL provided that the samples are not exposed to ambient air prior to the annealing step. These observations are further analyzed using time-resolved photoluminescence spectroscopy for determining the characteristic decay times of the Er^{3+} energy levels in the different samples. It is found that the UCL yield scales to a good approximation linearly with the product of the decay times of the two lowest-lying Er^{3+} excited energy levels ($^4I_{11/2}$ and $^4I_{13/2}$). The combined data provide strong evidence that the reduction in UCL is due to the opening of non-radiative decay channels from the Er^{3+} excited levels. Structural measurements show no change of the amorphous samples upon annealing, so these decay channels are most likely related to energy transfer between Er^{3+} and defect states in the TiO_2 bandgap. The non-radiative decay could possibly be related to the loss of hydrogen termination of dangling bonds or related to the oxygen vacancies in TiO_2 .

I. INTRODUCTION

As a simple, fast, and inexpensive method for synthesizing thin films on a large scale, radio-frequency-magnetron sputtering (RF-MS) presents a widely accepted tool for manufacturing solar cells and other photonic devices¹⁻⁴. Despite comparatively high deposition rates⁵, the synthesized films can be highly uniform and continuous, even below 10 nm in thickness, with ultra-low surface roughness^{6,7}. Fabrication of TiO_2 thin films via RF-MS is well-studied⁷. The wide band gap^{8,9}, low phonon energy¹⁰, and chemical stability¹¹ of TiO_2 makes it suitable for a process called upconversion, i.e. the conversion of two or more low-energy photons into one of higher energy¹². Specifically, erbium ions are useful for conversion of 1500 nm near-infrared (NIR) light to 980 nm NIR and to visible light when incorporated into an appropriate host¹³. The conversion in Er^{3+} ions involves an excitation of electrons from the $^4I_{15/2}$ level to the $^4I_{9/2}$ level by absorption of two photons and an emission of one photon on the $^4I_{11/2} \rightarrow ^4I_{15/2}$ transition¹⁴. Based on the above-mentioned properties, Er^{3+} -doped TiO_2 films have applications in photo-voltaic industries, and have recently been investigated for upconversion^{6,15}. The highest upconversion yield was previously achieved with films

deposited at elevated substrate temperatures (> 250 °C) with a particular dopant concentration (~ 5 at%)⁶. However, the small absorption cross section of Er ions and the non-linear nature of the upconversion process limit the upconversion efficiency, which is hence small under normal intensities from solar radiation. In previous work¹⁶, we have investigated plasmonic gold (Au) structures, in close vicinity of Er^{3+} emitters, as a possible method for enhancing the upconversion yield in Er^{3+} -doped TiO_2 films. For practical applications, however, a further improvement in upconversion is required, for instance by using multi-layers of plasmonically-enhanced upconverting layers. One route could be placing Au nanostructures within sputtered Er^{3+} -doped TiO_2 films, which could involve several fabrication steps at elevated temperatures. It is thus important to know the effect of temperature treatments on the upconversion properties of the deposited layers, which is the main focus of the present work.

Johannsen et al.^{6,15} have shown that the upconversion luminescence (UCL) of sputtered Er^{3+} -doped TiO_2 films is strongly linked to the substrate temperature during deposition and explained the UCL variation with the crystallinity of the films. However, such variations are seen even with amorphous films, which calls for further investigation of the issue. Despite the importance in UCL optimization, annealing of such deposited films in different atmospheres is poorly studied. Therefore an in-depth investigation of UCL dependency on deposition and on

^{a)}Electronic mail: brianj@phys.au.dk

annealing temperatures of the sputtered films will open a path for improved upconversion.

In this work, we study the influence of deposition and annealing temperatures on the optical properties of Er^{3+} -doped TiO_2 thin films synthesized by RF-MS. The report involves the fabrication of multiple sets of films at different deposition temperatures within the limits of the RF-MS equipment. Recent studies have shown the importance of the ambient gas in post-deposition treatments¹⁷, and therefore a set of films is subjected to annealing in an Ar/O_2 environment, with and without prior air exposure. The steady-state UCL from the transition ${}^4I_{11/2} \rightarrow {}^4I_{15/2}$ and time-resolved photoluminescence (PL) from the transitions ${}^4I_{13/2} \rightarrow {}^4I_{15/2}$ and ${}^4I_{11/2} \rightarrow {}^4I_{15/2}$ of all films are measured and analyzed. The impact of the temperature treatments on the atomic dynamics and in turn on the obtained UCL is determined.

II. EXPERIMENTAL APPROACH

Er^{3+} -doped TiO_2 thin films were fabricated on quartz and on Si with a native SiO_2 layer by a RF-MS system from AJA Orion ATC. The targets were commercially produced (Able Targets) by mixing powders of TiO_2 and Er_2O_3 to achieve 5.1 at% concentration of Er^{3+} ions. The fabrication chamber was held under 3 mTorr gaseous pressure of Ar with 2 % O_2 . The sputtering power was set to 100 W for a deposition rate of around 0.1 Å/s. Several sets of samples with 50 nm thickness were prepared at substrate temperatures ranging from 25 °C to 350 °C. After retaining one set of samples untreated, the remaining sets were exposed to 150 °C, 250 °C, or 350 °C annealing temperatures for a duration of 90 minutes (same as the deposition time). One set of films was annealed in an Ar/O_2 ambient within the fabrication chamber without being exposed to air, and another set was exposed to air (for one day or more) before being annealed in Ar/O_2 at 3 mTorr within the fabrication chamber. The thickness of the films was measured to be 50 ± 3 nm by ellipsometry using a Sentech SE850 PV Spectroscopic Ellipsometer. The surface roughness of the films, which was in range of 2–5 nm, was determined using a Bruker Edge atomic force microscope. X-ray diffraction (XRD) confirmed an amorphous nature of all as-deposited and annealed films using $\text{Cu K}\alpha$ radiation in a Rigaku instrument. Rutherford backscattering spectrometry was performed on several films to measure the concentration of Er^{3+} ions, which was 4.7 ± 0.3 at%.

For the optical investigations, the steady-state UCL spectra of the films were recorded under continuous-wave (CW) laser illumination at a wavelength of 1500 nm using a power of 18.9 mW, a beam area of 0.20 ± 0.02 mm², and a resultant intensity of 9.5 W/cm². This intensity corresponds to the partly saturated regime of upconversion, where the UCL scales approximately as $I^{1.5}$ (as previously reported¹⁶). The samples were placed inside an integrating sphere to ensure an identical collection effi-

ciency for all samples. The emitted light was captured by a Princeton Instruments spectrograph, consisting of an Acton SP2358 monochromator and a PIXIS:100BR CCD camera. The time-resolved PL measurements were performed using a 35 fs pulsed Ti:sapphire laser with a peak wavelength of 800 nm to populate the ${}^4I_{9/2}$ level of the Er^{3+} ions. These measurements were performed outside the integrating sphere using two identical Princeton Instruments monochromators with different detectors; one monochromator was equipped with a Hamamatsu R5509-73 photo-multiplier tube (PMT) for 1500 nm luminescence detection whereas the other was equipped with a Perkin Elmer avalanche photo diode (APD) single-photon counting module for 980 nm luminescence detection.

III. RESULTS

In order to ease a comparison between samples across the figures in this manuscript, a common color code is based on the deposition temperatures (see caption of Fig. 1). In addition, a set of symbols is introduced to distinguish between as-deposited samples, and samples post annealed at different temperatures (see the caption Fig. 2). Solid lines connecting filled symbols represent samples that were exposed to air before the annealing, while dashed lines connecting open symbols are chosen for samples that were kept unexposed to ambient air between treatments.

A. Steady-state UCL versus deposition and post-annealing temperatures

The inset of Fig. 1 shows schematically the mechanisms behind the UCL measurements. These involve the population of the first excited state (${}^4I_{13/2}$) via ground state absorption of laser light of 1500 nm wavelength. A further transition to the higher excited state (${}^4I_{9/2}$) involves either energy-transfer upconversion (ETU), excited-state absorption (ESA), or a combination of both. The de-excitations involve a fast non-radiative relaxation to ${}^4I_{11/2}$ followed by the emission of the UCL, with examples of spectra shown in the main part of Fig. 1. The shown spectra correspond to films deposited at different substrate temperatures without further annealing treatments. For deposition temperatures ≤ 150 °C, the UCL is undetectable, whereas a slight amount of UCL is observed for deposition at 200 °C. A further increase in temperature shows a drastic change in the observed signal and gives a maximum upconversion at a deposition temperature of 350 °C. Further increase in deposition temperature is not considered in this article; however, a complete absence of UCL was observed previously using a deposition temperature of 420 °C for a similar sample with 100 nm thickness at otherwise identical deposition conditions.

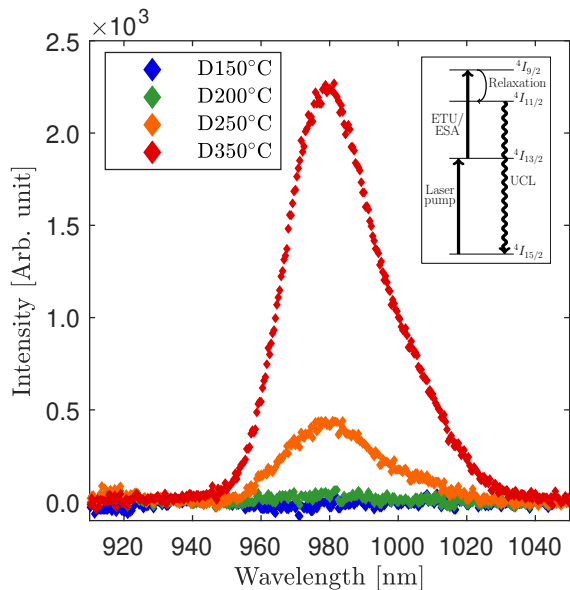


FIG. 1. Upconversion luminescence of the unannealed films for different deposition temperatures (Dxxx°C). The inset is a schematic representation of the excitation and luminescence transitions between the 4f-energy levels of Er^{3+} .

For each sample, the UCL yield is defined as the area under the UCL peak, exemplified in Fig. 1, and this yield is shown in Fig. 2 for all samples, with and without post-annealing treatment. It is evident from Fig. 2 that all films deposited at higher substrate temperatures exhibit a drop in UCL yield upon annealing, the drop becoming more pronounced with higher annealing temperatures. However, the drop also depends on whether the sample was exposed to ambient air before annealing. The 350 °C annealing temperature essentially eliminates the UCL of air-exposed films, while unexposed films deposited at 350 °C stay optically active, giving roughly 25 % of the UCL of the unannealed sample. However, all air-exposed films deposited at lower substrate temperatures (150 °C and 200 °C) do not show any significant change in the UCL signals of the films upon annealing. A set of unexposed samples, deposited at 150 °C temperature, shows an increased UCL trend with the higher annealing temperatures compared to its air exposed counterpart. This implies that air-exposed films become relatively poor UCL performers at any annealing temperature.

B. Time-resolved PL versus deposition and post-annealing temperatures

The decay curves of all as-deposited films are shown in Fig. 3. The figure shows the luminescence from the two different energy levels $^4I_{11/2}$ and $^4I_{13/2}$ to the ground state $^4I_{15/2}$ in two separate panels, after excitation by

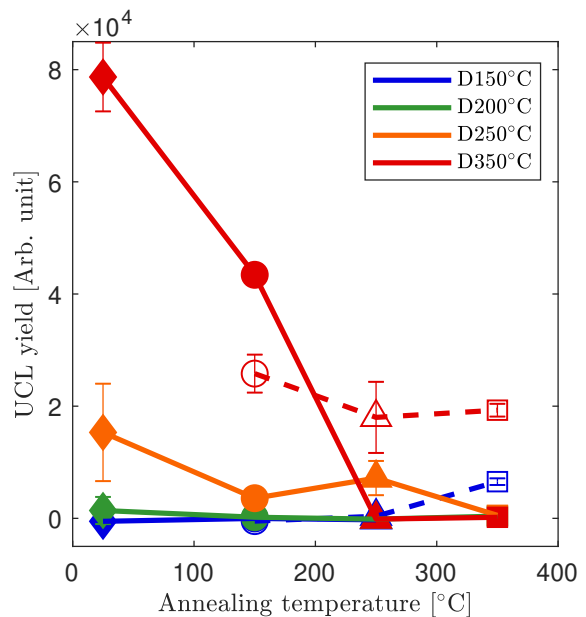


FIG. 2. Variation in upconversion luminescence yield with annealing temperature for films deposited at different deposition temperatures (Dxxx°C). The diamonds represent the unannealed samples whereas circles, triangles, and squares correspond to the samples annealed at temperatures 150 °C, 250 °C, and 350 °C, respectively. The solid and open symbols correspond to samples being exposed and unexposed to ambient air, respectively, before annealing.

an 800 nm laser pulse. The insets display the associated excitation and relaxation processes. The decay curves from the $^4I_{11/2}$ level, presented in Fig. 3(a), are well fitted with single-exponential decays following the formula $f(t) = A_{11/2} \exp(-t/\tau_{11/2})$, i.e. $\tau_{11/2}$ is the decay time of the measured luminescence curve from the $^4I_{11/2}$ level. In Fig. 3(b) the decay curves from the $^4I_{13/2}$ level are presented. Here the decay curves are more complex: The low-deposition-temperature samples show bi-exponential decays and are fitted to the model $g(t) = A_1 \exp(-t/\tau_1) + A_2 \exp(-t/\tau_2)$ whereas the high-deposition-temperature samples show single-exponential decays with an initial exponential rise factor. The latter are fitted to the model $h(t) = (1 - a_{\text{rise}} \exp(-t/\tau_{\text{rise}}))A \exp(-t/\tau_{13/2})$, where $\tau_{13/2}$ is the characteristic decay time of the luminescence from the $^4I_{13/2}$ level. The rise factor can be explained by the ions relaxing first from the $^4I_{9/2}$ to the $^4I_{13/2}$ level before any light can be detected, meaning that a delay must occur before significant luminescence is observed. For the bi-exponential decay curves, the existence of the two components could have its origin in the existence of two classes of ions being affected differently by the varying deposition temperature. Hence, the characteristic decay time is chosen as the weighted average, $\tau_{13/2} = (A_1\tau_1 + A_2\tau_2)/(A_1 + A_2)$. In any case, for both panels in Fig. 3 and no matter the underlying fitting model and interpretation, there is a clear common

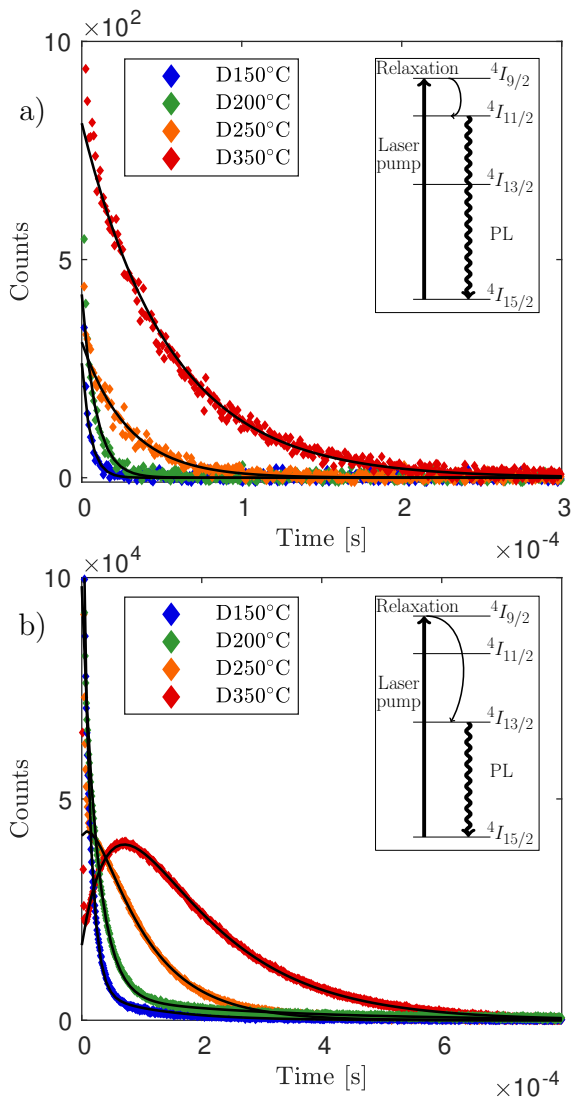


FIG. 3. Decay curves of all unannealed samples deposited at different deposition temperatures (Dxxx°C). Panels (a) and (b) show the decay curves from the ${}^4I_{11/2} \rightarrow {}^4I_{15/2}$ and ${}^4I_{13/2} \rightarrow {}^4I_{15/2}$ transitions, respectively. The insets of each panel give a schematic representation of the involved excitation and relaxation processes. The black curves in both panels represent the fitting models described in the text.

trend: When the deposition temperature is decreased from its optimum value of 350°C, both the characteristic decay times and the areas under the decay curves decrease. This is a clear indication that more non-radiative decay channels are opened up for the lower deposition temperatures. If, on the contrary, the faster decay had been caused by increased radiative decay rates, the observed luminescence would expectedly be more intense, i.e. present larger amplitudes of the decay curves and typically preserve the areas under the curves.

The above analysis is also carried out for the post-

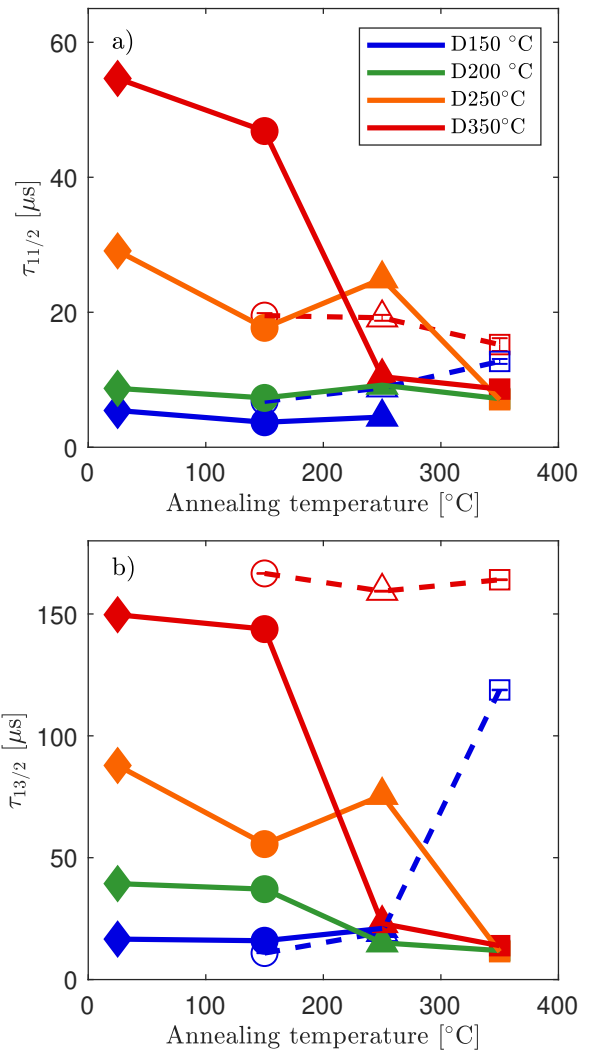


FIG. 4. Characteristic decay times for (a) the ${}^4I_{11/2} \rightarrow {}^4I_{15/2}$ and (b) the ${}^4I_{13/2} \rightarrow {}^4I_{15/2}$ transitions for various conditions of deposition (Dxxx°C) and annealing temperature and air exposure. The diamonds represent the unannealed samples whereas circles, triangles, and squares correspond to the samples annealed at temperatures 150 °C, 250 °C, and 350 °C, respectively.

annealed films and the characteristic decay times have been plotted in Fig. 4. In general, the trend is similar to the observations for the steady-state UCL yield in Fig. 2: A higher post-annealing temperature will in general decrease the decay times, but if unexposed to air, the post annealing may re-establish a longer decay time. It is interesting that the characteristic time $\tau_{13/2}$ corresponding to the lowest transition ${}^4I_{13/2} \rightarrow {}^4I_{15/2}$ is essentially cured to the best unannealed value (red solid diamond in Fig. 4(b)) of 150 μs for high-temperature annealing of the two unexposed samples (open red and blue squares in Fig. 4(b)). In comparison, the characteristic decay time $\tau_{11/2}$ for the ${}^4I_{11/2} \rightarrow {}^4I_{15/2}$ is much further from being

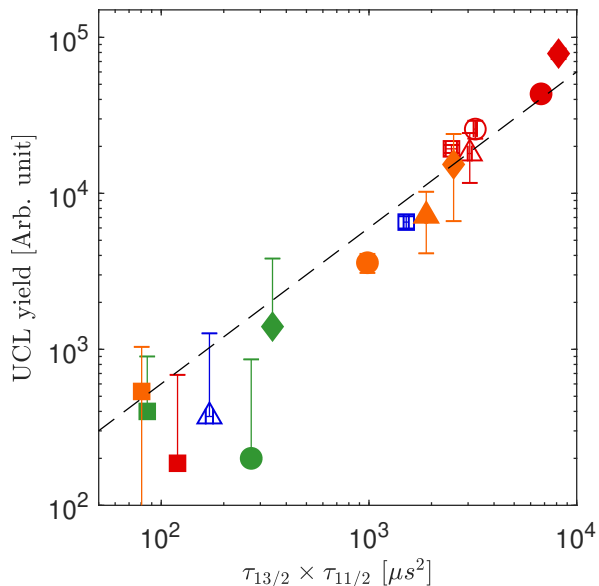


FIG. 5. The UCL yield as a function of the product of characteristic decay times $\tau_{11/2}$ and $\tau_{13/2}$, shown on a double-logarithmic scale. The color code and the symbols are identical to previous figures. The dashed line represents a proportional fit.

re-established at the largest observed value.

C. Correlation between steady-state UCL and time-resolved PL measurements

While speculations regarding the physical mechanisms behind the variations in the characteristic decay times, $\tau_{11/2}$ and $\tau_{13/2}$, will be deferred to Sec. IV, it is still interesting to investigate the relation between these decay times and the observed steady-state UCL. First, if non-radiative decay channels are opened from the ${}^4I_{11/2}$ level and hence decreasing the value of $\tau_{11/2}$, the probability of observing UCL on the ${}^4I_{11/2} \rightarrow {}^4I_{15/2}$ transition will consequently decrease. It is thus plausible that the UCL yield is an increasing function of $\tau_{11/2}$. Likewise, if non-radiative decay channels are opened from the ${}^4I_{13/2}$ level and shortening $\tau_{13/2}$, the time that a given Er^{3+} ion spends in this level will decrease, resulting in a smaller probability of absorbing another photon via the ESA process or interacting with another closely-spaced Er^{3+} ion via the ETU process. Hence, the UCL yield would expectedly also be an increasing function of $\tau_{13/2}$. For these reasons, the UCL yield is plotted as a function of the product $\tau_{11/2} \times \tau_{13/2}$ in Fig. 5, and it is indeed established as an experimental fact that the data exhibit to a good approximation a proportionality between the UCL yield and this product of decay times. This is illustrated by the black dashed line of the plot, which represents the best proportional fit. In fact, this relationship can be argued on the basis of a simple rate-equation model, the

details of which will be discussed elsewhere¹⁸.

The proportionality of Fig. 5 presents a very convenient link between, on the one hand, the UCL yield with its application within e.g. photovoltaics and, on the other hand, the time-resolved PL experiments which present a possibility for a more detailed understanding of the limiting factors behind the UCL process. It should be emphasized that comparing the UCL yield across different samples requires the use of the integrating sphere, since the exact emission pattern of the UCL and hence the light collection efficiency may in practice vary from sample to sample. In contrast, the time-resolved PL measurements are insensitive to such variations, since they would only affect the amplitudes of the decay curves and not the measured time scales. With the above-mentioned proportionality, it is thus possible to make quantitative comparisons between samples without the need for an integrating sphere, which in turn increases significantly the sensitivity and allows for examining also poorly performing samples.

IV. DISCUSSIONS

The experimental facts concerning the possible physical mechanisms behind the UCL performance of the samples can be summarized in the following observations: (i) Despite large variations in UCL yield and luminescence decay times, all investigated samples showed an amorphous structure when investigated by XRD. Hence, the relevant structural variations between samples occur most likely at the atomic scale, e.g. in the form of point defects in the TiO_2 host material. (ii) The decreasing UCL yield is accompanied by opening of non-radiative decay channels, and in turn, a decrease in the luminescence decay times $\tau_{11/2}$ and $\tau_{13/2}$. However, these variations may occur differently for the corresponding levels ${}^4I_{11/2}$ and ${}^4I_{13/2}$ as observed most clearly for the unexposed samples in Fig. 4. (iii) The best performing sample was deposited at 350 °C during 90 minutes in an Ar/O_2 atmosphere. Still, a post annealing in exactly the same atmosphere and for the same duration caused a significant decrease in UCL yield (by $\sim 75\%$) for the unexposed sample. This raises the question why the best performing samples actually worked in the first place. The answer must lie in the difference between the two cases, being only that the plasma of the RF-MS process was on during deposition and off during post annealing. (iv) The UCL yield increases with increasing deposition temperature up to 350 °C for the as-deposited samples. (v) While the annealing process can be advantageous for the UCL yield in some cases (for unexposed samples deposited at a low temperature), it is mostly decreasing the UCL yield and always so for the air-exposed samples.

Let us discuss which physical mechanisms could cause the above observations. Point defects, as a possible explanation for the variation in UCL yields and decay times, were previously studied in several sputtered oxide

films, e.g. TiO₂ and SnO₂^{19–22}. The oxygen vacancies, being a relevant candidate in our samples, were studied in atomic-layer-deposited amorphous-TiO₂ (a-TiO₂) films^{23,24}. In a detailed study, Pham et al.²³ observed the O-vacancy defect states at about 1.0–1.5 eV above the top of the valence band in a-TiO₂ films deposited at 300 °C. We propose that such oxygen vacancies are present in our Er³⁺-doped TiO₂ thin films and that they open some energy-transfer channels for the excited states of Er³⁺ ions. The energy difference between the O-vacancy defect states and the valence band in TiO₂ is in good agreement with the transition energy (~ 1.27 eV) of the $^4I_{11/2} \rightarrow ^4I_{15/2}$ transition of Er³⁺, and hence non-radiative decay of the $^4I_{11/2}$ state in Er³⁺ could be associated with excitation of valence-band electrons to the O-vacancy defect states in TiO₂. The transition energy (~ 0.82 eV) of the $^4I_{13/2} \rightarrow ^4I_{15/2}$ transition is somewhat smaller than the above-mentioned energy range for the O-vacancy states. We cannot rule out that these O-vacancy defects could have a low-energy tail; however, the different behavior of the two decay times, $\tau_{11/2}$ and $\tau_{13/2}$, as mentioned in observation (ii), suggests that non-radiative decay of the $^4I_{13/2}$ states could be associated with a different class of defects (with lower energy). Such defects would then have to be susceptible to curing by annealing, at least for the unexposed samples, in consistency with the dashed lines in Fig. 4(b).

The explanation regarding observation (iii) could lie in the possible creation of a H plasma during the fabrication process, whereas no plasma was present during post annealing. It should be noted that our sputtering process had no intentional hydrogen source, so the H content of the plasma would be due to residual H₂ in the chamber. Previous studies have reported on the role of hydrogen passivation of O vacancies in c-TiO₂²⁵ as well as of dangling bonds in a-TiO₂ films^{19,26} through formation of O–H bonds²⁶. We thus suggest that such defects in our sputtered Er³⁺-doped TiO₂ films are passivated by hydrogen during the fabrication process. The post annealing in the same atmosphere as during deposition (except for the absence of the plasma) might then remove the H atoms or hydroxyl groups from the host, causing the 75 % lowering of the UCL yield. The possible creation of oxygen vacancies and the dissociation of hydroxyl bonds due to annealing of c-TiO₂ films (at $T \geq 400$ °C) in an oxygen-depleted atmosphere (i.e. Ar or vacuum) are well-reported^{26,27}.

The above considerations are also consistent with observation (iv): At elevated deposition temperatures, the density of defect states is most likely smaller due to the higher surface diffusion of atoms, providing a larger probability for reaching energy minima during growth.

The impact of annealing on the UCL yield also depends strongly on whether the as-deposited films have been exposed to ambient air before the annealing step or not, as stated in observation (v). The exposure to ambient air allows the interaction of the surface of the sputtered Er³⁺-doped TiO₂ films with O₂, water vapor, N₂, CO₂, etc. at

atmospheric pressure and room temperature. Such interactions have previously been studied in physical-vapor-deposited c-TiO₂ films and reported to involve these molecules, collectively, in the temporary passivation of defects^{26,28,29}. We propose that gas molecules attach to the surface by dissociative or molecular chemisorption. Presumably, the presence of loosely bound and dissociated ambient-air molecules promote the removal of hydrogen from defects during the post annealing and hence more efficient de-hydrogenation and resulting activation of defects in these samples. The unexposed films, however, do not contain such loosely bound molecules and activation of H-passivated defects by dissociation of O–H bonds during annealing might require a higher temperature. Therefore the observed drop in UCL yield after annealing is significantly lower than for the air-exposed counter-part.

V. CONCLUSION

A study of the influence of deposition- and annealing temperatures on the UCL yield and the associated decay times of the two lowest excited states (i.e. $\tau_{11/2}$ and $\tau_{13/2}$) of Er³⁺ ions in sputtered Er³⁺-doped TiO₂ films was performed. An elevated deposition temperature was a prerequisite for the luminescence of the films. The highest UCL yield and the associated long decay times of the Er³⁺ levels were obtained at a deposition temperature of 350 °C. The post annealing of the as-deposited films in general reduced the UCL. It was observed that exposure of as-deposited films to ambient air prior to post annealing was detrimental for the UCL of the films. However, the effect of post annealing on the films deposited at lower substrate temperatures and unexposed to air before the annealing step was found to be beneficial. The decay curves, observed in time-resolved PL measurements, showed that the decrease in the UCL yield was caused by the opening of non-radiative decay channels from the Er³⁺ excited states. The linear scaling between the UCL yield and the product of $\tau_{11/2}$ and $\tau_{13/2}$ for all samples provided a convenient link between decay dynamics and the obtained UCL yield. In light of the structural similarities (i.e. atomic structure) among the samples, the UCL variation with the temperature was attributed to the activation and/or passivation of defects, originated during the sputtering.

VI. ACKNOWLEDGMENTS

This work is supported by Innovation Fund Denmark under the project “SunTune.”

¹C. Chen, Y. Cheng, Q. Dai, and H. Song, *Sci. Rep.* **5**:17684, 1 (2015).

²A. D.Compaan, A. Gupta, S. Lee, S. Wang, and J. Drayton, *Solar Cells* **77**(6), 815 (2004).

- ³A. Gupta, and A. D. Compaan, *Appl. Phys. Lett.* **85**(4), 684 (2004).
- ⁴V. A. Daa, H. Choia, J. Heoa, H. Parka, K. Yoona, Y. Leea, Y. Kima, N. Lakshminarayanc, and J. Yi, *Curr. Appl. Phys.* **10**(3), 506 (2010).
- ⁵D. K. Maurya, A. Sardarinejad and K. Alameh, *Coatings* **4**, 756 (2014).
- ⁶S. R. Johannsen, L. R. Lauridsen, B. Julsgaard, P. T. Neuvonen, S. K. Ram, and A. N. Larsen, *Thin Solid Films* **550**, 499 (2014).
- ⁷D. Yoo, I. Kim, S. Kim, C. H. Hahn, C. Lee, and S. Cho, *App. Surf. Sci.* **253**, 3888 (2007).
- ⁸B.E. Yoldas, and T.W. O'Keeffe, *Appl. Optics.* **18**(18), 3133 (1979).
- ⁹L. Martinu, and D. Poitras, *J. Vac. Sci. Technol.* **A**(18), 2619 (2000).
- ¹⁰E. Shojae, and M. R. Mohammadizadeh, *J. Phys.: Condens. Matter* **22**, 015401 (2010).
- ¹¹A. Enesca, L. Andronic, A. Duta, and S. Manolache, *Romanian J. Info. Sci. and Tech.* **10**(3), 269 (2007).
- ¹²A. Patra, C. S. Friend, R. Kapoor, and P. N. Prasad, *Chem. Mater.* **15**, 3650 (2003).
- ¹³F. Azuel, *Chem. Rev.* **104**, 139 (2004).
- ¹⁴P. Blixt, J. Nilsson, J. Carlnas, and B. Jaskorzynska, *IEEE Trans. Photonics Technol.* **3**, 996 (1991).
- ¹⁵S. R. Johannsen, S. Roesgaard, B. Julsgaard, R. A. S. Ferreira, J. Chevallier, P. Balling, S. K. Ram, and A. N. Larsen, *Optic. Mat. Exp.* **6**(5), 1664 (2016).
- ¹⁶H. Lakhotiya, A. Nazir, S. P. Madsen, J. Christiansen, E. Eriksen, J. Vester-Petersen, S. R. Johannsen, B. R. Jeppesen, P. Balling, A. N. Larsen, and B. Julsgaard, *Appl. Phys. Lett.* **109**, 2631021 (2016).
- ¹⁷F.-H. Wang, J.-C. Chao, H.-W. Liu, and F.-J. Liu, *J. vacuum* **11**, 005 (2016).
- ¹⁸J. D. Christiansen, H. Lakhotiya, E. H. Eriksen, S. P. Madsen, P. Balling, and B. Julsgaard, in preparation.
- ¹⁹M. Nakamura, S. Kato, T. Aoki, L. Sirghi, and, Y. Hatanaka, *J. Appl. Phys.* **90**(7), 3391 (2001).
- ²⁰S. Bansal, D. K. Pandya, and S. C. Kashyap, *Appl. Phys. Lett.* **104**5, 082108 (2014).
- ²¹K Koski, J Hölsä, and P Juliet, *Surface and Coatings Tech.* **115**, 163 (1999).
- ²²X. Pan, M.-Q. Yang, X. Fu, N. Zhang and Y.-J. Xu, *Nanoscale* **5**, 3601 (2013).
- ²³H. H. Pham, and L.-W. Wang, *Phys. Chem. Chem. Phys.* **17**, 541 (2015).
- ²⁴S. Hu, M. R. Shaner, J. A. Beardslee, M. Lichterman, B. S. Brunshwig, and N. S. Lewis, *Science* **344**(6187), 1005 (2014).
- ²⁵W. Göpel, G. Rocker, and R. Feierabend, *Phys. Rev. B* **28**, 3427 (1983).
- ²⁶U. Diebold, *Surf. Sci. Rep* **48**, 53 (2003).
- ²⁷J.-M. Pan, B. L. Maschhoff, U. Diebold, and T. E. Madey, *J. Vac. Sci. Techno. A* **10**(4), 2470 (1992).
- ²⁸M. A. Henderson, *Surf. Sci. Rep* **66**, 185 (2011).
- ²⁹M.S. Lazarus, and T. K. Sham, *Chem. Phy. Lett.* **92**, 670 (1982).

Article 3

This document is confidential and is proprietary to the American Chemical Society and its authors. Do not copy or disclose without written permission. If you have received this item in error, notify the sender and delete all copies.

Resonant Plasmon-Enhanced Upconversion in Monolayers of Core-Shell Nanocrystals: Role of Shell Thickness

Journal:	<i>Nano Letters</i>
Manuscript ID	Draft
Manuscript Type:	Communication
Date Submitted by the Author:	n/a
Complete List of Authors:	Lakhotiya, Harish; Aarhus Universitet, Physics and Astronomy Nazir, Adnan; Aarhus Universitet, Department of Physics and Astronomy Roesgaard, Søren; Aarhus Universitet, iNANO Eriksen, Emil; Aarhus Universitet, Department of Physics and Astronomy Christiansen, Jeppe; Aarhus Universitet, Physics and Astronomy Bondesgaard, Martin; Aarhus Universitet, Department of Chemistry Iversen, Bo; Aarhus Universitet, Department of Chemistry van Veggel, Frank; University of Victoria, Chemistry Balling, Peter; Aarhus Universitet, Physics and Astronomy Julsgaard, Brian; Aarhus University, Department of Physics and Astronomy

SCHOLARONE™
Manuscripts

Resonant Plasmon-Enhanced Upconversion in Monolayers of Core-Shell Nanocrystals: Role of Shell Thickness

Harish Lakhotiya,[†] Adnan Nazir,[†] Søren Roesgaard,[†] Emil Eriksen,[†] Jeppe Christiansen,[†] Martin Bondesgaard,[‡] Frank C.J.M. van Veggel,[¶] Bo Brummerstedt Iversen,^{‡,§} Peter Balling,^{†,§} and Brian Julsgaard^{*,†,§}

[†]*Department of Physics and Astronomy, Aarhus University, DK-8000 Aarhus C, Denmark*

[‡]*Department of Chemistry, Aarhus University, DK-8000 Aarhus C, Denmark*

[¶]*Department of Chemistry, University of Victoria, Victoria BC, Canada*

[§]*Interdisciplinary Nanoscience Center (iNANO), Aarhus University, DK-8000 Aarhus C, Denmark*

E-mail: brianj@phys.au.dk

Abstract

The upconversion luminescence (UCL) of colloidal lanthanide-doped upconversion nanocrystals (UCNCs) can be improved either by precise encapsulation of the surface by optically inert shells around the core, by an alteration of the nearby environment via metal nanoparticles, or by a combination of both. Considering their potential importance in crystalline silicon photovoltaics, an investigation of both effects for two-dimensional arrangements of UCNCs for the conversion of >1100 nm wavelength light is the topic of the present work. We study the variation in the luminescence from an Er³⁺-doped NaYF₄ core as a function of the thickness of a NaLuF₄ shell in colloidal

1
2
3 solutions as well as in spin-cast-assisted self-assembled monolayers of UCNCs. The ob-
4 served UCL yields and decay times of Er^{3+} ions of the UCNCs increase with increasing
5 shell thickness in both cases, and nearly no variation in decay times is observed in
6 the transition of the UCNCs from solution to film configurations. The luminescence
7 efficiency of the UCNC monolayers is further enhanced by the deposition of electron-
8 beam-lithographic-designed Au-nanodiscs either on top or buried within of the mono-
9 layer. Structural tuning of the discs, to achieve localized surface plasmon resonance at
10 the excitation wavelength (~ 1500 nm) enables near-field enhancement of the excitation
11 intensity and in turn, an increased UCL. The UCL efficiency of the core-UCNCs in
12 the monolayer configuration is enhanced by a factor of five and the UCL-enhancement
13 factor decreases with an increase in the spacing between the Er^{3+} ions and the Au-discs
14 in the buried Au-disc configuration.
15
16
17
18
19
20
21
22
23
24
25
26
27

28 **Keywords**

29 Plasmon enhancement, upconversion, core-shell nanocrystals, monolayer, shell thickness
30

31 **Introduction**

32 Trivalent lanthanide (Ln^{3+})-doped upconversion nanocrystals (UCNCs) are well-known for
33 their remarkable ability of merging two or more low-energy photons into one high-energy
34 photon. The UCNCs hold significant impact in a broad range of applications, ranging from
35 biomedical imaging^{1,2} to photovoltaic (PV)³⁻⁶ and display technologies.⁷ The ladder-like $4f^n$
36 energy levels and the shielding effect of their electrons restrict the range of excitation and
37 emission wavelengths for the UCNCs.^{8,9} Therefore, based on the particular application dif-
38 ferent dopants are chosen for UCNCs. For instance, the single lanthanide-doped (i.e. Er^{3+}
39 or Tm^{3+})^{10,11} UCNCs are more appropriate for the efficiency improvements in PV (specif-
40 ically crystalline silicon (c-Si) solar cells) due to the conversion of near-infrared photons
41
42
43
44
45
46
47
48
49
50
51
52
53
54
55
56
57
58
59
60

1
2
3 ($\lambda > 1100$ nm) into visible photons whereas the codoped (i.e. Er^{3+} - Yb^{3+}) UCNCs are ap-
4 appropriate for the biomedical applications where the focus is on the conversion of 980 nm
5 photons instead. The chemical synthesis of the nanocrystals has been extensively studied
6
7 for a decade.¹²⁻¹⁴ However, a small absorption cross section of dopants,^{15,16} concentration
8 quenching,^{17,18} and non-radiative emission channels at the surface of the nanocrystals¹⁹ may
9 impose some limitations to the upconversion luminescence (UCL) of the UCNCs. Recently,
10 extensive attempts have been performed to improve the UCL efficiency either by changing
11 the chemistry of the nanocrystals or by altering their nearby environment. Tailoring at the
12 doping level, variation in host lattices,²⁰ formation of optically active^{21,22} or inert shells²³
13 around the core are a few approaches at the materials level, whereas using metal nanos-
14 tructures²⁴ or photonic crystals²⁵⁻²⁷ exemplify external environmental adjustments to deal
15 with the aforementioned UCL limitations. A substantial research effort has been performed
16 in smart nanoengineering of such colloidal UCNCs by formation of inert shells around the
17 optically active core to reduce surface-quenching processes.^{12,23,28-33}

31
32
33 Fabrication of two-dimensional (2D) arrangements of the colloidal UCNCs demonstrate a
34 high level of control of mono-layer film formations, and their UCL study is important to ex-
35 amine the applicability of UCNCs in PV devices. The transition from solution to film config-
36 uration allows for investigation of the possible activation of non-radiative emission channels.
37 The liquid/air interface method is the most extensively used technique to develop monolayers
38 of the nanocrystals.³⁴⁻³⁶ However, the involvement of organic solvents in the method lim-
39 its the chemical stability of the UCNC monolayers for possible next stage processes, which
40 could for instance consist of lithographic patterning of metal nanoparticles (NPs) on top of
41 the monolayers for UCL enhancement. The patterning involves harsh chemical and thermal
42 environments which could destabilize the UCNCs arrangements. Spin coating, in contrast
43 to the interface method, is an easy and controlled technique for monolayer fabrication.³⁷⁻⁴⁰
44 This technique can produce a host-independent chemically stable 2D ordered arrangement

1
2
3 of UCNCs if the process parameters and dispersion properties are precisely controlled. Spin
4 coated monolayers are thus applicable for such next stage processes.
5
6

7 The UCL efficiency of the UCNC monolayers can be further enhanced by altering the
8 nearby environment of the luminescent centers through metal NPs.^{24,41–44} A resonant inter-
9 action of metal NPs with incident light creates collective oscillations of their free electrons
10 called localized surface plasmon resonances (LSPRs) that localize electromagnetic fields (E-
11 fields)⁴⁵ close to the metal NP surface. The concentrated E-fields can either enhance both
12 absorption^{41,43,44} and emission⁴¹ or enhance absorption but quench emission³⁴ in the emitters
13 within the UCNCs. An enhanced absorption and emission in the emitters can be achieved
14 by matching the LSPRs frequency of metal NPs with the excitation wavelength and by opti-
15 mizing the distance between the metal NPs and the emitters for a slow non-radiative decay,
16 respectively. The above optimizations of plasmonic structures allow for investigating the
17 fundamentals about the interactions between the emitters and metal NPs. In addition, they
18 also demonstrate a good control of the fabrication of upconversion-based PV devices. The
19 distance optimization between the NPs and the emitters for an efficient enhancement in the
20 UCL has been studied previously using physical vapor deposited spacer layers for varying
21 the spacing.^{34,46} The resonant frequency of the LSPRs depends on the NP geometry⁴⁴ and
22 the refractive indices of the materials and the surroundings.^{44,47,48} The geometry of the NPs
23 is controlled by the choice of fabrication method. Chemical synthesis and lithography are
24 the two prominent ways to fabricate Au NPs. In a low and constant refractive index system
25 like UCNC monolayers, the geometric alteration of the NPs is a challenge due to a required
26 relatively bigger diameter in achieving in-resonance plasmon enhancement. A shift in the
27 LSPR peak positioning by the geometric alteration to $\lambda > 1100$ nm is possible by chemical
28 synthesis methods but highly tedious and inefficient.^{49,50} Most of the previous studies are
29 thus focused on off-resonant coupling,^{34,41} very few are on resonance at $\lambda \sim 980$ nm,^{41,48}
30 but none are reported on resonant plasmon-enhanced upconversion for $\lambda > 1100$ nm with
31 chemically synthesized NPs. However, the nanofabrication of such metal NPs by lithographic
32
33
34
35
36
37
38
39
40
41
42
43
44
45
46
47
48
49
50
51
52
53
54
55
56
57
58
59
60

1
2
3 techniques, i.e. nanosphere lithography,⁵¹⁻⁵³ electron beam lithography (EBL),⁴⁴ or nanoim-
4
5 printing,⁵⁴ present alternative methods for the desired metal NPs fabrication.
6
7
8

9
10 The present letter involves the fabrication of spin-cast self-assembled monolayers of
11 $\text{Er}^{3+}:\text{NaYF}_4\text{-NaLuF}_4$ (core-shell) UCNCs. A dependence of the upconversion luminescence
12 on the shell thickness is investigated in 2D arrangements of UCNCs. The decay times of
13 the ${}^4I_{11/2}$ and the ${}^4I_{13/2}$ energy levels of Er^{3+} ions are examined in the transition of UCNCs
14 from colloidal solutions to monolayers. Furthermore, the electron-beam lithography (EBL)
15 defined Au-nanodiscs are placed either on top of or below the monolayers, and the structures
16 are geometrically optimized for a resonant plasmon-enhanced upconversion of 1500 nm light.
17 The distance dependence of the plasmon enhancement factors in the UCL are examined
18 through the varied shell thickness of the UCNCs, which creates a variable spacing between
19 Au-discs and Er^{3+} ions, in the buried Au-discs configuration. The optimizations of both
20 shell thickness of UCNCs in the ordered structures and Au-nanodiscs are important to find
21 the applicability of UCNCs at the PV device level.
22
23
24
25
26
27
28
29
30
31
32
33
34
35
36

37 Results and discussion

38
39
40 The present work is focused on the luminescence study of Er^{3+} -doped NaYF_4 UCNCs in the
41 monolayer configuration. For the work, nearly spherical, 19.7 ± 0.7 nm diameter 20 mol%
42 Er^{3+} -doped $\beta\text{-NaYF}_4$ core nanocrystals were chemically fabricated. A sample of core-only
43 nanocrystals was retrieved while the rest went under chemical process of variable NaLuF_4
44 shell formation, with thicknesses ranging from 0.8 nm to 10.1 nm (Supporting Informa-
45 tion, Section 1). The structural and optical measurements of colloidal core and seven other
46 core-shell nanocrystals were performed and results are presented either in the supporting
47 information or below in the letter. In the letter, we present results of three representative
48
49
50
51
52
53
54
55
56
57
58
59
60

1
2
3 samples in the monolayer configuration. These samples are the core (CS0), core with 2.8 nm
4 shell thickness (CS3), and core with 10.1 nm shell thickness (CS10) UCNCs. To avoid am-
5 biguity, a color code is maintained for the representative samples in all figures throughout
6 the letter: blue for CS0, green for CS3, and red for CS10 UCNCs.
7
8
9

10
11
12
13 High-resolution transmission electron microscope (HR-TEM) images of single UCNCs of
14 the representative samples, shown in the top-left corner of each colored box of Figure 1, con-
15 firm the isotropic growth of shells around the core UCNCs. The monolayer formation of the
16 UCNCs is performed by a spin coating technique. The homogeneity in the UCNCs arrange-
17 ments was achieved by optimizing the dispersion properties (i.e. volatility and viscosity),
18 particle size distributions, and spin-coating parameters (i.e. the rotation and acceleration
19 rates). However, even at optimum condition we observed a concentration gradient from the
20 center of rotation to the substrate corners from one monolayer to one and a half monolayers.
21 Despite this gradient, at least 2×2 mm² regions near the center of rotation was achieved
22 with one monolayer for all samples and only these regions were used for the subsequent in-
23 vestigation. The top-right corner of each colored box in Figure 1 are the top-view scanning
24 electron micrographs (SEMs) of the representative samples. The images show the intentional
25 terminations of nanocrystal arrangements (by scotch-tape removal) along with the presence
26 of naked quartz to verify the monolayer formation. The next top-view SEMs, bottom im-
27 age of each colored box of Figure 1, show the uniformity in the 2D arrangements of the
28 UCNCs. The SEMs exhibit a regular close-packed ordering of the nanocrystals with some
29 minor defects. The smaller size particles (i.e. CS0 and CS3 samples) show the crystallo-
30 graphic ordered arrangement due to the dominance of the capillary forces during the solvent
31 evaporation, whereas such arrangement becomes less obvious when the size of particles gets
32 comparably larger (i.e. CS10 sample). The SEMs of all other samples are reported in Sup-
33 porting Information, Figure S4.
34
35
36
37
38
39
40
41
42
43
44
45
46
47
48
49
50
51
52
53
54
55
56
57
58
59
60

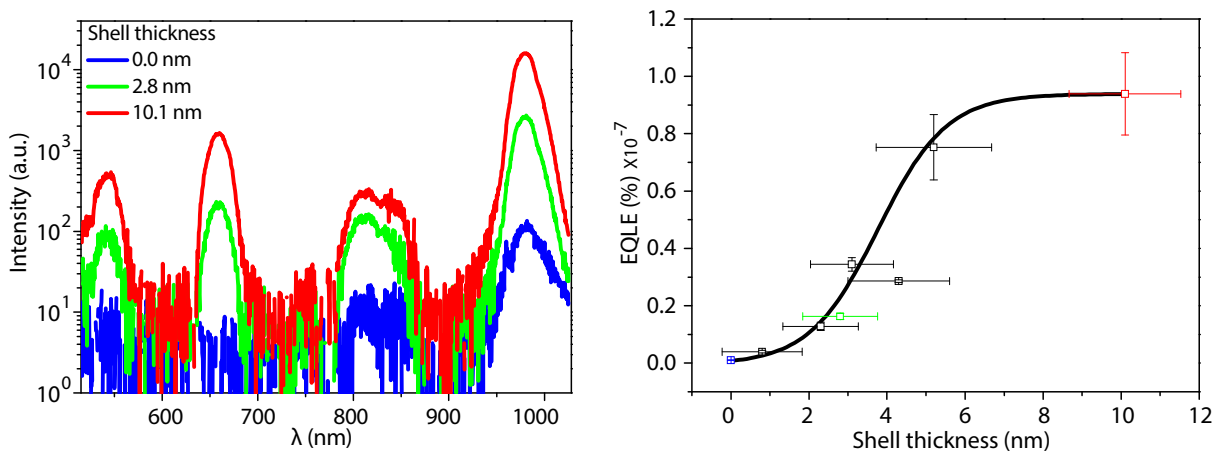
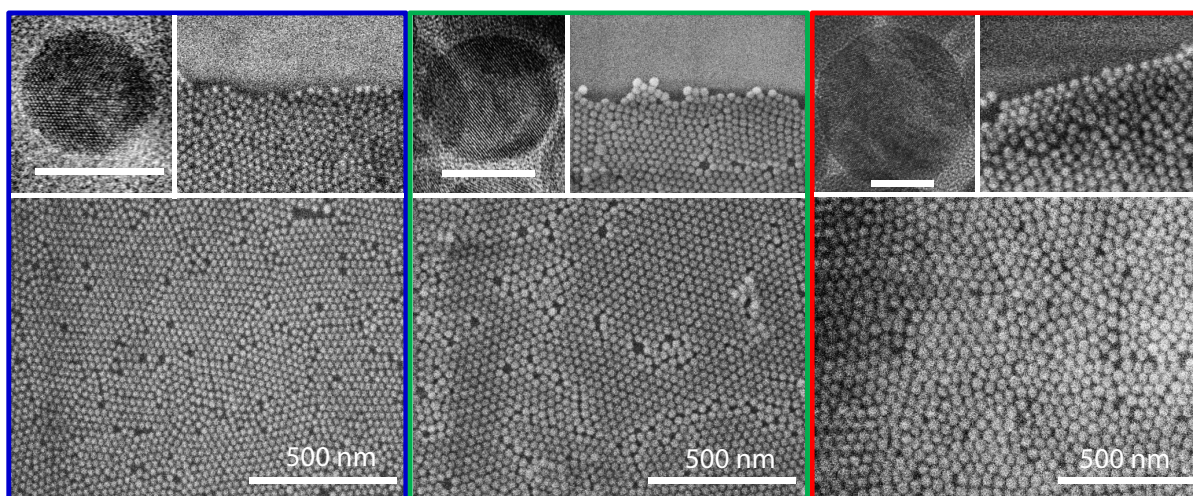


Figure 1: Scanning electron microscope images and upconversion luminescence of UCNCs monolayers are presented in top and bottom panels, respectively. A color code is maintained in the figure for the core (blue), core with the shell of 2.8 nm (green), and 10.1 nm (red) UCNCs. Each colored box of the top panel has one HR-TEM image with a scale bar of 20 nm (on top-left corner) and two top-view SEMs of the corresponding UCNC monolayers on quartz. The top-right SEM of each boxes represent the intentional termination of monolayer and the presence of the naked substrate. The bottom panels (from left to right) show the UCL spectra (semi-log scale) of the UCNC monolayers of the representative samples and the derived EQLE versus shell thickness of all samples. The colored symbols of the plot represent the EQLE of the representative samples. The black curve is a guide to the eye.

1
2
3 For the optical investigations, the steady-state UCL measurements of all samples were
4 performed under laser illumination at a wavelength of 1500 nm using a peak intensity of
5 0.3 kW/cm². The UCL spectra of all UCNC monolayers were normalized to the total amount
6 of Er³⁺ present within the constant laser illuminated area. An increase in the shell thick-
7 ness around the core reduces the total number of particles and hence the amount of Er³⁺
8 in the illuminated area. The spectra are shown in the lower-left panel of Figure 1. It is
9 evident that the growth of the shell around the core improves the UCL yield of the core
10 nanocrystals. The UCL yields of all samples are calculated by summing the area under
11 the peaks for each spectrum and the UCL yields of CS3 and CS10 samples are found to
12 be 16.5 and 94.4 times, respectively, higher than the UCL yield of core nanocrystals in the
13 2D arrangements. The external quantum luminescence efficiency (EQLE), a ratio between
14 the number of upconverted photons and the incident 1500 nm photons, of all samples are
15 calculated (explained in Supporting Information, Section 2.3.2) and plotted against the shell
16 thickness of UCNCs in the monolayer configuration in the lower-right panel of Figure 1. An
17 increase in the EQLE with the shell thickness is expected due to a reduction in the non-
18 radiative decay at the nanocrystal surface. Furthermore, the increase has a low slope until
19 nearly 1 nm shell thickness, a steep slope from 1 nm to 6 nm shell thickness (as per the
20 guided black solid curve in the figure), and followed by a slower increase (saturated EQLE)
21 at higher shell thickness around the core. The obtained results indicate nearly two orders of
22 magnitude improvement in the upconversion yield with the 10.1 nm shell thickness around
23 the core nanocrystals. Interestingly, the trend of variation in EQLE with shell thickness of
24 UCNCs in their monolayer configuration is similar to the variation in upconversion quantum
25 yield of UCNCs in colloidal solutions found by Fischer *et al.*³⁰ When comparing the absolute
26 value of quantum yields of the UCNCs to the previous work,³⁰ the current values are lower
27 for several reasons: (i) The previous work has reported the internal quantum yield, whereas
28 the present report consists of the external quantum yields. (ii) The present experiment is
29 performed only with Er³⁺ ions. (iii) The present dopant concentration is lower than the
30
31
32
33
34
35
36
37
38
39
40
41
42
43
44
45
46
47
48
49
50
51
52
53
54
55
56
57
58
59
60

1
2
3 previously reported work.³⁰ (iv) The EQLE is measured for the monolayers instead of the
4 concentrated colloidal solutions. The power of the excitation laser was varied in order to
5 determine the scaling of the upconverted light intensity (I_{UC}) with the intensity of incoming
6 light (I_{in}) for each monolayer. In the double-logarithmic plot of Figure 2(a), the data of the
7 core UCNC monolayers fall on a straight line with a small deviation at higher power density
8 with an average slope of ≈ 1.5 . This indicates $I_{UC} \propto I_{in}^{1.5}$ scaling. With an increase in the
9 shell thickness the slope drops to nearly 1 which indicates a linear ($I_{UC} \propto I_{in}^1$) scaling, indi-
10 cating saturation of the first excited level ($^4I_{13/2}$) of Er^{3+} ions due to very low non-radiative
11 decay rates in the thick shelled UCNC monolayers.
12
13
14
15
16
17
18
19
20
21
22

23 To comprehend the dynamics regulating the UCL process, time resolved photolumines-
24 cence measurements were performed. An 800 nm laser populated the $^4I_{9/2}$ energy level
25 of Er^{3+} ions, for all samples in both solution and monolayer configuration, and the detec-
26 tion of the emitted light provided the decay curves for both the $^4I_{11/2} \rightarrow ^4I_{15/2}$ and the
27 $^4I_{13/2} \rightarrow ^4I_{15/2}$ transitions of Er^{3+} ions. The decay curves of all samples, in both solution
28 and monolayer configurations, were fitted to either a single-exponential decay with the for-
29 mula $f(t) = A_x \exp(-t/\tau_x)$ or single-exponential decay with an initial exponential rise factor
30 following the formula $h(t) = (1 - a_{rise} \exp(-t/\tau_{rise}))A_x \exp(-t/\tau_x)$, where A_x and τ_x rep-
31 resent the amplitude and the characteristic decay times of the luminescence, respectively,
32 from either the $^4I_{11/2}$ or the $^4I_{13/2}$ levels. A delay in terms of relaxation of the ions from
33 higher-energy level to the emission level (i.e. $^4I_{11/2}$ or $^4I_{13/2}$) before being significantly lu-
34 minescent can explain the rise factor. The decay curves from the $^4I_{15/2}$ transition of three
35 representative samples in both monolayer and solution configurations are presented in Fig-
36 ure 2(b1) and (b2), respectively, with the remaining decay curves deferred to the Supporting
37 Information, Figure S3 and S5. The curves in Figure 2(b1) and (b2) are fitted with single
38 exponential decay with an initial exponential rise factor except the core UCNCs in mono-
39 layer configuration, which has no observable rise before the decay. From Figure 2(b1) it is
40
41
42
43
44
45
46
47
48
49
50
51
52
53
54
55
56
57
58
59
60

1
2
3 evident that an increase in shell thickness causes longer decay times and also larger areas
4 under the curves which resembles the increased amount of light emitted from the monolayers
5 of UCNCs. However, the unknown concentrations of UCNCs in the colloidal solutions do
6 not allow the comparison of area under the decay curves among samples but the decay times
7 are irrespective to the concentrations and shows a similar trend to the UCNC monolayers,
8 presented in Figure 2(b2). This is a clear indication of the effective closing of non-radiative
9 decay channels at the surface of UCNCs with an increase in shell thickness.
10
11
12
13
14
15
16
17

18
19 Figure 2(c) shows one of the main results of the letter: a comparison of the characteristic
20 luminescence decay times of UCNCs in the transition from the solution to the monolayer
21 configuration. The figure shows the decay times of the ${}^4I_{11/2}$ and the ${}^4I_{13/2}$ levels as a func-
22 tion of UCNCs shell thickness in both configurations. The decay times are calculated from
23 the respective fitted models and abbreviated as $\tau_{11/2}$ for ${}^4I_{11/2} \rightarrow {}^4I_{15/2}$ transition and $\tau_{13/2}$
24 for ${}^4I_{13/2} \rightarrow {}^4I_{15/2}$ transition. For both energy levels and both configurations, the variation
25 in decay time as a function of shell thickness is similar; an increasing function first with low,
26 then steep, and finally nearly zero slopes. It is important to note that the variational trends
27 in $\tau_{11/2}$ and $\tau_{13/2}$ are maintained in the transformation of UCNCs from colloidal solutions to
28 the monolayer configuration. Therefore, it is evident that the colloidal UCNCs do not lose
29 the luminescence efficiency in their two-dimensional arrangements. This proves the practi-
30 cability of UCNCs in upconversion-based solar cell devices for photo-current enhancement.
31
32
33
34
35
36
37
38
39
40
41
42
43
44

45 It is interesting that the trend in decay times is similar to the observations of the steady-
46 state UCL (EQLE) plot of Figure 1. This indicates a simple correlation between EQLE
47 and decay times for the samples in monolayer configuration. The opening of non-radiative
48 decay channels from the ${}^4I_{11/2}$ level and, consequently, shortening the value of $\tau_{11/2}$ for ei-
49 ther core or thin-shelled UCNCs, results in a reduction in the EQLE for ${}^4I_{11/2} \rightarrow {}^4I_{15/2}$
50 transition. Therefore, the EQLE is an increasing function of $\tau_{11/2}$. Similarly, the opening of
51
52
53
54
55
56
57
58
59
60

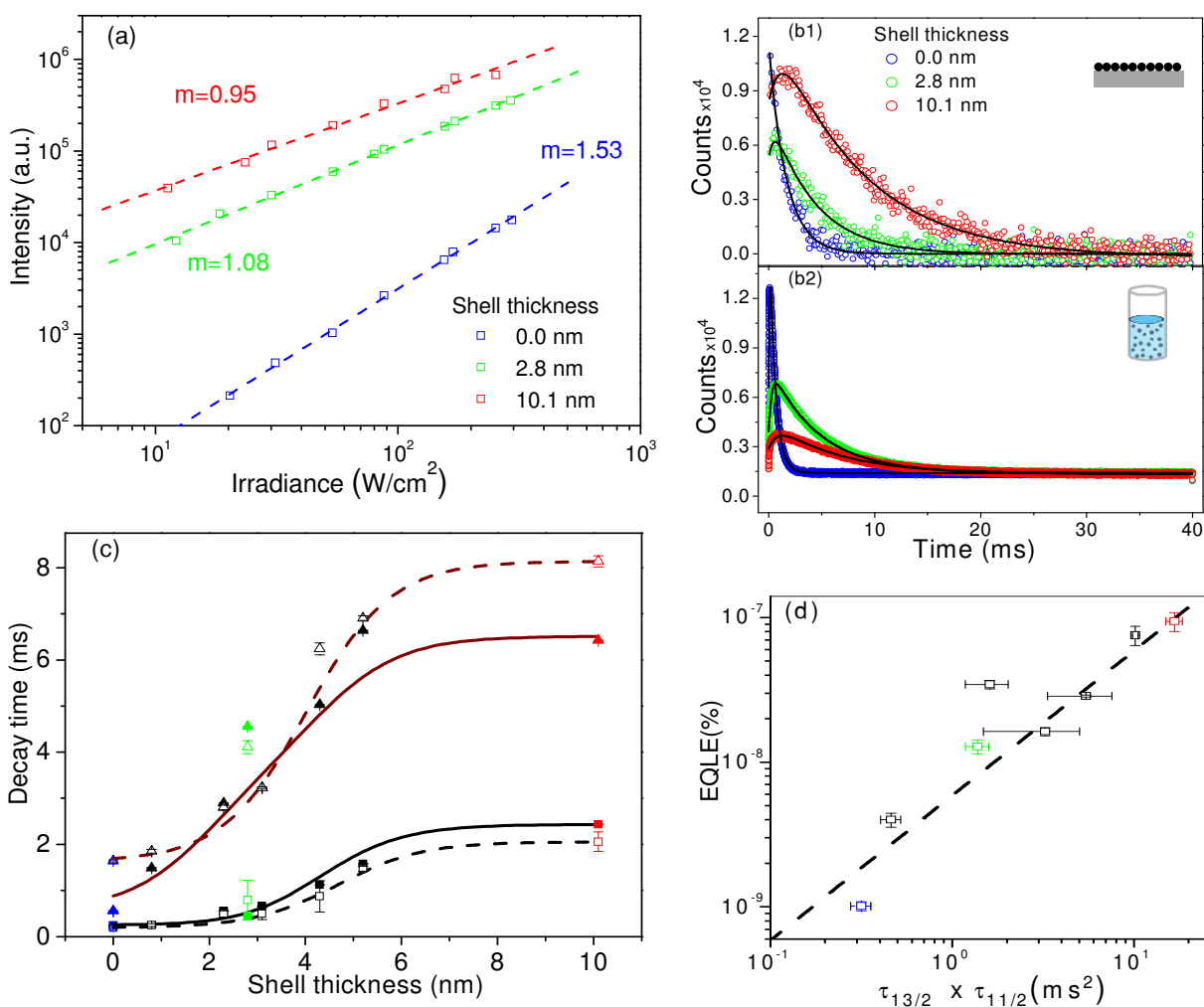


Figure 2: [The color code is in agreement with Figure 1.] (a) The variation in integrated UCL intensity with the pump intensity for the representative samples [measured outside the integrating sphere to increase the sensitivity]. The slope of the curves are represented by the m -value. (b) Decay curves from the ${}^4I_{13/2} \rightarrow {}^4I_{15/2}$ transition of the representative samples in both monolayer configuration (b1) and colloidal-solution configuration (b2). The data are fitted with the models (described in the text) represented by the black curves in both panels. (c) Characteristic decay times for the ${}^4I_{11/2} \rightarrow {}^4I_{15/2}$ and the ${}^4I_{13/2} \rightarrow {}^4I_{15/2}$ transitions of all samples in both solution and monolayer configurations. The squares and triangles represent the transitions from ${}^4I_{11/2}$ and ${}^4I_{13/2}$ energy levels, respectively. The hollow and solid nature of the symbols show the UCNCs in monolayer and solution configurations, respectively. The dashed and solid curves are guides to the eyes for hollow and solid symbols, respectively. (d) The EQLE as a function of the product of characteristic decay times $\tau_{11/2}$ and $\tau_{13/2}$ for all UCNCs monolayers, shown on a double-logarithmic scale. The dashed line represents a proportional fit.

1
2
3 non-radiative channels from the ${}^4I_{13/2}$ level and hence, the reduced $\tau_{13/2}$ for the same sam-
4 ples, implies a low probability of absorbing another photon via the energy transfer or the
5 excited state absorption processes. The EQLE is thus an increasing function of $\tau_{13/2}$. With
6 these considerations, we plotted EQLE versus $\tau_{11/2} \times \tau_{13/2}$ for all samples in the monolayer
7 configuration on a double-logarithmic scale in Figure 2(d). It demonstrates an approximate
8 proportionality between the EQLE and $\tau_{11/2} \times \tau_{13/2}$, which is in good agreement with our
9 previous findings in another Er^{3+} -doped system.⁵⁵
10
11
12
13
14
15
16
17
18

19 In order to use the Au NPs as a plasmonic upconversion enhancer in the UCNC mono-
20 layer, we designed truncated nano-cone shaped (named as nanodiscs) Au-structures with
21 the LSPR peak position matched with the excitation wavelength (1500 nm) and fabricated
22 these via an EBL process. The characteristics of this process are mentioned briefly in the
23 Experimental section and discussed in detail in the Supporting Information, Section 3.1.
24 The nanodiscs were placed in close vicinity of the UCNCs in two different positions: on top
25 of the monolayers and buried in the monolayers after being deposited on quartz. In either
26 position, Au-structures were designed in $1 \times 1 \text{ mm}^2$ regions such that measurements both
27 in the presence and the absence of Au-structures could be performed on one sample. In
28 this way systematic effects due to variation in sample fabrication could be reduced. Exper-
29 imentally, the height and shape of Au-structures were kept constant and the diameter was
30 varied to achieve the desired LSPR peak position. The height of the structures was fixed to
31 20 nm to achieve full coverage of the smallest UCNCs ($\sim 20 \text{ nm}$ sized core) in the buried-Au
32 experimental pattern. The truncated cone shape is possibly the simplest geometry that can
33 be designed with a short EBL processing time. A transmission electron micrograph of a
34 similarly shaped Au disc is reported in our previous work.⁴⁴ In the present work, we first
35 optimized the diameters of Au-nanodiscs for LSPR at 1500 nm wavelength by trial and error
36 and then verified numerically with the obtained diameter, see Figure 3(b). The placement
37 of the nanodiscs on top or buried positions and the variation in the size of UCNCs tuned
38
39
40
41
42
43
44
45
46
47
48
49
50
51
52
53
54
55
56
57
58
59
60

1
2
3 the refractive index of the surrounding medium felt by the nanodiscs, which consequently
4 affected the LSPR peak position. Therefore, the obtained diameters of the nanodiscs for
5 Au-on-top position was found bigger than for the buried-Au configuration.
6
7

8
9 Numerically, we solved the Maxwell equations using the finite element method (FEM) to
10 find the distribution of electric field around a single nanodisc induced by a normal-incident
11 plane wave. The collected scattered power from the distribution provided the scattering
12 cross section while the absorption cross section was calculated from the ohmic losses of the
13 Au-disc. Summation of both corresponds to the calculated extinction cross section. This was
14 divided by the geometrical cross section (A) of the Au-disc to achieve the relative extinction
15 cross section (σ_E/A), from which the LSPR peak positioning of Au-discs is found and com-
16 pared with the experimental findings, see Figure 3(b). The nanoscale structural variation
17 in the experimentally produced monolayers of UCNCs were smaller than the wavelength of
18 the plane wave, and therefore we considered the monolayers as a homogeneous films in our
19 calculations. The numerical analysis used the tabulated refractive index of Au whereas the
20 refractive indices of quartz and UCNCs in the monolayer configuration were measured by
21 ellipsometry. The refractive indices of the representative UCNCs monolayers (before being
22 EBL processed) were measured at 50° , 60° , and 70° angles and the averaged refractive index
23 of monolayers were used for the numerical calculation.
24
25
26
27
28
29
30
31
32
33
34
35
36
37
38
39
40

41 The fabrication of in-resonance Au-structures on top of the UCNC films will open a new
42 path towards an Au-embedded multilayered design for an observable photo-current enhance-
43 ment in *c*-Si PV devices. In this regards, we attempted to prove the fabrication concept by
44 designing Au-discs on top of the spin-coated UCNC monolayers via the EBL process. We
45 ensured the diminutiveness in the possible deformation caused by the EBL process in the
46 UCNCs arrangements by the selection of an appropriate solvent, the ligand concentrations,
47 and the isotropic thermal treatments. The chemical and thermal stabilities of the monolayers
48 allowed the EBL process, see the Supporting Information, Figure S6. Despite the fabrication
49
50
51
52
53
54
55
56
57
58
59
60

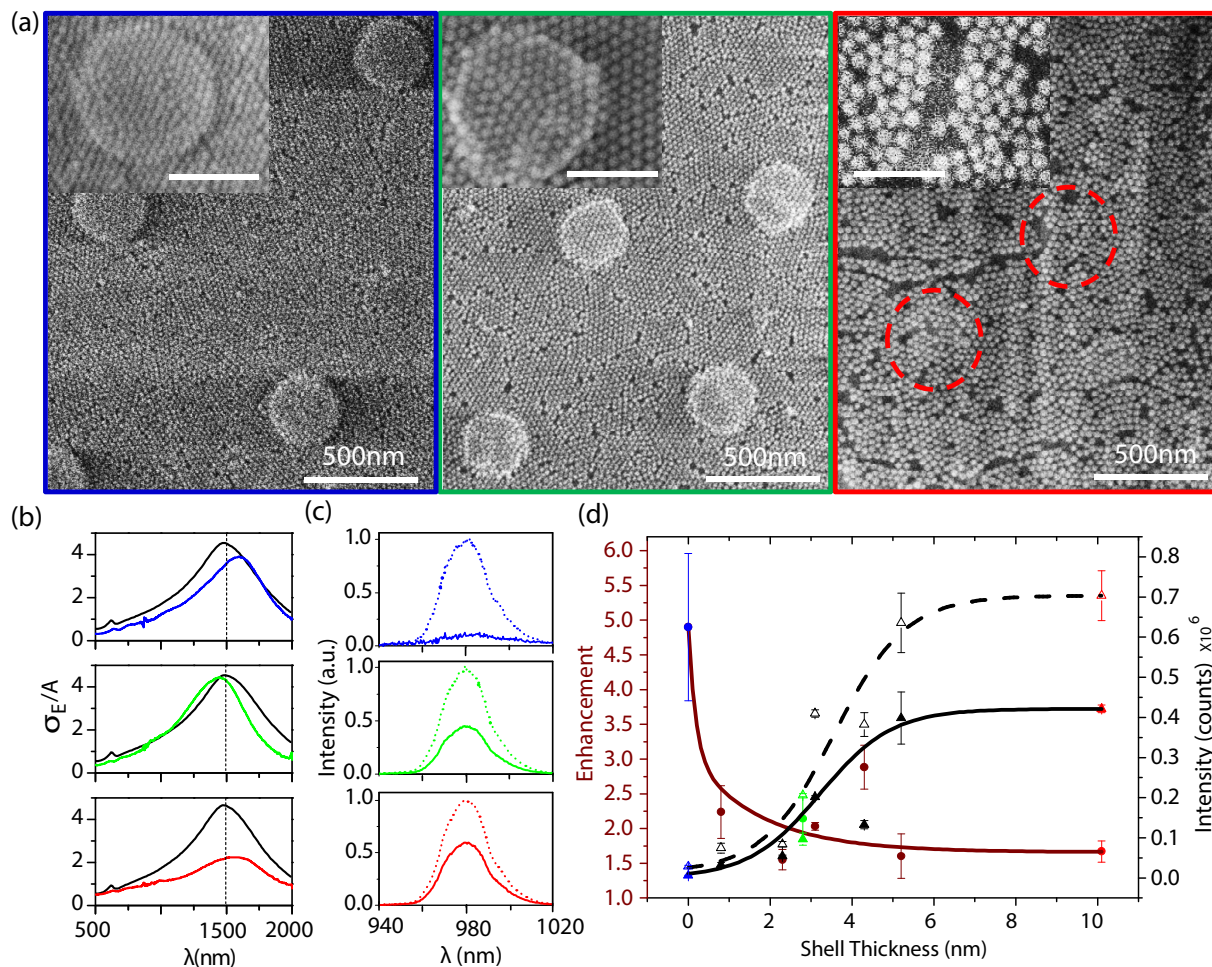


Figure 3: The structural and optical studies of UCNCs monolayers with buried Au nanodiscs are presented in top (a) and bottom (b,c, and d) panels, respectively. The color code is in agreement with Figure 1. Each colored box of (a) shows a top-view SEM of one of the representative samples and a magnified image of a single buried Au-disc with a scale bar of 200 nm (top-left corner). The red dashed-circles indicate the presence of Au-discs hidden under the UCNCs. Panel (b) shows the experimental (colored curves) and numerical (black curves) LSPR peaks of Au-discs in extinction cross section per unit area (relative extinction cross section) curve. The black dotted line marks the 1500 nm excitation wavelength. The luminescence spectra of the same samples measured with (dashed curves) and without (solid curves) Au-discs are presented in (c). Panel (d) depicts the total UCL yield measured in presence and absence of Au-discs, and the UCL enhancement (the ratio between the two UCL yields) as a function of the shell thickness of UCNCs for all Au-buried monolayers. The errors in the shell thickness are excluded for clarity. The hollow and solid black squares represent the UCL data measured with and without Au-discs. The color of some data points match the predefined color code. The wine colored curve is a guide to the eyes for the enhancement data points whereas the solid and dashed black curves are guides for the total UCL yield measured without and with Au-discs.

1
2
3 success, the luminescence of the EBL-treated monolayers was observed to be lower than the
4 non-treated monolayers (mentioned in the Supporting Information, Figure S8(b)), possibly
5 due to the electron-beam (e-beam) induced defects in the nanocrystals. However, the re-
6 placement of the EBL to a non e-beam nanofabrication, eg. nanoimprinting, for the discs
7 formation could possibly resolve the observed UCL drop.
8

9
10 The present study is focused on the UCL enhancement of the monolayers in a buried con-
11 figuration of Au-discs. The configuration involved the EBL-fabrication of Au-discs on bare
12 quartz and the subsequent formation of UCNC monolayers. The structural and optical re-
13 sults of the representative samples are discussed here while the results of other samples are
14 presented in Supporting Information, Figure S6, S7 and S8. The top-view SEMs of the rep-
15 resentative samples are shown in Figure 3(a). The color code is in agreement with the upper
16 panel of Figure 1. The positions of Au-nanodiscs are random and visible in CS0 and CS3
17 samples whereas the dashed circles in CS10 sample show the location of the barely visible
18 Au-discs. The poor visibility of the buried discs in CS10 sample can be explained by the
19 bigger size of the nanocrystals (40 nm) compared to the height of the Au-discs (20 nm). In
20 order to show the traces of the nanodiscs, a region of a slightly less compact monolayer of
21 CS10 is deliberately shown in the figure. The distributions of the UCNCs on top of Au-discs
22 are homogeneous and show a similar arrangements as shown in the upper panel of Figure 1).
23 This defines the reproducibility of the UCNCs arrangements irrespective of the surface treat-
24 ments of quartz during the EBL process. The magnified images in (a) show the full coverage
25 of the discs by the UCNCs, which is important for efficiently capturing the enhanced electric
26 field generated by the discs.
27
28
29
30
31
32
33
34
35
36
37
38
39
40
41
42
43
44
45
46

47
48
49 Shifting from the structural to the optical results, the spectra of relative extinction
50 cross section and hence the LSPR wavelengths of the representative samples are depicted
51 in the Figure 3(b). The figure shows the presence of LSPRs at the excitation wavelength
52 (~ 1500 nm) which confirms the fabrication of in-resonance Au-discs. The extinction plots
53
54
55
56
57
58
59
60

1
2
3 also show a very good agreement between the experimentally achieved and the numerically
4 calculated LSPRs peak positioning for the representative samples which further validates
5 the single-particle FEM numerical approach. Experimentally, we maintained the LSPR
6 peak positioning nearly at 1500 nm wavelength for all samples by reducing the size of the
7 EBL-defined Au-discs going from CS0 to CS10 UCNCs. The extinction cross section, $\sigma_E =$
8 $(1 - T_D - R_D) / PD$, was calculated by measuring the direct transmittance, T_D , and direct re-
9 flectance, R_D in the spectrophotometer. In the equation PD represents the Au-nanodisc
10 density of 6000 per unit $100 \times 100 \mu\text{m}^2$ fabricated area. After confirming the deposition of
11 in-resonance Au-discs for the UCL enhancement, we performed the luminescence experiment
12 on and off Au-discs for all samples. Figure 3(c) shows the spectrum of the upconverted light
13 at 980 nm for the representative samples, and the UCL intensity is clearly enhanced in the
14 presence of Au nanodiscs. In addition, we do not see any significant change in the shape of
15 the UCL spectrum due to the presence of the metal discs. The total UCL enhancement is de-
16 fined by the ratio of the area of all upconversion luminescence peaks in the presence and the
17 absence of Au-discs. The enhancement along with the total UCL with and without Au-discs
18 of all samples are shown in Figure 3(d). It is interesting to see that the trend of the variation
19 in UCL with the shell thickness is maintained in the buried Au-discs configuration for both
20 the presence and the absence of Au-discs measurements. The maximum around five fold UCL
21 enhancement is observed in the core UCNCs; however, a decrease in the enhancement was
22 observed with increasing shell thickness, see the plot. As the shell thickness increases, the
23 spacing between the ions and the discs increases which prevents the nonradiative quenching
24 at small separation distances as reported previously^{34,46} therefore, the enhancement should
25 be an increasing function with the shell thickness. However, the increased shell thickness
26 simultaneously passivates the UCNCs surface defects also and consequently, improves the
27 UCL of the monolayers. Now if the surface passivation of the UCNCs gets dominant, no
28 signs of the improvement in the metal induced quenching appears. Therefore, instead of im-
29 proving the UCL-enhancement with the spacer distance at small distances ($\sim 5\text{-}10\text{nm}$), we
30
31
32
33
34
35
36
37
38
39
40
41
42
43
44
45
46
47
48
49
50
51
52
53
54
55
56
57
58
59
60

1
2
3 observe a continuous drop due to the growing distance of the Er^{3+} ions (present in the core)
4 from the concentrated E-field of Au-discs. The observed maximum UCL enhancement in the
5 UCNC monolayers from Au-discs, ~ 5 fold, is way too small compared to the enhancement
6
7 achieved by the inert-shell formation around the core, ~ 100 fold. The specially designed
8
9 (e.g. by topology optimization⁵⁶) Au-structures could possibly replace the nanodiscs for a
10
11 higher enhanced-upconversion in core-shell UCNC monolayers. In the present work, we prove
12
13 the possible implementations of both the chemical modification at material surface and the
14
15 alteration of their near environment strategies in the fabrication of an efficient upconversion-
16
17 based solar cells.
18
19
20
21
22

23 In conclusion, we investigated the relationship between the upconversion luminescence
24 and the shell thickness of $\text{Er}^{3+}:\text{NaYF}_4\text{-NaLuF}_4$ UCNCs in their monolayer configuration. We
25 demonstrated that the decay times of the first two excited states (the $^4I_{11/2}$ and the $^4I_{13/2}$)
26 of Er^{3+} ions were essentially uninfluenced in the transition of colloidal solutions to 2D-
27 arrangements of the UCNCs which further excludes the possible opening of non-radiative
28 decay channels. This conservation of the luminescence efficiency enables the possible use
29 of thin films of such UCNCs in c-Si photovoltaic devices for the upconversion of 1500 nm
30 wavelength photons. In addition, the linear scaling between the UCL yield and the $\tau_{11/2} \times \tau_{13/2}$
31 for all UCNC monolayers provided an appropriate connection between decay dynamics and
32 the obtained UCL yield. We further enhanced the UCL yield by introducing EBL-defined
33 resonant Au-nanodiscs in the top and bottom of the chemically and thermally stable UCNCs
34 monolayers. We experimentally tuned the disc diameters in both configurations to achieve
35 the LSPR at 1500 nm wavelength and verified the position numerically. By depositing Au-
36 discs on top of the monolayers, we demonstrated good control of the fabrication process which
37 can further be extended to multilayered experiments, and by burying Au-discs in the UCNC
38 monolayers, we determined the possible achievable UCL-enhancement. The maximum five
39 fold UCL enhancement was achieved with the core nanocrystals and a drop with the increase
40
41
42
43
44
45
46
47
48
49
50
51
52
53
54
55
56
57
58
59
60

1
2
3 in the shell thickness was observed in the buried-Au discs configurations.
4
5
6

7 8 **Experimental**

9
10 **Synthesis of $\text{Er}^{3+}:\text{NaYF}_4\text{-NaLuF}_4$ (core-shell) nanocrystals.** The core of Er^{3+} -doped
11 $\beta\text{-NaYF}_4$ nanocrystals were prepared by a solvo-thermal method.⁵⁷ The shells of NaLuF_4
12 around the core were fabricated by the combination of both successive layers growth^{29,30,32}
13 and one-shot injection methods. The successive layers growth method, on the one hand,
14 involves a sequential injection of shell precursors in the hot reaction vessels of the target
15 nanocrystals and the one-shot injection method, on the other hand, only includes one-time
16 injection of shell precursors into the hot reaction vessels of the core nanocrystals for the
17 desired shell thickness. All nanocrystals were structurally characterized by transmission
18 electron microscopy (TEM), X-ray diffraction (XRD), and inductive coupled plasma-optical
19 emission spectroscopy (ICP-OES) and some selective nanocrystals were also analyzed by
20 scanning transmission electron microscopy (STEM) and energy dispersive X-ray spectrom-
21 etry (EDS)-line scan. The details of the synthesis and the results of structural analysis are
22 mentioned in the supporting information, Section 1.
23
24
25
26
27
28
29
30
31
32
33
34
35

36 **Fabrication of UCNC monolayers.** The monolayers of $\text{Er}^{3+}:\text{NaYF}_4\text{-NaLuF}_4$ (core-shell)
37 nanocrystals were developed by a drop-cast assisted spin coating technique. The technique
38 involved the placement of the optimized concentration of colloidal solutions onto quartz fol-
39 lowed by a subsequent rotation at a defined spinning speed. The selection of solvent, the
40 concentration of nanocrystals, and the spinning parameters were optimized to achieve mono-
41 layers for each sample. The experimental details are reported in the supporting information,
42 Section 2. The thickness and the optical constants of monolayers were obtained by ellipsom-
43 etry using a Sentech SE850 PV Spectroscopic Ellipsometer.
44
45
46
47
48
49
50
51

52 **Fabrication of Au-nanodisc-consisting UCNC monolayers.** Electron beam lithogra-
53 phy (EBL) was used for preparing Au nanodiscs with optimized geometries for the LSPR at
54
55
56
57
58
59
60

1
2
3 1500 nm wavelength for all samples. The monolayer formation was performed as described
4
5 in the previous section. Depending on whether the Au-nanodiscs were placed on top of the
6
7 UCNC monolayers or buried within, this work is performed in two ways. In the first case,
8
9 the monolayers were prepared on quartz and heated at 110°C for 15 min in an oven, followed
10
11 by fabrication of the Au-nanodiscs on top of the films. In the second case, the Au-nanodiscs
12
13 were prepared on naked quartz and then monolayers were prepared on top. The annealing
14
15 step was excluded for this purpose.
16

17
18
19 **Optical investigations.** The steady-state UCL spectra were recorded under continuous-
20
21 wave (CW) laser illumination at a wavelength of 1500 nm using a power of 18.9 mW and
22
23 a beam area (full width at half maximum) of 6.5×10^{-5} cm². The monolayers were placed
24
25 inside an integrating sphere to confirm a similar collection efficiency for all UCNCs samples.
26
27 A Princeton Instruments spectrograph, consisting of an Acton SP2358 monochromator and
28
29 a PIXIS:100BR CCD camera captured the emitted light. The time-resolved PL (TRPL)
30
31 measurements were performed using a 35 fs pulsed Ti:sapphire laser with a peak wavelength
32
33 of 800 nm. The TRPL measurements were performed outside the integrating sphere. These
34
35 measurements used two identical Princeton Instruments monochromators with different de-
36
37 tectors. A Hamamatsu R5509-73 photo-multiplier tube (PMT) for 1500 nm luminescence
38
39 detection and a Perkin Elmer avalanche photo diode (APD) single-photon counting module
40
41 for 980 nm luminescence detection. In addition, the wavelength-dependent transmittance
42
43 and reflectance were measured using a Perkin Elmer Lambda 1050 spectrophotometer.
44

45 46 47 **Acknowledgement** 48

49
50 We thank Stefan Fischer and Noah JJ Johnson for nanocrystal synthesis advise, Peter Hald
51
52 and Bo Ritcher for help in chemical synthesis setup preparation, and Aref Mamakhel for
53
54 HR-TEM analysis. This work is supported by Innovation Fund Denmark under the project
55
56
57
58
59
60

Supporting Information Available

The Supporting Information is available free of charge.

Synthesis procedure, structural, and optical characterizations of colloidal solutions of UC-NCs; Fabrication, structural, and optical characterizations of UCNCs monolayers; Sample preparation, structural, and optical characterizations of Au-nanodiscs consisted UCNCs monolayers.

References

- (1) Wang, F.; Banerjee, D.; Liu, Y.; Chen, X.; Liu, X. Upconversion nanoparticles in biological labeling, imaging, and therapy. *Analyst* **2010**, *135*, 1839–1854.
- (2) Liu, Y.; Tu, D.; Zhu, H.; Chen, X. Lanthanide-doped luminescent nanoprobes: controlled synthesis, optical spectroscopy, and bioapplications. *Chemical Society Reviews* **2013**, *42*, 6924–6958.
- (3) Chen, X.; Xu, W.; Song, H.; Chen, C.; Xia, H.; Zhu, Y.; Zhou, D.; Cui, S.; Dai, Q.; Zhang, J. Highly Efficient $\text{LiYF}_4:\text{Yb}^{3+},\text{Er}^{3+}$ Upconversion Single Crystal under Solar Cell Spectrum Excitation and Photovoltaic Application. *ACS Applied Materials & Interfaces* **2016**, *8*, 9071–9079, PMID: 26791114.
- (4) Ramachari, D.; Esparza, D.; López-Luke, T.; Romero, V.; Perez-Mayen, L.; la Rosa, E. D.; Jayasankar, C. Synthesis of co-doped $\text{Yb}^{3+}\text{-Er}^{3+}:\text{ZrO}_2$ upconversion nanoparticles and their applications in enhanced photovoltaic properties of quantum dot sensitized solar cells. *Journal of Alloys and Compounds* **2017**, *698*, 433 – 441.

- 1
2
3
4
5
6
7
8
9
10
11
12
13
14
15
16
17
18
19
20
21
22
23
24
25
26
27
28
29
30
31
32
33
34
35
36
37
38
39
40
41
42
43
44
45
46
47
48
49
50
51
52
53
54
55
56
57
58
59
60
- (5) van Sark, W. G.; de Wild, J.; Rath, J. K.; Meijerink, A.; Schropp, R. E. Upconversion in solar cells. *Nanoscale Research Letters* **2013**, *8*, 81.
 - (6) Goldschmidt, J. C.; Fischer, S. Upconversion for Photovoltaics -a Review of Materials, Devices and Concepts for Performance Enhancement. *Advanced Optical Materials* **2015**, *3*, 510–535.
 - (7) Zhong, H.; Wang, Z.; Lu, W.; Liu, J.; Wang, Y. In *Phosphors, Up Conversion Nano Particles, Quantum Dots and Their Applications: Volume 2*; Liu, R.-S., Ed.; Springer Singapore: Singapore, 2016; pp 503–523.
 - (8) Auzel, F. Upconversion and Anti-Stokes Processes with f and d Ions in Solids. *Chemical Reviews* **2004**, *104*, 139–174, PMID: 14719973.
 - (9) Auzel, F. Upconversion processes in coupled ion systems. *Journal of Luminescence* **1990**, *45*, 341 – 345.
 - (10) Favilla, E.; Cittadino, G.; Veronesi, S.; Tonelli, M.; Fischer, S.; Goldschmidt, J. C.; Cassanho, A.; Jenssen, H. P. Comparative analysis of upconversion efficiencies in fluoride materials for photovoltaic application. *Solar Energy Materials and Solar Cells* **2016**, *157*, 415 – 421.
 - (11) Fischer, S.; Favilla, E.; Tonelli, M.; Goldschmidt, J. C. Record efficient upconverter solar cell devices with optimized bifacial silicon solar cells and monocrystalline BaY₂F₈:30% Er³⁺ upconverter. *Solar Energy Materials and Solar Cells* **2015**, *136*, 127 – 134.
 - (12) Haase, M.; Schäfer, H. Upconverting Nanoparticles. *Angewandte Chemie International Edition* **2011**, *50*, 5808–5829.
 - (13) Nordmann, J.; Buczka, S.; Voss, B.; Haase, M.; Mummenhoff, K. In vivo analysis of the size- and time-dependent uptake of NaYF₄:Yb,Er upconversion nanocrystals by pumpkin seedlings. *Journal of Materials Chemistry B* **2015**, *3*, 144–150.

- 1
2
3
4
5
6
7
8
9
10
11
12
13
14
15
16
17
18
19
20
21
22
23
24
25
26
27
28
29
30
31
32
33
34
35
36
37
38
39
40
41
42
43
44
45
46
47
48
49
50
51
52
53
54
55
56
57
58
59
60
- (14) Naduviledathu Raj, A.; Rinkel, T.; Haase, M. Ostwald Ripening, Particle Size Focusing, and Decomposition of Sub-10 nm NaREF₄ (RE = La, Ce, Pr, Nd) Nanocrystals. *Chemistry of Materials* **2014**, *26*, 5689–5694.
- (15) Agger, S. D.; Povlsen, J. H. Emission and absorption cross section of thulium doped silica fibers. *Optics Express* **2006**, *14*, 50–57.
- (16) Zhang, D.-L.; Sun, W.-B.; Wong, W.-H.; Pun, E. Y.-B. Emission and absorption cross sections of Er³⁺:LiNbO₃ crystal: composition effect. *Optical Materials Express* **2015**, *5*, 1920–1926.
- (17) Wei, W.; Chen, G.; Baev, A.; He, G. S.; Shao, W.; Damasco, J.; Prasad, P. N. Alleviating Luminescence Concentration Quenching in Upconversion Nanoparticles through Organic Dye Sensitization. *Journal of the American Chemical Society* **2016**, *138*, 15130–15133, PMID: 27933882.
- (18) Chen, C.; Li, C.; Shi, Z. Current Advances in Lanthanide-Doped Upconversion Nanostructures for Detection and Bioapplication. *Advanced Science* **2016**, *3*, 1600029.
- (19) Würth, C.; Fischer, S.; Grauel, B.; Alivisatos, A. P.; Resch-Genger, U. Quantum Yields, Surface Quenching, and Passivation Efficiency for Ultrasmall Core/Shell Upconverting Nanoparticles. *Journal of the American Chemical Society* **2018**, *140*, 4922–4928, PMID: 29570283.
- (20) Fischer, S.; Martin-Rodriguez, R.; Frohlich, B.; Kramer, K. W.; Meijerink, A.; Goldschmidt, J. C. Upconversion quantum yield of Er³⁺-doped β -NaYF₄ and Gd₂O₂S: The effects of host lattice, Er³⁺ doping, and excitation spectrum bandwidth. *Journal of Luminescence* **2014**, *153*, 281 – 287.
- (21) Li, X.; Shen, D.; Yang, J.; Yao, C.; Che, R.; Zhang, F.; Zhao, D. Successive Layer-by-Layer Strategy for Multi-Shell Epitaxial Growth: Shell Thickness and Doping Position

- 1
2
3 Dependence in Upconverting Optical Properties. *Chemistry of Materials* **2013**, *25*,
4 106–112.
5
6
7
- 8 (22) Tong, L.; Li, X.; Zhang, J.; Xu, S.; Sun, J.; Zheng, H.; Zhang, Y.; Zhang, X.;
9 Hua, R.; Xia, H.; Chen, B. NaYF₄:Sm³⁺/Yb³⁺@NaYF₄:Er³⁺/Yb³⁺ core-shell struc-
10 tured nanocalorifier with optical temperature probe. *Optics Express* **2017**, *25*, 16047–
11 16058.
12
13
14
15
- 16 (23) Rinkel, T.; Raj, A. N.; Dühnen, S.; Haase, M. Synthesis of 10 nm β -
17 NaYF₄:Yb,Er/NaYF₄ Core/Shell Upconversion Nanocrystals with 5 nm Particle Cores.
18 *Angewandte Chemie International Edition* **2015**, *55*, 1164–1167.
19
20
21
22
- 23 (24) Park, W.; Lu, D.; Ahn, S. Plasmon enhancement of luminescence upconversion. *Chem-*
24 *ical Society Review* **2015**, *44*, 2940–2962.
25
26
27
- 28 (25) Hofmann, C. L. M.; Eriksen, E. H.; Fischer, S.; Richards, B. S.; Balling, P.;
29 Goldschmidt, J. C. Enhanced upconversion in one-dimensional photonic crystals: a
30 simulation-based assessment within realistic material and fabrication constraints. *Op-*
31 *tics Express* **2018**, *26*, 7537–7554.
32
33
34
35
- 36 (26) Niu, W.; Su, L. T.; Chen, R.; Chen, H.; Wang, Y.; Palaniappan, A.; Sun, H.;
37 Yoong Tok, A. I. 3-Dimensional photonic crystal surface enhanced upconversion emis-
38 sion for improved near-infrared photoresponse. *Nanoscale* **2014**, *6*, 817–824.
39
40
41
42
- 43 (27) Johnson, C. M.; Reece, P. J.; Conibeer, G. J. Slow-light-enhanced upconversion for
44 photovoltaic applications in one-dimensional photonic crystals. *Optics Letters* **2011**,
45 *36*, 3990–3992.
46
47
48
49
- 50 (28) Dühnen, S.; Haase, M. Study on the Intermixing of Core and Shell in NaEuF₄/NaGdF₄
51 Core/Shell Nanocrystals. *Chemistry of Materials* **2015**, *27*, 8375–8386.
52
53
54
55
56
57
58
59
60

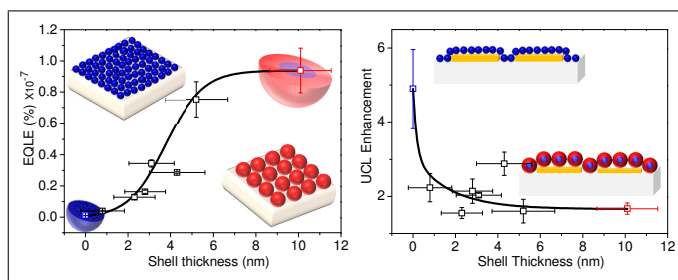
- 1
2
3
4
5
6
7
8
9
10
11
12
13
14
15
16
17
18
19
20
21
22
23
24
25
26
27
28
29
30
31
32
33
34
35
36
37
38
39
40
41
42
43
44
45
46
47
48
49
50
51
52
53
54
55
56
57
58
59
60
- (29) Fischer, S.; Swabeck, J. K.; Alivisatos, A. P. Controlled Isotropic and Anisotropic Shell Growth in β -NaLnF₄ Nanocrystals Induced by Precursor Injection Rate. *Journal of the American Chemical Society* **2017**, *139*, 12325–12332, PMID: 28777550.
- (30) Fischer, S.; Bronstein, N. D.; Swabeck, J. K.; Chan, E. M.; Alivisatos, A. P. Precise Tuning of Surface Quenching for Luminescence Enhancement in Core-Shell Lanthanide-Doped Nanocrystals. *Nano Letters* **2016**, *16*, 7241–7247, PMID: 27726405.
- (31) Johnson, N. J. J.; van Veggel, F. C. J. M. Sodium lanthanide fluoride core-shell nanocrystals: A general perspective on epitaxial shell growth. *Nano Research* **2013**, *6*, 547–561.
- (32) Johnson, N. J. J.; Korinek, A.; Dong, C.; van Veggel, F. C. J. M. Self-Focusing by Ostwald Ripening: A Strategy for Layer-by-Layer Epitaxial Growth on Upconverting Nanocrystals. *Journal of the American Chemical Society* **2012**, *134*, 11068–11071, PMID: 22734596.
- (33) Johnson, N. J. J.; van Veggel, F. C. J. M. Lanthanide-Based Heteroepitaxial Core-Shell Nanostructures: Compressive versus Tensile Strain Asymmetry. *ACS Nano* **2014**, *8*, 10517–10527, PMID: 25289882.
- (34) Saboktakin, M.; Ye, X.; Oh, S. J.; Hong, S.-H.; Fafarman, A. T.; Chettiar, U. K.; Engheta, N.; Murray, C. B.; Kagan, C. R. Metal-Enhanced Upconversion Luminescence Tunable through Metal Nanoparticle-Nanophosphor Separation. *ACS Nano* **2012**, *6*, 8758–8766, PMID: 22967489.
- (35) Ye, X.; Collins, J. E.; Kang, Y.; Chen, J.; Chen, D. T. N.; Yodh, A. G.; Murray, C. B. Morphologically controlled synthesis of colloidal upconversion nanophosphors and their shape-directed self-assembly. *Proceedings of the National Academy of Sciences* **2010**, *107*, 22430–22435.

- 1
2
3
4
5
6
7
8
9
10
11
12
13
14
15
16
17
18
19
20
21
22
23
24
25
26
27
28
29
30
31
32
33
34
35
36
37
38
39
40
41
42
43
44
45
46
47
48
49
50
51
52
53
54
55
56
57
58
59
60
- (36) Wang, F.; Han, Y.; Lim, C. S.; Lu, Y.; Wang, J.; Xu, J.; Chen, H.; Zhang, C.; Hong, M.; Liu, X. Simultaneous phase and size control of upconversion nanocrystals through lanthanide doping. *Nature* **2010**, *463*, 1061–1065.
- (37) Acton, O.; Hutchins, D.; Árnadóttir, L.; Weidner, T.; Cernetic, N.; Ting, G. G.; Kim, T.; Castner, D. G.; Ma, H.; Jen, A. K. Spin-Cast and Patterned Organophosphate Self-Assembled Monolayer Dielectrics on Metal-Oxide-Activated Si. *Advanced Materials* **2010**, *23*, 1899–1902.
- (38) Jiang, C.; Markutsya, S.; Tsukruk, V. V. Collective and Individual Plasmon Resonances in Nanoparticle Films Obtained by Spin-Assisted Layer-by-Layer Assembly. *Langmuir* **2004**, *20*, 882–890, PMID: 15773119.
- (39) Wang, Q.; Ye, L.; Wang, L.; Li, P.; Cao, Y.; Li, Y. Rapid nanopatterning technique based on monolayer silica nanosphere close-packing by spin coating. *Science China Technological Sciences* **2016**, *59*, 1573–1580.
- (40) Toolan, D. T. W.; Fujii, S.; Ebbens, S. J.; Nakamura, Y.; Howse, J. R. On the mechanisms of colloidal self-assembly during spin-coating. *Soft Matter* **2014**, *10*, 8804–8812.
- (41) Wu, D. M.; García-Etxarri, A.; Salleo, A.; Dionne, J. A. Plasmon-Enhanced Upconversion. *The Journal of Physical Chemistry Letters* **2014**, *5*, 4020–4031, PMID: 26276488.
- (42) Schietinger, S.; Aichele, T.; Wang, H.-Q.; Nann, T.; Benson, O. Plasmon-Enhanced Upconversion in Single NaYF₄:Yb³⁺/Er³⁺ Codoped Nanocrystals. *Nano Letters* **2010**, *10*, 134–138, PMID: 20020691.
- (43) Fischer, S.; Hallermann, F.; Eichelkraut, T.; von Plessen, G.; Krämer, K. W.; Biner, D.; Steinkemper, H.; Hermle, M.; Goldschmidt, J. C. Plasmon enhanced upconversion luminescence near gold nanoparticles-simulation and analysis of the interactions: Errata. *Optics Express* **2013**, *21*, 10606–10611.

- 1
2
3
4
5
6
7
8
9
10
11
12
13
14
15
16
17
18
19
20
21
22
23
24
25
26
27
28
29
30
31
32
33
34
35
36
37
38
39
40
41
42
43
44
45
46
47
48
49
50
51
52
53
54
55
56
57
58
59
60
- (44) Lakhotiya, H.; Nazir, A.; Madsen, S. P.; Christiansen, J.; Eriksen, E.; Vester-Petersen, J.; Johannsen, S. R.; Jeppesen, B. R.; Balling, P.; Larsen, A. N.; Julsgaard, B. Plasmonically enhanced upconversion of 1500 nm light via trivalent Er in a TiO₂ matrix. *Applied Physics Letters* **2016**, *109*, 263102.
- (45) Møller, S. H.; Vester-Petersen, J.; Nazir, A.; Eriksen, E. H.; Julsgaard, B.; Madsen, S. P.; Balling, P. Near-field marking of gold nanostars by ultrashort pulsed laser irradiation: experiment and simulations. *Applied Physics A* **2018**, *124*, 210.
- (46) Feng, A. L.; You, M. L.; Tian, L.; Singamaneni, S.; Liu, M.; Duan, Z.; Lu, T. J.; Xu, F.; Lin, M. Distance-Dependent Plasmon-Enhanced Fluorescence of Upconversion Nanoparticles using Polyelectrolyte Multilayers as Tunable Spacers. *Scientific Reports* **5**, 7779.
- (47) Liu, X.; Yuan Lei, D. Simultaneous excitation and emission enhancements in upconversion luminescence using plasmonic double-resonant gold nanorods. *Scientific Reports* **2015**, *5*, 15235.
- (48) Wang, Y.-L.; Mohammadi Estakhri, N.; Johnson, A.; Li, H.-Y.; Xu, L.-X.; Zhang, Z.; Alù, A.; Wang, Q.-Q.; Shih, C.-K. K. Tailoring Plasmonic Enhanced Upconversion in Single NaYF₄:Yb³⁺/Er³⁺ Nanocrystals. *Scientific Reports* **2015**, *5*, 10196.
- (49) Khanal, B. P.; Zubarev, E. R. Purification of High Aspect Ratio Gold Nanorods: Complete Removal of Platelets. *Journal of the American Chemical Society* **2008**, *130*, 12634–12635, PMID: 18754620.
- (50) Xu, X.; Zhao, Y.; Xue, X.; Huo, S.; Chen, F.; Zou, G.; Liang, X.-J. Seedless synthesis of high aspect ratio gold nanorods with high yield. *Journal of Materials Chemistry A* **2014**, *2*, 3528–3535.
- (51) Jensen, T. R.; Malinsky, M. D.; Haynes, C. L.; Van Duyne, R. P. Nanosphere Lithog-

- 1
2
3 raphy: Tunable Localized Surface Plasmon Resonance Spectra of Silver Nanoparticles.
4
5 *The Journal of Physical Chemistry B* **2000**, *104*, 10549–10556.
6
7
- 8 (52) Chan, G. H.; Zhao, J.; Hicks, E. M.; Schatz, G. C.; Van Duyne, R. P. Plasmonic Prop-
9 erties of Copper Nanoparticles Fabricated by Nanosphere Lithography. *Nano Letters*
10 **2007**, *7*, 1947–1952.
11
12
- 13 (53) Jensen, T. R.; Schatz, G. C.; Van Duyne, R. P. Nanosphere Lithography: Surface
14 Plasmon Resonance Spectrum of a Periodic Array of Silver Nanoparticles by Ultraviolet-
15 Visible Extinction Spectroscopy and Electrodynamics Modeling. *The Journal of Physical*
16 *Chemistry B* **1999**, *103*, 2394–2401.
17
18
- 19 (54) Weihua, Z.; Fei, D.; Stephen, Y. C. Large Enhancement of Upconversion Lumines-
20 cence of NaYF₄:Yb³⁺/Er³⁺ Nanocrystal by 3D Plasmonic Nano-Antennas. *Advanced*
21 *Materials* **2012**, *24*, OP236–OP241.
22
23
- 24 (55) Lakhotiya, H.; Christiansen, J. D.; Hansen, J. L.; Balling, P.; Julsgaard, B. *Journal of*
25 *Applied Physics Submitted*
26
27
- 28 (56) Balling, P. et al. Improving the efficiency of solar cells by upconverting sunlight using
29 field enhancement from optimized nano structures. *Optical Materials* **2018**, *83*, 279.
30
31
- 32 (57) Li, Z.; Zhang, Y. An efficient and user-friendly method for the synthesis of hexagonal-
33 phase NaYF₄: Yb, Er/Tm nanocrystals with controllable shape and upconversion flu-
34 orescence. *Nanotechnology* **2008**, *19*, 345606.
35
36
37
38
39
40
41
42
43
44
45
46
47
48
49
50
51
52
53
54
55
56
57
58
59
60

Graphical TOC Entry



SUPPORTING INFORMATION

Resonant Plasmon-Enhanced Upconversion in Monolayers of Core-Shell Nanocrystals: Role of Shell Thickness

Harish Lakhotiya,[†] Adnan Nazir,[†] Søren Roesgaard,[†] Emil Eriksen,[†] Jeppe
Christiansen,[†] Martin Bondesgaard,[‡] Frank C.J.M. van Veggel,[¶] Bo
Brummerstedt Iversen,^{‡,§} Peter Balling,^{†,§} and Brian Julsgaard^{*,†,§}

[†]*Department of Physics and Astronomy, Aarhus University, DK-8000 Aarhus C, Denmark*

[‡]*Department of Chemistry, Aarhus University, DK-8000 Aarhus C, Denmark*

[¶]*Department of Chemistry, University of Victoria, Victoria BC, Canada*

[§]*Interdisciplinary Nanoscience Center (iNANO), Aarhus University, DK-8000 Aarhus C,
Denmark*

E-mail: brianj@phys.au.dk

Section 1: Colloidal solution of nanocrystals

1.1: Synthesis of nanocrystals

1.1.1: Precursors

Yttrium acetate hydrate $\text{Y}(\text{CH}_3\text{CO}_2)_3 \cdot x\text{H}_2\text{O}$ (99.9%), erbium acetate hydrate $\text{Er}(\text{CH}_3\text{CO}_2)_3 \cdot x\text{H}_2\text{O}$ (99.9%), lutetium oxide Lu_2O_3 (99.9%), sodium trifluoroacetate NaCF_3CO_2 (98%), sodium

hydroxide NaOH ($\geq 98\%$), ammonium fluoride NH_4F ($\geq 99.9\%$), trifluoroacetic acid $\text{CF}_3\text{CO}_2\text{H}$ (99%), and oleic acid (90%) were purchased from Sigma-Aldrich. Oleylamine (80-90%) and 1-octadecene (90%) were purchased from Acros Organics and TCI Deutschland, respectively. All the chemicals were used without further purification.

1.1.2: Synthesis of the core nanocrystals

The synthesis of $\text{Er}^{3+}:\beta\text{-NaYF}_4$ core nanocrystals was performed as published by Li *et al.*¹ and Fischer *et al.*^{2,3} with minor modifications. For the fabrication of 5 mmol, 20 mol % Er^{3+} -doped core nanocrystals, the acetate precursors of yttrium (4 mmol) and erbium (1 mmol) were mixed into a 250 mL three-neck flask filled with 25 mL oleic acid and 90 mL 1-octadecene. The solution was heated at a constant 125°C under vacuum for approximately one hour which turned the solution translucent. The solution was cooled down to room temperature afterwards. Simultaneously, another solution of 20 mmol ammonium fluoride and 12.5 mmol sodium hydroxide in a 40 mL methanol was prepared in a vial under a constant 30 min stirring, ensuring that all fluoride was consumed completely. The prepared methanol solution was added drop-wise into the reaction vessel filled with lanthanide precursors and stirred for 45 min. Subsequently, the prepared turbid solution was heated to 70°C with open necks to evaporate methanol, further heated for 10 min to 100°C under argon flow to remove residual water, and then the solution was heated for 90 min with the rate of $18\text{-}20^\circ\text{C}/\text{min}$ to 300°C under argon atmosphere and a constant stirring. The rotation speed and the geometry of the magnetic needle were the deciding parameters in the stirring for the size determination of the nanocrystals. Here, we worked with a spindle shaped, medium sized needle with a 1100 rpm rotation speed to achieve the desired size of the structures. Next, the heating was turned off and the flask was detached from the heating element to let the solution cool down to room temperature. After storing 4 mmol amount of the solution, 1 mmol solution was precipitated in absolute ethanol and collected by centrifuge. The process is repeated 3 times to ensure the proper wash of the core nanocrystals. The collected precipitate was then

dispersed in 10 mL hexane.

1.1.3: Growth of shell

Preparation of shelling precursor

In the process, we prepared the fluoro-acetate precursor of lutetium from the commercial oxide. We dissolved 5 mmol lutetium oxide in 25 mL trifluoroacetic acid and 75 mL distilled water in a 250 mL three-neck flask. This solution was heated in a condenser column to 90 °C overnight (8-10 hours) in an oil bath. The milky solution became transparent after the dissolution of Lu_2O_3 during the evaporation-condensation process. The excess trifluoroacetic acid and water from the transparent solution were removed by evaporating at 65 °C after removing the condenser column. Heating of around 5 hours provided a white powder of 10 mmol $\text{Lu}(\text{CF}_3\text{CO}_2)_3$. The prepared powder was added into a 10 mL oleic acid, 15 mL 1-octadecene, and 2.5 mL oleylamine filled flask. The heating at 120 °C temperature in vacuum made the solution clear but yellowish in color. Afterwards, the solution was cooled down and transferred to a vial. The prepared solution was stored for the shell formation process. Similarly, another solution of 10 mmol of sodium trifluoroacetate in 7.5 mL oleic acid and 7.5 mL 1-octadecene were prepared at the same temperature and conditions. The heating was turned off after obtaining a clear solution. The liquid was stored into a vial for the shell formation process. Both precursor solutions were mixed in an equal volumetric ratio to make the shelling precursor solution soon before the injection to grow the $\beta\text{-NaLuF}_4$ shell.

The shell formation

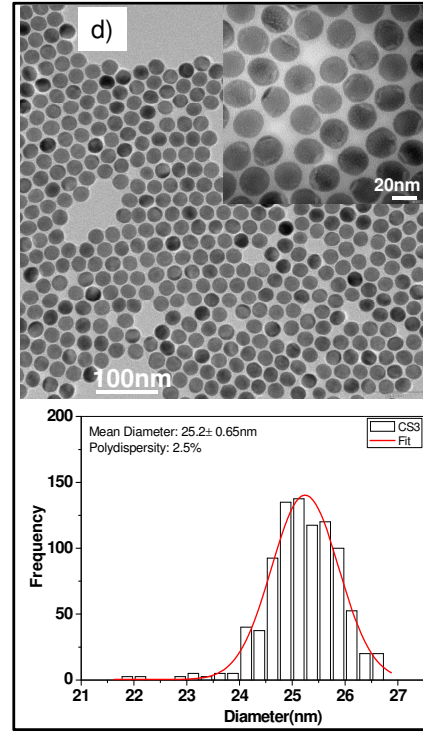
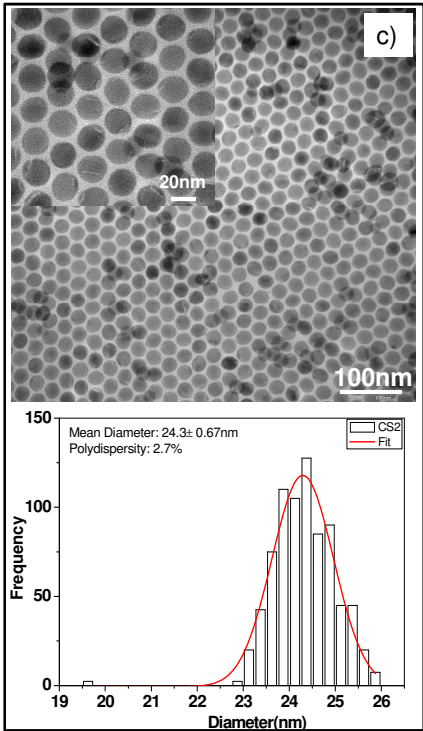
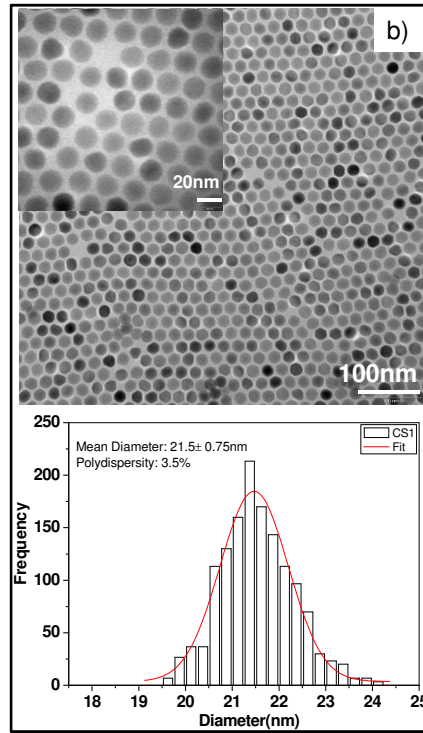
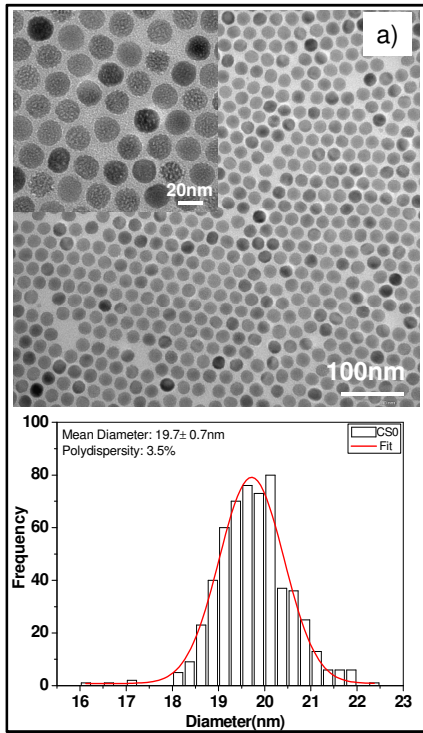
The NaLuF_4 shells around the core were fabricated by a combination of both one-shot injection⁴ and successive layers growth^{3,4} methods. In the one-shot injection method, we prepared 4 subsolutions of 1 mmol each from the 4 mmol of unwashed core nanocrystals solution. Each core nanocrystals subsolution was then used for the core-shell nanocrystals formation by developing the desired shell thickness. The 1 mmol unwashed core nanocrystals

was taken into a 100 mL three-neck flask and then heated quickly (20 °C/min) to 300 °C under a constant argon flow. The injected amount of the shelling precursor was based on the desired shell thickness, and the volumetric concentration and size of the core nanocrystals. The shelling precursor was added in one-shot through the septum of one neck of the flask. Depending upon the injected amount, the time for the decomposition of trifluoroacetate to grow a NaLuF₄ shell varied from 5 min to 15 min. For the one-shot procedure we targeted 1, 3, 5, and 10 nm shell thickness around the core. The prepared core-shell nanocrystals were collected by the steel syringe (appropriate for extracting 300 °C hot solutions) into the glass vials. After extracting the volumetric half (equivalent to 0.5 mmol nanocrystals) of the prepared mixture from each subsolutions, the remaining 0.5 mmol of newly prepared core-shell nanocrystals of each subsolutions were used for the successive layered growth method. In this procedure, the shelling precursor is added again in one-shot to the remaining mixture of each subsolution which is already at 300 °C. After the 5-10 min period (depending upon the amount of added precursor), the solution is cooled down. With the layered growth, we targeted 2, 4, 6, and 11 nm shell thickness around the core by making 1 nm shell around the one-shot method prepared core-shell nanocrystals. Now, all core-shell samples were precipitated in ethanol and centrifuged at 7000 rpm for 10 min in Sigma 2-16P centrifuge with a fixed-angle 12181 rotor. The cleaning process has been repeated 2 more times and the sediments of each solution were dispersed into 10 ml hexane. The combination of these two techniques allowed us to fabricate multiple samples with minimal efforts in ensuring the isotropic shell compared to the successive layered growth method used in Fischer et.al.³

1.2: Structural characterizations

The fabricated nanocrystals were structurally characterized by transmission electron microscope (TEM), scanning transmission electron microscopy (STEM), energy dispersive X-ray spectroscopy (EDS)-line scan, X-ray diffraction (XRD), and inductive coupled plasma optical emission spectroscopy (ICP-OES) techniques. The TEM images were captured by Technai

G2 Spirit Twins instrument whereas the HR-TEM images of the representative samples (CS0, CS3, and CS10), presented in the letter, were taken by a FEI Talos F200X instrument. The TEM images and the corresponding size distributions of the core and the core-shell nanocrystals, and the measured shell thicknesses are shown in Figure S1. The polydispersity of the nanocrystals are maintained $< 5\%$ in all samples. From the TEM micrographs and the size distributions, we can claim that the shell formation is nearly isotropic. Table S1 consists of the targeted (from the synthesis) and achieved (acquired from TEM results) shell thicknesses of the fabricated UCNCs. The color and name codes are given to the samples and maintained in all presented figures.



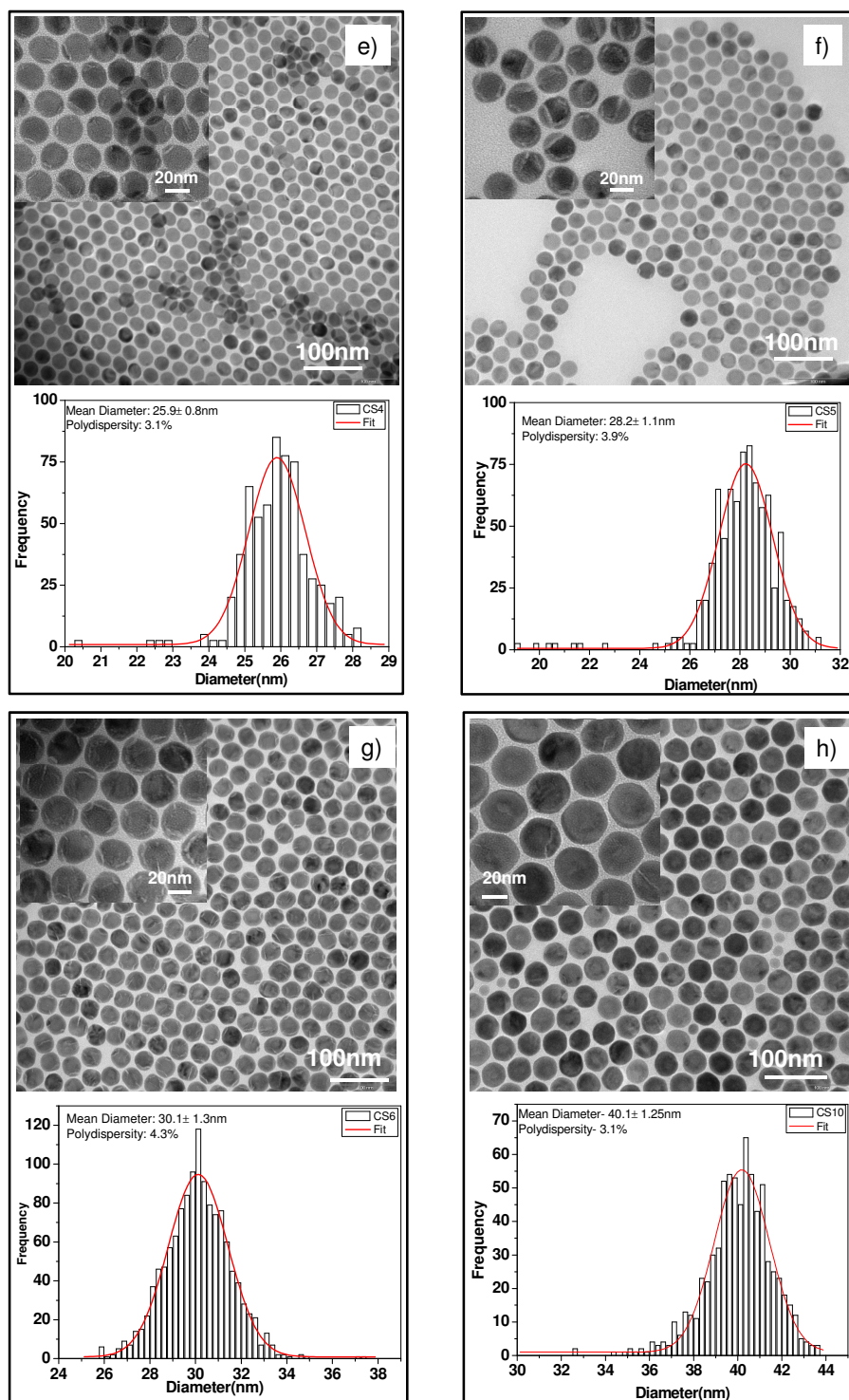


Figure S1: Transmission electron micrographs and the associated particle size distributions of all UCNCs. From (a) to (h): the core (CS0) and the core with increasing shell thickness UCNCs. The magnified TEMs are in the top-corners of each micrograph.

The STEM images are captured by the same TEM instrument (FEI Talos F200X instrument) in STEM mode. It was performed on two representative UCNCs samples: Core with thin shell (2.8 nm shell thickness) and with thick shell (10.1 nm shell thickness). Figure S2 shows the distinct presence of both core and shell as dark and bright regions in the images. It is clear that the formation of the shell around the core is uniform in both lower and higher shell thickness growth.

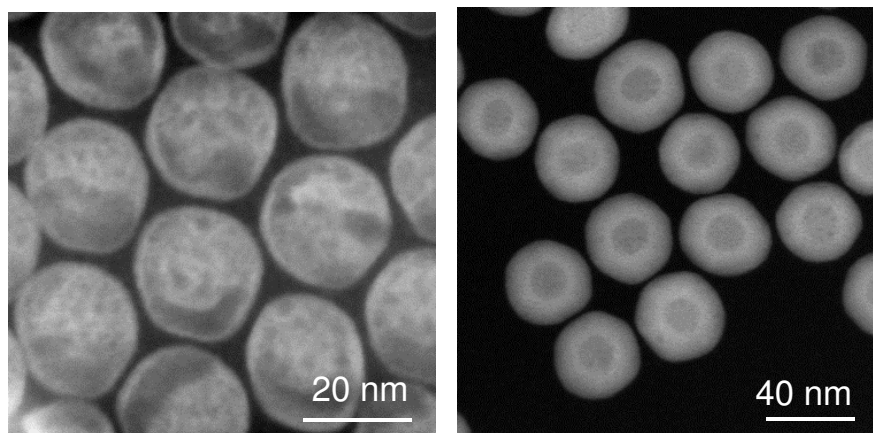


Figure S2: STEM images of core with shell of 2.8 nm (left) and shell of 10.1 nm (right) UCNCs. The core (dark) and shell (bright) are visible in both images.

EDS-line scan were performed in order to confirm the presence of Y and Lu in the core and shells, respectively. In Figure S3, we show the distributions of both Y and Lu across a single core with 10.1 nm shell nanocrystal. It is clear that the Y located in the core of the particle and Lu is in the shell.

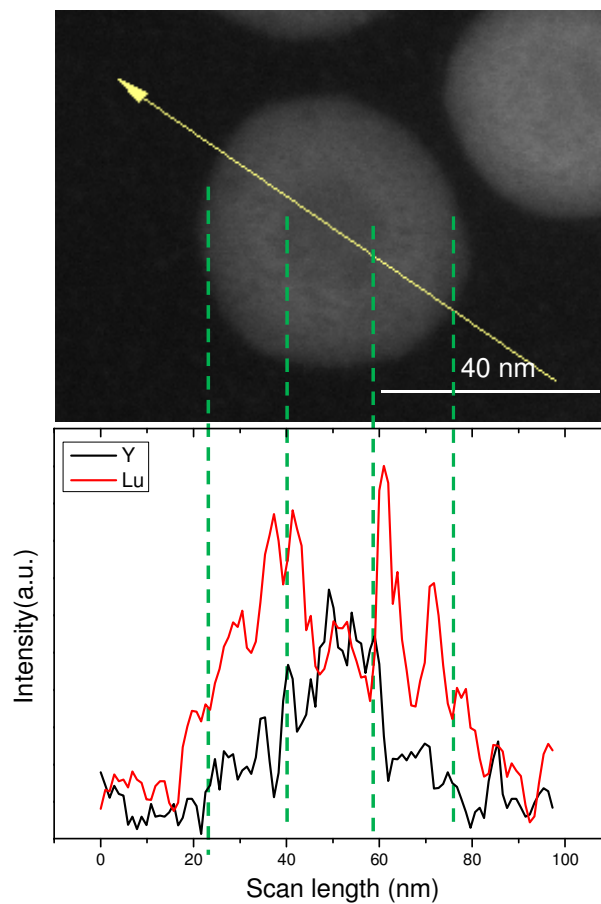


Figure S3: EDS line scan across a single $\text{NaYF}_4\text{-NaLuF}_4$ core-shell UCNC presenting distributions of Y and Lu.

Table S1: The name and color codes are given and maintained for all UCNCs in both their solution and monolayer configurations throughout the Supporting Information. The targeted and achieved shell thickness are associated presented.

Sample name	Targeted shell thickness (nm)	Achieved shell thickness (nm)	Color code
CS0	0.0	0.0	Blue
CS1	1.0	0.8	Black
CS2	2.0	2.3	Cyan
CS3	3.0	2.8	Green
CS4	4.0	3.1	Orange
CS5	5.0	4.3	Wine
CS6	6.0	5.2	Dark cyan
CS10	10.0	10.1	Red

Powder X-ray diffraction (PXRD) using Cu $K\alpha$ radiation in the Bragg–Brentano geometry (Bruker D8 Discover), confirms that the samples are crystalline and that two phases are present in the samples when compared to the peak positions from the database. Figure S4 shows a clear right-shift in the peak positioning going from core UCNCs with the dominance of β -NaYF₄ to core-shell UCNCs where β -NaLuF₄ introduces and gets dominant over β -NaYF₄ with increasing shell thickness. The gradual shift in peak positioning occurs due to gradual compression of the core by the epitaxially grown β -NaLuF₄ shell.

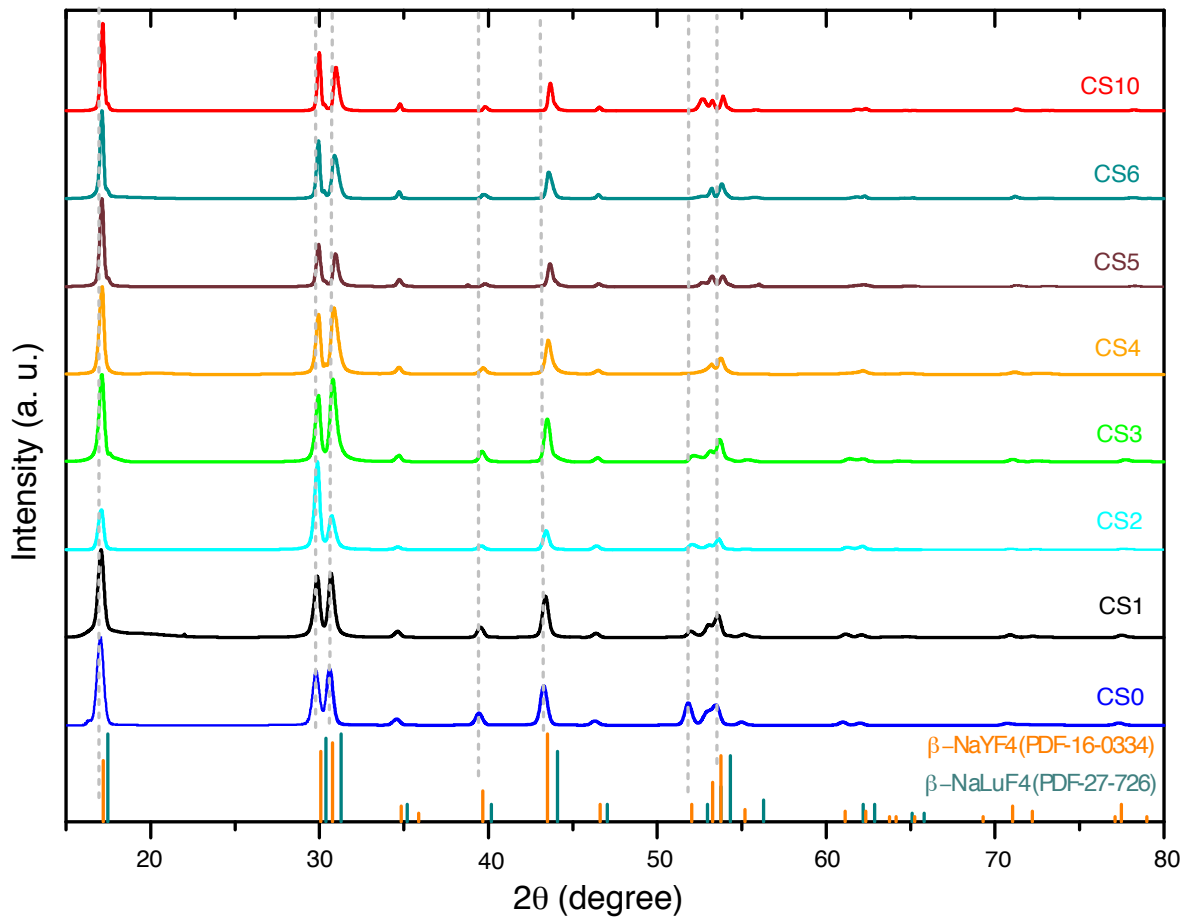


Figure S4: XRD patterns of the core and core-shell upconverting nanocrystals with different shell thicknesses as indicated. The ICDD pdf (powder diffraction file) database of NaLuF₄ and NaYF₄ are mentioned.

The elemental composition of the UCNCs was determined by inductive coupled plasma optical emission spectroscopy, presented in Table S2. The concentration of the dopant varied $< 2\%$ throughout the samples. The amount of erbium precursor was added to achieve 20 at% concentration of Er³⁺ ions however, the average achieved concentration is 17.5 at%, which is in an acceptable error range.

Table S2: Nanocrystal composition of erbium and yttrium as measured by inductive coupled plasma optical emission spectroscopy (ICP-OES). The average and expected values of both elements are mentioned. The last column has the ratio of both.

Sample	Y(mol%)	Er(mol%)	Y/Er ratio
CS0	83.00±0.20	17.00±0.06	4.88
CS1	83.20±0.16	16.76±0.12	4.96
CS2	82.80±0.45	17.20±0.07	4.81
CS3	82.70±0.65	17.30±0.04	4.77
CS4	82.70±0.80	17.20±0.08	4.80
CS5	82.67±0.97	17.30±0.07	4.77
CS6	81.57±0.70	18.40±0.55	4.42
CS10	81.40±0.70	18.60±0.15	4.37
Average	82.76	17.50	4.72
Expected	80	20	4

1.3: Optical characterizations

The steady-state UCL experiments on colloidal UCNCs were excluded due to previously reported similar results of Fischer et.al.³ Time-resolved photoluminescence (TRPL) experiments, on the other side, were performed on the UCNCs in toluene using a femtosecond laser with a peak wavelength at ~ 800 nm to excite the $^4I_{9/2}$ energy-level of Er^{3+} ions. The transition of $^4I_{11/2} \rightarrow ^4I_{15/2}$ and $^4I_{13/2} \rightarrow ^4I_{15/2}$ were recorded and are presented in Figure S5. All the decay curves obtained from TRPL are fitted with the single-exponential decay with an initial exponential rise factor, the details of the fit are explained in the letter. It is important to note that the amplitudes of the decay curves are not comparable due to an unknown

concentration of the colloidal solutions. However, the lifetimes are comparable and reported in Figure 2 of the letter.

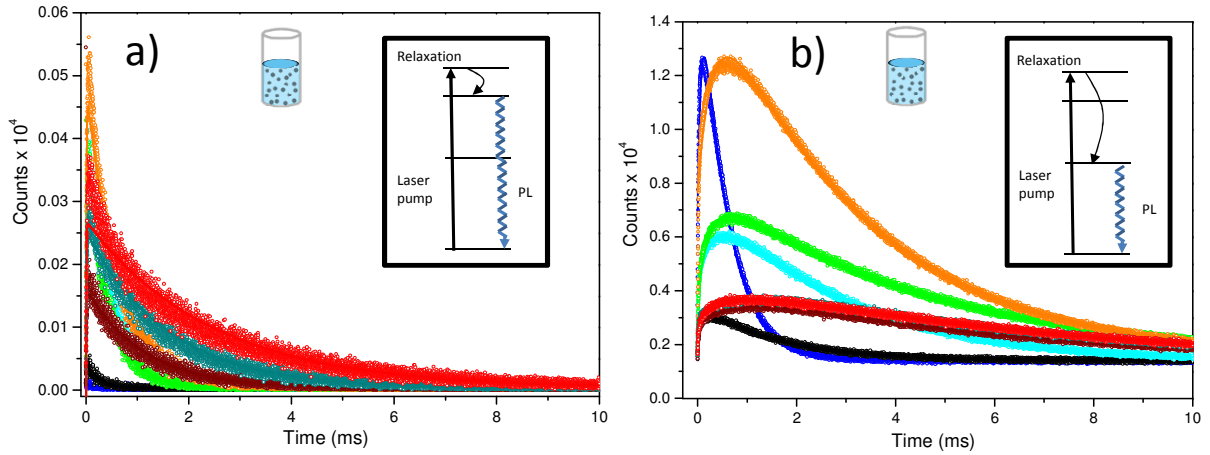


Figure S5: Decay curves from the ${}^4I_{11/2} \rightarrow {}^4I_{15/2}$ (presented in (a)) and the ${}^4I_{13/2} \rightarrow {}^4I_{15/2}$ (presented in (b)) transitions of colloidal UCNCs. The color code is in agreement with Table S1. The insets of each panel give a schematic representation of the involved excitation and emission processes. The data are fitted with a model (described in the text) and represented by the same colored curves in both panels. The non-zero background levels are due to dark counts in the detectors.

Section 2: Monolayers of nanocrystals

2.1: Fabrication of monolayers

The UCNC monolayer fabrication was performed with the colloidal solution of UCNC in toluene. The choice of the solvent was based on its boiling point and viscosity. The lower boiling point of hexane and the higher viscosity of dimethyl sulfoxide (DMSO) excluded these solvents as a choice for the continuous monolayer formation. Therefore, the hexane from the fabricated colloidal solution of UCNCs was evaporated first by Ar-flow and then a new colloidal solution of the UCNCs was prepared with toluene. The substrate surface cleaning is one of the prerequisites for obtaining a uniform monolayer. In the drop-cast assisted spin-coating technique, an equal volume but an unequal concentration of colloidal UCNCs were spread on quartz. An optimized concentration of the core UCNCs for a monolayer

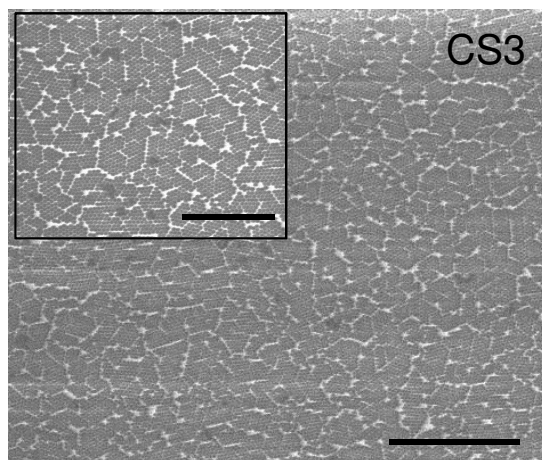
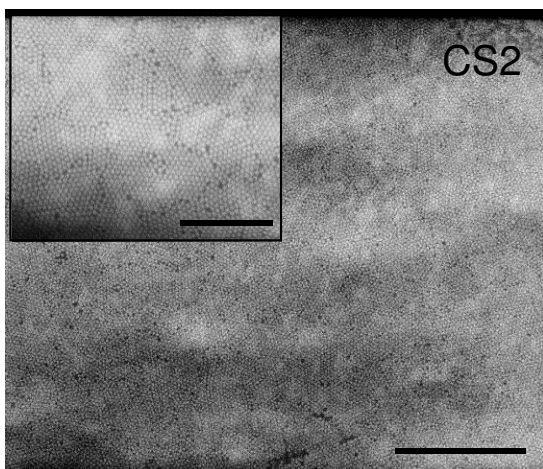
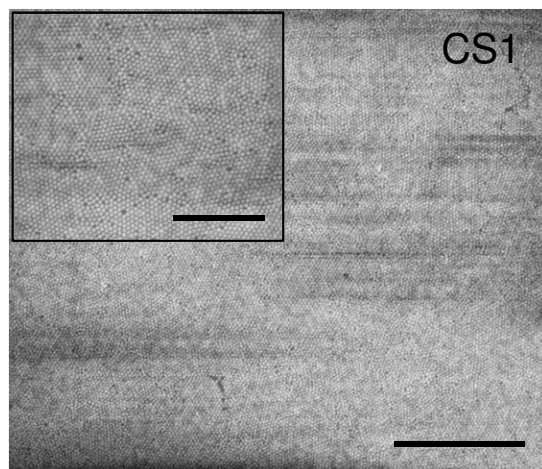
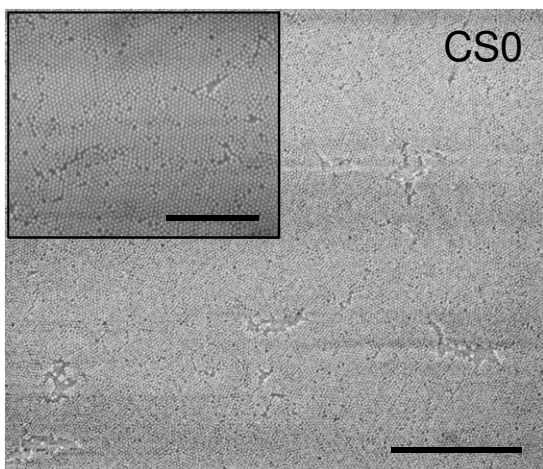
formation was obtained by trial and error. The required concentration obtained for the core-only particles and knowledge of the size of the targeted core-shell UCNCs allowed the formation of monolayers for all samples using a simple calculation. As the shell thickness increased, the size of the particle got bigger and that reduced the number on a fixed and defined (10 X 12 mm²) area of quartz. The calculation is as follows:

$$C_{CSx} = C_{CS0} \cdot (A_{CS0}/A_{CSx}), \quad (1)$$

where C and A represent the concentration and size of nanocrystals in their solutions. The spinning of the solution was proceeded at optimized parameters of the spin coater. The spinning parameters were optimized for core UCNCs by the trial and error and kept constant (rotation speed 2500 rpm and acceleration 500 rpm for 40 s duration) for other UCNCs. The fluid thinning occurred due to both shear forces and evaporation of the solvent, resulting in the formation of a dry film within a matter of seconds. The narrow size distributions (see the histograms of Figure S1) of all the nanocrystal solutions helped in achieving monolayers. The monolayer was obtained at the center of the rotation in an approximately 2×2 mm² area of the substrate and a gradient in thickness has been observed afterwards. The maximum observed thickness at the corners were 1.5 monolayers. The post-deposition processes of the films were performed based on the next stage processes. The deposition of Au-nanodiscs on top of the films demands the chemical and thermal stability. The stabilities were ensured by dipping the sample in acetone with some mechanical stresses and by drying the films in an uniform heating environment of an oven at the temperature of 110 °C. The deposition of a UCNC monolayer on top of the Au-decorated quartz, in contrast, did not require any thermal or chemical treatments. We did not see any significant structural and optical changes in the monolayers after being chemically and thermally treated, except for the formation of some nanosized cracks in the films shown in Figure S8. The optical comparison between untreated and thermally treated monoalyers are shown in Figure S10(b).

2.2: Structural characterization of monolayers

Scanning Electron Micrographs (SEMs) of all UCNC monolayers are presented in Figure S6. It is evident that the arrangements of the monolayers are different for different monolayers. However, the domains are created in thin-shelled UCNC monolayers whereas the arrangements are more random in thick-shelled UCNC monolayers as mentioned in the letter.



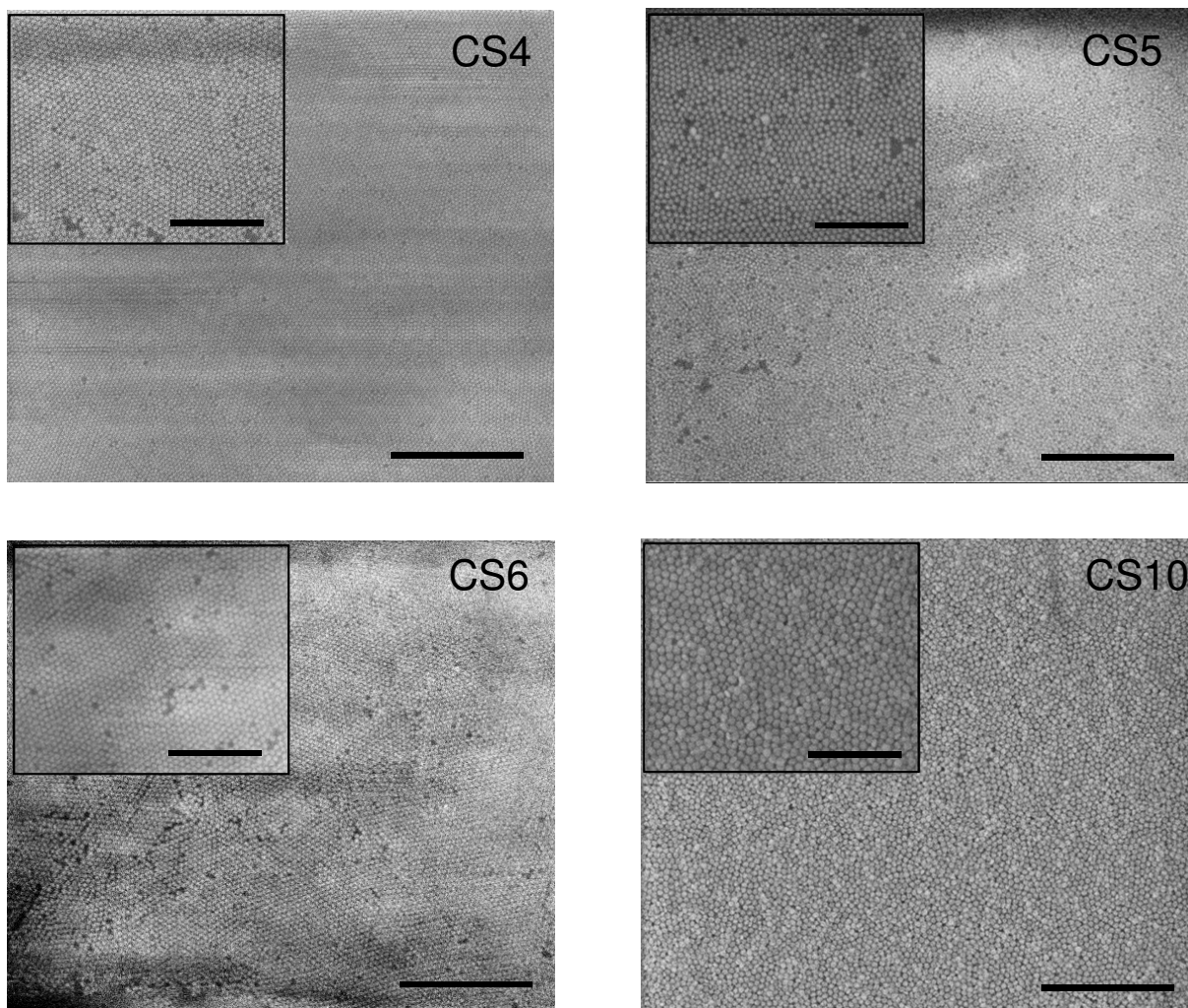


Figure S6: Scanning electron micrographs (SEMs) of UCNC monolayers deposited on quartz. The sample names, linked with Table S1, are given in each image. The scale bar is $1\ \mu\text{m}$. The black regions of the SEMs are substrate in all the images except the image of sample CS3, where the white regions are substrate. The magnified SEMs are in the top corner of each image with a scale bar of 500 nm.

2.3: Optical characterizations of monolayers

The upconversion luminescence (UCL) experiments were performed on all UCNC monolayers and the results are presented in the letter.

2.3.2: Time-resolved photoluminescence (TRPL) measurements

TRPL experiments were performed exactly in the same way as performed for the colloidal solutions. The decay curves are presented in Figure S7. The decay curves of the transition ${}^4I_{11/2} \rightarrow {}^4I_{15/2}$ are fitted with a single-exponential decay and the transition ${}^4I_{13/2} \rightarrow {}^4I_{15/2}$ with a single-exponential decay with an initial exponential rise factor, the details of both models are presented in the letter.

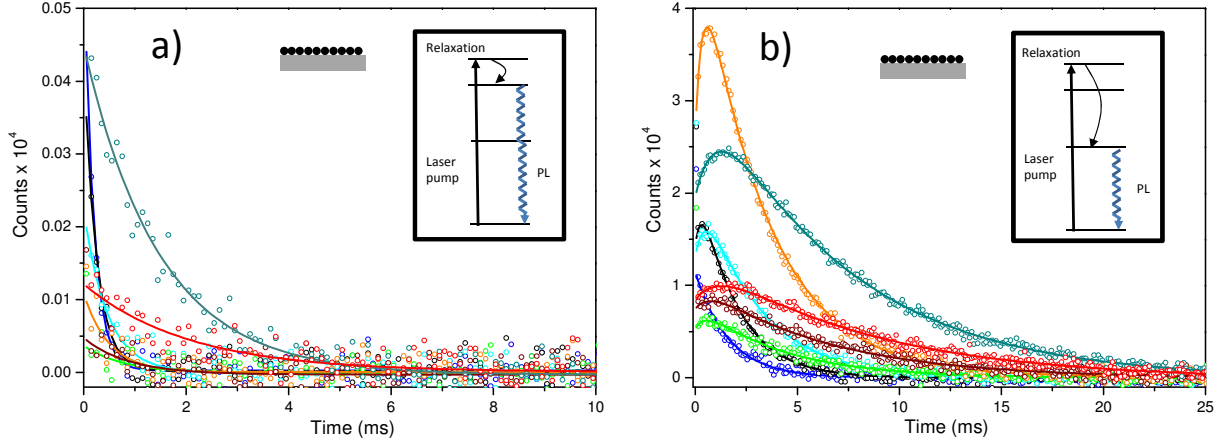


Figure S7: Decay curves from the ${}^4I_{11/2} \rightarrow {}^4I_{15/2}$ (presented in (a)) and ${}^4I_{13/2} \rightarrow {}^4I_{15/2}$ (presented in (b)) transitions of UCNC monolayers. The color code is in agreement with Table S1. The insets of each panel give a schematic representation of the involved excitation and emission processes. The data are fitted with the models (described in the text) represented by the corresponding colored curves in both panels.

Section 3: Nanocrystal monolayers with Au-nanodiscs

3.1: Electron beam lithography (EBL) process

The fabrication of Au-nanodiscs via the EBL process both on top of UCNC monolayers and on quartz was exactly the same. The EBL process was performed with a 30 kV FEI Magellan scanning electron microscopy equipped with a Raith pattern generator. The e-beam patterning was performed by a polymethylmethacrylate (PMMA) mask. A combination of both methyl isobutyl ketone and isopropanol (IPA) was used for dissolving the patterned

part of the mask and pure IPA was used as a stopper. The deposition of Au on the patterned substrates was performed by an e-gun evaporation. Finally, the unexposed mask was dissolved in acetone and Au nanodiscs of size ranging between 350 nm to 430 nm were prepared to achieve LSPR of Au-discs at 1500 nm wavelength.

3.2: Structural characterizations

The SEMs of Au-discs buried in UCNC monolayers are shown in the letter, so here we present the SEMs of Au-discs on top of the representative monolayers in Figure S8. The cracks in the CS0 sample are bigger than the other two due to intense heating effects. However, the observed cracks do not impede the EBL process. The distributions of Au-discs were kept random with $\sim 1\mu\text{m}$ minimum distance between any two discs. The optimized diameter of the discs for LSPR at 1500 nm wavelength were achieved by the trial and error.

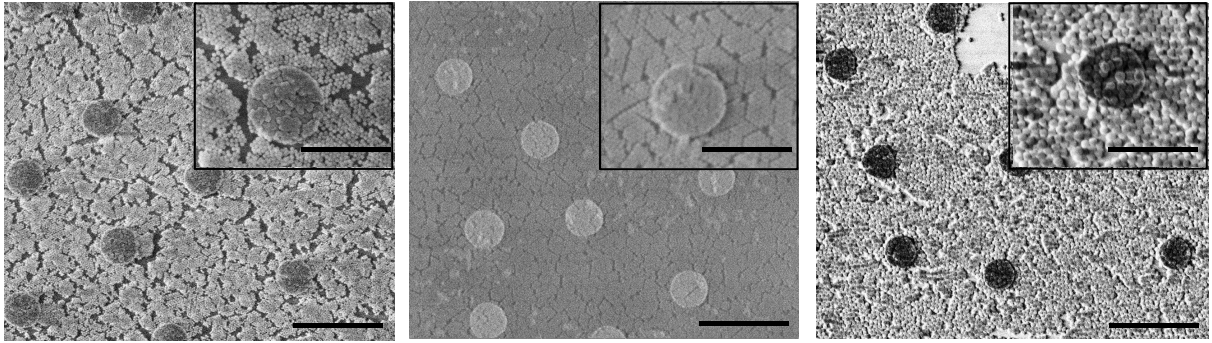


Figure S8: Scanning electron micrographs (SEMs) of Au-nanodiscs on top of the representative UCNC monolayers. From left to right : Core UCNC monolayer and core-shell UCNC monolayers with 2.8 and 10.1 nm shell thickness. The scale bar is $1\ \mu\text{m}$. The magnified SEMs are in the top corner of the each image with a scale bar of 500 nm. The size of the Au-discs was varied from ~ 370 nm to 430 nm to achieve LSPR of the discs at 1500 nm wavelength.

3.3: Optical characterizations

3.3.1: Extinction measurements

From the transmittance and reflectance measurements, we determined the extinction of the monolayers with both configurations of Au-nanodiscs, presented in Figure S9. The method for the calculation of the extinction was given in the letter.

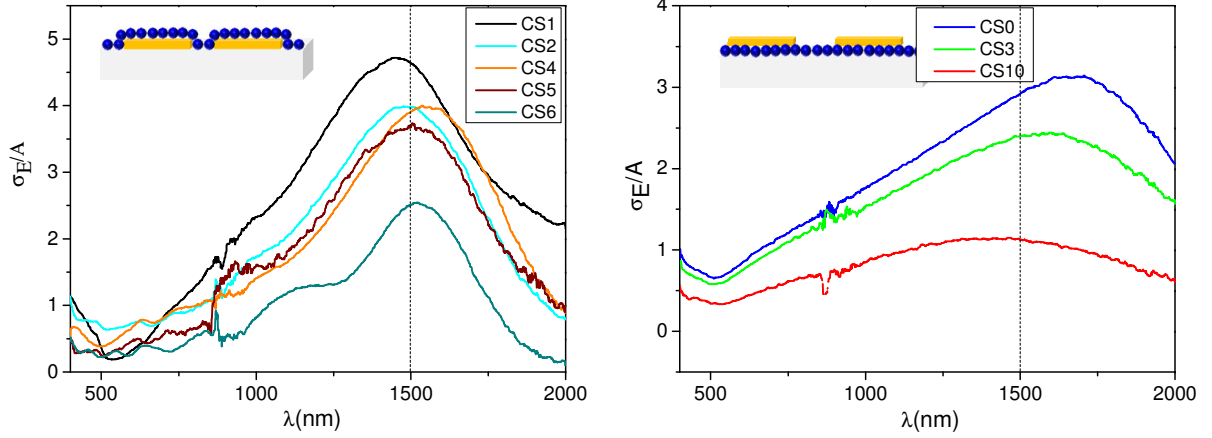


Figure S9: The experimental variation in extinction with the emission wavelength. The left panel shows the schematic representations of a buried-Au discs in an UCNC monolayer and the associated extinction plots of all the monolayers except the representative samples. The right panel shows the extinction of only the representative nanocrystals, but with the Au-discs deposited on top of the monolayer configuration. The color code is in agreement with Table S1. The vertical-dashed lines of both panels indicate the desired LSPR peak position at 1500 nm resonant with the ${}^4I_{13/2} \rightarrow {}^4I_{15/2}$ transition.

3.3.1: Steady-state upconversion measurements

The UCL results of the different stages of the fabrication process, where Au-discs are deposited on top of UCNC monolayers, are presented here. Figure S10(a) shows the schematic representation of the samples developed at different stages of the fabrication. The obtained UCL results from these samples are presented in Figure S10(b) and (c). It is evident that the luminescence of the sample drops to about half after the e-beam exposure, whereas the thermal treatment does not affect the performance. Figure S10(c) shows a consistency in the UCL-drop due to the e-beam exposure and a negligible UCL-enhancement from Au-discs in

the representative samples.

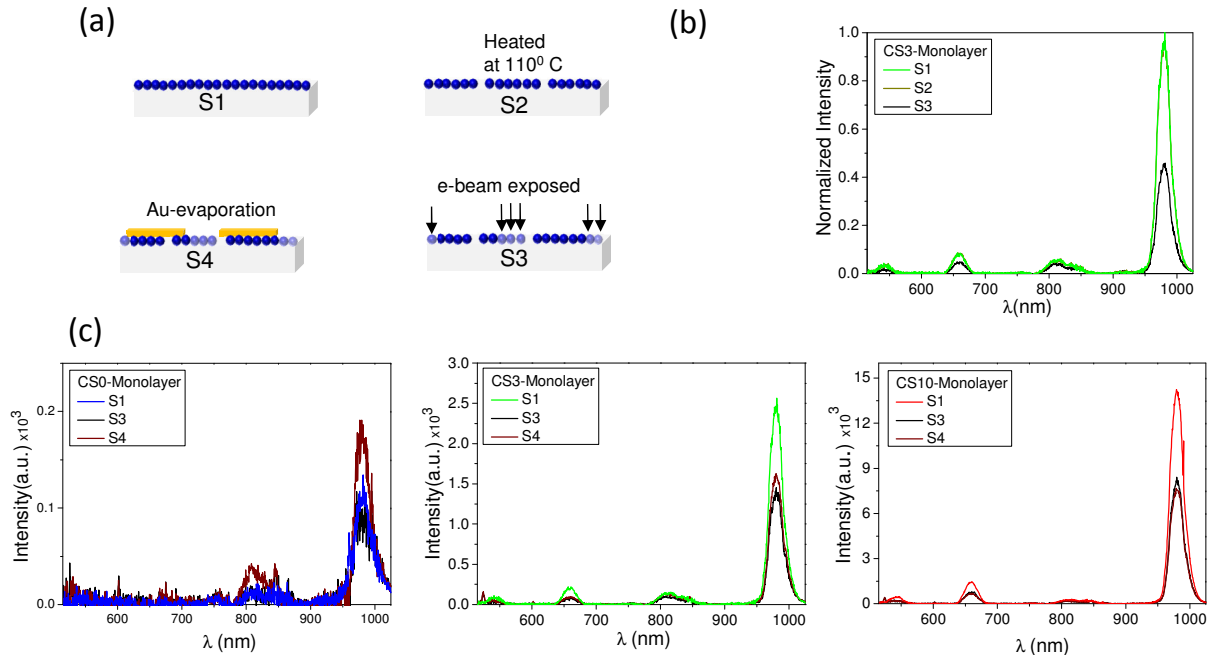


Figure S10: (a) Schematics of the samples at different stages, denoted S 1 to S 4, of Au-disc deposition on top of the monolayers process. (b) A variation in the upconversion luminescence of the samples before Au-disc depositions. The spectrum of S 2 is hidden below the S 1 spectrum. (c) The luminescence spectra of the representative samples in three different stages of the process. The color code is maintained for the untreated representative monolayers (S1).

References

- (1) Li, Z.; Zhang, Y. An efficient and user-friendly method for the synthesis of hexagonal-phase NaYF₄: Yb, Er/Tm nanocrystals with controllable shape and upconversion fluorescence. *Nanotechnology* **2008**, *19*, 345606.
- (2) Fischer, S.; Swabeck, J. K.; Alivisatos, A. P. Controlled Isotropic and Anisotropic Shell Growth in β -NaLnF₄ Nanocrystals Induced by Precursor Injection Rate. *Journal of the American Chemical Society* **2017**, *139*, 12325–12332, PMID: 28777550.
- (3) Fischer, S.; Bronstein, N. D.; Swabeck, J. K.; Chan, E. M.; Alivisatos, A. P. Precise

Tuning of Surface Quenching for Luminescence Enhancement in Core-Shell Lanthanide-Doped Nanocrystals. *Nano Letters* **2016**, *16*, 7241–7247, PMID: 27726405.

- (4) Johnson, N. J. J.; Korinek, A.; Dong, C.; van Veggel, F. C. J. M. Self-Focusing by Ostwald Ripening: A Strategy for Layer-by-Layer Epitaxial Growth on Upconverting Nanocrystals. *Journal of the American Chemical Society* **2012**, *134*, 11068–11071, PMID: 22734596.